Studien der elektrochemischen Konversion von Kohlenstoffdioxid zu Wertprodukten und der Optimierung von industriell relevanten Elektroreduktionen

Inauguraldissertation
zur Erlangung des akademischen Grades
eines *Doktor rerum naturalium (Dr. rer. nat.)*
vorgelegt dem Fachbereich 09: Chemie, Pharmazie, Geographie und Geowissenschaften

eingereicht von

JOHANNES SEIDLER
(geb. Pößnecker)

geboren in Löbau (DE)

Mai 2023

Dekanin: Prof. Dr. Eva Rentschler

Erster Gutachter: Prof. Dr. Siegfried R. Waldvogel

Zweiter Gutachter: Personenbezogene Daten

Fachnahes Mitglied der Prüfungskommission: Personenbezogene Daten

Datum der Promotionsprüfung: 11.09.2023

Wissen ist Nacht.
(Walter Moers)

Deklaration

Die experimentelle und schriftliche Ausarbeitung dieser Arbeit wurde von April 2019 bis Mai 2023 am Fraunhofer Institut für Grenzflächen-und Bioverfahrenstechnik IGB Straubing mit der Betreuung von Dr. Luciana Vieira durchgeführt. Die Experimente zur Reduktion von ʟ-Cystin sowie die Reduktion von 3-Nitrobenzotrifluorid wurden in den ESy-Labs Labors und an der Universität Mainz durchgeführt. Die wissenschaftliche Leitung lag bei Prof. Dr. S. R. Waldvogel. Hiermit erkläre ich, dass die vorliegende Dissertation von mir selbständig, ohne fremde Hilfe und mit keinen anderen als den darin angegebenen Hilfsmitteln angefertigt wurde, und dass die wörtlichen oder dem Inhalt nach aus fremden Arbeiten entnommenen Stellen, Zeichnungen, Skizzen, bildlichen Darstellungen und dergleichen als solche genau kenntlich gemacht sind.

Regensburg, 21.05.2023   Johannes Seidler

Danksagung

Personenbezogene Daten

Auflistung aller Publikationen

[1] J. Seidler, J. Strugatchi, T. Gärtner, S. R. Waldvogel, *Does Electrifying Organic Synthesis Pay off? The Energy Efficiency of Electro-Organic Conversions*, MRS Energy Sustain. **2020**, 7, E42. [DOI: 10.1557/mre.2020.42]

[2] J. Seidler, V. Landgraf, L. Vieira, D. Van Opdenbosch, S. R. Waldvogel, *Novel Cuprous Oxide Morphologies Using Amino Acids and Carboxylic Acids as Structure Directing Agents in a Simple Hydrothermal Method*, Mater. Lett. **2021**, 292, 129553. [DOI: 10.1016/j.matlet.2021.129553]

[3] J. Seidler, A. Roth, L. Vieira, S. R. Waldvogel, *Electrochemical CO_2 Utilization for the Synthesis of α-Hydroxy Acids.* ACS Sustain. Chem. Eng. **2023**, 11 (1), 390-398. [DOI: 10.1021/acs-suschemeng.2c06046]

[4] J. Seidler, R. Bernhard, S. Haufe, C. Neff, T. Gärtner, S. R. Waldvogel, *From Screening to Scale-Up: The DoE-Based Optimization of Electrochemical Reduction of L-Cystine at Metal Cathodes*, Org. Process Res. Dev. **2021**, 25 (12), 2622–2630. [DOI: 10.1021/acs.oprd.1c00153]

[5] C. M. Kisukuri, J. Seidler, T. Gärtner, D. F. Rohrmann, S. R. Waldvogel, *Scalable Electrochemical Reduction of Nitrobenzotrifluorides to 3-Trifluoromethylanilines*, Org. Process Res. Dev. **2023**, Article ASAP. [DOI: 10.1021/acs.oprd.3c00067]

Inhaltsverzeichnis

1 Einleitung und Motivation

1.1 Elektroorganische Synthese

Die Grundlage zur Erforschung elektrochemischer Prozesse wurde im Jahr 1800 von Alessandro Volta mit der Vorstellung der Volta'schen Säule gelegt.[1] Der Stapel aus Zink- und Kupferschichten stellt den Vorläufer heutiger Batterien dar und ermöglichte als Stromquelle elektrochemische Untersuchungen. Es dauerte noch bis 1833 bis Michael Faraday mit den Faradaygesetzen einen grundlegenden Zusammenhang zwischen übertragener Ladungsmenge und umgesetzter Materie beschrieb.[2] Auf Experimentbasis fand er, dass die umgesetzte Masse m einer Spezies proportional zur applizierten Ladung $Q = i * t$ ist:

$$m = const. * Q = const. * i * t$$

Die applizierte Ladung für die Oxidation bzw. Reduktion eines Mols Q_M ergibt sich aus der Avogadro-Konstante und der Elementarladung: $Q_M = N_A * e_0$. Das Produkt ergibt $96\,485\,\mathrm{C\,mol^{-1}}$ und wird als Faraday-Konstante F bezeichnet. Für die benötigte Ladung zur Elektrokonversion von n mol eines beliebigen Stoffes mit z Elektronen je Mol gilt der zentrale Zusammenhang:

$$Q = n * z * F$$

Für die thermodynamische Beschreibung des elektrochemischen Systems wird die freie Enthalpie (Gibbs-Energie) G verwendet. Allgemein gilt für die freie Enthalpie (als totales Differenzial):

$$dG = V\,dp - S\,dT + \delta W_x$$

Hierbei ist V das Volumen, p der Druck, S die Entropie, T die Temperatur und W_x eine weitere Energieform, welche im Fall des Ladungstransfers die Form EdQ mit der Ladung Q und der Potentialdifferenz $E = E_{Kathode} - E_{Anode}$ annimmt. Für konstanten Druck und Temperatur ergibt sich:

$$dG = EdQ$$

Nach Einsetzen der übertragenen Ladung pro Mol ($dQ = -zF$) erhält man:

$$dG = -zFE$$

Unter Standardbedingungen gilt $dG° = -zFE°$. Weiterhin gilt für die Gibbs-Energie unter Verwendung des idealen Gasgesetzes $\Delta G = \Delta G° + RTln(a_{red}/a_{ox})$. Setzt man nun die beiden

vorangegangenen Gleichungen ein und stellt nach E um, so erhält man die Nernst-Gleichung:[2]

$$E = E^\circ + \frac{RT}{zF} ln(\frac{a_{ox}}{a_{red}})$$

Dabei ist E das Elektrodenpotential, E° das Standardelektrodenpotential, R die universelle Gaskonstante, T die Temperatur, z die Anzahl der übertragenen Elektronen, F die Faraday-Konstante und a die Aktivitäten der Redoxspezies. Die Nernst-Gleichung erlaubt die Berechnung der Elektrodenpotentiale aus den Standardpotentialen, der Temperatur und den Aktivitäten, wobei häufig die Konzentrationen der Redoxspezies verwendet werden.

Die elektroorganische Synthese ist die elektrochemische Konversion von organischen Molekülen. Als frühes Beispiel wird häufig die Kolbe-Elektrolyse (nach Hermann Kolbe, Mitte 19. Jh.) aufgeführt. Oxidativ werden Carbonsäuren $R-COOH$ decarboxyliert, wobei die Kupplung der Reste zum $R-R$ Produkt führt.[1] Überraschenderweise hat die elektroorganische Synthese im ausklingenden 19. und dem folgenden 20. Jahrhundert vergleichsweise wenig Aufmerksamkeit erhalten. Einsatzgebiete der Elektrochemie waren vorwiegend elektroanalytische Methoden, die Batterietechnik oder anorganische Anwendungen, wie die Chlor-Alkali-Elektrolyse.[3,4] Ein nennenswertes Beispiel aus der elektroorganischen Synthese ist die Hydrodimerisierung von Acrylnitril zu Adiponitril im Baizer-Prozess aus den 1960er Jahren:[5] $2\,CH_2=CHCN + 2\,H^+ + 2\,e^- \longrightarrow NC(CH_2)_4CN$. Das erhaltene Adiponitril ist ein wichtiges Zwischenprodukt in der Herstellung von Polyamiden.

Erst in den vergangenen Jahrzehnten erlebte die elektroorganische Synthese eine Renaissance. Entscheidende Faktoren sind das allgemein wachsende Interesse an ressourcenschonenden, nachhaltigen Technologien und die zunehmende Verfügbarkeit von regenerativem Strom. In der elektroorganischen Synthese werden chemische Reduktions- und Oxidationsmittel durch das Elektron selbst ersetzt. Damit können Reagenzien eingespart, Sicherheitsvorkehrungen entschärft, chemischer Abfall reduziert und bestenfalls die Produktaufbereitung vereinfacht werden. Des Weiteren sind elektroorganische Konversionen von Natur aus skalierbar.[4] Außerdem kann im Gegensatz zu konventionellen Redoxreaktionen in der elektroorganischen Synthese über die Steuerung des Elektrodenpotentials gezielt Einfluss auf den Reaktionsweg genommen werden, und Limitierungen von herkömmlichen Reduktions- oder Oxidationsmitteln überwunden werden.[3]

Elektroorganische Reaktionen können unterschiedlichen Reaktionswegen folgen, abhängig von den herrschenden Bedingungen. Gemeinsam ist ihnen allerdings der initiale Elektronentransfer, welcher die vorliegende Spezies R in eine reaktive Form umsetzt (Abbildung 1.1). An der Anode wird ein Elektron aus dem höchsten besetzten Molekülorbital (*HOMO*) der organischen Komponente entfernt und die reaktive Spezies $R^{\bullet+}$ gebildet. Analog wird an der Kathode ein Elektron in das niedrigste unbesetzte Molekülorbital (*LUMO*) transferiert und die Spezies $R^{\bullet-}$ gebildet.[5] Die Folgereaktionen der reaktiven Spezies hängen stark von Reaktionsbedingungen ab. Ein Beispiel liefert die Oxidation von Carboxylaten. Nach dem Elektronentransfer wird
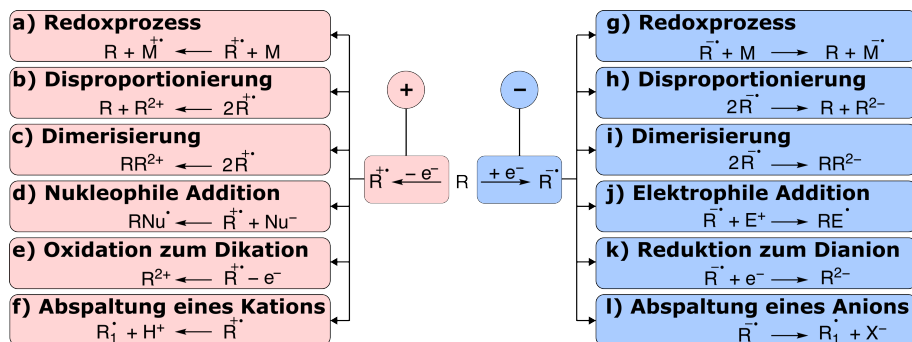
a) Redoxprozess
$$R + M^{\cdot+} \longleftarrow R^{\cdot+} + M$$
b) Disproportionierung
$$R + R^{2+} \longleftarrow 2R^{\cdot+}$$
c) Dimerisierung
$$RR^{2+} \longleftarrow 2R^{\cdot+}$$
d) Nukleophile Addition
$$RNu^{\cdot} \longleftarrow R^{\cdot+} + Nu^{-}$$
e) Oxidation zum Dikation
$$R^{2+} \longleftarrow R^{\cdot+} - e^{-}$$
f) Abspaltung eines Kations
$$R_1^{\cdot} + H^{+} \longleftarrow R^{\cdot+}$$

g) Redoxprozess
$$R^{\cdot-} + M \longrightarrow R + M^{\cdot-}$$
h) Disproportionierung
$$2R^{\cdot-} \longrightarrow R + R^{2-}$$
i) Dimerisierung
$$2R^{\cdot-} \longrightarrow RR^{2-}$$
j) Elektrophile Addition
$$R^{\cdot-} + E^{+} \longrightarrow RE^{\cdot}$$
k) Reduktion zum Dianion
$$R^{\cdot-} + e^{-} \longrightarrow R^{2-}$$
l) Abspaltung eines Anions
$$R^{\cdot-} \longrightarrow R_1^{\cdot} + X^{-}$$

$$R^{\cdot+} \xrightarrow{-e^{-}} R \xrightarrow{+e^{-}} R^{\cdot-}$$

Abbildung 1.1: Folgereaktionen von anodisch und kathodisch generierten Radikalionen.[2]

CO_2 abgespalten und es entsteht ein Alkylradikal, welches vier verschiedene Folgereaktionen eingehen kann. Bei hohen Stromdichten, Abwesenheit von Wasser und niedriger Temperatur (etwa Raumtemperatur) entsteht das Rekombinationsprodukt. Bei Anwesenheit von Wasser wird nach weiterer Oxidation der endständige Alkohol gebildet, wohingegen erhöhte Temperaturen ($>65\,^\circ$C) die Disproportionierung des Radikals fördern. Niedrige Stromdichten schieben die Produktpalette Richtung Alkohol und Olefin.[6,7]

Bei der Durchführung elektroorganischer Synthesen müssen daher zusätzlich zu den klassischen Parametern Temperatur, Druck und Konzentration der Reaktanten noch eine Reihe weiterer Faktoren berücksichtigt werden: Zelldesign (z.B. Topf- oder Flusszelle, Elektrodenabstand), Elektrolytzusammensetzung, Elektrodenmaterialien, Stromdichte und applizierte Ladungsmenge. Ein Beispiel für den besonderen Effekt des Lösungsmittels ist die Kupplung von Arenen in 1,1,1,3,3,3-Hexafluor-2-propanol (HFIP). Bei der Kupplung unterschiedlicher Arene wird üblicherweise ein statistisches Gemisch aus Homo- und Kreuzkupplungsprodukten erreicht. Es konnte gezeigt werden, dass mithilfe von HFIP die Selektivität stark in Richtung der Kreuzkupplungsprodukte verschoben werden kann.[8]

In jeder elektrochemischen Reaktion laufen Anoden- und Kathodenvorgänge gleichzeitig ab. Die Reaktion an der Gegenelektrode ist häufig die Konversion von Leitsalz oder die Dekomposition des Lösungsmittels.[9] Zur Verbesserung der Stromeffizienz und Nachhaltigkeit des Systems können unter Umständen beide Elektrodenreaktionen genutzt werden. Für diese "gepaarten Elektrosynthesen" gibt es verschiedene Szenarien: parallele gepaarte Elektrosynthese, konvergente und divergente Elektrosynthese und Dominoelektrosynthese (Abbildung 1.2).[10] In allen Fällen der gepaarten Elektrosynthese ist die Abstimmung bzw. Kompatibilität der jeweiligen Elektrodenpotentiale extrem wichtig.
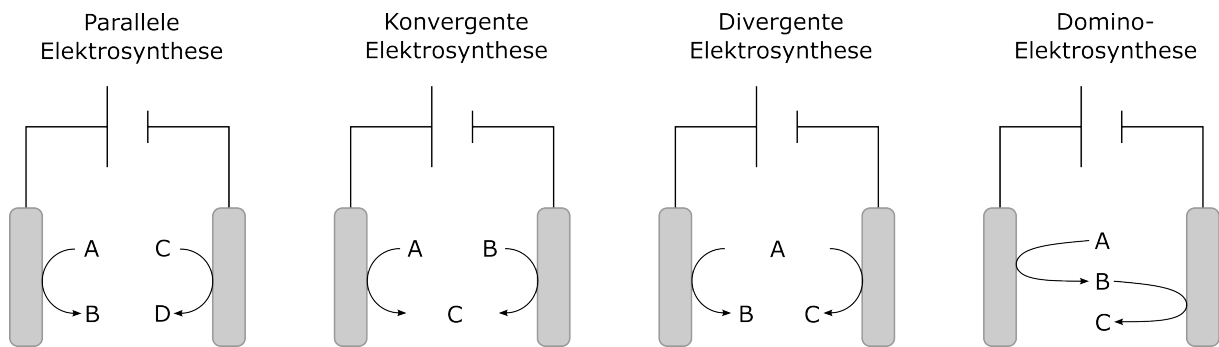
Abbildung 1.2: Verschiedene Modi von gepaarten Elektrosynthesen.[10]

1.2 Elektrochemische Zellen und Elektrodenmaterialien

Der einfachste Aufbau einer elektrochemischen Zelle besteht aus einem inerten Gefäß (z.B. Glas oder Teflon), der Kathode, der Anode und dem Elektrolyten (Abbildung 1.3).[11] Befinden sich Anode und Kathode im selben Kompartment, spricht man von einer ungeteilten Zelle. Werden beide Elektroden durch einen Separator (z.B. eine Ionenaustauschermembran oder eine poröse Keramik) separiert, wird dies eine geteilte Zelle genannt. Da die stattfindenden Reaktionen prinzipiell abhängig von dem angelegten Elektrodenpotential sind, kommt in manchen Anwendungen eine Referenzelektrode hinzu, mithilfe derer sich das Elektrodenpotential gegenüber der jeweiligen Arbeitselektrode steuern bzw. messen lässt (Abbildung 1.4a). Ein
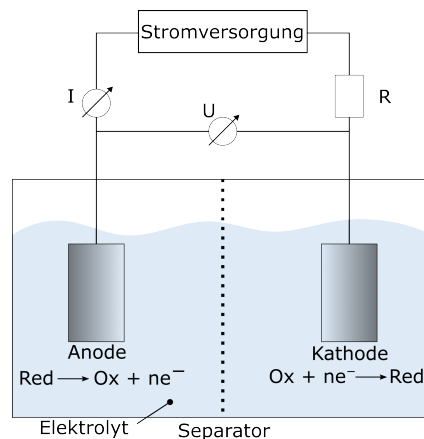

Abbildung 1.3: Schematischer Aufbau einer einfachen elektrochemischen Zelle.

Drei-Elektroden-Aufbau kommt zum Einsatz, wenn das Elektrodenpotential eingestellt wird (*potentialkontrolliert*) oder während der Elektrolyse gemessen werden soll. Dies ist beispielsweise bei Cyclovoltammetriemessungen der Fall.[2] Ein Zwei-Elektroden-Aufbau, beispielsweise in Form einer H-Typ Zelle (Abbildung 1.4b) wird in galvanostatischen Elektrokonversionen verwendet. Die Ausführung als ungeteilte Zelle wird Topfzelle genannt. Um das Verhältnis von Elektrodenfläche zu Zellvolumen zu vergrößern und den Abstand zwischen den Elektroden zu verringern, können Flusszellen (Abbildung 1.4c) verwendet werden.[10] Der Elektrolyt wird durch einen schmalen Spalt zwischen den Elektroden gepumpt. Der geringe Elektrodenabstand verringert die Zellspannung,
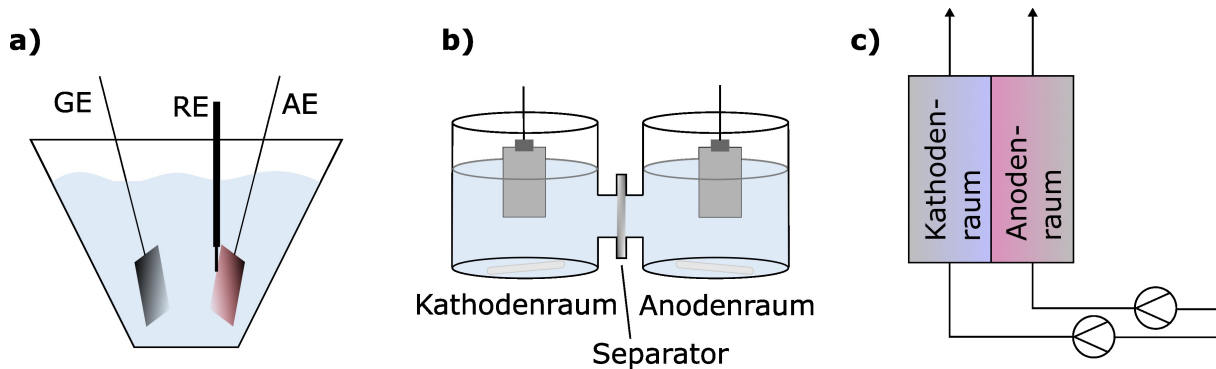
Abbildung 1.4: Beispiele von elektrochemischen Zellen: a) Drei-Elektroden-Aufbau mit Arbeitselektrode (AE), Gegenelektrode (GE) und Referenzelektrode (RE). b) H-Typ-Zelle mit Magnetrührer und Separator. c) Flusszelle.

wodurch der Energiebedarf der Reaktion gesenkt wird. Ein großes Elektroden/Zellvolumen-Verhältnis verbessert außerdem den Stofftransport zur Elektrode. Durch das Anströmen der Elektroden mit frischem Elektrolyten wird eine effektivere Temperierung im Vergleich zu Topfzellen erreicht. Der Einsatz von Flusszellen erleichtert außerdem den Übertrag auf einen kontinuierlichen Prozess. Die transferierte Ladung kann entweder während eines Zelldurchgangs (*single-pass*) oder mehrerer Zelldurchgänge (*batch-recycle* oder als Kaskade) appliziert werden. Im einfachen Zelldurchlauf ist die Durchflussgeschwindigkeit $\dot{V}$ nicht unabhängig wählbar, da sie von der Stromstärke $I = J * A$, der Stoffmengenkonzentration c und der applizierten Ladung z (Elektronen je Molekül Edukt) abhängt:

$$\dot{V} = \frac{J * A}{c * z * F}$$

Wobei F die Faraday-Konstante darstellt.

Für die Reaktorauslegung im Zuge einer Skalierung können die konventionellen idealen Reaktortypen herangezogen werden: a) *Batch*-Reaktor, b) *Plug flow* Reaktor, c) *Continuous stirred tank reactor* (CSTR). In der Elektrokonversion wird dann die Änderung der Konzentration mithilfe des Faradaygesetzes beschrieben. So wird aus der Veränderung der Konzentration im *Batch*-Reaktor (Reaktion erster Ordnung angenommen)[12]

$$\frac{\mathrm{d}c_t}{\mathrm{d}t} = -kc_t$$

unter Verwendung des Faradaygesetzes zu

$$-\frac{\mathrm{d}c_t}{\mathrm{d}t} = \frac{i_t}{zFV_R}$$

Über das Einsetzen von $i_t = k_L A z F c_t$ (aus dem Faraday-Gesetz und der Definition des Stoffübergangskoeffizienten k_L) enthält die Differentialgleichung wieder die zeitabhängige Konzentration. Analog kann für die übrigen idealen Reaktortypen vorgegangen werden, wobei

der entscheidende Schritt die Verwendung des Faradaygesetzes ist.[12]

Zum Aufbau des elektrochemischen Systems gehören neben den elektrochemischen Zellen die Elektroden. Da der Ladungstransfer in der Elektrosynthese zwischen Elektrode und umgebendem Medium stattfindet, spielt die für den Stoffumsatz verwendete Elektrode meist eine besonders große Rolle. Dabei sind neben dem Material der Elektrode auch die Oberflächenbeschaffenheit (rau, glatt, porös), Elektrodengeometrie oder Abstand zwischen Anode und Kathode von Bedeutung.[13] Ein Beispiel für den Einfluss des Elektrodenmaterials findet sich in der elektrochemischen CO_2-Reduktion, wo CO_2 weitgehend selektiv zu CO (Ag-Elektroden) oder Formiat (Sn-Elektroden) reduziert wird.[14] Welchen Effekt ein bestimmtes Elektrodenmaterial hervorruft, kann meist nicht vorhergesagt werden. Die Auswahl des Materials erfolgt daher meist empirisch auf Basis eines Elektroden-Screenings.[15] Eine Auswertung von über 900 Studien zu Elektrosynthesen von Heard und Lennox[13] ergab, dass die Elektrodenmaterialien Platin, Glaskohlenstoff und Graphit gemeinsam in über 75 % der einschlägigen Veröffentlichungen vorkommen.

Der Mechanismus des Elektronentransfers an der Elektrode kann durch zwei Grenzfälle beschrieben werden.[13] Im ersten Fall stellt die Elektrode lediglich eine Elektronensenke oder -quelle dar und der Ladungsübertrag ist unabhängig vom inerten Elektrodenmaterial. Bei diesen *outer-sphere* Elektronentransfers sind die gebildeten Produkte für unterschiedliche Elektrodenmaterialien gleich. Im zweiten Grenzfall ist der Mechanismus des Elektronenübergangs eng mit dem Material der Elektrode verknüpft. In diesem Fall werden Produkte, Reaktionsmechanismus und Kinetik stark vom Elektrodenmaterial beeinflusst und unterscheiden sich mitunter drastisch bei einem Wechsel des verwendeten Materials.

Das für eine Reaktion benötigte Potential, welches über das Standardpotential hinausgeht, wird Überpotential genannt.[13] Das Überpotential für verschiedene Reaktionen wird häufig durch das verwendete Elektrodenmaterial beeinflusst. Beispielsweise benötigt die Wasserstoffentwicklung ($2\,H^+ + 2\,e^- \longrightarrow H_2\uparrow$) an der Bleielektrode und der Bor-dotierten Diamantelektrode (BDD) ein besonders hohes Überpotential. Dadurch können Elektrokonversionen von organischen Molekülen in protischen Medien auch bei sehr negativem Potential durchgeführt werden, mit nur geringem Ladungsverlust durch die parasitäre Wasserstoffentwicklung. Andersherum kann ein Elektrodenmaterial das Überpotential für eine bestimmte Reaktion herabsetzen wodurch diese thermodynamisch begünstigt wird. Man spricht von Elektrokatalyse bzw. Elektrokatalysatoren. Meist kommen in Elektrokonversionen planare Elektroden zum Einsatz. Sie sind vergleichsweise simpel in der Herstellung und lassen sich leicht reinigen. Für eine vergrößerte Oberfläche werden Gitter oder poröse Schäume verwendet. Eine weitere Möglichkeit ist die Immobilisierung von Elektrokatalysatorpartikeln auf einem leitenden Trägermaterial.[16] Eine besondere Bauform stellen Gasdiffusionselektroden dar. Sie bestehen aus einer porösen, semi-permeablen Schicht auf Kohlenstoffbasis und trennen den flüssigen Elektrolyten von einem anliegenden Gas. Das Gas diffundiert durch die Gasdiffusionsschicht und gelangt zum Katalysatormaterial, wo es nun gleichzeitig mit dem flüssigen Elektrolyten vorliegt (Abbildung 1.5). Hier kann es nun eine elektrochemisch initiierte Reaktion eingehen. Gasdiffusionselektroden kommen zum Einsatz,

wenn das zu reagierende Gas eine besonders schlechte Löslichkeit im Elektrolyten besitzt und nur im gasförmigen Zustand an die Elektrode gebracht werden kann. Frühe Beispiele sind Brennstoffzellen in denen H_2 und O_2 umgesetzt werden.[2] Gasdiffusionselektroden werden auch in der elektrochemischen CO_2-Reduktion eingesetzt.[17]
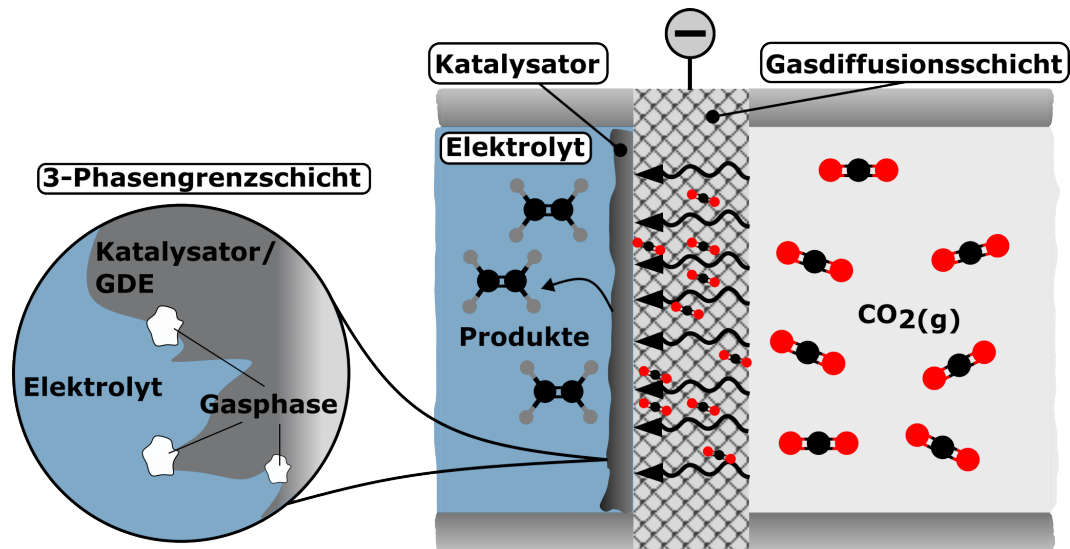

Abbildung 1.5: Schema einer Gasdiffusionselektrode am Beispiel der elektrochemischen CO_2-Reduktion.

1.3 Cyclovoltammetrie

Zur Charakterisierung elektrochemischer Systeme kommen häufig elektroanalytische Methoden wie Chronoamperometrie und Voltammetrie zum Einsatz. Eine oft angewandte Methode ist die Cyclovoltammetrie (CV), bei welcher das Elektrodenpotential mit einer bestimmten Geschwindigkeit verändert wird und der resultierende Strom gemessen wird.[2] Üblicherweise kommen in CV-Messungen Aufbauten mit drei Elektroden zum Einsatz (Arbeitselektrode, Gegenelektrode und Referenzelektrode). Das anliegende Elektrodenpotential wird mithilfe eines Potentiostaten gesteuert. Dabei handelt es sich stets um das Elektrodenpotential der Arbeitselektrode in Bezug auf die Referenzelektrode. Bezüglich des Designs der Messzelle ist zu beachten, dass der Abstand zwischen Arbeits- und Referenzelektrode minimal ist, um den Spannungsabfall (*iR-drop*) über den dazwischen liegenden Elektrolyten zu minimieren.

Während der Messung wird das Elektrodenpotential konstant mit der Vorschubgeschwindigkeit v verändert, bis das jeweilige Umkehrpotential E_t^a bzw. E_t^c erreicht wird (Abbildung 1.6). Auf diese Weise können mehrere Zyklen hintereinander aufgenommen werden. Befinden sich im Elektrolyten Komponenten, welche im Bereich zwischen E_t^a und E_t^c redoxaktiv sind, so kann die Reduktion bzw. Oxidation als Peak im Cyclovoltammogramm sichtbar werden. Der so gemessene Strom, welcher mit einem Stoffumsatz an der Elektrode einhergeht, wird als Faraday-
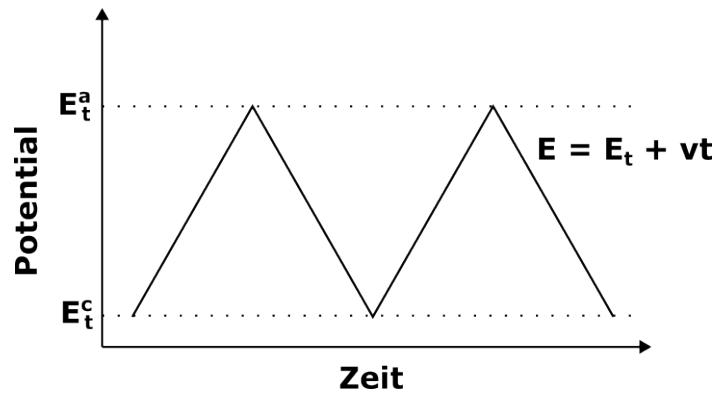
Abbildung 1.6: Zeitliche Veränderung des Elektrodenpotentials während einer CV-Messung. Die Änderungsrate wird als Vorschubgeschwindigkeit v bezeichnet.

Strom bezeichnet.[18] Dabei wird die Spezies des Elektrolyten an der Elektrode umgesetzt und diffundiert entweder zurück oder wird als neue Phase abgeschieden, bzw. betritt die Gasphase. Diese Prozesse folgen den Faradayschen Gesetzen (Proportionalität zwischen umgesetzter Stoffmenge und applizierter Ladung), daher wird von Faraday-Strom gesprochen.

Zusätzlich kommt es durch das angelegte Potential zu einer Akkumulation von Ladung entlang der Elektrode. Dabei gibt es zwischen Elektrode und umgebender Phase keinen Übergang von Elektronen. Solche Prozesse werden nicht-faradaisch oder kapazitiv genannt.

Entsteht als Folge des angelegten Potentials ein Faraday-Strom, nimmt der gemessene Strom zunächst mit dem Betrag des Elektrodenpotentials stark zu. Die übliche Vorzeichenkonvention sieht einen negativ gehenden Strom für Reduktions- und einen positiv gehenden Strom für Oxidationsvorgänge vor. Wird durch das erreichte Potential ein Elektronenübertrag initiiert,
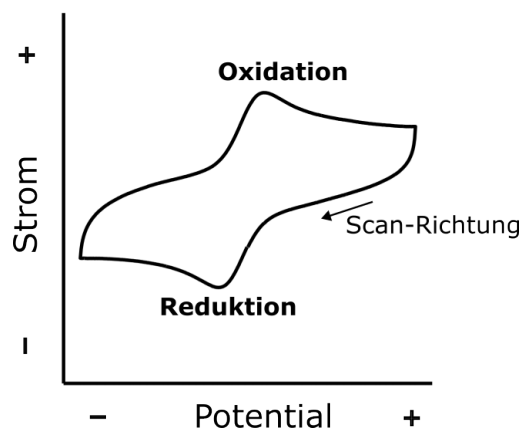

Abbildung 1.7: Beispielhaftes Cyclovoltammogramm mit Reduktions- und Oxidationswelle.

steigt der Strom aufgrund der stattfindenden Reaktion an. Gleichzeitig sinkt die Konzentration der umgesetzten Spezies an der Elektrodenoberfläche gegenüber der Konzentration in größerer Distanz zur Elektrode. Durch den Konzentrationsgradienten kommt es zur Diffusion der aktiven Spezies hin zur Elektrode. Die Diffusionsschicht verbreitert sich dabei mit zunehmender Zeit. Ist letztlich der Elektronenübergang schneller als die Diffusion der redoxaktiven Spezies hin zur

Elektrode, so nimmt der Strom ab. Als Resultat kann ein Peak im Voltammogramm beobachtet werden.

Mithilfe von Cyclovoltammetriemessungen können verschiedene Erkenntnisse über das elektrochemische System gewonnen werden. So kann beispielsweise mit CV-Messungen das elektrochemische Fenster des Systems bestimmt werden. Der maximale Potentialbereich in dem keine elektrochemische Zersetzung des Elektrolyten oder der Elektrode auftritt, wird elektrochemisches Fenster genannt. Der Potentialbereich ist abhängig von dem Elektrolytsystem und der verwendeten Elektrode und ist verknüpft mit dem Überpotential, welches für die Elektrolytzersetzung im jeweiligen System nötig ist.[19] In elektroorganischen Reaktionen wird üblicherweise angestrebt, den gewünschten Stoffumsatz innerhalb des elektrochemischen Fensters durchzuführen, sodass es zu keiner Zersetzung des Elektrolyten kommt. Beispielsweise werden für Reduktionen in protischen Medien Bleielektroden, Bleilegierungen oder Kohlenstoffmaterialien wie die Bor-dotierte Diamantelektrode verwendet, da diese ein hohes Überpotential für die Wasserstoffentwicklung besitzen.[19–21]

Eine weitere Anwendung ist die Bestimmung der elektrochemischen aktiven Oberfläche der Elektrode (ECSA – *electrochemical active surface area*). Üblicherweise wird die Stromdichte als Strom, bezogen auf die geometrische Fläche der Elektrode angegeben. In manchen Fällen, beispielsweise im Vergleich von nanostrukturierten Elektrokatalysatoren, ist es ratsam, den applizierten Strom für bessere Vergleichbarkeit der Systeme auf die tatsächlich aktive Fläche zu beziehen.[14] Für die Bestimmung der ECSA mithilfe von CV-Messungen gibt es grundsätzlich zwei Möglichkeiten: kapazitive und faradaische Methoden.

Der kapazitive Ansatz bedient sich der Bestimmung der Kapazität der elektrochemischen Doppelschicht C_{DL}. Sie ist ein quantitativer Indikator der für Elektrolytspezies zur Verfügung stehenden Elektrodenfläche.[16] Für die Umrechnung wird die flächenspezifische Kapazität C_S benötigt, welche die Kapazität einer perfekt ebenen Elektrodenoberfläche darstellt.[22]

$$ECSA = \frac{C_{DL}}{C_S}$$

Für die Bestimmung von C_{DL} wird ein Potentialfenster ohne Faraday-Ströme gewählt und es werden Zyklen bei verschiedenen Vorschubgeschwindigkeiten aufgenommen (Abbildung 1.8). Dabei korreliert die Vorschubgeschwindigkeit linear mit dem mittig zwischen den Umkehrpotentialen gemessenen Strom.[16] Die Kapazität der Doppelschicht wird dann über den Anstieg in Abbildung 1.8b berechnet:

$$C_{DL} = \frac{\mathrm{d}j_c}{\mathrm{d}v}$$

Die Achillesferse der ECSA-Bestimmung über die Kapazität der elektrochemischen Doppelschicht ist die Verwendung der flächenspezifischen Kapazität C_S. Diese ist stark abhängig von der Natur des Elektrodenmaterials sowie des Elektrolyten. Oxidschichten auf der Elektrode haben ebenfalls einen großen Effekt auf den Wert von C_S und verschiedene Oxidationszustände
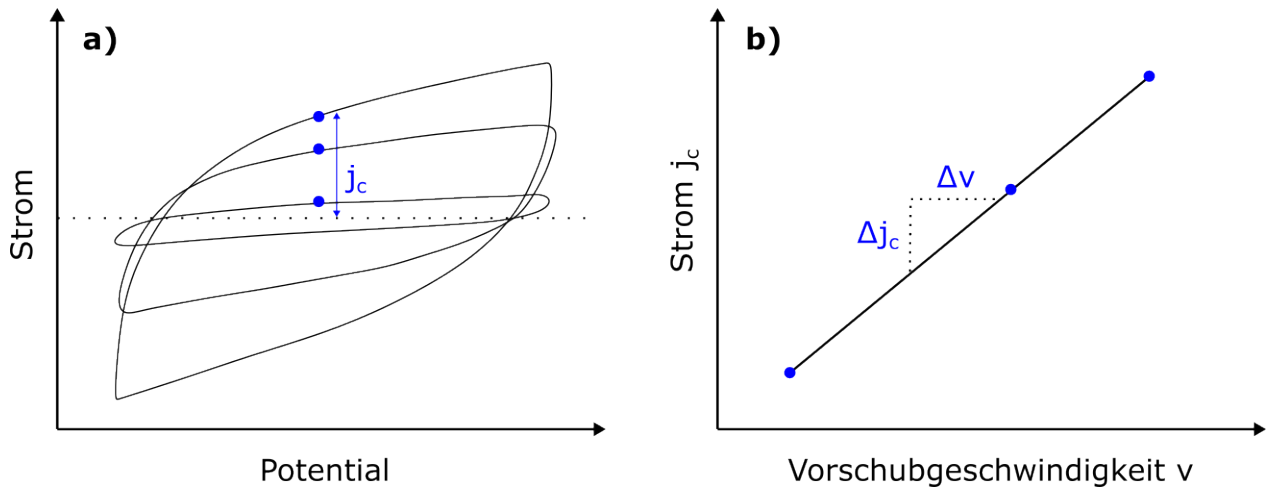
Abbildung 1.8: CV bei verschiedenen Vorschubgeschwindigkeiten im nicht-faradaischen Bereich (a) und Auftragung der Vorschubgeschwindigkeiten gegen die gemessene Stromstärke in der Mitte des Potentialfensters (b).

des selben Elements können C_S um teils 100 % variieren.[22]

Alternativ zum kapazitiven Ansatz können auch Faraday-Ströme zur Berechnung der ECSA genutzt werden. Hierbei werden ebenfalls Zyklen mit unterschiedlichen Vorschubgeschwindigkeiten aufgenommen. Gemessen wird der Faraday-Strom bei Konversion einer redoxaktiven Spezies an der Elektrode (Abbildung 1.9). Der mathematische Zusammenhang wird über die
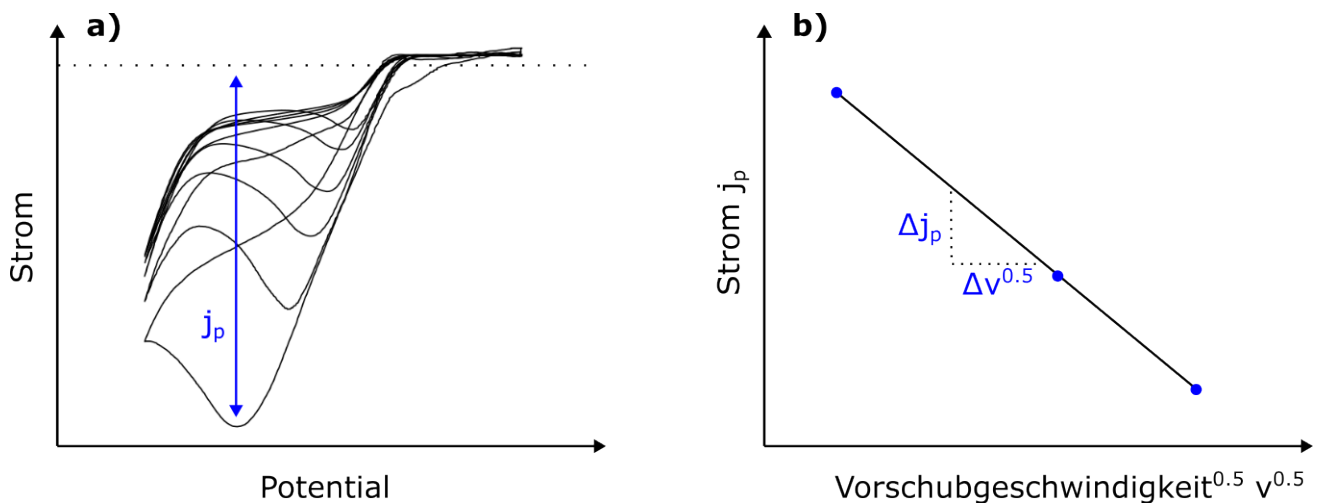

Abbildung 1.9: CV bei verschiedenen Vorschubgeschwindigkeiten im faradaischen Bereich (a) und Auftragung der Wurzel der Vorschubgeschwindigkeiten gegen die gemessene Peak-Stromdichte (b).

Randles-Sevcik Gleichung beschrieben. Für schnellen Elektronentransfer gilt:[2]

$$j_{max} = \frac{I_{max}}{A_{Elektrode}} = 2.69 \times 10^5 * n^{\frac{3}{2}} * D^{\frac{1}{2}} * c^0 * v^{\frac{1}{2}}$$

Dabei ist j_{max} die gemessene Peak-Stromdichte, n ist die Anzahl der übertragenen Elektronen, D ist der Diffusionskoeffizient der redoxaktiven Spezies und c^0 dessen initiale Konzentration

und v ist die Vorschubgeschwindigkeit. Mithilfe des bestimmten Anstiegs aus Abbildung 1.9b kann die aktive Elektrodenfläche bestimmt werden:

$$\frac{\mathrm{d}I_{max}}{\mathrm{d}(v^{\frac{1}{2}})} = 2.69 \times 10^5 * n^{\frac{3}{2}} * D^{\frac{1}{2}} * c^0 * A_{Elektrode}$$

Allerdings gibt es auch bei dieser Herangehensweise eine Schwachstelle, da bei der Bestimmung der aktiven Fläche A der Diffusionskoeffizient der umgesetzten Spezies bekannt sein muss. Häufig werden Referenzsubstanzen wie Ferrocen verwendet, bei denen der Diffusionskoeffizient im genutzten Medium bekannt ist.

1.4 Elektrochemische Verwendung von Kohlenstoffdioxid

Kohlenstoffdioxid (CO_2) ist das Endprodukt aller Verbrennungsprozesse von kohlenstoffhaltigen Materialien und akkumuliert seit der industriellen Revolution und der massenhaften Verbrennung fossiler Rohstoffe zunehmend in der Atmosphäre.[23] Da die CO_2-Konzentration in der Atmosphäre einen signifikanten Beitrag zum Treibhauseffekt liefert und fossile Rohstoffe auf lange Sicht in ihrer Förderung unwirtschaftlich werden, ist es naheliegend, Ansätze zu entwickeln, Kohlenstoffdioxid aus der Atmosphäre zurückzugewinnen und als Rohstoff nutzbar zu machen. Ein wichtiger Schritt in Richtung eines geschlossenen Kohlenstoffkreislaufs ist die Nutzung von CO_2 für die Herstellung von Treibstoffen und Chemikalien.

Chemisch gesehen ist CO_2 ein stabiles Molekül, wodurch es nicht beliebig zur Reaktion gebracht werden kann.[24] In CO_2 hat der Kohlenstoff seine höchste Oxidationsstufe ($+4$) und mit einer Standardbildungsenthalpie von $\Delta G_f^\circ = -394\,\mathrm{kJ\,mol^{-1}}$ ist CO_2 ein sehr energiearmes Molekül.[24] Wird das lineare CO_2 Molekül, beispielsweise durch Adsorption an einer Katalysatoroberfläche, in eine leicht gewinkelte Form gebracht, so verringert sich die Energie des LUMOs deutlich, wodurch ein Elektronentransfer erleichtert wird.[24] Außerdem kann Kohlenstoffdioxid mit starken Nukleophilen, wie Grignard-Verbindungen, reagieren.[25]

Aufgrund der Limitierungen in der Aktivierung von CO_2 existieren erst wenige industrielle Prozesse, welche Kohlenstoffdioxid als C_1-Baustein verwenden (Abbildung 1.10). Für ein nachhaltiges Szenario mit geschlossenem Kohlenstoffkreislauf muss die Triebkraft für die Aktivierung von CO_2 aus erneuerbaren Quellen stammen. Eine elektrochemisch initiierte Konversion von CO_2, welche mit regenerativem Strom betrieben wird, bietet sich daher besonders an. Durch die direkte Bereitstellung von Elektronen für die Reduktion werden chemische Reduktionsmittel vermieden. Generell findet dabei die Aktivierung von CO_2 entweder direkt über Elektronentransfer statt, oder es wird elektrochemisch eine nukleophile Spezies gebildet, welche anschließend mit CO_2 reagiert.

Die Studien zur elektrochemischen Nutzung von CO_2 können grob in zwei Themengebiete geteilt werden (Abbildung 1.11). Das erste beschäftigt sich mit der Konversion von CO_2 in
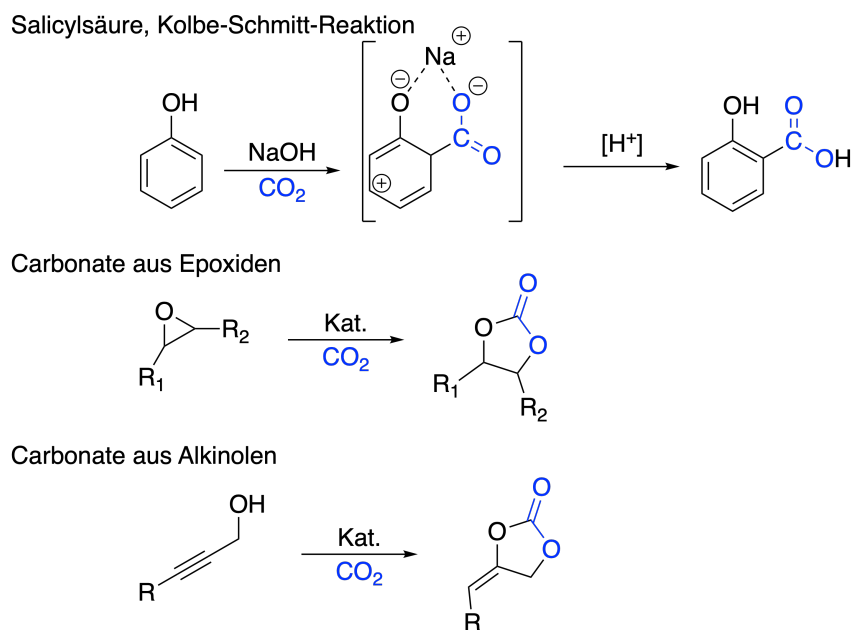
Abbildung 1.10: Industrielle Reaktionen für die Inkorporation von Kohlenstoffdioxid in organische Moleküle.[25,26]

energiereichere, aber ebenfalls kleine Moleküle, wie Formiat, Kohlenstoffmonoxid oder Ethylen. Dieser Ansatz gliedert sich demnach in die *Carbon Capture and Utilization* (CCU) Strategie ein.[23] Langfristiges Ziel ist hierbei die Umwandlung von Kohlenstoffdioxid in großem Stil und die Produktion von Plattformchemikalien. Die Produkte können beispielsweise per Drop-in in die Herstellung von Polymeren (Polyethylen) oder Kohlenwasserstoffen (CO und H_2, Fischer-Tropsch-Synthese) fließen. Um die Konsistenz des Ansatzes zu wahren, muss in der technischen Anwendung regenerativer Strom für die Konversion genutzt werden. Die direkte Reduktion von CO_2 zu Plattformchemikalien würde im Idealfall unter geeigneten Rahmenbedingungen die fossil-basierte Herstellung ablösen.[27] Die treibende Kraft in diesem Themenkomplex ist die Schaffung geschlossener Kohlenstoffkreisläufe unter Verwendung von Kohlenstoffdioxid als Rohstoff. Die in der Literatur häufig anzutreffende Formulierung „Elektrochemische CO_2-Reduktion" meint meist die Konversion im Rahmen dieses Themengebiets, nicht aber die Inkorporation in organische Verbindungen.[28–33] Häufig ist auch die Abkürzung CO_2RR (CO_2 reduction reaction), welche auch in dieser Arbeit verwendet wird, zu finden. Die CO_2RR wird meist in wässrigen Elektrolyten durchgeführt.[38] Da die Löslichkeit von CO_2 in Wasser vergleichsweise niedrig ist, werden Gasdiffusionselektroden eingesetzt, wodurch die Konzentration von Kohlenstoffdioxid an der Elektrodenoberfläche angehoben wird. Folglich kann die Reaktion mit einer schnelleren Rate (also höheren Stromdichte) betrieben werden. Da ein hohes Überpotential nötig ist um CO_2 zur Reaktion zu bringen, kommt es neben der CO_2-Reduktion zur Wasserstoffentwicklung, welche die zentrale parasitäre Reaktion zur CO_2RR darstellt.

Die elektrochemische CO_2-Reduktion kann auch in nicht-wässrigen Lösungsmitteln, wie Acetonitril, *N,N*-Dimethylformamid oder Methanol durchgeführt werden.[38] Gegenüber Wasser haben diese eine höhere CO_2-Löslichkeit und führen aufgrund der geringeren Protonenkonzentration
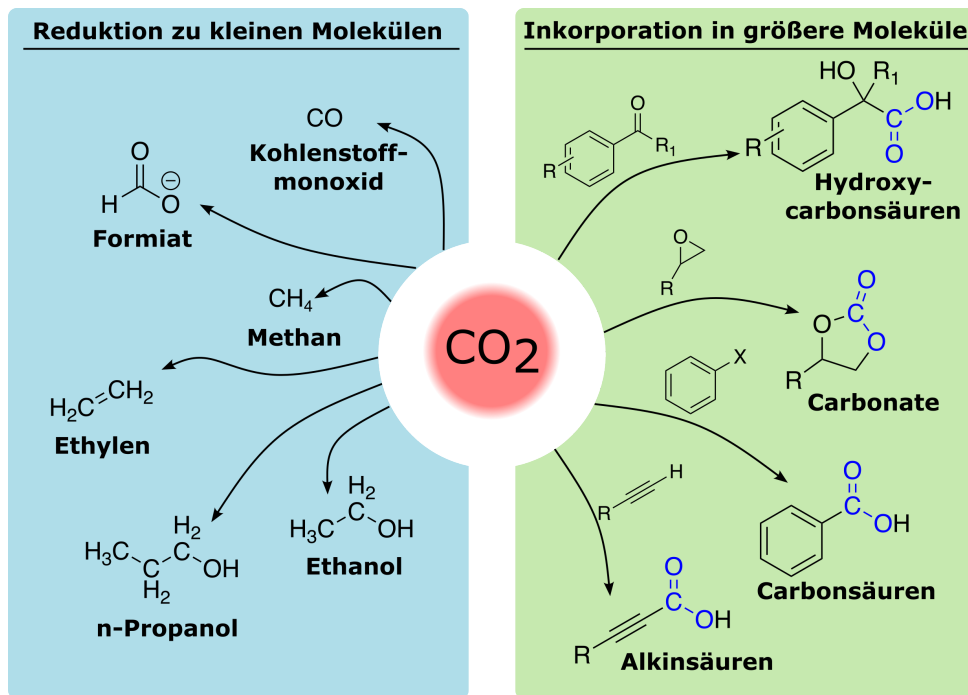
Abbildung 1.11: Elektrochemische Konversionen von CO_2 zu Wertprodukten.[34–37]

zu weniger H_2-Entwicklung.[38] Da bei der Verwendung von organischen Lösungsmitteln die Reaktionsprodukte grundsätzlich von CO_2 und/oder dem Lösungsmittel stammen können, müssen besondere Vorkehrungen getroffen werden (z.B. Isotopenmarkierung) um den Ursprung des Produkts einwandfrei nachzuweisen. Die Faraday-Effizienz für CO_2R-Produkte ist in organischen Lösungsmitteln generell niedriger als in wässrigen Elektrolyten, was eine industrielle Anwendung deutlich erschwert.[38]

In wässrigen Elektrolyten spielt der lokale pH-Wert an der Elektrode im Hinblick auf die Produktselektivität eine wichtige Rolle.[38] Dieser wird allerdings sowohl durch die H_2-Entwicklung ($2\,H_2O + 2\,e^- \longrightarrow H_2 + 2\,OH^-$) als auch durch das Sättigen mit Kohlenstoffdioxid (im Basischen: $CO_2(aq) + OH^- \rightleftharpoons HCO_3^-$) beeinflusst. Des Weiteren puffert das Hydrogencarbonat das entstandene Hydroxid ($HCO_3^- + OH^- \rightleftharpoons CO_3^{2-}$), wodurch die genaue Einstellung eines optimalen pH schwierig bis unmöglich ist.[38] Um den lokalen pH unabhängiger vom anliegenden CO_2 zu machen und die CO_2-Konzentration an der Elektrode auf einem hohen Niveau zu halten kann die Schnittstelle zwischen Katalysator und Elektrolyt modifiziert werden. Ein hybrides Katalysatordesign wurde vom Arbeitskreis um Sargent (University of Toronto) vorgestellt, wobei gasförmiges CO_2, Elektronentransfer und Ionentransport lokal getrennt werden.[39] Mithilfe von hydrophoben und hydrophilen Domänen um einen Kupferkatalysator konnte eine Faraday-Effizienz für Ethylen von über 65 % bei Stromdichten oberhalb von $1\,A\,cm^{-2}$ erreicht werden.[39]

Neben der beschriebenen Anpassung des Katalysatordesigns gibt es zahlreiche weitere Ansätze um die Bildung einzelner CO_2-Reduktionsprodukte zu fördern. Durch bimetallische Katalysatoren (meist Cu+M) wird versucht die materialspezifische Adsorption von CO_2 und Intermediaten

zu beeinflussen. Beispielsweise wird im Cu-Ag System CO an der Silberoberfläche gebildet, welches anschließend an der Kupferoberfläche zu C_{2+}-Produkten weiterreagiert.[40] Ein weiterer Ansatz zur Katalysatoroptimierung befasst sich mit der Modifikation der Katalysatoroberfläche mit kleinen organischen Molekülen, zum Beispiel Aminen.[41] Die immobilisierten Additive sollen durch ihre funktionellen Gruppen bestimmte CO_2RR-Intermediate stabilisieren und so die Selektivität beeinflussen.[42]

Der in Abschnitten dieser Arbeit verwendete Ansatz ist die Veränderung der Katalysatormorphologie und des Oxidationszustandes des Metallkatalysators. In zahlreichen Studien konnte gezeigt werden, dass Oxid-basierte Katalysatoren während der Reduktion ihre Struktur verändern und dadurch die Aktivität bzgl. der CO_2RR erhöht wird.[41]
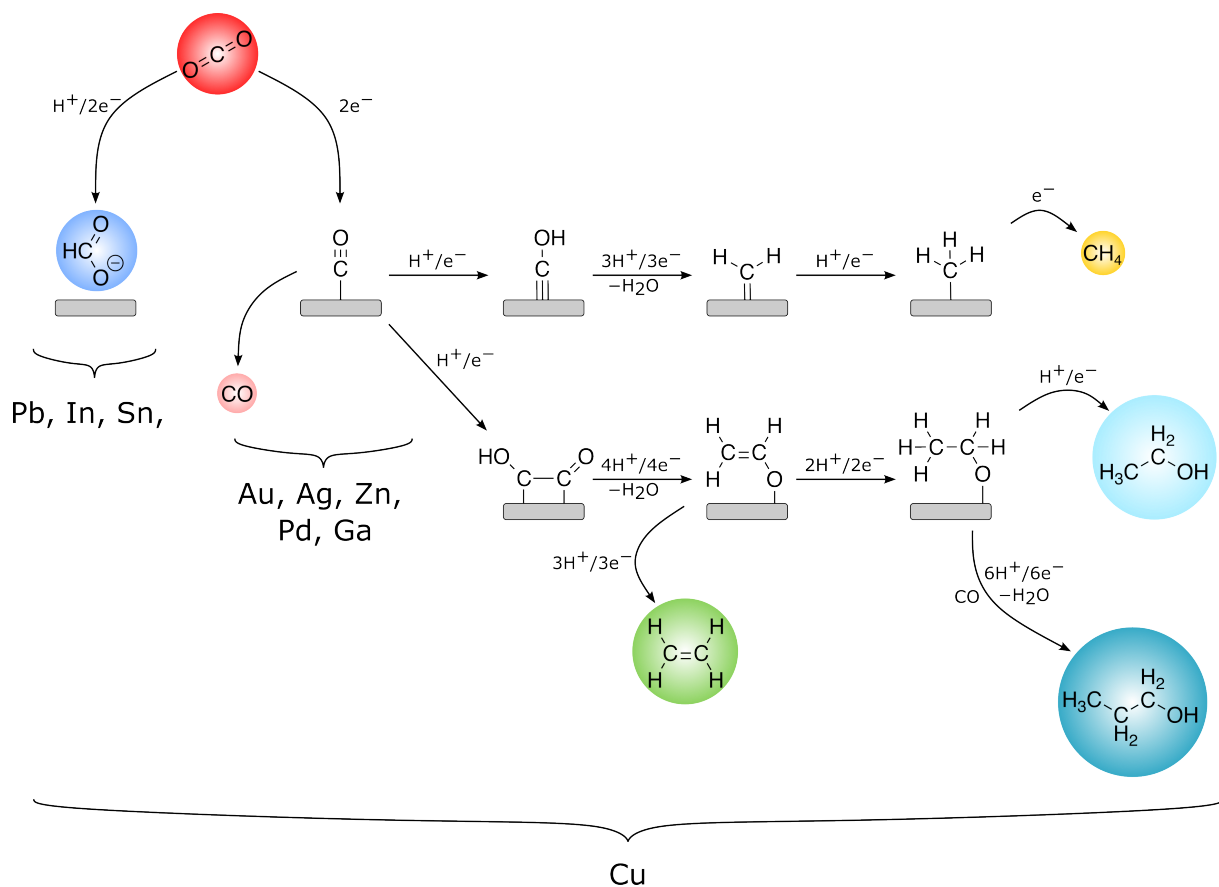

Abbildung 1.12: Wahrscheinlicher Mechanismus der elektrochemischen CO_2-Reduktion unter Verwendung der verschiedenen Metallkathoden.[29,41,43,44]

Der zweite Themenbereich der elektrochemischen Konversion von Kohlenstoffdioxid befasst sich mit der Inkorporation von CO_2 in größere Moleküle zur Einführung von Funktionalitäten wie organischen Carbonaten oder Carboxylgruppen (Abbildung 1.11). Motivation ist dabei meist nicht die quantitative Verringerung des atmosphärischen CO_2-Gehalts oder die Verbindung mit CCU-Technologien. Vielmehr werden die Vorteile der Elektrokonversion (z.B. Vermeidung chemischer Reduktionsmittel, Verwendung von regenerativem Strom als Energiequelle) mit der Verwendung von CO_2 als Rohstoff (ungiftig, gut verfügbar) kombiniert. Dabei steht im

Vordergrund, klassische Synthesen durch die elektrochemische Verwendung von CO_2 *grüner* zu machen oder neue Synthesen zu ermöglichen. Beispielsweise kann die Herstellung von Carbonsäuren auf klassische Weise mit Grignard-Verbindungen und CO_2 erreicht werden, allerdings fallen dabei stöchiometrische Mengen von Metallsalzen an.[45] Alternativ können halogenierte Substrate elektrochemisch dehalogeniert und mit CO_2 verknüpft werden.[36] Die Herstellung der metallorganischen Grignard-Verbindung entfällt.

Im Rahmen der vorliegenden Arbeit wurde CO_2 in Aldehyde und Ketone inkorporiert und auf diese Weise α-Hydroxycarbonsäuren hergestellt.

Beide Themenkomplexe der elektrochemischen CO_2-Konversion ergänzen sich und bilden eine wichtige Grundlage für die Etablierung eines geschlossenen Kohlenstoffkreislaufs.

1.5 Energieeffizienz von elektroorganischen Synthesen

Erklärung meines Beitrags:

Personenbezogene Daten

Innerhalb der vergangenen Jahrzehnte hat die Elektrosynthese stark an Bedeutung gewonnen.[46,47] Industrielle Prozesse wie der *Baizer-* oder der *Lysmeral-*Prozess zeugen von dem Potential großskalig angewandter Elektrokonversionen. Die Verwendung von elektrischem Strom als Triebkraft chemischer Reaktionen bietet eine Reihe von Vorteilen, wie der Verzicht auf stöchiometrische Oxidations- und Reduktionsmittel oder die Reaktionsführung unter milden Bedingungen. Des Weiteren können mithilfe des elektrosynthetischen Ansatzes die Selektivität verbessert und neuartige chemische Transformationen ermöglicht werden.[46,48,49]

Die elektrochemische Herstellung synthetischer Kraftstoffe ist in den letzten Jahren zunehmend in den Fokus gerückt. Hierfür wird CO_2 in Gegenwart von Wasser zu Energieträgern bzw. Plattformchemikalien wie Methanol, Methan, Ethylen oder Ethanol reduziert. Die Knüpfung von C-C Bindungen wird üblicherweise an Kupfer-basierten Katalysatoren vorgenommen, wobei allerdings ein Gemisch verschiedener Kohlenwasserstoffe wie z.B. Ethanol, Propanol, Formiat,

CO und Ethylen entsteht.[29] Hinzu kommen nicht umgesetztes CO_2 sowie H_2 aus der Wasserreduktion. Die aufwändige Produktisolation sowie der generell geringe Absatzpreis der genannten Plattformchemikalien limitiert hierbei die ökonomische Anwendung.[27]

Im Gegensatz zu synthetischen Kraftstoffen werden Feinchemikalien in geringeren Mengen bei kleineren Anlagengrößen produziert und mit deutlich höherem Kilopreis verkauft. Starke Oxidations- oder Reduktionsmittel wie $LiAlH_4$ können vermieden und somit Kosten für Chemikalien sowie Sicherheitseinrichtungen eingespart werden.

Für die Effizienzbewertung der Elektrosynthese müssen verschiedene Aspekte betrachtet werden. Der Energiebedarf der Elektrolyse wird hauptsächlich durch die angelegte Zellspannung bestimmt. Die Zellspannung wird vom angelegten Strom i, dem ohmschen Widerstand der Zelle R_{cell} und der Differenz der kathodischen und anodischen Redoxpotentiale $E_{cathode/anode}$ beeinflusst.

$$U_{cell}(V) = E_{anode} - E_{cathode} + iR_{cell}$$

Die Redoxpotentiale sowie der angelegte Strom sind intrinsische Eigenschaften der Reaktion selbst, bzw. ergeben sich aus der Optimierung der Elektrokonversion. Der Zellwiderstand wird durch eine Reihe von Parametern bestimmt: Zelldesign (z.B. Elektrodenabstand), Leitfähigkeit des Elektrolyten und Verwendung eines Separators (z.B. Ionenaustauschmembran). Der Zellwiderstand R_{cell} hat sehr großen Einfluss auf die Zellspannung. Dies kommt besonders zum Tragen, wenn geteilte Zellen verwendet werden, wobei die Zellspannung leicht über 5 V steigen kann.

Die Zellspannung R_{cell} darf nicht mit dem Redoxpotential E verwechselt werden. Letzteres beinhaltet nicht den ohmschen Widerstand der Zelle. Der Verbrauch elektrischer Energie durch die Elektrolyse (*electric energy consumption — EEC*) wird durch folgende Gleichung beschrieben:

$$EEC(kWh/kg) = \frac{z * F * U_{cell}}{CE * M}$$

Dabei ist z die Anzahl von Elektronen die pro Molekül übertragen werden, F ist die Faraday-Konstante, U_{cell} ist die Zellspannung, M ist die molare Masse und CE ist die Stromeffizienz. Die Stromeffizienz CE wird auch als Faraday-Effizienz FE bezeichnet und ist das Verhältnis aus der Ladung, welche effektiv zur Bildung des Produkts verwendet wird, zur insgesamt applizierten Ladungsmenge. Daher kann die Stromeffizienz (oder Faraday-Effizienz) auch als Selektivität des Prozesses interpretiert werden.

Die Energieeffizienz der Elektrokonversion EE beschreibt, mit welcher Effizienz das angelegte Potential zur Bildung des Zielprodukts führt:

$$EE(\%) = \frac{E°}{E° + \eta} * FE = \frac{E°}{E} * FE$$

Dabei wird die Faraday-Effizienz mit dem benötigten Überpotential η kombiniert, wobei das Überpotential die Abweichung des Elektrodenpotentials E vom Gleichgewichtsredoxpotential

E° ist. Das Überpotential hat seinen Ursprung in einer limitierten Elektronenübergangsrate (Elektronentransferüberpotential), einem langsamem Massentransport (Diffusionsüberpotential) und der Reaktionsgeschwindigkeit selbst (Reaktionsüberpotential).[2] Da die angelegte Zellspannung in diese Gleichung nicht einbezogen wird (obwohl sie maßgeblichen Einfluss auf den Energieverbrauch der Reaktion hat), ist die Aussagekraft begrenzt. Daher kann eine alternative Definition der Energieeffizienz etabliert werden:

$$EE'(\%) = \frac{Q_i * (E_a^\circ - E_c^\circ)}{Q_{total} * (E_a^\circ + \eta_a - E_c^\circ + |\eta_c| + iR_{cell})}$$
$$= FE \frac{U^\circ}{U^\circ + \eta_a + |\eta_c| + iR_{cell}}$$

Dabei stellt U° die Gleichgewichtszellspannung dar. Aus der modifizierten Gleichung EE' kann abgeleitet werden, dass die Effizienz maximal wird, wenn (i) die gesamte applizierte Ladung für die gewünschte Elektrokonversion verwendet wird ($FE = 100\%$) und (ii) die Überpotentiale η sowie der Zellwiderstand so gering wie möglich sind. Für skalierte Reaktoren weicht der Zellwiderstand jedoch signifikant von Null ab, sodass die Minimierung des Widerstands ein Schlüsselaspekt in der Optimierung industrieller Elektrolyseure darstellt.
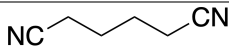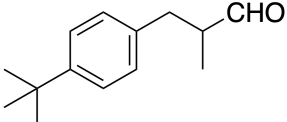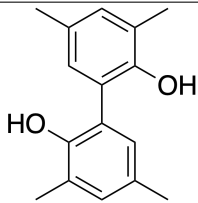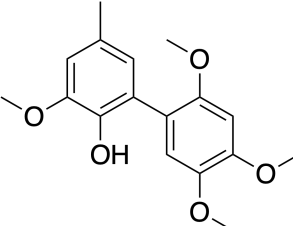
Dies wird besonders deutlich, wenn man die elektrochemische CO_2-Reduktion zu Wertprodukten mit der Synthese von komplexeren Molekülen vergleicht. Für Plattformchemikalien aus CO_2 werden aufgrund der benötigten Produktmengen und wegen der großskaligen Konversion von CO_2, hohe Stromdichten ($>100\,\mathrm{mA\,cm^{-2}}$) angestrebt. Wegen des nicht vernachlässigbaren Zellwiderstandes schlägt sich dies in einer vergleichsweise hohen EEC nieder (Tabelle 1.1). Hinzu kommt, dass für die Reduktion von CO_2 zu beispielsweise Ethylen große Ladungsmengen nötig sind (12 Elektronen je Molekül C_2H_4). Berechnungen von De Luna et al. zufolge sind zudem die hohen Investitionskosten für die elektrochemische CO_2-Reduktion, die aufwändige Produktisolation sowie der niedrige Preis fossil-basierter Produkte Hemmnisse für den Markteintritt.[27]

Tabelle 1.1: Beispiele von Produkten aus der elektrochemischen CO_2-Reduktion. Für die angegebenen Faraday-Effizienzen wurden lediglich Studien mit Stromdichten $>100\,mA\,cm^{-2}$ berücksichtigt. Davon ausgenommen ist Methanol, für das keine Stromdichten über $50\,mA\,cm^{-2}$ berichtet wurden. Die Berechnung der EEC basiert auf einer angenommenen Zellspannung von $3\,V$ und der höchsten im Bereich angegebenen FE. Ein Strompreis von $0.1\,€/kWh$ wurde angenommen.

| Reaktion	FE (%)	EEC (kWh/kg)	Stromkosten (€/kg)
$CO_2 + 2\,H^+ + 2\,e^- \longrightarrow CO + H_2O$	90–99[50]	5	0.5
$CO_2 + 6\,H^+ + 6\,e^- \longrightarrow CH_3OH_{(aq)} + H_2O$	25–70[51,52]	20	2.0
$2\,CO_2 + 12\,H^+ + 12\,e^- \longrightarrow C_2H_5OH_{(aq)} + 3\,H_2O$	15–25[53,54]	75	7.5
$2\,CO_2 + 12\,H^+ + 12\,e^- \longrightarrow C_2H_4 + 4\,H_2O$	50–70[39,55]	50	5.0

Produkte welche nicht auf dem Umsatz von CO_2 basieren, resultieren in der Regel in geringeren Stromverbrauch. Industriell implementierte Elektrosynthesen wie bei der Herstellung von 2-(4-*tert*-Butylbenzyl)propionaldehyd (*Lysmeral*) oder Adiponitril (*Baizer*-Prozess) haben einen deutlich geringeren Verbrauch elektrischer Energie. In diesen Fällen ist der Beitrag der Stromkosten zu den Gesamtkosten der Herstellung verschwindend gering (1.2).

Tabelle 1.2: Beispiele von Produkten aus der elektro-organischen Synthese. Die Berechnung der EEC basiert auf einer angenommenen Zellspannung von $3\,V$. Ein Strompreis von $0.1\,€/kWh$ wurde angenommen.

Reaktion	Produkt	FE (%)	EEC (kWh/kg)	Stromkosten (€/kg)
Baizer		90[56]	2.43	0.24
Lysmeral		70[57]	2.94	0.29
Anodic homo-coupling		71[58]	0.93	0.09
Anodic cross-coupling		69[59]	0.77	0.08

Zusammengefasst tragen folgende Aspekte zu einer ökonomischen Elektrosynthese bei:

- Simple Produktaufbereitung: idealerweise wird durch die Elektrosynthese die nachfolgende Aufarbeitung vereinfacht

- Der alternative elektrosynthetische Ansatz führt zur Einsparung von Reduktions- oder Oxidationsmitteln

- Der Zellwiderstand wird durch Zelloptimierung minimiert

- Es werden eher wenige Elektronen je Molekül transferiert

- Ungünstige Kombinationen aus hohem Ladungstransfer, hoher Stromdichte (hoher Spannung) und gleichzeitig geringem Kilopreis des Produkts werden vermieden
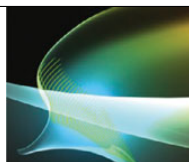
REVIEW

Does electrifying organic synthesis pay off? The energy efficiency of electro-organic conversions

Johannes Seidler[†], ESy-Labs GmbH, An der Irler Höhe 3a, 93055 Regensburg, Germany; Department of Chemistry, Johannes Gutenberg University, Duesbergweg 10–14, 55128 Mainz, Germany

Jana Strugatchi[†], Department of Chemistry, Johannes Gutenberg University, Duesbergweg 10–14, 55128 Mainz, Germany

Tobias Gärtner, ESy-Labs GmbH, An der Irler Höhe 3a, 93055 Regensburg, Germany

Siegfried R. Waldvogel, ESy-Labs GmbH, An der Irler Höhe 3a, 93055 Regensburg, Germany; Department of Chemistry, Johannes Gutenberg University, Duesbergweg 10–14, 55128 Mainz, Germany

Address all correspondence to Siegfried R. Waldvogel at waldvogel@uni-mainz.de and Tobias Gärtner at tobias.gaertner@esy-labs.de
[†] These authors contributed equally to this work.

(Received 17 July 2020; accepted 26 October 2020)

ABSTRACT

The electrification of organic syntheses is a vividly growing research field and has attracted tremendous attention by the chemical industry. This review highlights aspects of electrosynthesis that are rarely addressed in other articles on the topic: the energy consumption and energy efficiency of technically relevant electro-organic syntheses.

Four examples on different scales are outlined.

Electro-organic synthesis has experienced a renaissance within the past years. This review addresses the energy efficiency or energy demand of electrochemically driven transformations as it is a key parameter taken into account by, for example, decision makers in industry. The influential factors are illustrated that determine the energy efficiency and discussed what it takes for an electrochemical process to be classified as "energy efficient." Typical advantages of electrosynthetic approaches are summarized and characteristic aspects regarding the efficiency of electro-organic processes, such as electric energy consumption, are defined. Technically well-implemented examples are described to illustrate the possible benefits of electrochemical approaches. Further, promising research examples are highlighted and show that the conversion of fine chemicals is rather attractive than the electrochemical generation of synthetic fuels.

Keywords: electrochemical synthesis; efficiency; sustainability

DISCUSSION POINTS

- What are the most important figures of merit in the evaluation of electrochemical processes and how do they contribute to the energy consumption of electrosynthesis?

- Electrosynthetic approaches toward organic commodities and fine chemicals are illustrated. What are the main drivers for their energy consumption and why are electro-synthesized commodities from CO_2 to date economically less attractive than fine chemicals?

Introduction

The first attempts of organic electrosynthesis date back over 170 years. However, electrochemical approaches had been underestimated for a long time and have experienced a renaissance within the past few years.[1,2] Many contemporary societal issues and also in chemistry deal with renewable energy, the avoidance of greenhouse gases and waste, as well as the replacement of fossil resources. Since electrochemistry may offer greener chemical routes, scientists have focused on electro-organic synthesis and conversions to support a sustainable ecological footprint.[1,3,4]

In the 21st century, electrochemistry and its application will play an important role in the industry, for example, within the Baizer or Lysmeral processes and also in the commercial world.[5,6] Electrochemistry offers numerous advantages, such as working under mild conditions, avoiding aggressive and hazardous reagents, and working with alternative feedstock. It is possible to improve the selectivity of existing reactions and to initiate novel chemical transformations.[2,7,8]

The generation of synthetic fuels has attracted much attention during recent years. Using electric current, CO_2 and water are reduced into energy carriers such as methanol or methane. In a scenario wherein electricity is generated by regenerative resources, power-to-fuel technologies may support the implementation of closed artificial carbon cycles.

However, the electrosynthesis of platform chemicals like alcohols, ethylene and methane from CO_2 is mostly achieved by using copper-based catalysts, which on the one hand is capable of generating C–C bonds, but on the other hand produces a variety of hydrocarbons at the same time. The gaseous and liquid fractions obtained represent multicomponent mixtures, which require costly purification. The electrolytes are mostly of aqueous nature, providing rather small concentrations of alcohols and formate, which makes the product separation even more cost-intensive. As these products are required in large quantities, the according capital costs for the downstream processing as well as its running costs are enormous. At the same time, platform chemicals are sold at a rather low price, narrowing down the profit margin.

In contrast, fine chemicals are produced at lower scale and with a significantly higher revenue per kilogram. Electrosynthetic approaches may offer two main benefits in the production of fine chemicals. As the reaction is driven by electrical current, strong and hazardous oxidizing or reducing agents like $LiAlH_4$ can be omitted, which saves on costs for reagents and safety precautions. Noteworthy, the electron is one of the cheapest and most versatile redox agents. Furthermore, electrosynthesis may help facilitate the downstream processing since reagent waste is avoided. For example, in the Baizer process, an annual amount of 300,000 tons adiponitrile are produced. The product adiponitrile forms due to lower miscibility an organic layer, which is easily separated from the aqueous electrolyte. The translation of the concept from a divided cell to an undivided cell could improve cost factors as investment, maintenance, and energy. The converted mass yields over 90%, and the separation of the biphasic phase of adiponitrile and acetonitrile is cost efficient.[9]

As illustrated in Fig. 1, electrochemical approaches may offer products in different sections, such as synthetic fuels, commodities, fine chemicals, and specialties. An important aspect to address, especially for decision makers in industry, is whether an electrochemical alternative is superior to the existing process in terms of costs. Energetic considerations are of particular interest in process development. Therefore, it is necessary to answer the question whether it is energy efficient to use electricity as a driving force for chemical reactions. Here, we survey whether electrifying organic syntheses pays off and under which circumstances it is superior over traditional chemical routes.

Energetic evaluation of electrochemical conversions

The evaluation of an electrochemical process involves multiple aspects, whereas the energy requirements are mainly governed by the applied cell voltage U_{cell} [which depends on the applied current (i), the Ohmic resistance (R_{cell}) of the electrolysis cell, and on the difference of the anodic and the cathodic redox potentials ($E_{anode/cathode}$)].

$$U_{cell} \text{ (V)} = E_{anode} - E_{cathode} + iR_{cell}$$

While the redox potentials and the current depend on the electrochemical reaction and its optimization, the cell resistance depends on multiple factors including the cell design (e.g., interelectrode gap), the electrolyte and its conductivity, and the usage of a separator (membrane) between catholyte and anolyte. Noteworthy, when conducting an electrochemical conversion at constant potential, all energy-consuming contributions (separator, Ohmic resistance, and overpotential) are set to zero, but are still there and require in the end most of the energy applied. The cell resistance R_{cell} has high impact onto the overall cell voltage. This is, in particular, the case for divided cells wherein the applied cell voltage easily reaches 5 V or more. All contributions to the Ohmic cell resistance having a direct impact onto applied cell voltage and the electric current have to be taken into account for optimization of the energy efficiency (Fig. 2).

The operating cell voltage U_{cell} (in some literature also written as E) should not be mixed up with the redox potential E as in the above equation. The redox potential does not take into account the Ohmic resistance of the cell. Noteworthy, when operating an electrolysis cell at higher productivity, the contributions like the overpotential. increase due to kinetics.

The electric energy consumption (EEC) is given by the following equation:

$$\text{EEC (kWh/kg)} = \frac{z*F*U_{cell}}{CE*M}$$

Where z is the number of electrons transferred per molecule, F is the Faraday constant, U_{cell} is the cell voltage, M is the molar mass, and CE is the current efficiency.

CE sets a target approaching 100% in order to maximize the performance. The current efficiency is calculated by the following equation:

$$\text{CE (\%)} = \frac{Q_{theoret.}}{Q_{pract.}} * \frac{n_{product}}{n_{substrate}} * 100\% = \frac{Q_i}{Q_{total}} * 100\%$$

The expression Q_i/Q_{total} is also known as the Faradaic efficiency (FE) that is used for the generation of a specific compound (Q_i) divided by the total charge (Q_{total}) that is applied during the reaction. In other words, it describes how much of
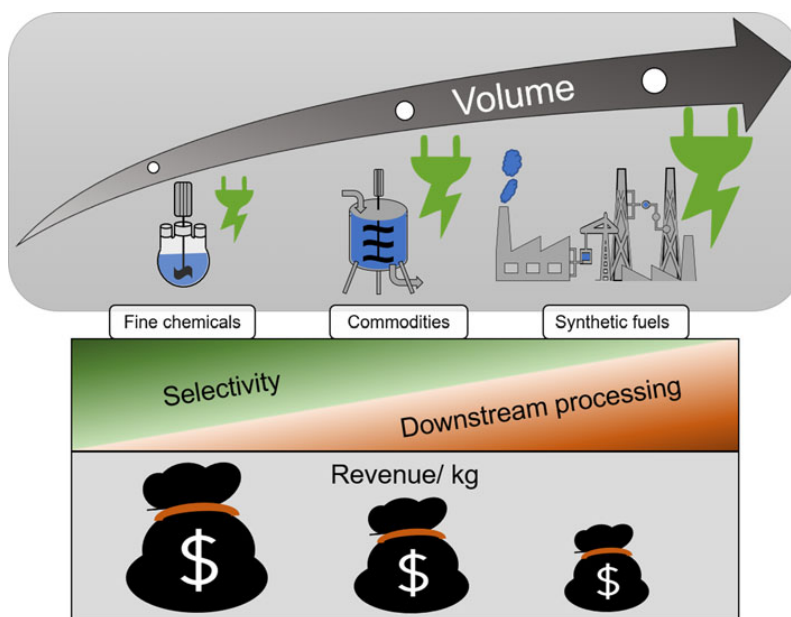
Figure 1. Characteristics of the different electro-organic products by volume of production, electricity, influence of crucial process aspects as selectivity and downstream processing, and revenue expected.
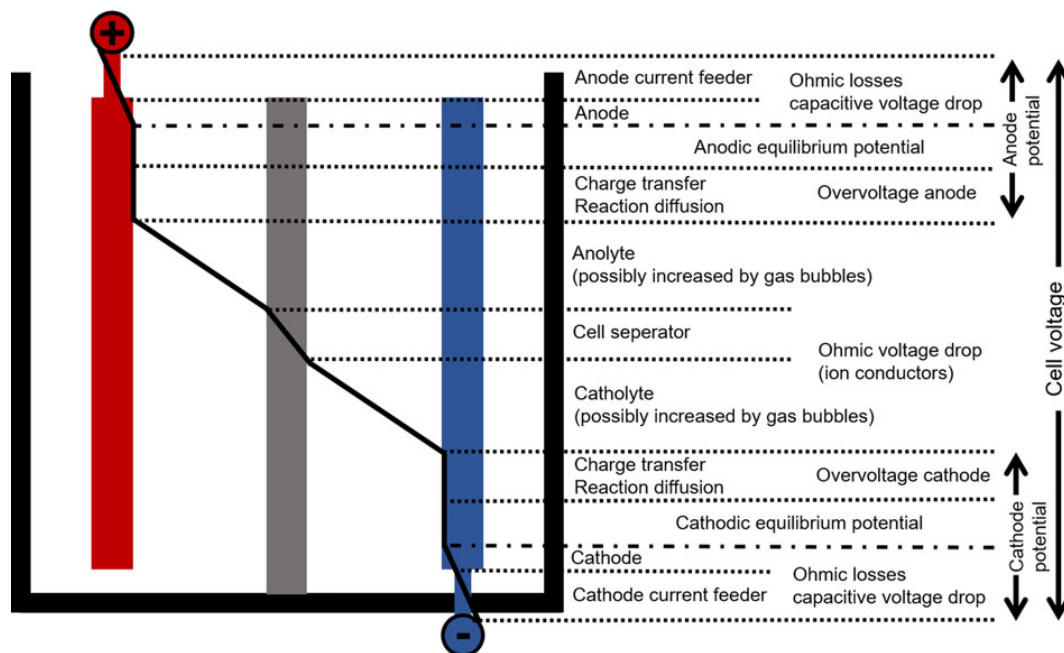

Figure 2. Individual contributions to the applied cell voltage and their locations in the electrochemical reactor.

22

the total charge is effectively used to produce the desired product. Therefore, it is a measure of the selectivity of the process. Reaching FEs (or CEs) close to 100% is challenging, especially for reductions in aqueous media, where the reaction of interest competes with the hydrogen evolution reaction. In general, the production of side products will always diminish the current efficiency.

As illustrated by the above equations, EEC depends on the efficiency of the conversion (CE) as well as the characteristics of the electrolyzer and the electrolyte, which influence the value of U_{cell}. Moreover, a reaction that involves the transfer of fewer electrons per mole of substrate will, of course, lead to smaller EECs as z contributes linearly to the EEC. In addition to the electric energy that is necessary to drive the electrochemical reaction, further energy might be required for heating, mechanical stirring, operating pumps, and downstream processing. The energetic efficiency (EE) characterizes the efficiency of converting electric potential into a desired product. It combines the Faradaic efficiency (FE) with the applied overpotential (η), which is the deviation of the electrode potential (E) from the equilibrium redox potential (E°).

$$\text{EE (\%)} = \frac{E^\circ}{E^\circ + \eta}\text{FE} = \frac{E^\circ}{E}\text{FE}$$

The overpotential may arise from the limiting rate of electron transfer (*electron transfer overpotential* – mainly at low current densities), from slow transport of reactants to the electrode surface (*diffusion overpotential*), and from the inability of the reaction itself to keep pace (*reaction overpotential*).[10] Obviously, when the overpotential is negligible small, the EE only depends on the efficiency of the electrochemical reaction, that is, the Faradaic efficiency. This consideration is providing only half of the information and becomes less valid when a high current density is applied. The system boundary for EE calculation does not include the applied cell voltage; therefore, an alternative definition of the energetic efficiency (EE′) can be established as a more meaningful figure of merit:

$$\text{EE' (\%)} = \frac{Q_i * (E_a^\circ - E_c^\circ)}{Q_{total} * (E_a^\circ + \eta_a - E_c^\circ + |\eta_c| + iR_{cell})}$$
$$= \text{FE} * \frac{U^\circ}{U^\circ + \eta_a + |\eta_c| + iR_{cell}}$$

where U° *is the equilibrium cell voltage.* From the above equation, it can be concluded that EE′ is maximized when the entire charge is used for the desired reaction (FE = 100%), when anodic and cathodic overpotentials as well as the cell resistance are small. However, an upscaled reactor cannot possess a negligible cell resistance, making the resistance of the cell one of the key aspects in optimizing the energy efficiency.

Furthermore, the applied current needs to be considered when maximizing the energy efficiency. It may influence the Faradaic efficiency as the selectivity is dependent on the applied current density. Furthermore, a faster electron transfer leads to higher overpotentials and finally the numeric value for the current i determines the product iR_{cell}.[11]

Conversion of CO_2 to synthetic fuels and commodity chemicals

The electrochemical production of commodity chemicals from CO_2 has become an emerging research field during the past decades. Via electrochemical CO_2 reduction (CO_2R), numerous products with large market sizes are potentially accessible (Fig. 3). The conversion of atmospheric or waste stream CO_2 to CO and hydrocarbons such as ethylene, formate, and ethanol is an attractive technique helping to close an artificial carbon cycle. Moreover, the usage of renewable energy leads to a second benefit: the conversion of electric to chemical energy enabling the storage of energy in the form of chemicals. In recent years, research of electrocatalysts and electrochemical cell design has led to significant improvements in selectivity and efficiency of the according reactions.

Research on the production of commodity chemicals from CO_2 mainly focuses on CO, formate, ethylene, and ethanol since they are accessible at relatively high Faradaic efficiencies.[12,13] While Ag and Sn catalysts are mainly used to reduce CO_2 to CO and formate, respectively, copper-based electrodes are applied for the production of chemicals with multiple C-atoms like ethanol and ethylene.[14]

Noteworthy, carbon electrodes are for the CO_2 reduction of limited interest due to their interface performance. Most carbon-based electrodes suffer from low electrocatalytic activity toward CO_2 reduction.[15] As electrochemical CO_2 reduction is mainly carried out in aqueous solutions, hydrogen is formed in a parasitic reaction. To overcome the poor solubility of CO_2 in aqueous media and to minimize the hydrogen evolution reaction at high current densities (>100 mA/cm^2), gas diffusion electrodes are applied.[16]

Nevertheless, main challenges remain increasing the Faradaic efficiency of the desired products at high current densities. At the same time, the cell resistance needs to be minimized to keep the cell voltage as low as possible. However, only CO has been generated from CO_2 under stable conditions, at relevant current densities, and high Faradaic efficiency. Other products are obtained at significantly lower FE*s*, which contribute to the high energy consumption of the according products (Fig. 4). Even at low cell voltages, the EEC is substantial. For example, assuming an electric energy price of 0.1 €/kWh[17] and an operating voltage of 3 V, the electricity for 1 kg ethanol would cost approx. 7.5€, excluding the workup of the sophisticated electrolysis mixture.

A number of reviews have been dedicated to investigate whether the electrocatalytic production of commodity chemicals from CO_2 can compete with traditional, mainly fossil fuel-derived alternatives in terms of production cost.[12,13,18,19]

De Luna et al. address multiple challenges that have to be overcome in order to replace petrochemical processes. Inhibiting factors are limited energy conversion efficiencies of
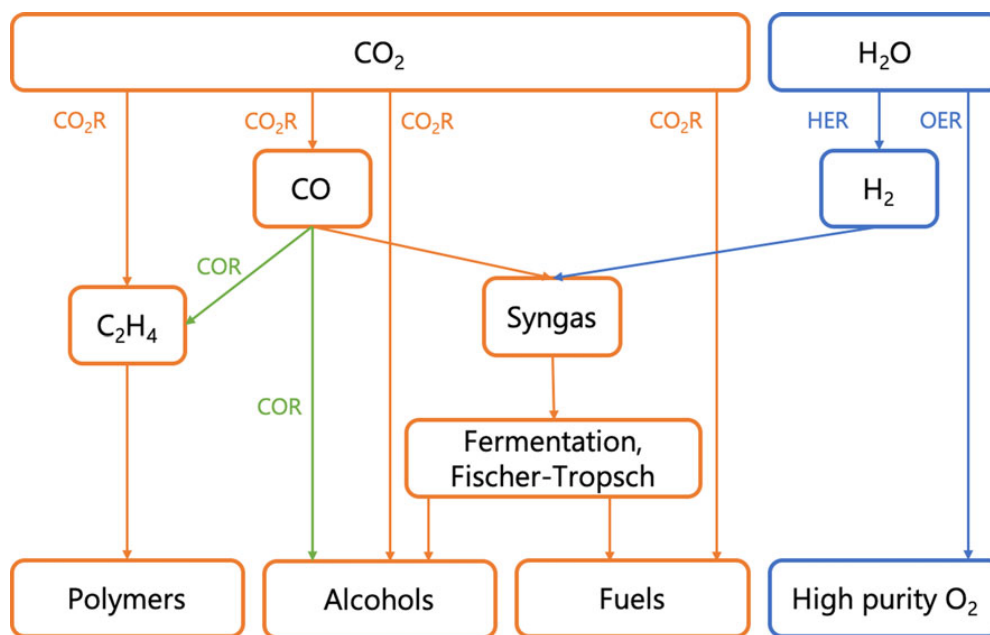
23

Figure 3. Possible CO$_2$R pathways to commodity products. COR: CO reduction; HER: hydrogen evolution reaction; OER: oxygen evolution reaction.

electrolyzers as well as the operating stability of these systems. Another key role plays the availability of low-cost renewable energy. The authors specify 4 cents/kWh as the maximum

electricity cost for a scenario where electrochemical approaches are competitive. Other challenges are costs for CO$_2$ capture and transportation. Especially, the large manufacturing scale and
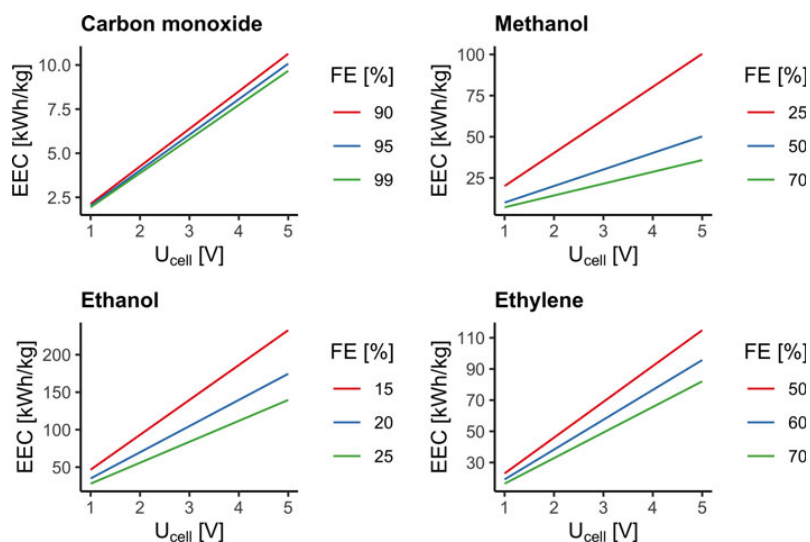

Figure 4. EEC of CO$_2$ electroreduction products at different cell voltages and Faradaic efficiencies. The FE values are based on the current literature, only FEs at current densities >100 mA/cm^2 were considered, except for methanol which has not been produced at comparable current densities yet.
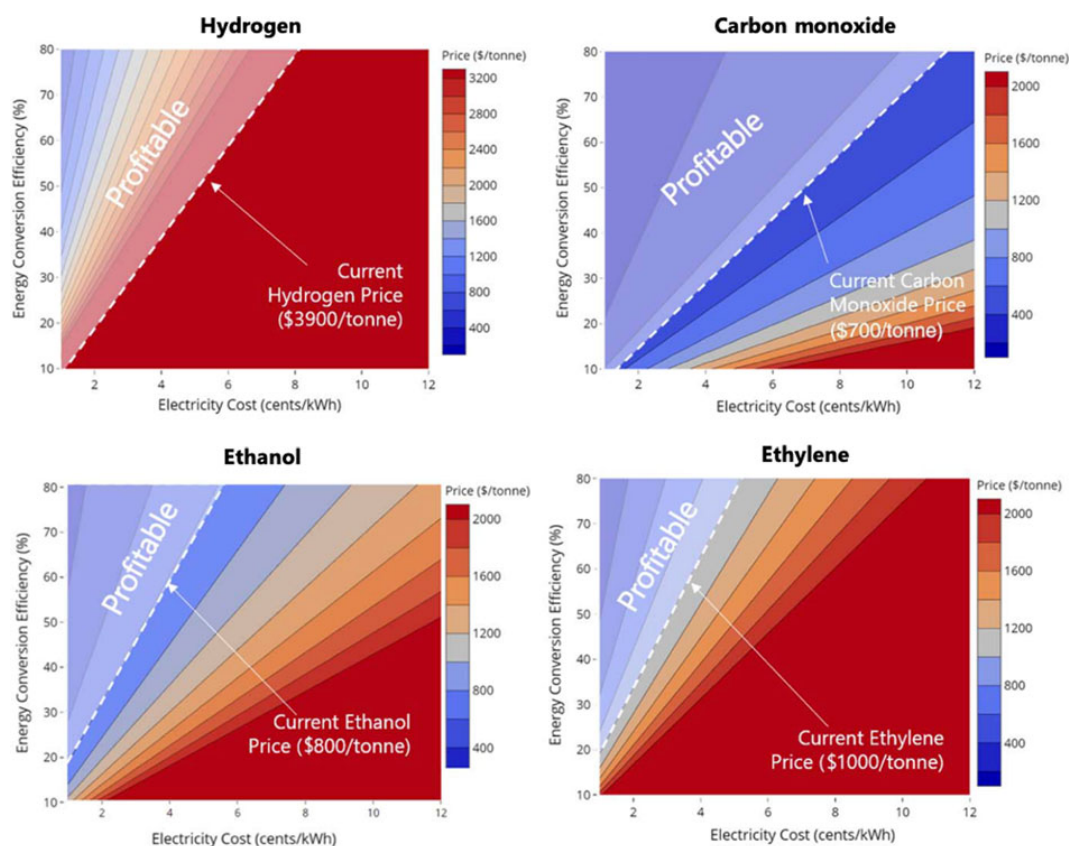
24

Figure 5. Production costs of electrosynthesized products. The graphs show technoeconomic analyses of hydrogen, carbon monoxide, ethanol, and ethylene costs as a function of electrolyzer energy conversion efficiency (=energy efficiency EE defined in this review without the FE term) and electricity costs. The authors assume a pure CO_2 price of \$30/t, Faradaic efficiency of 90%, current density of 500 mA/cm^2, electrolyzer costs of \$300/kW, and plant lifetime of 30 years. The area above the white dashed line in lighter color indicates profitable production costs based on average global prices. From [13]. Reprinted with permission from AAAS.

the saturation and complexity of the market for commodity chemicals such as ethylene are major barriers for the new technology.[13] From all CO_2 reduction products, CO appears to have the highest chance for an industrial implementation (Fig. 5).

In the scenario calculated by De Luna et al., the electricity cost must not exceed approx. 5 cents/kWh, even at high energy conversion efficiencies as high as 80% for ethanol and ethylene to be economic. Also, the values for Faradaic efficiencies of 90% and current densities of 500 mA/cm^2 are rather optimistic, making the profitable region for ethylene and ethanol even more difficult to reach. The high current densities will lead to a substantial hydrogen evolution, which lowers the FEs for CO_2 reduction products. Therefore, FEs of 90% for ethanol and ethylene can be considered a best-case scenario. CO_2 reduction to CO is already feasible at high Faradaic efficiencies (>90%) using Ag catalysts as there is no C–C bond formation

involved, which can potentially lead to side products. Also, high current densities above 200 mA/cm^2 have already been demonstrated.[20] In contrast, CO_2R to methanol suffers from low efficiencies and has mainly been reported at current densities below 50 mA/cm^2.[21,22] Hybrid processes, which combine thermocatalytic and electrocatalytic transformations to methanol, might be more promising until FEs and current densities for CO_2R to methanol are significantly increased, at least two orders of magnitude higher than current laboratory results (currently less than 50% FE and currents below 50 mA/cm^2).[23]

Among the accessible products from CO_2R, CO and formic acid come along with the highest revenue per mole of electrons.[12] However, most CO_2R reactions are carried out in basic media with formic acid being present as formate. The follow-up step to generate the protonated form might consume equal amounts of acid, making the process

25

uneconomical. Other challenges addressed by Chen et al. are the high capital costs (approx. $300/kW[13]) and the associated risks that come with the large production scale of commodity chemicals. Furthermore, pure CO_2 is a bulk chemical itself and providing CO_2 in adequate quality represents a substantial hurdle.[12]

The electrochemical production of commodity chemicals like CO, formate, ethanol, and ethylene from CO_2 needs to meet several requirements in order to be a sensible and competitive technique, including the following aspects:

1. The electricity used has to originate from a carbon-neutral source. Burning fossil fuels in order to generate electricity with the goal of reducing CO_2 electrochemically is not useful.
2. High Faradaic efficiencies at low overpotentials and high current densities are necessary, combined with a low applied cell voltage.
3. CO_2 needs to be converted at high manufacturing scales, both to benefit from the economy of scale and to be able to enter the market of commodity chemicals.
4. Price for renewable electricity must not exceed a threshold (relative to prices for fossil fuels) in order to make CO_2R economical. For example, De Luna et al. specify $0.04/kWh as threshold.[13]
5. CO_2 reduction plants have to be flexible in terms of electricity supply. To make the best use of intermittent energy sources, the CO_2 electrolyzers should allow running at higher capacities when a surplus of energy is available (which leads to lower energy prices).

Products of higher complexity than ethanol, ethylene, CO, and formate may not have to compete directly with the fluctuating and highly complex fossil fuel market. In those cases, the implementation of electrochemical approaches can be beneficial compared with traditional chemical routes, as we will show for the Baizer and Lysmeral processes.

Industrially implemented processes

In comparison to traditional chemical processes, electrochemistry offers many advantages as the easy accessibility of appropriate reagents and the controlled reaction. For industrial processes, advantages as the avoidance of reagent waste, the adjustable reaction speed, and power are important aspects. One emerging view is the possibility of using renewable energy as a driving force for a specific and selective conversion. Furthermore, electrochemistry is inherently safe and reduces the use of rare elements and metals. The performance of speed up the catalytic cycles is given by using electricity and avoiding of runaway reactions is possible.

Numerous companies have tried to exploit these advantages. To limit the size of the electrolysis cells, the current densities are kept in a range of 10–30 mA/cm^2.[24] Following the conversion, a work-up strategy as the separation of the products from unreacted reactants and electrolytes should be developed. The supporting electrolyte is an important factor, because it should be compatible with wastewater and explosive precipitates (e.g., from perchlorates) need to be avoided.

The following section describes two brilliant electro-organic methods, which could be considered as landmarks.

Baizer process

The Baizer process is one of the biggest and most important industrial electro-organic synthesis methods with a market size within the past two decades of 300,000 tons/year.[25] In 1960, the electro-organic chemist Manuel M. Baizer was working at the company Monsanto's Technical Center in Florida, because of this the process is also called Monsanto process. In the early 1970s, the Baizer process was a milestone in electrochemistry. After reduction of acrylonitrile, the product is adiponitrile, which represents a central intermediate to manufacture polyamides but also polyurethanes (Scheme 1).[24]

To produce adiponitrile, a cathodic electro-hydrodimerization of acrylonitrile is required. The break-through of this process was in an undivided work cell by using quarternary ammonium salts such as tetraethylammonium p-toluensulfonates as supporting electrolytes which led to mass yields of 90%. Before that, a divided cell with an aqueous catholyte mixture of acetonitrile and adiponitrile in tetraethyl ammonium sulfate and an anolyte of diluted sulfuric acid was used.[9] Because of their high overpotential, cadmium or lead electrodes were used, and the anode had an alloy of silver.[24] The cadmium cathodes were partially replaced by copper–lead alloys or stainless steel because of the significant environmental issues. The current densities were high with 4.5 kA/m^2.

The problem of the prior process was that, because of high current densities, the cathodes were not stable and caused high maintenance costs. The undivided cell, in comparison with a divided cell, provided a better performance and the cost of electric energy for the conversion was lower. With such cells, the energy consumption was reduced. The cell voltage decreased from 11.65 to 3.83 V, and the specific energy consumption was reduced from 6.61 to 2.43 kWh/kg which is an improvement in electric efficiency of approx. 40%.[25] The

Scheme 1. Used technical electrochemical process called Baizer process: electro-conversion of acrylonitrile in industrial processes.
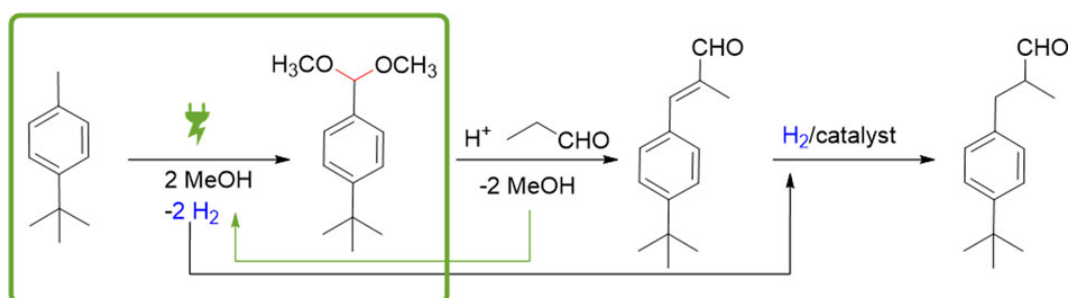
Scheme 2. Anodic dimethoxylation reaction within the Lysmeral process.

current efficiency is above 90%. Significant in the process is the use of water as the hydrogen source. Molecular oxygen and propionitrile are the byproducts. The production of oxygen is one safety problem because of the possibility to corrode metals and react with other chemicals. Additionally, oxygen needs a departure in the used cell to avoid a pressure increase. Nevertheless, the separation of the resulting biphasic electrolyte–adiponitrile mixture facilitates the downstream processing. The crude adiponitrile is purified by distillation, whereas the electrolyte fraction is enriched with water and acrylonitrile prior returning to electrolysis.[9]

Baizer extended the hydrodimerization to a variety of activated olefins.[26] The initial scientific discovery happened almost 20 years prior Baizer implemented the process and demonstrates the power of chemical engineering and process development to translate such research onto an industrial scale.[6,27]

Lysmeral process

The company BASF is using electro-organic synthesis on an industrial scale. One of their most important electric conversions is to afford protected benzaldehydes. The technically most relevant intermediate reacts with propanal and via subsequent hydrogenation to Lysmeral. The electrochemical synthesis of this benzaldehyde equivalent is conducted in several 10,000 tons/year. For the production of the protected benzaldehyde, 4-*tert*-butyltoluene is dimethoxylated at a graphite anode (Scheme 2).

Lysmeral is a fragrance and smells like lily of the valleys.[28] Methanol is used as solvent and reagent. One important point is the recovery of methanol by condensation reaction with propanal within the subsequent step. The hydrogen formed by the electrolysis could be partially used in the hydrogenation reaction. Another product of such anodic dimethoxylation is anisaldehyde. It is used as intermediate for drug synthesis or as fragrance to cover unpleasant odors, for example, in sanitary applications. For the anodic dimethoxylation, BASF designed a bipolar packed electrode stack, which is called capillary gap cell. Versatile electrode materials such as graphite, platinum, and mixed-oxide electrodes can be used, whereas graphite

represents the working horse. The reaction temperature is 50 °C, the current density is 4.2 A/dm^2, and yields up to 78% for the acetal are reached. The process shows a high selectivity with 91%. The theoretical required charge is 4 F, and the applied charge is 4.5 F. The current efficiency is up to 70%.[29] With a voltage of 4 V, the calculation of the EEC resulted in 2.94 kWh/kg. Assuming an electric energy price of 0.1 €/kWh,[17] the electricity for 1 kg Lysmeral would cost approx. 0.29 €, excluding the workup. Meanwhile, the cell design is used in a number of technical processes, for example, in water treatment.[30]

In consideration of the two aspects: selectivity and downstream cost, companies such as Monsanto with Baizer and BASF with Lysmeral were able to implement important industrial electrochemical processes with high performance.

Current state of art

Meanwhile, electro-organic synthesis is successfully explored at a laboratory scale. With new approaches, it is possible to achieve the C–C-bond formation in excellent yields and exclusive selectivity.[31,32]

Here, some innovative syntheses of symmetric and mixed biphenols and phenol-(hetero) arenes using dehydrogenative cross-coupling strategies will be introduced. Cross-coupling products and nonsymmetric biaryls represent valuable products in organic synthesis. Biaryls are utilized in the synthesis of natural products, catalysis, and material science.[33] An important application of biphenols is their usage as ligand components in transition metal catalysis.[34,35] 3,3′,5,5′-Tetramethyl-2,2′-biphenol is one of these useful building blocks but challenging in its synthesis. This biphenol is used, for example, as a ligand precursor for copper[34] or rhodium[36] in catalytic asymmetric addition of an alkyl radicals to a double bond. One of the most important applications is the oxo synthesis for the production of oxo chemicals (Scheme 3). Technically, such biphenols have their main application area in hydroformylation producing about 10.4 million tons/year of oxo chemicals.[37,38]

The classical synthesis of this biphenol needs stoichiometric or even more oxidizing agent. With the conventional method, a

27
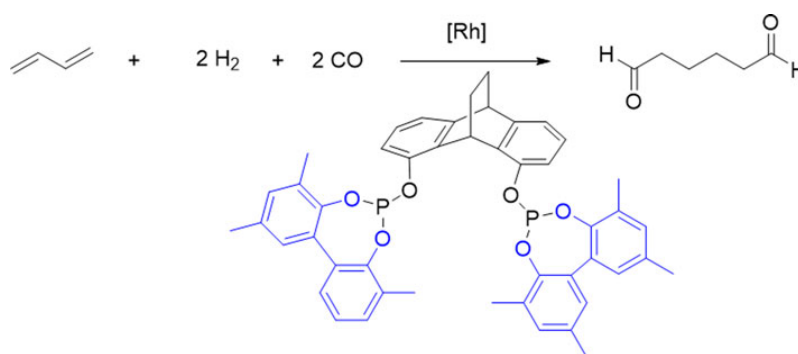
Scheme 3. Twofold hydroformylation of 1,3-butadiene.

large amount of reagent waste is generated, and the selectivity and yields might be low. Another synthetic approach uses transition metal catalysts as VO(acac)$_2$, methyltrioxorhenium, or RuCl$_3$.[39-41] However, with the transition metal method, the yields are also often low. Additionally, the used catalysts are mostly expensive and toxic. The conventional chemical route can neither be considered ecological nor economical.

Regarding the current global challenges as climate change and resource scarcity, the interest in renewable technologies for chemical industry increases. With electro-organic synthesis, some of these issues can be successfully tackled. Electrochemistry uses only electrons as clean reagent for oxidation or reduction

processes. Avoiding amounts of catalysts and oxidizing or reducing agents are significant for sustainability strategies (Fig. 6).

The following will show the electrochemical development for a synthetic strategy to produce 3,3′,5,5′-tetramethyl-2,2′-biphenol. In the conventional synthetic approaches, overoxidation and the formation of different polycyclic derivates, for example the Pummerer ketone, are unavoidable (Scheme 4).[42-45]

To prevent other byproducts and overoxidation, a two-step synthesis via tetraphenoxy borates is used (Scheme 5).[46]

The borates are used as templated substrates for oxidative cyclization as well as a supporting electrolyte.[42,47] Yields up to 85% are achieved even in a multi-kilogram scale.[48] However, this
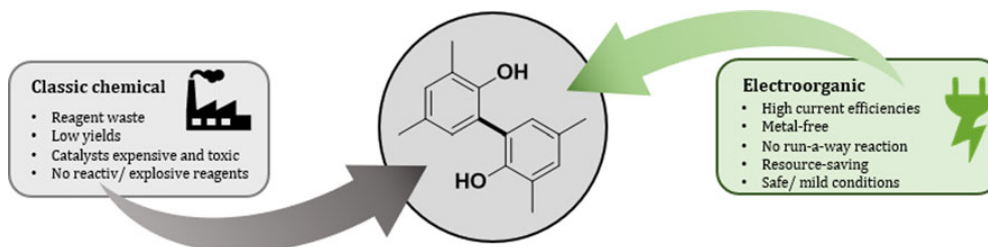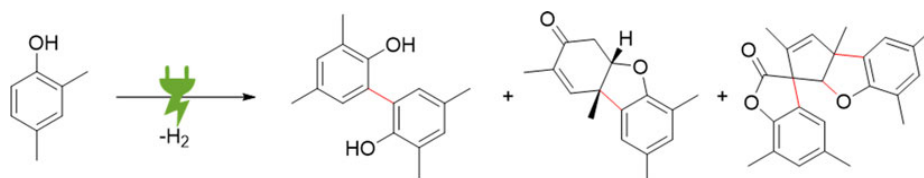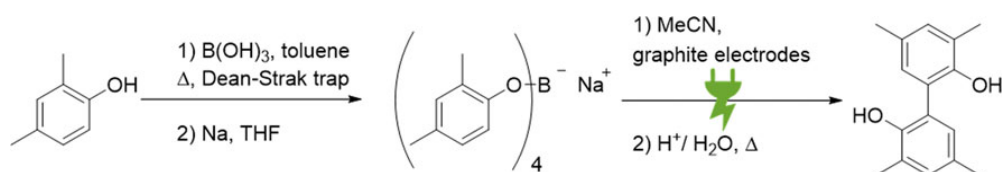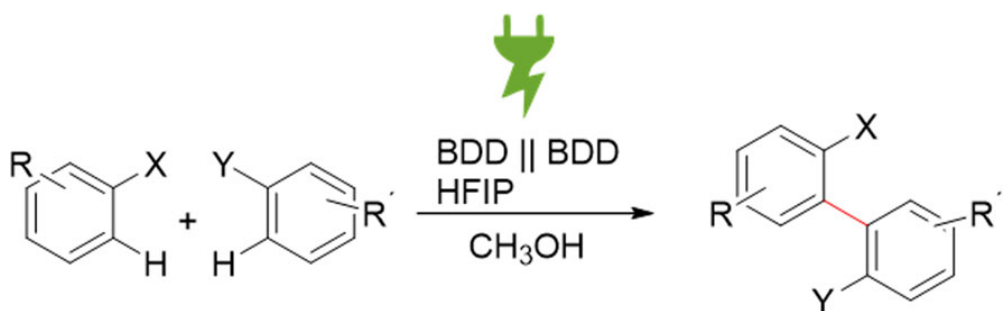

Figure 6. Advantages of electrochemical methods in comparison to conventional organic chemistry.

Scheme 4. Synthetic strategy to 3,3′,5,5′-tetramethyl-2,2′-biphenol and polycyclic derivatives.

28

Scheme 5. Two-step synthesis via boron-tethered phenolates for anodic phenol-coupling.

Scheme 6. Phenol/aniline-arene cross-coupling. X = OH, NHR; Y = H, OH, NHR, OTIPS.[33]

electrosynthesis generates borate containing wastewater which is problematic within the EU. In addition, the process is a multi-step protocol. In order to reduce the multi-step protocol, the first direct way for the anodic cross-coupling of phenols without using leaving functionalities, protecting groups, or reagents was introduced in an undivided cell with a boron-doped diamond (BDD) anode and nickel as a cathode.[49] Either hexafluoroisopropanol (HFIP) or HFIP/methanol is used as an electrolyte with methyl triethylammonium methylsulfate as a supporting electrolyte. By using HFIP-based electrolytes, a high selectivity is achieved.[50] Working with BDD electrodes in combination with HFIP as a solvent showed a high performance and robustness.[51] In protic media, the electrochemical window is extended with HFIP at BDD electrodes to 5 V. HFIP has a stabilizing effect on anodically generated radicals, so the decomposition of reactants is avoided.[51] Additionally, the recovery and direct reuse of this solvent is almost completely achieved.[31,52] BDD has unique properties such as a high chemical stability and high hydrogen overpotential in aqueous solutions. Due to its properties, BDD opens a wide field of new synthetic strategies.[53,54]

The method was improved by using HFIP with 5 vol.% pyridine as an electrolyte and electrolysis was conducted with a

Table 1. Products obtained by electrochemical CO_2 reduction and associated energy consumption.

Reaction	Faradaic efficiency[a] (%)	EEC (kWh/kg)[b]	Electricity costs[d] (€/kg)
$CO_2 + 2H^+ + 2e^- \rightarrow CO + H_2O$	90–99[20]	5	0.5
$CO_2 + 6H^+ + 6e^- \rightarrow CH_3OH_{(aq)} + H_2O$	[c]25–70[21,22]	20	2.0
$2CO_2 + 12H^+ + 12e^- \rightarrow C_2H_5OH_{(aq)} + 3H_2O$	15–25[59,60]	75	7.5
$2CO_2 + 12H^+ + 12e^- \rightarrow C_2H_{4(g)} + 4H_2O$	50–70[61,62]	50	5.0
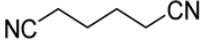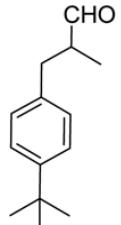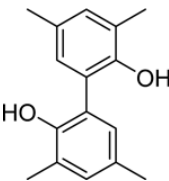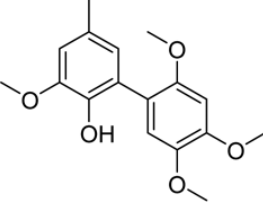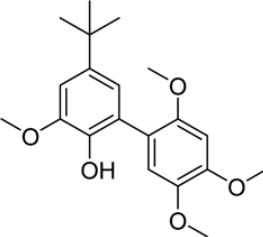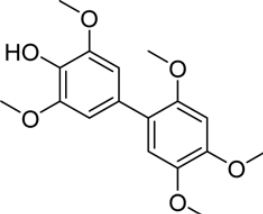
[a]Data regarded as reasonable based on the literature. Only current densities >100 mA/cm^2 were considered.
[b]Hypothetical cell operating voltage = 3 V, highest FE of range assumed.
[c]Current densities higher than 50 mA/cm^2 have not been reported.
[d]Assumed electricity price = 0.1 €/kWh.

Table 2. Energy consumption in the electrosynthesis of chemicals.

Process	Products	Current efficiency (%)	EEC (kWh/kg)[a]	Electricity costs[b] (€/kg)
Baizer		90	2.43	0.24
Lysmeral		70	2.94	0.29
Anodic homo-coupling		71[58]	0.93[b]	0.09
Anodic cross-coupling		69[57]	0.77[b]	0.08
Anodic cross-coupling		60[57]	0.77[b]	0.08
Anodic cross-coupling		62[57]	0.81[b]	0.08

[a]Operating at average terminal cell voltage = 3 V.
[b]Assumed electricity price = 0.1 €/kWh.

30

current density of 60 mA/cm^2. By using pyridine as a base, salt-based additional supporting electrolytes are avoided. This is a big advantage over previous works because an expensive supporting electrolyte recovering is prevented. The flow process is very efficient, has satisfactory yields up to 59%, and is suitable for technical processes.[7,55,56] The lower yield is beneficial for the sake of recovery and reuse of starting materials. Particularly, the presented reaction could be used industrially since important key steps have already been developed. Especially, the application of a flow cell is superior to conventional batch reactions. In the flow cell, the electrode surface to volume ratio can be improved by the narrow gap design. Because of this setup, the electrolysis time is reduced, the temperature control is possible, and the cell voltage can be lowered. Due to the small electrode distance, no conducting salt is necessary.[56] By the flow rate, the contact time of the reactant with the electrode surface can be controlled and overoxidation is avoided. These advantages offer about 40% more electric efficiency.

Other anodic carbon–carbon bond formations, for example, with aniline-arenes are also possible. Over 70 derivatives are known with yields up to 92%. For high selectivity, a bipolar electrode arrangement is used.[33,57,58] Only the outer electrodes are connected, and the electrodes in between are polarized by the electric field. The electrode surface is drastically enhanced by this approach. Furthermore, using bipolar cells has the advantage that the number of electrodes can be varied and used flexible in different cells (Scheme 6).

Conclusions

Electro-organic synthesis has experienced a renaissance during the past years, as it offers conversions under mild conditions, replaces chemical oxidizing and reducing agents, and opens up novel synthesis routes and strategies. From an industrial point of view, the energy efficiency or energy demand plays a key role. The electrochemical production of synthetic fuels and commodities from CO_2 is mainly challenged by high capital costs, the price of electric energy, and the enormous size of the petroleum-based market. Furthermore, it takes comparatively high amounts of charge to produce C_{2+} products from CO_2. For example, in order to generate one mole of ethanol from CO_2, 12 electrons are needed, which is substantially higher compared to fine chemical synthesis, where usually less than 5 electrons are transferred per product molecule which exhibit substantially larger molecular weight. The amount of charge contributes to the high EEC (Table 1).

Other than platform chemicals and synthetic fuels, electrochemically synthesized fine chemicals do not have to compete with the feedstock of crude oil itself. They are higher priced and at the same time produced more selectively and at lower scales, which lead to smaller capital costs.

In comparison to the CO_2 conversion, the discussed industrial processes show significantly lower EECs per kg product (Table 2). Since, on the laboratory scale, multi-purpose cells

were employed and not as on a technical process the energy optimized and tailor-made electrolyzer, the energy efficiency on a laboratory scale is usually significantly lower.

In cases where large amounts of chemical oxidizing and reducing agents can be avoided, an electrochemical approach is highly favorable. The downstream processing is often neglected but is crucial for a later translation into technical use, as outlined with the formation of borate containing wastewater. The application of stabilizing agents like HFIP opens up new synthesis strategies, reaching increased selectivity and in turn higher energy efficiency as well.

The chemical route from CO_2-based commodities to fine chemicals still provides a gap, as building complex molecules from CO_2 is challenging. A more efficient approach might be fermentation. The electrochemical generation of aromatic structures from CO_2 cannot be achieved directly; however, aromatic compounds would be accessible by reforming of CO_2-based hydrocarbons.

We conclude that electro-organic synthesis is more likely to pay off when fine chemicals rather than commodities are produced. Capital costs, energy prices, and downstream processing are driving factors. The margin becomes more favorable when the costs for electrolyzers and downstream processing are low, and the product can be sold for a high price, which is the case for fine chemicals.

REFERENCES:

1. Waldvogel S.R. and Janza B.: Renaissance of electrosynthetic methods for the construction of complex molecules. *Angew. Chem. Int. Ed*. 53, 7122–7123 (2014).
2. Wiebe A., Gieshoff T., Möhle S., Rodrigo E., Zirbes M., and Waldvogel S.R.: Electrifying organic synthesis. *Angew. Chem. Int. Ed*. 57, 5594–5619 (2018).
3. Anastas P.T. and Kirchhoff M.M.: Origins, current status, and future challenges of green chemistry. *Acc. Chem. Res*. 35, 686–694 (2002).
4. Frontana-Uribe B.A., Little R.D., Ibanez J.G., Palma A., and Vasquez-Medrano R.: Organic electrosynthesis: A promising green methodology in organic chemistry. *Green Chem*. 12, 2099–2119 (2010).
5. Pollok D. and Waldvogel S.R.: Electro-organic synthesis: A 21st Century Technique. *Chem. Sci*. (2020). In progress. doi:10.1039/D0SC01848A.
6. Moeller K.D.: Using physical organic chemistry to shape the course of electrochemical reactions. *Chem. Rev*. 118, 4817–4833 (2018).
7. Waldvogel S.R., Lips S., Selt M., Riehl B., and Kampf C.J.: Electrochemical arylation reaction. *Chem. Rev*. 118, 6706–6765 (2018).
8. Yan M., Kawamata Y., and Baran P.S.: Synthetic organic electrochemical methods since 2000: On the verge of a renaissance. *Chem. Rev*. 117, 13230–13319 (2017).
9. Puettner H.: *Organic Electrochemistry*, 4th ed., Chapter 31, Lund H. and Hammerich O.: (Crc Press Inc, Boca Raton, 2000), pp. 1259-1307.
10. Hamann C.H., Hamnett A., and Vielstich W.: *Electrochemistry* (Wiley-VCH, Weinheim, 2007), pp. 159-164.
11. Bard A.J., Stratmann M., Schaefer H.J., and Jörissen J.: Practical aspects of preparative scale electrolysis. *Encyclopedia of Electrochemistry* 8, 35 (2004).

12. Chen C., Khosrowabadi Kotyk J.F., and Sheehan S.W.: Progress toward commercial application of electrochemical carbon dioxide reduction. *Chem* 4, 2571–2586 (2018).

13. De Luna P., Hahn C., Higgins D., Jaffer S.A., Jaramillo T.F., and Sargent E.H.: What would it take for renewably powered electrosynthesis to displace petrochemical processes? *Science* 364, 1–9 (2019).

14. Nitopi S.A., Bertheussen E., Scott S.B., Liu X., Engstfeld A.K., Horch S., Seger B., Stephens I.E.L., Chan K., Hahn C., Nørskov J.K., Jaramilo T.F., and Chorkendorff I.: Progress and perspectives of electrochemical CO_2 reduction on copper in aqueous electrolyte. *Chem. Rev.* 119, 7610–7672 (2019).

15. Yang N., Waldvogel S.R., and Jiang X.: Electrochemistry of carbon dioxide on carbon electrodes. *ACS Appl. Mater. Interfaces* 8, 28357–28371 (2016).

16. Higgins D., Hahn C., Xiang C., Jaramillo T.F., and Weber A.Z.: Gas-diffusion electrodes for carbon dioxide reduction: A new paradigm. *ACS Energy Lett.* 4, 317–324 (2019).

17. Rademaekers K., Smith M., Yearwood J., Saheb Y., Moerenhout J., Pollier K., Debrosses N., Badouard T., Peffen A., Pollitt H., Heald S., and Altman M.: Study on energy prices, costs and subsidies and their impact on industry and households. *Trinomics* 74 (2018).

18. Li X., Anderson P., Jhong H.M., Paster M., Stubbins J.F., and Kenis P.J.A.: Greenhouse gas emissions, energy efficiency, and cost of synthetic fuel production using electrochemical CO_2 conversion and the Fischer-Tropsch process. *Energy Fuels* 30, 5980–5989 (2016).

19. Pletcher D.: The cathodic reduction of carbon dioxide – What can it realistically achieve? A mini review. *Electrochem. Commun.* 61, 97–101 (2015).

20. Küngas R.: Review – Electrochemical CO_2 reduction for CO production: Comparison of low- and high-temperature electrolysis technologies. *J. Electrochem. Soc.* 167, 044508 (2020).

21. Al-Rowaili F.N., Jamal A., Ba Shammakh M.S., and Rana A.A.: Review on recent advances for electrochemical reduction of carbon dioxide to methanol using metal-organic framework (MOF) and non-MOF catalysts: Challenges and future prospects. *ACS Sustain. Chem. Eng.* 6, 15895–15914 (2018).

22. Dexin Yang Y., Qinggong Z., Chunjun C., Huizhen L., Zhimin L., Zhijuan Z., Xiaoyu Z., Shoujie L., and Buxing H.: Selective electroreduction of carbon dioxide to methanol on copper selenide nanocatalysts. *Nat. Commun.* 10, 1–9 (2019).

23. Tackett B.M., Gomez E., and Chen J.G.: Net reduction of CO_2 via its thermocatalytic and electrocatalytic transformation reactions in standard and hybrid processes. *Nat. Catal.* 2, 381–386 (2019).

24. Möhle S., Zirbes M., Rodrigo E., Gieshoff T., Wiebe A., and Waldvogel S.R.: Modern electrochemical aspects for the synthesis of value-added organic products. *Angew. Chem. Int. Ed.* 57, 6018–6041 (2018).

25. Wendt H., Vogt H., Kreysa G., Kolb D.M., Engelmann G.E., Ziegler J.C., Goldacker H., Jüttner K., Gallla U., Schmieder H., and Steckhan E.: *Ullmann's Encyclopedia of Industrial Chemistry* (Wiley, Weinheim, 2000); p. 73–85.

26. Vernon D.: Mechanisms of the electrohydrodimerization of activated olefins. The mechanism in proton donor poor solvents, a revelation. *Acta Chem. Scand.* 35, 51–52 (1981).

27. Vyazankin I.L. and Knunyants N.S.: Hydrodimerization of acrylonitrile. *Proc. Natl. Acad. Sci. USA* 6, 253–256 (1958).

28. Vaze A.S., Sawant S.B., and Pangarkar V.G.: Electrochemical oxidation of p-t-butyltoluene to p-t-butylbenzaldehyde. *J. Appl. Chem.* 28, 623–626 (1998).

29. Hannebaum H., Voss H., and Weiper-Idelmann A.: patent EP 0638665 B1, 1996.

30. Wang L., Kong Y., Jiang J., Wei D., Li P., Yang S., and Ting Y.: Optimal wastewater treatment using a packed-bed electrode reactor (PBER): From laboratory experiments to industrial-scale approaches. *Chem. Eng. J.* 334, 707–713 (2018).

31. Wiebe A., Schollmeyer D., Dyballa K.M., Franke R., and Waldvogel S.R.: Selective synthesis of partially protected nonsymmetric biphenols by reagent- and metal-free anodic cross-coupling reaction. *Angew. Chem. Int. Ed.* 55, 11801–11805 (2016).

32. Schäfer H.J.: *Recent Contributions of Kolbe Electrolysis to Organic Synthesis* (Springer, 2005), Berlin, Heidelberg; pp. 91–151. ISBN 978-3-540-48139-3.

33. Kirste A., Schnakenburg G., Stecker F., Fischer A., and Waldvogel S.R.: Anodic phenol: Arene cross-coupling reaction on boron-doped. *Angew. Chem. Int. Ed.* 49, 971–975 (2010).

34. Alexakis A. and Polet D.: Biphenol-based phosphoramidite ligands for the enantioselective copper-catalyzed conjugate addition of diethylzinc. *J. Org. Chem.* 69, 5660–5667 (2004).

35. Brunel J.M. and Ce P.: BINOL: A versatile chiral reagent. *Chem. Rev.* 105, 857–898 (2005).

36. Monti C., Gennari C., and Piarulli U.: Enantioselective conjugate addition of phenylboronic acid to enones catalysed by a chiral tropos/atropos rhodium complex at the coalescence temperature. *Chem. Commun.* 42, 5281–5283 (2005).

37. Franke R., Selent D., and Bo A.: Applied hydroformylation. *Chem. Rev.* 112, 5675–5732 (2012).

38. Mormul J., Mulzer M., Rosendahl T., Rominger F., Limbach M., and Hofmann P.: Synthesis of adipic aldehyde by n-selective hydroformylation of 4-pentenal. *Organometallics* 34, 4102–4108 (2015).

39. Yadav J.S., Reddy B.V.S., Uma Gayathri K., and Prasad A.R.: [Bmim]PF$_6$/RuCl$_3$·xH$_2$O: A novel and recyclable catalytic system for the oxidative coupling of β-naphthols. *New J. Chem.* 27, 1684–1686 (2003).

40. Hwang D., Chen C., and Uang B.: Aerobic catalytic oxidative coupling of 2-naphthols and phenols by VO (acac)$_2$. *Chem. Commun.* 13, 1207–1208 (1999).

41. Sharma V.B., Jain S.L., and Sain B.: Methyltrioxorhenium-catalyzed aerobic oxidative coupling of 2-naphthols to binaphthols. *Tetrahedron Lett.* 44, 2655–2656 (2003).

42. Malkowsky I.M., Fröhlich R., Griesbach U., Pütter H., and Waldvogel S.R.: Facile and reliable synthesis of tetraphenoxyborates and their properties. *Eur. J. Inorg. Chem.* 8, 1690–1697 (2006).

43. Malkowsky I.M., Rommel C.E., Wedeking K., Fröhlich R., Bergander K., Nieger M., Quaiser C., Griesbach U., Pütter H., and Waldvogel S.R.: Facile and highly diastereoselective formation of a novel pentacyclic scaffold by direct anodic oxidation of 2,4-dimethylphenol. *Eur. J. Org. Chem.* 2006, 241–245 (2006).

44. Barjau J., Königs P., Kataeva O., and Waldvogel S.R.: Reinvestigation of highly diastereoselective pentacyclic spirolactone formation by direct anodic oxidation of 2,4-dimethylphenol. *Synlett* 15, 2309–2312 (2008).

45. Barjau J., Schnakenburg G., and Waldvogel S.R.: Diversity-oriented synthesis of polycyclic scaffolds by modification of an anodic product derived from 2,4-dimethylphenol. *Angew. Chem. Int. Ed.* 50, 1415–1419 (2011).

46. Rommel C., Malkowsky I., Waldvogel S. R., Pütter H., and Griesbach U.: patent WO 2005/075709 A2, 2005.

47. Malkowsky I.M., Rommel C.E., Fröhlich R., Griesbach U., Püttner H., and Waldvogel S.R.: Novel template-directed anodic phenol-coupling reaction. *Chemistry* 12, 7482–7488 (2006).

48. Rommel C. E., Malkowsky I., Waldvogel S., Puetter H., and Griesbach U.: Anodic dimerization of substituted benzenes for the production of biarylalcohols, PCT Int. Appl. WO 2005075709 A2 20050818, 2005.

49. Malkowsky I.M., Griesbach U., Pütter H., and Waldvogel S.R.: Unexpected highly chemoselective anodic ortho-coupling reaction of 2,4-dimethylphenol on boron-doped diamond electrodes. *Eur. J. Org. Chem.* 20, 4569–4572 (2006).

50. Kirste A., Nieger M., Malkowsky I.M., Stecker F., Fischer A., and Waldvogel S.R.: Ortho-selective phenol-coupling reaction by anodic treatment on boron-doped diamond electrode using fluorinated alcohols. *Chem. Eur. J.* 15, 2273–2277 (2009).

51. Ayata S., Stefanova A., Ernst S., and Baltruschat H.: The electro-oxidation of water and alcohols at BDD in hexafluoroisopropanol. *J. Electroanal. Chem.* 701, 1–6 (2013).

52. Lips S., Wiebe A., Elsler B., Schollmeyer D., Dyballa K.M., Franke R., and Waldvogel S.R.: Synthesis of meta-terphenyl-2,2′′-diols by anodic C—C cross-coupling reactions. *Angew. Chem. Int. Ed.* 55, 10872–10876 (2016).

32

53. Cheng J. and Deming T.J.: Synthesis of polypeptides by ring-opening polymerization of α-amino acid N-carboxyanhydrides. *Pept. Mater*. 310, 1–26 (2011).

54. Lips S. and Waldvogel S.R.: Use of boron-doped diamond electrodes in electro-organic synthesis. *ChemElectroChem* 6, 1649–1660 (2019).

55. Selt M., Mentizi S., Schollmeyer D., Franke R., and Waldvogel S.R.: Selective and scalable dehydrogenative electrochemical synthesis of 3,3',5,5'-tetramethyl-2,2'-biphenol. *Synlett* 30, 2062–2067 (2019).

56. Selt M., Franke R., and Waldvogel S.R.: Supporting-electrolyte-free and scalable flow process for the electrochemical synthesis of 3,3',5,5'-tetramethyl-2,2'-biphenol. *Org. Process Res. Dev*. (2020). In progress. doi:10.1021/acs.oprd.0c00170.

57. Kirste A., Elsler B., Schnakenburg G., and Waldvogel S.R.: Efficient anodic and direct phenol-arene C,C cross-coupling: The benign role of water or methanol. *J. Am. Chem. Soc*. 134, 3571–3576 (2012).

58. Röckl J.L., Schollmeyer D., Franke R., and Waldvogel S.R.: Dehydrogenative anodic C−C coupling of phenols bearing electron-withdrawing groups. *Angew. Chem. Int. Ed*. 59, 315–319 (2020).

59. Kuilin L., Yanchen F., Ying Z., Yi Y., Jinrong W., Ying Z., and Qianfan Z.: Elastic Ag-anchored N-doped graphene/carbon foam for the selective electrochemical reduction of carbon dioxide to ethanol. *J. Mater. Chem. A* 6, 5025–5031 (2018).

60. Hoang T.T.H., Verma S., Ma S., Fister T.T., Timoshenko J., Frenkel A.I., Kenis P.J., and Gewirth A.A.: Nanoporous copper-silver alloys by additive-controlled electrodeposition for the selective electroreduction of CO_2 to ethylene and ethanol. *J. Am. Chem. Soc*. 140, 5791–5797 (2018).

61. Li F., Thevenon A., Rosas-Hernández A., Wang Z., Li Y., Gabardo C.M., Ozden A., Dinh C.T., Li J., Wang Y., Edwards J.P., Xu Y., McCallum C., Tao L., Liang Z.-Q., Luo M., Wang X., Li H., O'Brien C.P., Tan C.-S., Nam D.-H., Quintero-Bermudez R., Zhuang T.-T., Li Y.C., Han Z., Britt R.D., Sinton D., Agapie T., Peters J.C., and Sargent E.H.: Molecular tuning of CO_2-to-ethylene conversion. *Nature* 577, 509–513 (2020).

62. García de Arquer F.P., Dinh C.-T.-, Ozden A., Wicks J., McCallum C., Kirmani A.R., Nam D.-H., Gabardo C., Seifitokaldani A., Wang X., Li Y.C., Li F., Edwards J., Richter L.J., Thorpe S.J., Sinton D., and Sargent E.H.: CO_2 electrolysis to multicarbon products at activities greater than $1\,A\,cm^{-2}$. *Science* 367, 661–666 (2020).

33

2 Experimentalteil (für unveröffentlichte Ergebnisse)

Die Ergebnisse der elektrochemischen CO_2-Reduktion und Teile der Katalysatorherstellung wurden nicht in wissenschaftlichen Zeitschriften publiziert. Dieses Kapitel umfasst den Methodenteil der unveröffentlichten Arbeiten.

Katalysatorherstellung Als Katalysatormaterial wurden Kupfer-basierte Partikel, meist Kupferoxide, verwendet. Diese wurden überwiegend mittels hydrothermaler Synthese hergestellt (Tabelle 2.1). Die meisten der hergestellten Partikel basieren auf dem thermischen Zerfall von Kupfer(II)-hydroxid:

$$Cu(OH)_2 \longrightarrow \Delta \, CuO + H_2O$$
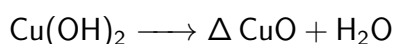
Als zusätzliche Methode diente die Calcinierung von basischem Kupfercarbonat. Das basische Kupfercarbonat selbst wurde aus Lösungen von Kupfer(II)-chlorid und Natriumcarbonat hergestellt:

$$3\,Na_2CO_3 + 3\,CuCl_2 + H_2O \longrightarrow 6\,NaCl + 2\,CuCO_3 \cdot Cu(OH)_2 \downarrow + CO_2 \uparrow$$
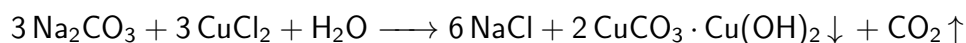
Tabelle 2.1: Hergestellte Katalysatormaterialien.

Kürzel	Kupferspezies	Herstellungsmethode
Cat_A	$CuCO_3 \cdot Cu(OH)_2$	**Präzipitation:** Eine 0.5 M $CuCl_2$ Lösung wurde langsam in eine 1 M Na_2CO_3 Lösung getropft. Der entstandene Feststoff wurde abfiltriert und mit Wasser gewaschen.
Cat_B	CuO	**Calcinierung:** Material Cat_A wurde im Ofen für 2 h auf 200 °C erhitzt.

Tabelle 2.1: Hergestellte Katalysatormaterialien. (Fortsetzung)

Kürzel	Kupferspezies	Herstellungsmethode
Cat_C	CuO	**Hydrothermale Synthese:** In 45 mL einer 1 M $NaHCO_3$ Lösung wurden 2.5 mmol $CuCl_2 \cdot 2\,H_2O$ (426.2 mg) gelöst und für 15 min gerührt. Anschließend wurde die Lösung in einen 100 mL Autoklaven gefüllt und für 4 h auf 200 °C erhitzt. Der Autoklav wurde mit einem Wasserbad auf Raumtemperatur abgekühlt und der entstandene Feststoff abfiltriert, mit Wasser gewaschen und getrocknet.
Cat_D	CuO	**Hydrothermale Synthese:** In 35 mL H_2O wurden 2.5 mmol $CuSO_4 \cdot H_2O$ gelöst. Langsam wurden 62 mmol NH_3 Lösung (32 %) zugetropft. Anschließend wurde 1 mL einer 1 M NaOH Lösung zugetropft. Anschließend wurde die Lösung in einen 100 mL Autoklaven gefüllt und für 4 h auf 130 °C erhitzt. Der Autoklav wurde mit einem Wasserbad auf Raumtemperatur abgekühlt und der entstandene Feststoff abfiltriert, mit Wasser gewaschen und getrocknet.
Cat_E	CuO	**Hydrothermale Synthese:** Analog zu Cat_D. Vor der Befüllung des Autoklaven wurden 199 mg multiwandiger Kohlenstoff-Nanoröhrchen (MWCNT, Merck) in der Lösung dispergiert.
Cat_F	CuO	**Hydrothermale Synthese:** Analog zu Cat_C. Vor der Befüllung des Autoklaven wurden 199 mg multiwandiger Kohlenstoff-Nanoröhrchen (MWCNT, Merck) in der Lösung dispergiert.
Cat_G	Cu, Cu_2O, CuO	**Solvothermale Synthese:** Ethylenglykol und Cholinchlorid wurden in einem 2:1 Molverhältnis gemischt und auf 80 °C erhitzt und gerührt bis eine klare Lösung entstand. Anschließend wurden 10 mL der Mischung mit 20 mL H_2O vermengt. In der Mischung wurden 2.5 mmol $CuCl_2 \cdot 2\,H_2O$ gelöst. Anschließend wurden 20 mL einer wässrigen 1 M NaOH-Lösung langsam zugetropft. Anschließend wurde die Lösung in einen 100 mL Autoklaven gefüllt und für 12 h auf 180 °C erhitzt. Der Autoklav wurde mit einem Wasserbad auf Raumtemperatur abgekühlt und der entstandene Feststoff abfiltriert, mit Wasser gewaschen und getrocknet.

Tabelle 2.1: Hergestellte Katalysatormaterialien. (Fortsetzung)

Kürzel	Kupferspezies	Herstellungsmethode
Cat_H	Cu, Cu$_2$O, CuO	**Solvothermale Synthese:** Zunächst wurden 25 mL H$_2$O mit 5 mL Ethylenglykol vermengt. In der Mischung wurden 2.5 mmol CuCl$_2 \cdot 2$ H$_2$O gelöst. Anschließend wurden 20 mL einer wässrigen 1 M NaOH-Lösung langsam zugetropft. Anschließend wurde die Lösung in einen 100 mL Autoklaven gefüllt und für 12 h auf 180 °C erhitzt. Der Autoklav wurde mit einem Wasserbad auf Raumtemperatur abgekühlt und der entstandene Feststoff abfiltriert, mit Wasser gewaschen und getrocknet.
Cat_I	CuO	**Hydrothermale Synthese:** Analog zu Cat_D. Nach Zugabe der Kupferspezies wurden 0.9 mmol L-Alanin in der Reaktionsmischung aufgelöst.
Cat_J	CuO	**Hydrothermale Synthese:** Analog zu Cat_D. Nach Zugabe der Kupferspezies wurden 0.9 mmol Zitronensäure in der Reaktionsmischung aufgelöst.

Elektrodenherstellung Für die Herstellung der Gasdiffusionselektroden wurden 20 mg des Katalysatormaterials in H$_2$O (200 µL), Isopropanol (200 µL) und 5 %-iger Nafion-Lösung (10 µL) suspendiert und für 30 min bei Raumtemperatur mit Ultraschall behandelt. Anschließend wurde die Suspension auf 4 cm^2 einer Gasdiffusionsschicht (H23C9, *Freudenberg Performance Materials*) getropft und für 24 h bei 30 °C getrocknet.

Gasdiffusionszelle Die elektrochemische CO$_2$-Reduktion wurde in einer eigens konzipierten Gasdiffusionszelle aus Teflon durchgeführt (Abbildung 2.1). Als Zellseparator diente eine Nafion-Membran. Das Katholytvolumen betrug 13 mL und das Anolytvolumen 23 mL. Als Kathode wurde die mit Katalysator beladene Gasdiffusionselektrode verwendet. Als Gegenelektrode wurde eine Mischoxidanode (RuO$_2$-IrO$_2$/Ti) verwendet. Eine Minireferenzelektrode (Ag/AgCl, eDAQ) wurde genutzt. Die Elektrolyse wurde galvanostatisch mithilfe eines Potentiostaten (Metrohm Autolab PGSTAT128N) durchgeführt. Das gemessene Elektrodenpotential wird gegenüber der verwendeten Ag/AgCl Referenzelektrode angegeben. Zur besseren Vergleichbarkeit mit Literaturdaten kann das Potential, bezogen auf die reversible Wasserstoffelektrode (RHE), angegeben werden:[60]

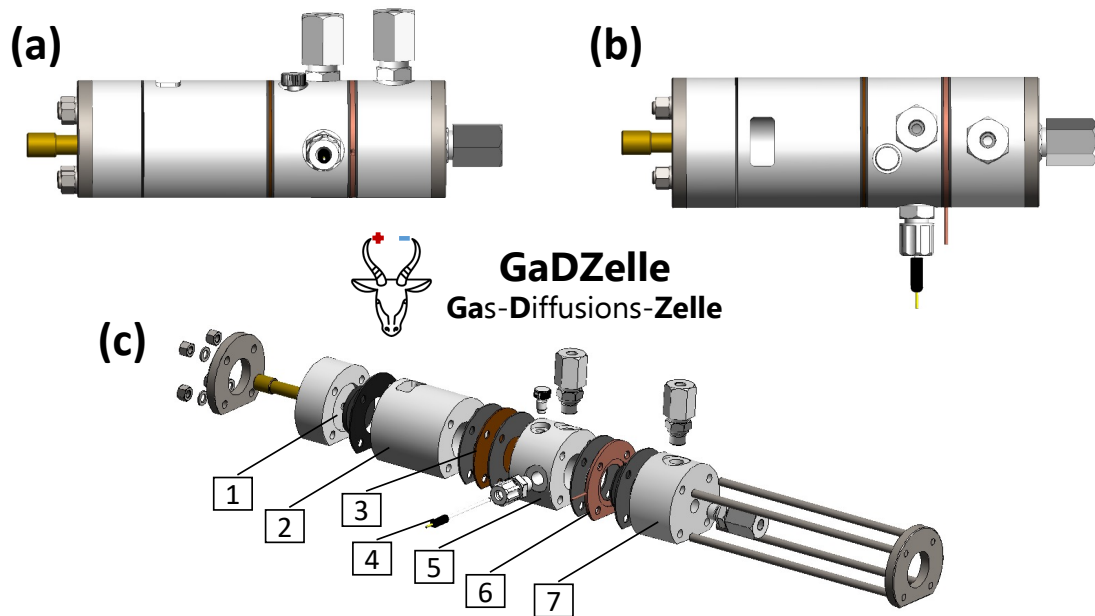$$E_{vs.RHE} = E_{vs.Ag/AgCl} + 0.197 + 0.056 * pH_{Elektrolyt}$$

Abbildung 2.1: Verwendete Gasdiffusionszelle: a) Seitenansicht, b) Draufsicht, c) Explosions-zeichnung. 1 = Anodenhalterung, 2 = Anodenraum, 3 = Nafion-Membran, 4 = Referenzelektrode, 5 = Kathodenraum, 6 = Kathodenkontaktierung und Gasdiffusionselektrode, 7 = Gaskompartment.

Der Elektrolyt wurde für 30 min vor der Elektrolyse mit CO_2 gesättigt. Während der gesamten Elektrolyse wurde die Gasdiffusionszelle mit einem konstanten CO_2-Volumenstrom versorgt. Gasförmige Produkte sowie unreagiertes CO_2 wurden in Gasbags gesammelt und im Anschluss an die Reaktion mittels GC-TCD analysiert. Die Elektrolyse wurde nach einer definierten Zeit abgebrochen und der Elektrolyt wurde mittels NMR untersucht.

Katalysator- und Produktanalytik Die hergestellten Katalysatormaterialien wurden kristallografisch mithilfe eines Pulverdiffraktometers (Miniflex, Rigaku, Tokyo, Japan) charakterisiert. Die Partikelform wurde mit einem Rasterelektronenmikroskop (Zeiss DSM 940A) untersucht. Flüssige Elektrolyseproben wurden mittels NMR (JEOL JNM-ECA 400 MHz) untersucht und über Natriumtrimethylsilylpropionat-d4 als internem Standard quantifiziert. Gasförmige Proben wurden mit einem GC-TCD System (Shimadzu, GC-2010) untersucht. Hierbei wurde über Kalibriergeraden quantifiziert.

Die Ergebnisse der elektrochemischen CO_2-Reduktion befinden sich in Unterabschnitt 3.1.3.

3 Ergebnisse und Diskussion

3.1 Elektrochemische CO$_2$-Reduktion (CO$_2$RR) zu Plattformchemikalien

Kohlenstoffdioxid kann in wässrigen Medien elektrochemisch zu Kohlenstoffmonoxid, Formiat, Alkoholen und Kohlenwasserstoffen umgesetzt werden. Dabei besitzen Kupfer-basierte Elektrodenmaterialien die einzigartige Eigenschaft, Bindungen zwischen Kohlenstoffatomen zu knüpfen. Auf diese Weise kann beispielsweise die Grundchemikalie Ethylen hergestellt werden. Bei der elektrochemischen CO$_2$-Reduktion (CO$_2$RR) mit Kupferkatalysatoren haben Materialeigenschaften wie Kupferspezies, Partikelgröße und Morphologie großen Einfluss auf die Selektivität der Konversion.

In diesem Kapitel wird die Herstellung verschiedener Kupferkatalysatoren beschrieben und die erhaltenen Materialien kristallographisch und mittels Rasterelektronenmikroskopie analysiert. Anschließend werden die Partikel als Katalysatormaterial für die elektrochemische CO$_2$-Reduktion verwendet und hinsichtlich der generierten Produkte verglichen.

3.1.1 Morphologie-Steuerung mithilfe hydrothermaler Synthese

Zu diesem Kapitel wurde ein Manuskript veröffentlicht:

J. Seidler, V. Landgraf, L. Vieira, D. Van Opdenbosch, S. R. Waldvogel, *Novel Cuprous Oxide Morphologies Using Amino Acids and Carboxylic Acids as Structure Directing Agents in a Simple Hydrothermal Method*, Mater. Lett. **2021**, 292, 129553. [DOI: 10.1016/j.matlet.2021.129553]

Reprinted with permission. Copyright 2021 Elsevier.

Erklärung meines Beitrags:

Personenbezogene Daten

Hintergrund   Die elektrochemische Reduktion von CO_2 zu Wertprodukten wie Ethanol oder Ethylen kann mithilfe von Kupfer-basierten Elektrokatalysatoren erreicht werden.[14] Dabei wird unter anderem die Morphologie des verwendeten Elektrokatalysators als mögliche Einflussgröße auf die Produktselektivität genannt.[32,61,62] Es existieren zahlreiche Methoden um die Partikelform und -größe zu beeinflussen. Dazu gehören die hydrothermale Synthese, Kalzinierung, Elektroabscheidung und chemische Gasphasenabscheidung.[63–67] In der hydrothermalen Synthese können Morphologie und Partikelgröße über Additive, welche dem wässrigen Medium zugefügt werden, gesteuert werden. Darüber hinaus beeinflusst die Wahl des Additivs die Oxidationsstufe des Kupfers (CuO, Cu_2O, Cu). In der vorliegenden Publikation werden verschiedene Additive auf ihren Effekt in der hydrothermalen Synthese untersucht.

Ergebnisse   Für die hydrothermale Synthese von Kupfer-basierten Partikeln wurde eine wässrige Lösung von Kupfer(II)-acetat verwendet. In einem Teflon-beschichten Autoklaven wurde die Lösung für 4 h auf 200 °C erhitzt. Vier Additive wurden in dem hydrothermalen System getestet: Citrat, Oxalat, Glycin und Threonin (1).

| Citrat | Oxalat | Glycin | Threonin |
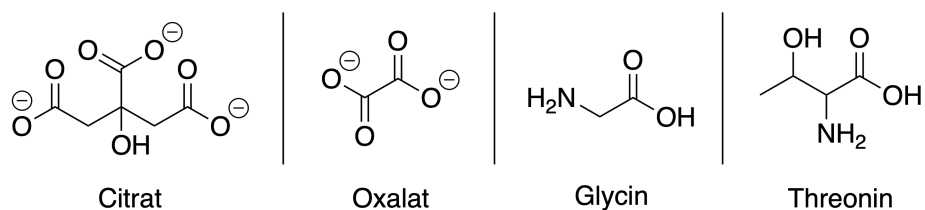
Schema 1: Verwendete Additive für die hydrothermale Synthese von Kupfer(oxid)-Partikeln.

Nach Zugabe des jeweiligen Additivs zur Kupferlösung, wurde die Bildung des eines neuen Kupferkomplexes durch eine Verschiebung des Absorptionsmaximums im UV-Vis-Spektrum bestätigt. Durch die anschließende Erwärmung auf 200 °C bei autogenem Druck wurden Kupfer- bzw. Kupferoxidpartikel verschiedener Größe und Morphologie erzeugt. Dabei wurde unter Verwendung von Oxalat und Citrat ausschließlich Cu_2O generiert. Der Zusatz von Aminosäuren (Glycin oder Threonin) führte während der hydrothermalen Synthese zu einer vollständigen Reduktion der Kupferspezies zu Cu^0. In einem Kontrollexperiment ohne zusätzliches Additiv wurde die Kupferoxidationsstufe nicht verändert wodurch kugelförmige CuO-Partikel erhalten wurden (Abbildung 3.1).
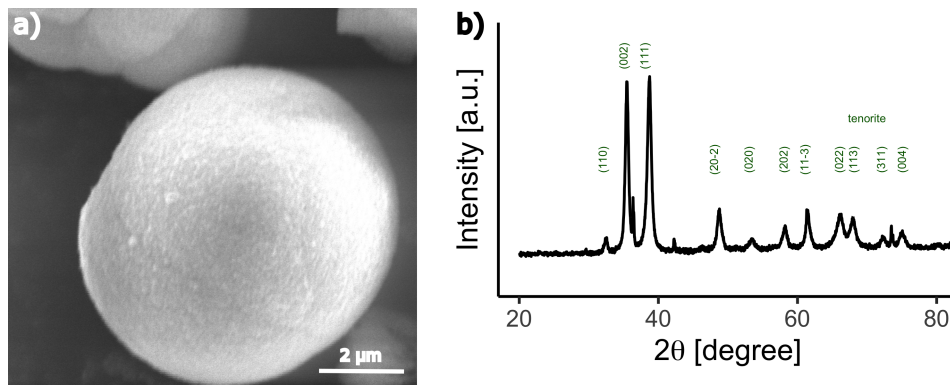
Abbildung 3.1: Kontrollversuch ohne komplexbildendes Additiv: a) REM-Aufnahme eines kugelförmigen Partikels, b) Pulverdiffraktogramm des Kupfer(II)-oxids.

In allen Reaktionen wurden lediglich eine Kupferspezies und keine Mischungen generiert. Die durchschnittliche Kristallitgröße lag bei allen generierten Materialien oberhalb von 100 nm. Die unterschiedlichen Oxidationsstufen des Kupfers bzw. die Identität der generierten Kupferspezies konnten durch die Wahl der Additive gezielt beeinflusst werden. Das eingesetzte Cu^{2+} wurde mithilfe von Stickstoff beinhaltenden Komplexbildnern am weitesten reduziert. In der Literatur werden thermische Zersetzungsprodukte wie CO und NH_3 als Reduktionsmittel angeführt.[68,69] Weiterhin kann die Aminogruppe ebenfalls reduzierend wirken,[70] während die eingesetzten Carboxylate wahrscheinlich nur über ihre Zersetzungsprodukte eine Reduktion bewirken. Interessanterweise wurde durch den alleinigen Einsatz von Kupfer(II)-acetat ohne weiteres Additiv keine Reduktion des Kupfers hervorgerufen. In Studien zur thermischen Zersetzung von Kupfer(II)-acetat in Luft wurden im Temperaturbereich von 200 bis 500 °C Mischungen von CuO und Cu_2O gefunden.[71]

Unter Verwendung des Citrat-Additivs wurden blütenförmige Octapod-Kristalle aus Cu_2O erzeugt. Über die Veränderung der Reaktionszeit können verschiedene Stadien im Kristallwachstum beobachtet werden. Zunächst bilden sich würfelförmige Partikel. Im weiteren Prozess scheinen die zugesetzten Citrat-Ionen das Kristallwachstum an den Flächenzentren sowie den Zentren der Kanten zu inhibieren. Dadurch wachsen vornehmlich die Ecken des Würfels weiter an (Abbildung 3.2).
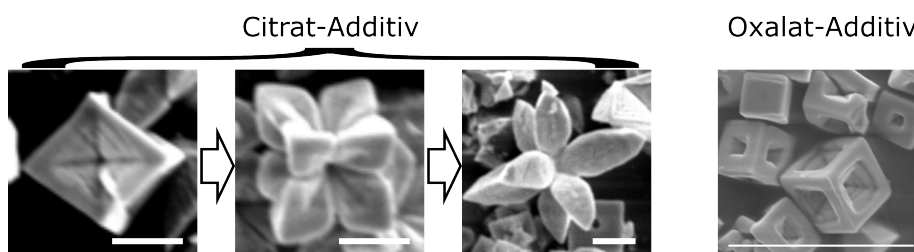
Citrat-Additiv   Oxalat-Additiv

Abbildung 3.2: Die blütenförmigen Cu_2O-Kristalle wachsen in Anwesenheit von Citrat aus würfelförmigen Partikeln heran (Maßstab = 5 μm). Das Oxalat-Additiv führt zu Cu_2O-Würfeln mit abgestuften Flächen (Maßstab = 20 μm).

Das Oxalat-Additiv führte zu würfelförmigen Cu_2O-Kristallen. Die Besonderheit der Würfel ist die flächenzentrierte Abstufung: An den sechs Flächen des Würfels finden sich stufenförmige Einbuchtungen, welche dem Würfelzentrum entgegenlaufen. Flächenzentrierte Löcher in kubischen Partikeln wurden bereits in der Literatur beschrieben,[72] allerdings wurden bisher keine Stufenformen berichtet.

Der Zusatz von den Aminosäuren Glycin und Threonin führte zu unregelmäßig geformten Cu-Kristallen. Die gebildeten Cu-Partikel waren deutlich kleiner als die Cu_2O-Kristalle. In einem Kontrollexperiment konnte gezeigt werden, dass bei Verwendung von Glycin zunächst ebenfalls Cu_2O (in Form von Hexapods) gebildet wird, welches bei längerer Reaktionsdauer vollständig zu Cu^0 reduziert wird. Die Reduktion geht aller Wahrscheinlichkeit nach mit einer Fragmentierung der Partikel einher, wodurch die unregelmäßige Form hervorgerufen wird.

Zusammenfassend bietet die beschriebene Methode ein einfaches Verfahren, die Morphologie und die Oxidationsstufe von Kupferkristallen zu beeinflussen.

Die hergestellten Partikel wurden als Katalysatormaterialien in der elektrochemischen CO_2-Reduktion eingesetzt. Den einzelnen Materialien wurden dabei folgende Kürzel zugeordnet:

Kürzel	Kupferspezies	Verwendetes Additiv
CuO_control	CuO	–
Cu_glycine	Cu	Glycin
Cu_threonine	Cu	Threonin
Cu2O_citrate	Cu_2O	Citrat
Cu2O_oxalate	Cu_2O	Oxalat

Contents lists available at ScienceDirect

Materials Letters

Novel cuprous oxide morphologies using amino acids and carboxylic acids as structure directing agents in a simple hydrothermal method

Johannes Seidler [a,b,c], Victor Landgraf [a], Luciana Vieira [a,*], Daniel Van Opdenbosch [d], Siegfried R. Waldvogel [b,c]

[a] Fraunhofer IGB, Bio, Electro and Chemocatalysis BioCat, Straubing Branch, Schulgasse 11a, 94315 Straubing, Germany
[b] Department of Chemistry, Johannes Gutenberg University, Duesbergweg 10–14, 55128 Mainz, Germany
[c] ESy-Labs GmbH, An der Irler Höhe 3a, 93055 Regensburg, Germany
[d] Campus Straubing for Biotechnology and Sustainability, Technical University of Munich, Schulgasse 16, 94315 Straubing, Germany

ARTICLE INFO

ABSTRACT

The reactivity and catalytic performance of cuprous oxide (Cu_2O) particles rely on the size and morphology of the Cu_2O crystals. In this study, a facile and mild hydrothermal route is applied to generate novel uniform cuprous oxide microcrystals, using non-toxic and low-cost carboxylic acids (O,O-type) and amino acids (N,O-type) as structure directing agents. N,O-type complexing agents showed a higher ability to reduce the copper species compared to the O,O-type ligands. Using oxalate and citrate complexes, pure Cu_2O was obtained after 4 h at 200 °C, whereas the oxalate-based complex leads to the morphology of uniformly stepped microcubes, the citrate complex as precursor leads to flower-like octapods that evolved from microcubes.

© 2021 Elsevier B.V. All rights reserved.

1. Introduction

Cuprous oxide (Cu_2O) has been extensively studied for many applications such as photocatalysts, gas sensors, superconductors, electrode materials in batteries, and as electrocatalyst in the reduction of carbon dioxide [1–3]. The morphology of the Cu_2O crystals is a key factor for most of its applications, as the reactions take place at the particle surface. Therefore, controlling shape and size is crucial in the preparation of uniform Cu_2O particles. Numerous methods concerning Cu_2O with different sizes and morphologies have been reported, including hydrothermal synthesis, calcination, electrodeposition, and chemical vapor deposition [1,3–6]. Cu^{2+} is well-known to form chelate complexes with a range of molecules such as carboxylates, amino acids, and diamines [7]. In a hydrothermal reaction, these ligands can serve as both, structure-directing reagent (SDA) and reducing agent, when a solid phase is formed at elevated temperatures. During nucleation and crystal growth, the SDA interacts with specific sites of the solid phase, which leads to an inhibition of the growth along certain crystal dimensions [8]. In this study, different N,O-type and O,O-type ligands are used to control the copper oxidation state and crystal growth via a hydrothermal method.

2. Materials and methods

2.1. Hydrothermal synthesis of Cu_2O and Cu microcrystals

5 mmol copper(II) acetate were dissolved in 50 mL H_2O using a round-bottom flask. 15 mmol of the complexing agent (glycine, threonine, sodium citrate and sodium oxalate respectively) was added while stirring. An immediate color change was observed. The reaction mixture was transferred into a 100 mL-Teflon lined autoclave and heated in an oven for 4 h. After cooling the autoclave to room temperature using an ice bath, the obtained precipitate was centrifuged, washed with H_2O and ethanol several times, and finally dried in the oven at 70 °C.

2.2. Characterization of complexes

The copper(II) complexes were analyzed using a Thermo Scientific Evolution 201/220 UV–Vis-Spectrophotometer.

* Corresponding author at: Fraunhofer IGB, Bio, Electro and Chemocatalysis BioCat, Straubing Branch, Schulgasse 11a, 94315 Straubing, Germany
E-mail addresses: luciana.vieira@igb.fraunhofer.de (L. Vieira), waldvogel@uni-mainz.de (S.R. Waldvogel).

2.3. Characterization of crystals

Crystallographic analysis of catalyst materials was performed using a powder diffractometer (Miniflex, Rigaku, Tokyo, Japan). The data were evaluated over the 2θ range of 20 to 80 by Rietveld refinement (BGMN, using the Profex interface) [9,10]. The particle shape was examined by scanning electrode microscopy using a Zeiss DSM 940A device. Visible light microscopy was performed on a Mikroskoptechnik Rathenow RMA5 microscope and the resulting images were processed with the imageJ software to obtain the particle size distribution.

3. Results and discussion

Different ligands (glycine, threonine, citrate or oxalate) were added to an aqueous solution containing Cu^{2+}. The formation of copper complexes with the ligands was confirmed by a shift in the UV–Vis spectra towards smaller wavelengths upon adding ligands to the Cu^{2+} solutions (Figure S1). Subsequent hydrothermal treatment led to copper particles with different morphology and oxidation states, depending on the copper complexes used.

O,O-type ligands (oxalate and citrate) led exclusively to Cu_2O, whereas N,O-type ligands (glycine and threonine) resulted in further reduction to Cu. In all cases, diffraction patterns attributed to only one phase were detected, indicating the pure nature of the products (diffractograms in SI, Figure S2). Furthermore, the absence of intensities correspondent to amorphous phases indicates the crystalline nature of all products. Cuprite samples showed preferred orientations, with weighting factors amounted to approximately 1.1, 1, and 0.87 for the lattice plane families {1 0 0}, {1 1 0} and {1 1 1}. These weighting factors indicate an orientation of crystallites relative to the outer shapes of larger-scale particles (compared with Fig. 1). No preferred orientations were detected for the Cu phases obtained from glycine and threonine copper complexes, in agreement with the SEM, which shows the irregular shape of the particles. The average crystallite sizes are above 100 nm for all materials, with no meaningful amounts of nanoscale crystallites (Table S1).

The reduction of Cu^{2+} species to Cu^+ and Cu^0 is likely to be conducted by CO and NH_3 molecules, originating from the decomposition of carboxylic and amino acid ligands [11,12]. A control experiment with no organic complexing agent led exclusively to CuO (XRD in Figure S3). Moreover, the amino functionality of the N,O-type ligands can act as a reducing agent, whereas the carboxylic acid reduces Cu^{2+} most likely via its decomposition products under hydrothermal conditions.

Flower-shaped octapods were obtained when using citrate as additive (Fig. 1a). SEM images of the octapod-particles reveal the growth mechanism of the crystals (Fig. 2). At an early stage of crystal growth, a cubic particle is formed (Fig. 2a). The citrate ligands appear to inhibit the growth of both centers: those of crystal faces and crystal edges. At the same time, the corners of the cube keep growing, which leads to a concave cubic structure (Fig. 2b). As crystal growth proceeds, the corners extend, resulting in Cu_2O octapods (Fig. 2c). The preparation of Cu_2O octapods with short extensions has been described using a dioctyl sulfosuccinate sodium salt surfactant as a structure directing agent [13]. In this study, octapods with longer extensions were prepared without surfactants. Moreover, they are significantly larger (almost one order of magnitude) compared to those described by Zhang and coworkers [13].

Hydrothermal treatment of the oxalate-copper complex led to cubic Cu_2O particles stepped inwards at their faces. The obtained cubic structures show a high degree of homogeneity with an edge
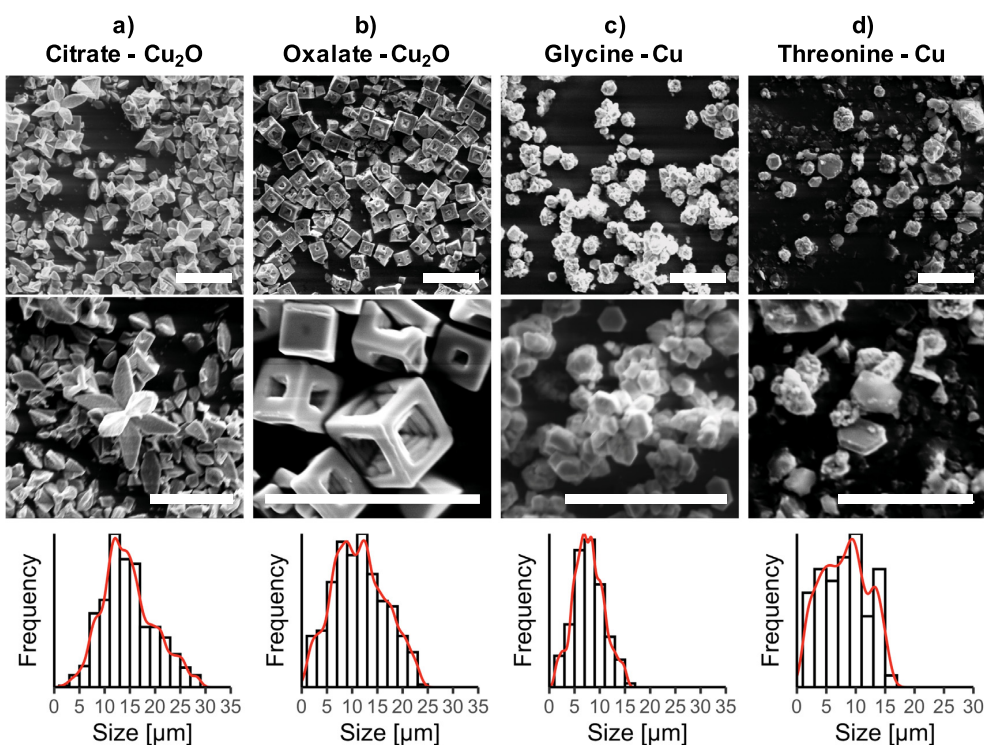

Fig. 1. Micrographs and particle size distribution of synthesized Cu_2O and Cu particles (200 °C for 4 h). Scale bar = 20 μm.
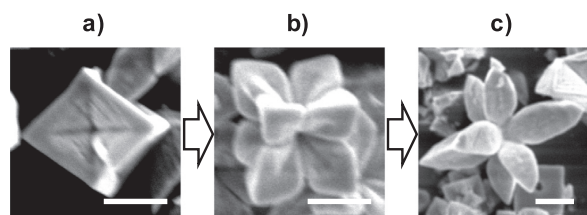
Fig. 2. Evolution of flower-like Cu_2O crystals using citrate as ligand. All evolution stages were observed in the same product (200 °C for 4 h). Scale bar = 5 μm. After 2 h of hydrothermal treatment, most particles have a cubic morphology as in a) (SEM, Figure S5), which verifies that the evolution occurs in the depicted order.

length of approx. 5–8 μm (Fig. 1b). Some of the cubes exhibit small face-centered cavities, while in other particles the steps occupy the entire crystal surface. Cu_2O cubes with face-centered pits have been reported by Zhang et al. [13], however no steps were observed.

Glycine and threonine complexes yield Cu with heterogeneous particle shapes (Fig. 1c and d). The size distribution shows that Cu particles are considerably smaller than the Cu_2O crystals. We suggest that the formation of Cu occurs from the reduction of Cu_2O and involves fragmentation of the crystals, which results in smaller particle size and irregular shape.

XRD patterns of the samples from Cu^{2+} glycine complex treated hydrothermally for 1 h show reflexes correspondent to a mixture of Cu_2O and Cu (Fig. 3), confirming Cu_2O as an intermediate to Cu. Moreover, the cuprite phase crystallites after 1 h treatment of the glycine complex are notably smaller than those obtained from citrate or oxalate (as these were subjected to a longer treatment of 4 h), and free from microstrain. EDX analysis reveals that the hexapods are composed of Cu_2O, similar to those reported by Huang and Stanciu [14,15]. The irregular shaped particles consist mostly of Cu (EDX, Figure S4 and Table S2).

4. Conclusions

Cu_2O and Cu microcrystals were successfully synthesized by a facile hydrothermal method starting from different copper(II) complexes. O,O-type ligands (carboxylic acids) lead to Cu_2O, whereas N,O-type ligands (amino acids) showed stronger reduction ability and yielded exclusively Cu. In both cases, the products contained only one oxidation state of copper. Thus, the desired copper species can be synthesized by tuning the complexing agent. The choice of complexing agent also led to a specific morphology of the microcrystals, such as cubes with inward steps (with oxalate ligand) or octapods with large extensions (with citrate ligand). This approach offers a facile method for the synthesis of copper with different oxidation states and morphology.

CRediT authorship contribution statement

Johannes Seidler: Conceptualization, Methodology, Validation, Investigation, Writing - original draft. **Victor Landgraf:** Data curation, Investigation. **Luciana Vieira:** Conceptualization, Resources,

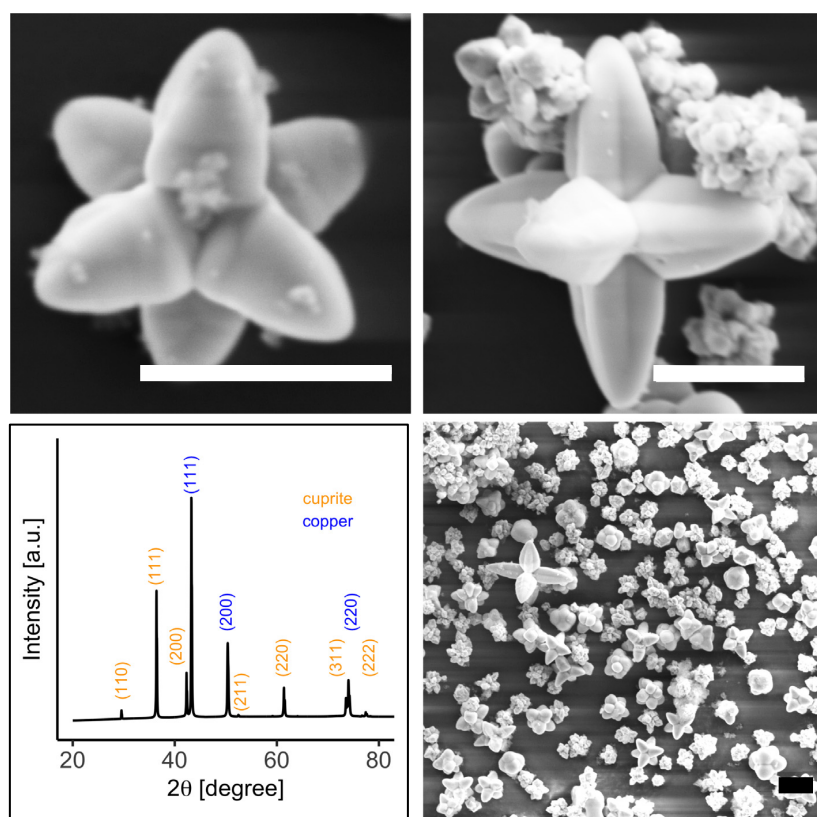
Fig. 3. Mixed Cu and Cu_2O material obtained after 1 h hydrothermal treatment of the Cu^{2+} glycine complex. Scale bar = 10 μm. Rietveld refinement of the obtained XRD pattern returns a composition of 40.4 wt% Cu_2O and 59.6 wt% Cu.

3

Visualization, Supervision, Writing - review & editing. **Daniel Van Opdenbosch:** Resources, Supervision, Writing – review & editing. **Siegfried R. Waldvogel:** Supervision, Writing - review & editing.

Declaration of Competing Interest

The authors declare that they have no known competing financial interests or personal relationships that could have appeared to influence the work reported in this paper.

Acknowledgement

Appendix A. Supplementary data

Supplementary data to this article can be found online at https://doi.org/10.1016/j.matlet.2021.129553.

References

[1] M.B. Gawande, A. Goswami, F.X. Felpin, T. Asefa, X. Huang, R. Silva, X. Zou, R. Zboril, R.S. Varma, Cu and Cu-Based Nanoparticles: Synthesis and Applications in Catalysis, Chem. Rev. 116 (2016) 3722–3811, https://doi.org/10.1021/acs.chemrev.5b00482.

[2] S. Nitopi, E. Bertheussen, S.B. Scott, X. Liu, A.K. Engstfeld, S. Horch, B. Seger, I.E.L. Stephens, K. Chan, C. Hahn, J.K. Nørskov, T.F. Jaramillo, I. Chorkendorff, Progress and Perspectives of Electrochemical CO2 Reduction on Copper in Aqueous Electrolyte, Chem. Rev. 119 (12) (2019) 7610–7672, https://doi.org/10.1021/acs.chemrev.8b0070510.1021/acs.chemrev.8b00705.s001.

[3] J. Singh, G. Kaur, M. Rawat, A Brief Review on Synthesis and Characterization of Copper Oxide Nanoparticles and its Applications, J. Bioelectron. Nanotechnol. 1 (2016), https://doi.org/10.13188/2475-224x.1000003.

[4] D. Barreca, E. Comini, A. Gasparotto, C. Maccato, C. Sada, G. Sberveglieri, E. Tondello, Chemical vapor deposition of copper oxide films and entangled quasi-1D nanoarchitectures as innovative gas sensors, Sensors Actuators B Chem. 141 (1) (2009) 270–275, https://doi.org/10.1016/j.snb.2009.05.038.

[5] S. Li, D. Chu, L. Wang, R. Rong, N. Zhang, One-step hydrothermal synthesis of CuO hollow spheres with high photocatalytic activity, Phys. E Low-Dimensional Syst. Nanostructures. 126 (2021) 114489, https://doi.org/10.1016/j.physe.2020.114489.

[6] F. Zhang, S. Huang, Q. Guo, H. Zhang, H. Li, Y. Wang, J. Fu, X. Wu, L. Xu, M. Wang, One-step hydrothermal synthesis of Cu2O/CuO hollow microspheres/reduced graphene oxide hybrid with enhanced sensitivity for non-enzymatic glucose sensing, Colloids Surfaces A Physicochem. Eng. Asp. 602 (2020), https://doi.org/10.1016/j.colsurfa.2020.125076 125076.

[7] I.E. Uflyand, G.I. Dzhardimalieva, Thermolysis of Low Molecular Weight Metal Chelates, Nanomater. Prep. by Thermolysis Met. Chelates (2018) 71–245, https://doi.org/10.1007/978-3-319-93405-1_3.

[8] J. Ortiz-Landeros, C. Gómez-Yáñez, R. López-Juárez, I. Dávalos-Velasco, H. Pfeiffer, Synthesis of advanced ceramics by hydrothermal crystallization and modified related methods, J. Adv. Ceram. 1 (3) (2012) 204–220, https://doi.org/10.1007/s40145-012-0022-0.

[9] N. Döbelin, R. Kleeberg, Profex: A graphical user interface for the Rietveld refinement program BGMN, J. Appl. Crystallogr. 48 (2015) 1573–1580.

[10] J. Bergmann, P. Friedel, R. Kleeberg, BGMN - a new fundamental parameters based Rietveld program for laboratory X-ray sources, its use in quantitative analysis and structure investigations, CPD Newsl. 20 (1998).

[11] F. Pietrucci, J.C. Aponte, R. Starr, A. Pérez-Villa, J.E. Elsila, J.P. Dworkin, A.M. Saitta, Hydrothermal Decomposition of Amino Acids and Origins of Prebiotic Meteoritic Organic Compounds, ACS Earth Sp. Chem. 2 (6) (2018) 588–598, https://doi.org/10.1021/acsearthspacechem.8b00025.

[12] K.-Y. Kang, B.-S. Chun, Behavior of amino acid production from hydrothermal treatment of fish-derived wastes, Korean J. Chem. Eng. 21 (6) (2004) 1147–1152, https://doi.org/10.1007/BF02719486.

[13] Y.H. Zhang, B.B. Jiu, F.L. Gong, J.L. Chen, H.L. Zhang, Morphology-controllable Cu2O supercrystals: Facile synthesis, facet etching mechanism and comparative photocatalytic H2 production, J. Alloys Compd. 729 (2017) 563–570, https://doi.org/10.1016/j.jallcom.2017.09.237.

[14] J.-Y. Ho, M.H. Huang, Synthesis of submicrometer-sized Cu2O crystals with morphological evolution from cubic to hexapod structures and their comparative photocatalytic activity, J. Phys. Chem. C. 113 (32) (2009) 14159–14164, https://doi.org/10.1021/jp903928p.

[15] Y.H. Won, L.A. Stanciu, Cu2O and Au/Cu2O particles: Surface properties and applications in glucose sensing, Sensors (Switzerland). 12 (2012) 13019–13033, https://doi.org/10.3390/s121013019.

Supporting Information

Novel Cuprous Oxide Morphologies using Amino Acids and Carboxylic Acids as Structure Directing Agents in a Simple Hydrothermal Method

Johannes Seidler, Victor Landgraf, Luciana Vieira*, Daniel Van Opdenbosch and Siegfried R. Waldvogel*

1. UV-Vis spectra
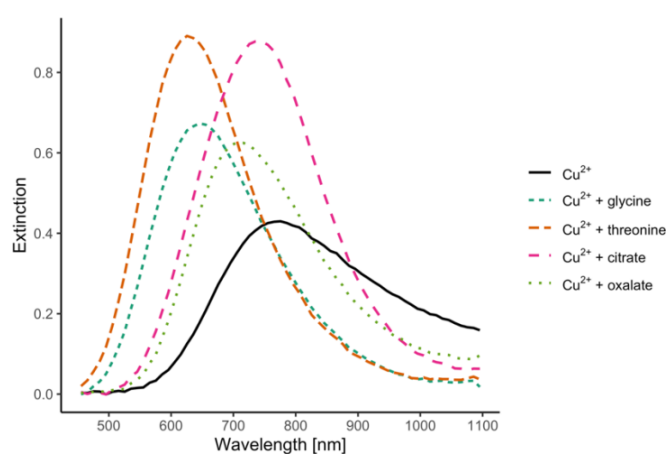
Figure S1. UV-Vis spectra of the prepared complex solutions.

2. Further details of crystallographic analysis

The diffractometer setup in detail: Goniometer radius 150 mm; both Soller slits 2.5°; divergence slit fixed at 0.625°, but closing variably below 10°2θ; anti-scatter slit 8 mm; no monochromator; kβ filter 0.06 mm nickel foil; effective receiving slit of the multiline detector 0.1 mm. The average crystallite sizes $\overline{L}$, the breadth of the microstrain distribution function $\phi^{-1}(0)$ [1], and the thermal factors B were refined isotropically. Texture was refined by an anisotropic weighting factor, using spherical harmonics of order n=6. The peak broadening as a function of scattering vector s is given by:

$$\Delta\beta(s) = \frac{1}{\overline{L}} + \phi^{-1}(0)\, s$$

In BGMN, the total sample function is then calculated as the product of one Lorentzian and one squared Lorentzian, whose half-width at half-maximum scale parameters are $1/\overline{L}$ for the former, and $\Delta\beta(s)$ for the latter; BGMN manual equations (5.15) to (5.18). [2] The machine line function was verified by refining NIST Standards 640e and 660c (silicon and lanthanum hexaboride for peak shapes and positions). Structural data for cuprite (space group 225, ICDD # 04-007-1413) and copper (space group 224, ICDD # 04-009-2090) were used for refinement.

Table S1. Average crystallite sizes ($\overline{L}$) and microstrain distributions (ϕ^{-1}).

Complexing agent	Phase	$\overline{L}$/nm	$\phi^{-1}(0)/10^{-3}$
Citrate (4 h)	Cuprite	180±5	0.15±0.04
Oxalate (4 h)	Cuprite	216±7	0.13±0.03
Glycine (4 h)	Copper	110±3	0.56±0.03
Threonine (4	Copper	154±4	0.46±0.02
Glycine (1 h)	Cuprite	126±2	0±0
Glycine (1 h)	Copper	146±6	0.8±0.03
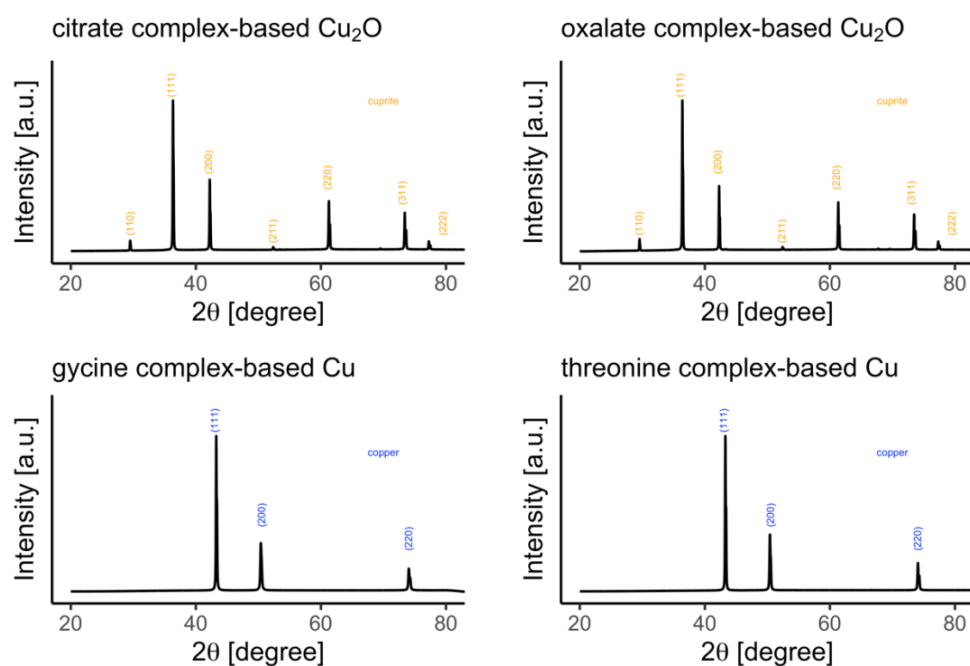
Figure S2. Powder diffraction patterns of obtained copper species.
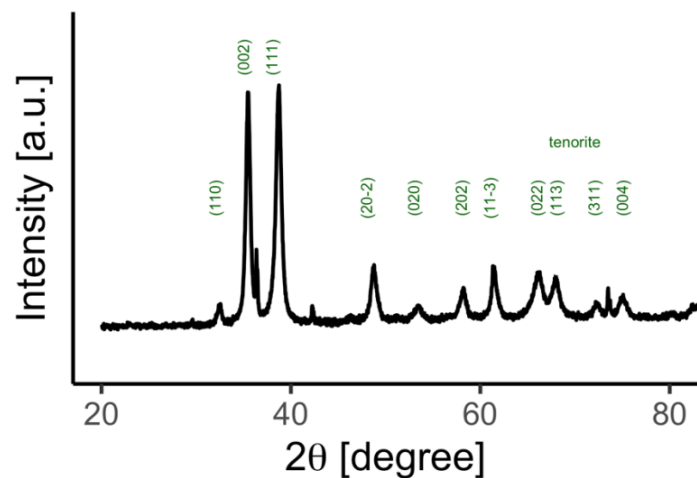
Figure S3. X-ray diffraction pattern for control experiment without complexing agent.

3. EDX analysis
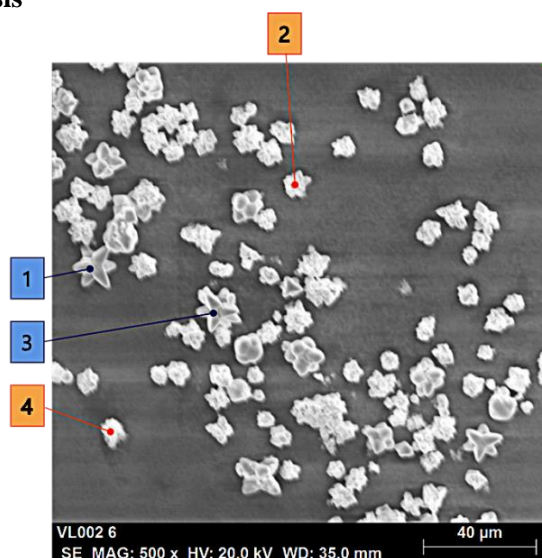
Figure S4. Micrographs of particles analyzed by EDX. The composition is shown in Table S2.

Table S2. Composition of particles obtained after 1 h of hydrothermal treatment using glycine as complexing agent. The oxygen content of the irregular shaped particles is most likely due to surface reoxidation in air, as the samples were exposed to atmospheric O_2 prior to SEM and EDX measurements.

Measured particle	Cu-atom%	O-atom%	Cu normalized	O normalized
1 (hexapod)	62.4	37.6	1.66	1
2 (irregular)	84.9	15.1	5.62	1
3 (hexapod)	66.5	33.5	1.99	1
4 (irregular)	85.1	14.9	5.71	1

4. Verification of crystal evolution of citrate complex-based Cu₂O

a)

b)
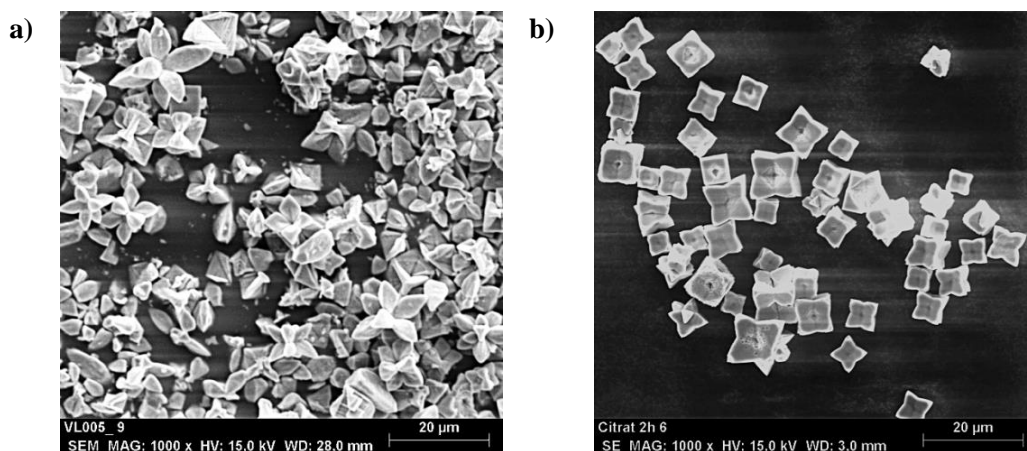
Figure S5. Micrographs of Cu₂O particles obtained after 4 h (a) and after 2 h (b) of hydrothermal treatment of the copper citrate complex. After 2 h most particles are cubic, while the particles possess an octapod morphology after 4 h. After a process time of only 1 h no solids were obtained.

References

[1] A. Stokes, A. Wilson, The diffraction of X-rays by distorted crystal aggregates-

IA, Proc. Phys. Soc. 56 (1944) 174.

[2] J. Bergmann, T. Taut, Manual, Rietveld analysis program BGMN, (2005).

3.1.2 Synthese weiterer Kupfer-basierter Partikel (unveröffentlicht)

Wird eine eine $CuCl_2$-Lösung mit Na_2CO_3 versetzt, bildet sich das türkise $CuCO_3 \cdot Cu(OH)_2$ als Niederschlag (Abbildung 3.3a). Die kristallographische Analyse des Präzipitats zeigt sowohl Reflexe von Azurit (13 %) als auch von Malachit (87 %). Dies ist plausibel, da durch die Fällung das unter atmosphärischen Bedingungen instabilere Azurit gebildet wird, welches im Anschluss zu Malachit weiter reagiert.[73] Die Partikel des Präzipitats sind von unregelmäßiger, teilweise dendritischer Form und im Elektronenmikroskop als Agglomerate sichtbar, wobei die einzelnen Partikel einen Durchmesser von etwa 1–4 μm besitzen. Die thermische Zersetzung des basischen Kupfercarbonats liefert Kupfer(II)-oxid (CuO):[74]

$$CuCO_3 \cdot Cu(OH)_2 \xrightarrow{\Delta} 2\,CuO + H_2O + CO_2\uparrow$$
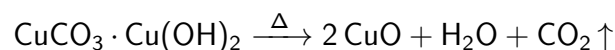
Das erhaltene Kupfer(II)-oxid besitzt, ähnlich wie das Ausgangsmaterial, eine unregelmäßige Partikelform (Abbildung 3.3b). Bei der Dekomposition werden Wasser und Kohlenstoffdioxid freigesetzt, wodurch sich die Partikelgröße verringert (Abbildung 3.5), sich allerdings keine definierte Morphologie erzielen lässt. Das Pulverdiffraktogramm bestätigt die Bildung von CuO, wobei das calcinierte Produkt noch geringe Mengen unzersetztes Startmaterial enthält.
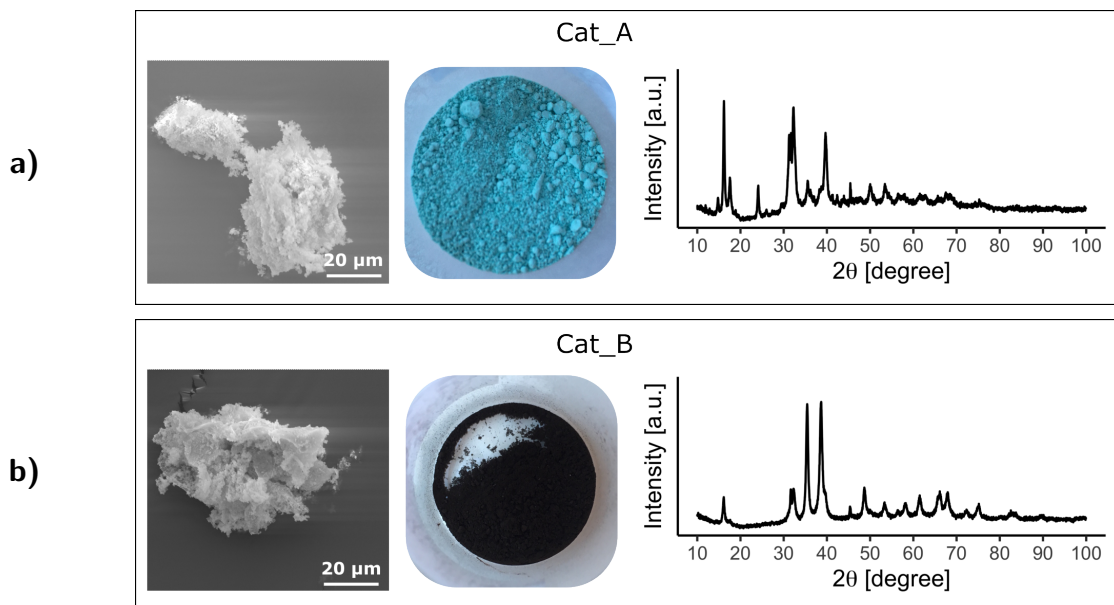
Abbildung 3.3: Generierte Kupferpartikel: a) Durch Präzipitation erhaltenes basisches Kupfer-carbonat. Kristallographische Daten stimmen zu ca. 87 % mit Malachit und 13 % mit Azurit überein. b) Kupfer(II)-oxid aus thermischer Dekomposition von basischem Kupfercarbonat.

Weitere Materialien wurden mittels solvothermaler Synthese hergestellt. Die erzeugten Partikel unterscheiden sich hinsichtlich Größe (Abbildung 3.5), Morphologie (Abbildung 3.4) und Kupferspezies.
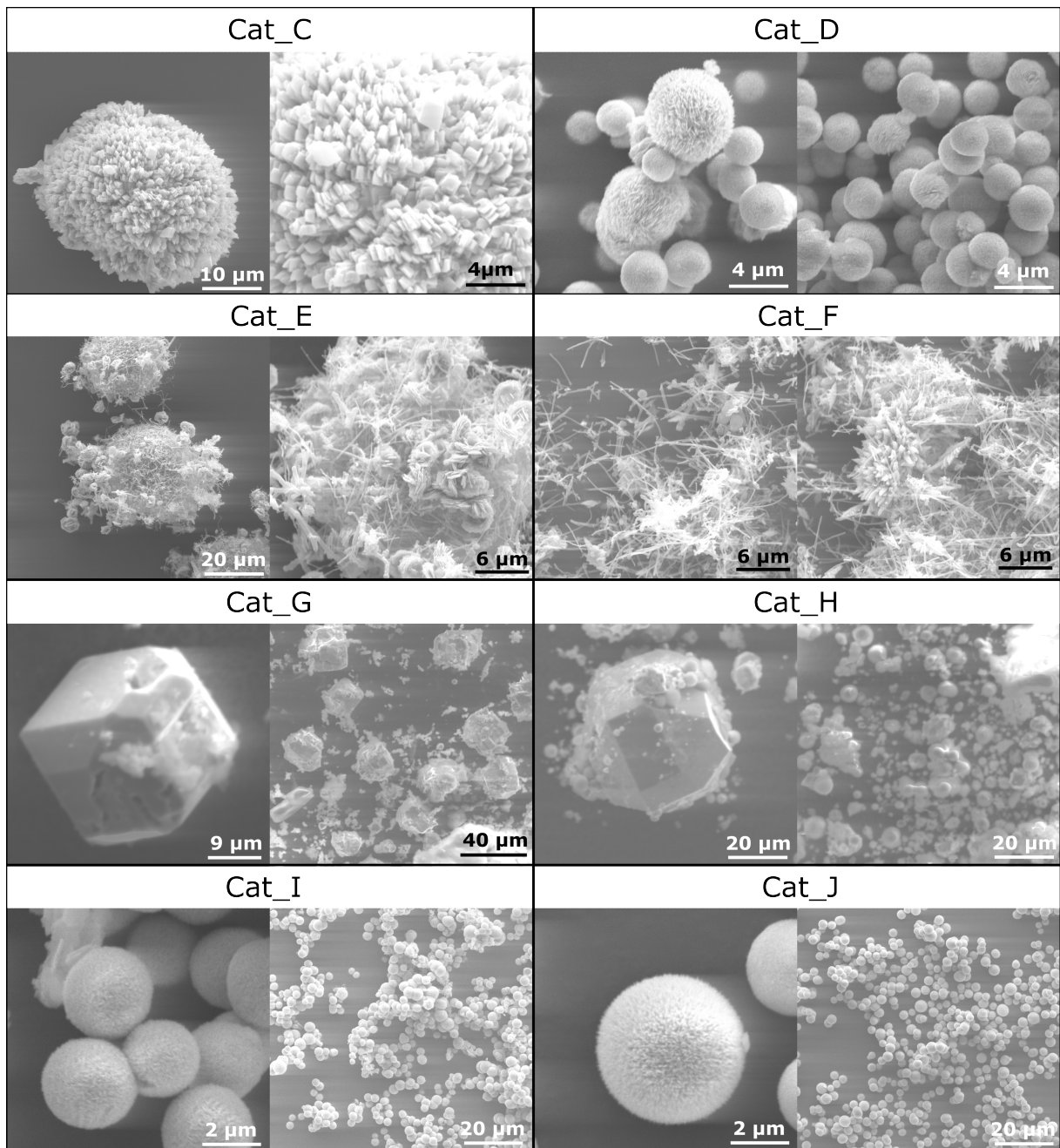
Abbildung 3.4: REM-Aufnahmen von mittels hydrothermaler Synthese hergestellten Materialien.

Die Behandlung von $CuCl_{2(aq)}$ in Anwesenheit von $NaHCO_{3(aq)}$ führte zu vergleichsweise großen CuO Partikeln von ca. 30 µm (Abbildungen 3.4 und 3.5, Cat_C). Die Reaktion wurde auf ähnliche Weise von Zhou et al. durchgeführt (300 °C, 5 h).[75] Dabei wurden kugelförmige Nanopartikel erzeugt. Damit unterscheiden sie sich deutlich von den hier erzeugten Partikeln, welche deutlich größer sind und eine besonders raue Oberfläche besitzen. Das zugefügte $NaHCO_3$ zersetzt sich unter den verwendeten Temperaturen zu H_2O und CO_2, wobei das entstandene CO_2 vermutlich durch die Anwesenheit von Bläschen einen zusätzlichen Einfluss auf die Morphologie nimmt.
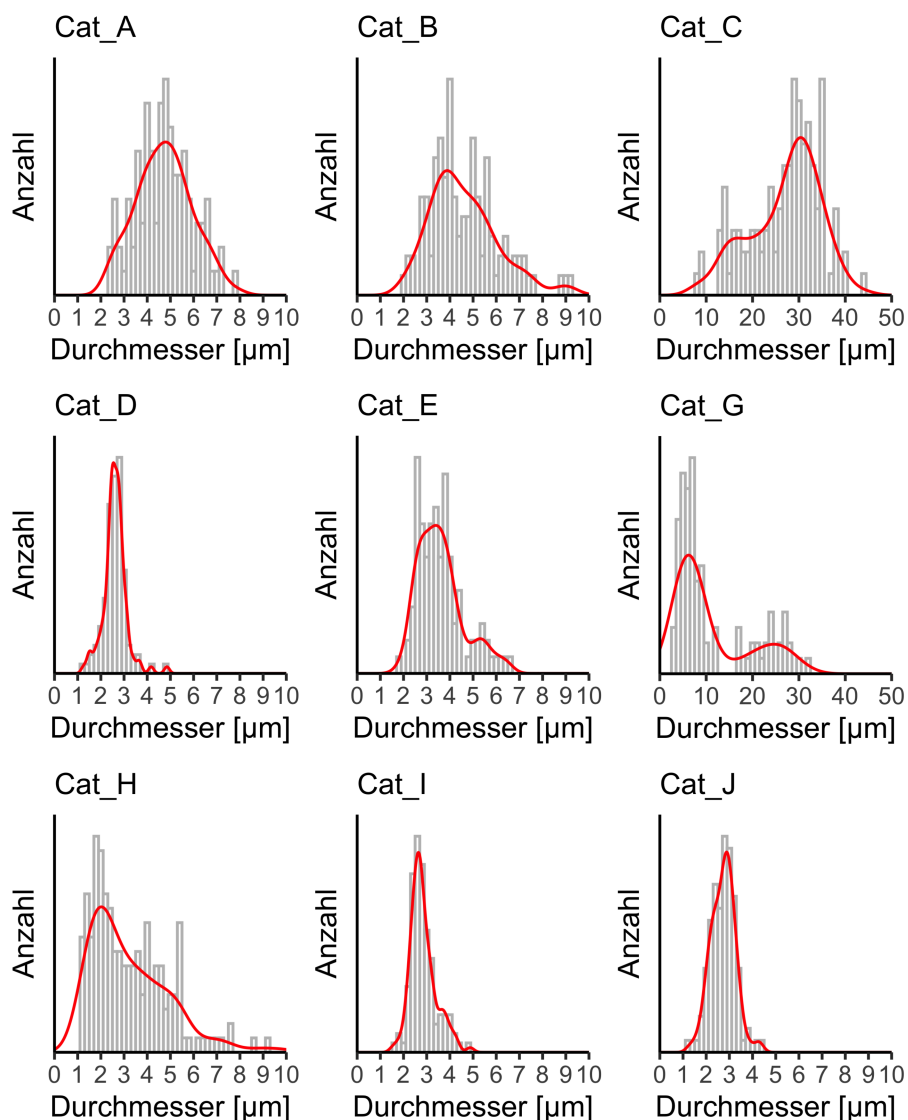
Abbildung 3.5: Partikelgrößenverteilung der hergestellten Katalysatoren. Für Material Cat_F konnte keine Partikelgröße ermittelt werden, da die Kupferpartikel nicht eindeutig von den MWCNTs abgegrenzt werden konnten. Im Fall von Cat_E bezieht sich die Verteilung auf die Größe der Kupferpartikel auf den MWCNT-Clustern. Die mittlere Größe der Cluster beträgt $(23.3 \pm 5.6)\,\mu m$.

Kugelförmige, überwiegend glatte CuO Partikel wurden aus einem Kupferkomplex mit NH_3 generiert (Abbildung 3.4, Cat_D). Material Cat_D zeichnet sich durch eine besonders schmale Partikelgrößenverteilung um ca. 2.5 µm aus (Abbildung 3.5). Zu einer $CuSO_4$-Lösung wurde eine NH_3-Lösung getropft, wodurch sich der dunkelblaue $[Cu(NH_3)_4]^{2+}$-Komplex bildet. Die Erhitzung unter autogenem Druck führte entgegen der Literaturstelle nicht zu einer blütenförmigen Oberfläche sondern zu kugelförmigen Partikeln.[76] Der Zusatz von L-Alanin führte zu keiner Veränderung, weder hinsichtlich der Partikelgröße, -morphologie oder Kupferspezies. Gleiches trifft auf Zitronensäure als Zusatzstoff zu (Abbildungen 3.4 und 3.5, Cat_I und Cat_J). Dies

ist interessant, da der Einfluss von Aminosäuren bzw. Di-, oder Tricarbonsäuren im basischen Milieu auf die gebildeten Partikel bereits demonstriert werden konnte.[77] Das Ausbleiben eines Effekts könnte in diesem Fall auf den Tetraaminkupfer(II)-komplex zurückzuführen sein. Bei Zugabe von L-Alanin oder Zitronensäure wurde keine Farbänderung beobachtet, was darauf hindeutet, dass nach wie vor der $[Cu(NH_3)_4]^{2+}$-Komplex vorliegt. Dies kann mit den verwendeten Konzentrationen erklärt werden, da ein Überschuss an NH_3 verwendet wurde. Der NH_3-Überschuss verschiebt das Gleichgewicht in Richtung des Aminkomplexes und eine Komplexbildung mit den organischen Additiven wird unterbunden. Die bloße Anwesenheit von L-Alanin oder Zitronensäure sorgt für keine Änderung bzgl. der generierten Kupferpartikel. Es kann geschlussfolgert werden, dass in den geschilderten Fällen die Komplexbildung essenziell für die Einflussnahme auf die Partikelmorphologie und Kupferspezies ist. Der maßgebliche Einfluss von Liganden auf die Bildung von Mikro- und Nanopartikeln konnte mehrfach demonstriert werden.[78–81] Dabei wird der Effekt von Liganden zum Beispiel auf die Stabilisierung von Nuklei, die spezifische Bindung an bestimmte Kristallflächen oder pH-Änderungen zurückgeführt. Außerdem kann die Oxidationsstufe des Kupfers mithilfe der Liganden gesteuert werden. Es wurde vorgeschlagen, dass die thermische Zersetzung der Amino- bzw. Carbonsäuren zu reduktiven Spezies wie CO oder NH_3 führen kann, welche ausgehend von Cu^{2+} zu einer reduzierten Form des Kupfers führen (z.B. Cu_2O oder Cu).[68,69,77] Im Fall von Cat_I und Cat_J wurden allerdings keine Cu- oder Cu_2O-Anteile gefunden (Tabelle 3.1), was einerseits auf die geringe Menge von L-Alanin und Zitronensäure, andererseits auf die geringe Temperatur von 130 °C zurückgeführt werden kann. Studien haben Zersetzungstemperaturen von Zitronensäure und verschiedenen Aminosäuren oberhalb von 150 °C gezeigt.[82,83] Um Eigenschaften der Kataly-

Tabelle 3.1: Mittels Rietveld-Verfeinerung bestimmte Zusammensetzung und Kristallitgrößen (CuO) der hergestellten Materialien. Für Materialien Cat_E und Cat_F bezieht sich die Zusammensetzung auf den metallischen Anteil. Der Anteil an Kohlenstoff beträgt bei beiden Materialien ca. 50 wt%.

Katalysator	Zusammensetzung [%]			Kistallitgröße CuO [nm]		
	Cu	Cu_2O	CuO	(100)	(010)	(001)
Cat_B	0	0	100	14	15	18
Cat_C	0	0	100	35	29	23
Cat_D	0	0	100	16	13	11
Cat_E	0	0	100	28	32	15
Cat_F	0	0	100	30	26	23
Cat_G	13	51	36	7	7	7
Cat_H	2	26	72	6	6	6
Cat_I	0	0	100	12	19	11
Cat_J	0	0	100	6	13	8

satoren zu beeinflussen, können Kohlenstoff-Nanoröhrchen (*multi-walled carbon nanotubes – MWCNTs*) mit Kupferspezies dekoriert werden.[84,85] In einem hydrothermalen Ansatz analog zu Cat_D wurden vor der Befüllung des Autoklaven kommerziell erhältliche MWCNTs beigemischt.

Bemerkenswerterweise formen die hinzugefügten MWCNTs große kugelförmige Cluster auf deren Oberfläche die CuO-Partikel angesiedelt sind (Abbildung 3.6). Vermutlich bilden sich aufgrund der Hydrophobie der Kohlenstoffröhrchen kugelförmige Agglomerate in dem wässrigen Medium. Die entstehenden CuO-Partikel nutzen die Kohlenstoffröhrchen als Keim und finden sich daher vorzugsweise auf der Oberfläche der MWCNT-Cluster. Interessanterweise sind die CuO-Partikel nach Beimischung der MWCNTs nicht mehr kugelförmig und weitgehend glatt, sondern besitzen eine deutlich strukturierte Oberfläche und blütenförmige Morphologie.

Die Zugabe von MWCNTs wurde ebenfalls auf die Prozedur zur Herstellung von Cat_C
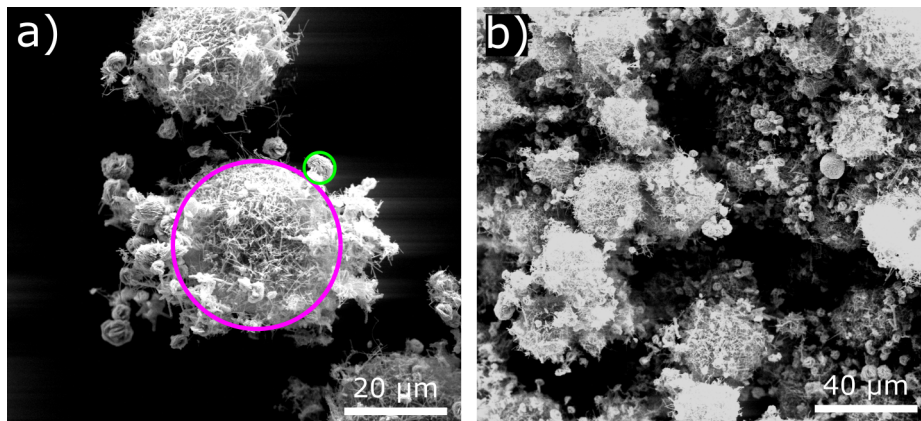
Abbildung 3.6: REM-Aufnahmen von Katalysatormaterial Cat_E. Die enthaltenen MWCNTs formen kugelförmige Cluster (rosa) von ca. 30 μm Durchmesser. Die CuO-Partikel (grün) lagern sich überwiegend auf der Oberfläche der MWCNT-Clustern an.

angewendet. Das resultierende Material Cat_F beinhaltet allerdings keine Cluster aus MWCNTs. Stattdessen sind die Kohlenstoffröhrchen sowie die Kupferpartikel zufällig verteilt (Abbildung 3.4, Cat_F). Eine mögliche Erklärung könnte das anwesende $NaHCO_3$ sein, welches bei den angewandten Temperaturen CO_2 freisetzt. Die Gasentwicklung zerstört die Agglomerate und das erhaltene Material besteht aus überwiegend gleichmäßig verteilten Kohlenstoff- und Kupferspezies.

Ein weiterer Ansatz auf die Partikeleigenschaften Einfluss zu nehmen, ist die Verwendung von stark eutektischen Lösungsmitteln (*deep eutectic solvents – DES*).[86–89] Dabei agieren die DES nicht nur als Lösungsmittel, sondern zusätzlich als strukturgebende Spezies. Beispielsweise verwendeten Hammond et al. ein System aus Cholinchlorid und Urea um nanostrukturiertes Cer(IV)-oxid herzustellen.[86] Um die Eignung von DES für die Herstellung von Kupferpartikeln zu testen, wurden zwei Lösungsmittelsysteme getestet: Cholinchlorid:Urea (CC:U 1:2) und Cholinchlorid:Ethylenglykol (CC:EG 1:2). Verwendet wurden Kupfer(II)-chlorid oder Kupfer(II)-acetat als Startmaterial. In keinem der Versuche wurden nach 12 h bei 180 °C Kupferspezies als Feststoff erhalten. Erst nach Mischung der DES mit wässriger NaOH (wodurch $Cu(OH)_2$ gebildet wird) wurden Kupferpartikel gebildet (Cat_G mit CC:EG und Cat_H lediglich mit Ethylenglykol). Kristallographische Untersuchungen haben gezeigt, dass es sich jeweils um Mischungen aus Cu,

Cu$_2$O und CuO handelt (Tabelle 3.1). Der größere Anteil von Cu und Cu$_2$O in Cat_G ist auf die Anwesenheit von Cholinchlorid zurückzuführen, welches unter den verwendeten Bedingungen unter anderem zu NH$_3$ zersetzt wird,[90] das wiederum als Reduktionsmittel wirken kann. Die gebildeten Cu$_2$O Partikel sind würfelförmig und deutlich größer als die unregelmäßig geformten Partikel der anderen Kupferspezies. Die Zuordnung der Kupferspezies basiert auf vorherigen EDX Messungen.[77] Die Anwesenheit von Kupferspezies mit deutlich verschiedener Größe zeigt sich besonders in der Partikelgrößenverteilung von Cat_G (Abbildung 3.5). Es gibt eine große Anzahl kleiner Partikel im Bereich 5–7 µm und ebenfalls eine große Anzahl deutlich größerer Partikel im Bereich 22–26 µm.

Die hergestellten Partikel wurden als Katalysatormaterialien für die elektrochemische Reduktion von CO$_2$ verwendet. Die Ergebnisse dieser Experimente werden im folgenden Kapitel diskutiert.

3.1.3 CO$_2$-Reduktion an Cu-basierten Elektrokatalysatoren (unveröffentlicht)

Die in den vorangegangenen Kapiteln beschriebenen Partikel wurden auf einer zugeschnittenen Gasdiffusionslage mithilfe einer Nafion-Lösung als Binder immobilisiert. Die somit hergestellte Gasdiffusionselektrode wurde als Kathode in einer eigens entworfenen Gasdiffusionszelle verwendet. Kathoden- und Anodenkompartment wurden durch eine Nafion-Membran separiert. Als Elektrolyt wurde eine wässrige KOH-Lösung (1 M) verwendet.

Zunächst wurden die Katalysatoren getestet, welche durch hydrothermale Behandlung verschiedener Kupferkomplexe hergestellt wurden.[77] Vier Additive bzw. Liganden (Glycin, Threonin, Oxalat und Citrat) wurden für die Herstellung der Partikel eingesetzt. Ein fünfter Versuch ohne zusätzliches Additiv wurde als Kontrolle durchgeführt. In der elektrochemischen CO$_2$-Reduktion eingesetzt, unterscheiden sich die fünf Materialien besonders in der Faraday-Effizienz bezüglich Kohlenstoffmonoxid (Abbildung 3.7). Besonders viel CO wurde mithilfe der Materialien aus elementarem Kupfer (Cu_glycine und Cu_threonine) erzeugt. Die höchste Faraday-Effizienz für Formiat, Ethanol und Propanol wurde mit dem CuO Material erzeugt, welches ohne Additiv hergestellt wurde (CuO_control). Betrachtet man den Anteil von Produkten mit mehreren C-Atomen an der gesamten Menge der gebildeten Kohlenstoffprodukte, so stellt man fest, dass die Knüpfung von C-C Bindungen besonders von CuO_control gefördert wurde (Tabelle 3.2, Einträge 1–5). Der Anteil wurde auf Basis der Faraday-Effizienz berechnet:

$$\eta_{C2+} = \frac{\sum_{i=1}^{n} FE_{C2+,i}}{\sum_{i=1}^{k} FE_{C,i}}$$

Dabei ist η_{C2+} die Fraktion von n Produkten mit mehreren Kohlenstoffatomen (C$_{2+}$) bezogen auf die Gesamtheit von allen k C-Produkten. Auffällig ist weiterhin, dass η_{C2+} für die Katalysatoren 1–5 in Tabelle 3.2 abnimmt, wenn die Oxidationsstufe des Kupfers im Katalysator gering
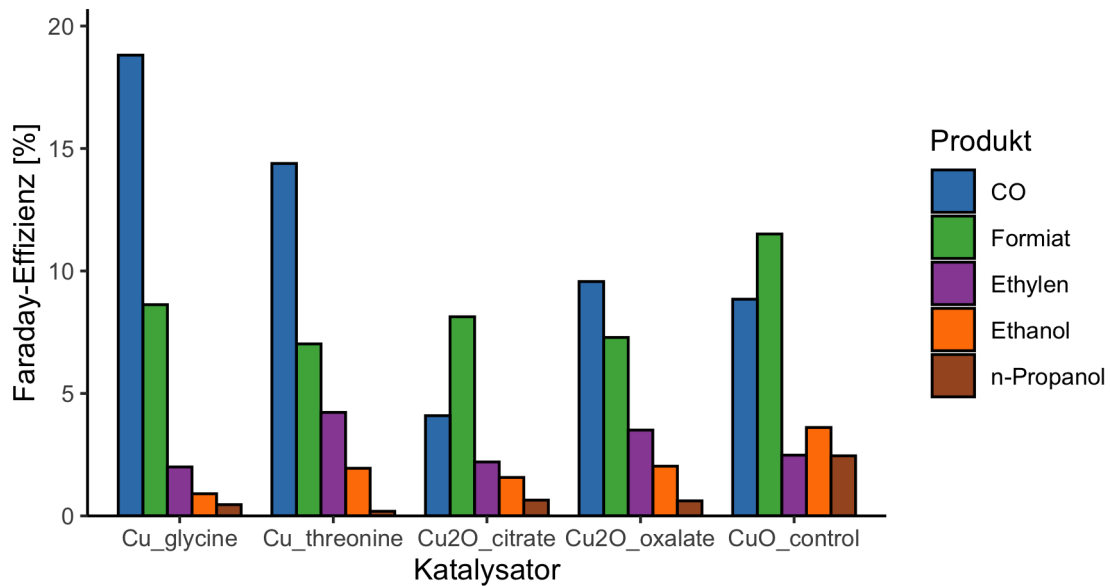
Abbildung 3.7: Faraday-Effizienz bei Verwendung der Komplex-basierten Katalysatoren aus eigener Publikation.[77] Bedingungen: 1 M KOH, 100 mA cm^{-2}. Die Differenz zu 100 % ergibt sich aus der Wasserstoffentwicklung.

ist. Dies ist auch deswegen bemerkenswert, da für alle Elektroden die selbe Katalysatormasse aufgetragen wurde (5 mg cm^{-2}). Geht man davon aus, dass der Kupferanteil auch in den Oxiden (welche aufgrund des kathodischen Stroms mindestens teilweise reduziert werden) der aktive Part ist, macht es Sinn, den Massenanteil des Kupfers an der aufgetragenen Masse zu betrachten:

$$x_{Cu} = \sum_{i=1}^{n} x_i k_{Cu,i} \frac{M_{Cu}}{M_i}$$

Hierbei ist x_{Cu} der Massenanteil von Kupfer innerhalb aller Kupferspezies im Katalysator, x_i ist der mittels Rietveld-Verfeinerung bestimmte Massenanteil der Kupferspezies i im hergestellten Material, $k_{Cu,i}$ ist die Anzahl der Kupferatome in der Kupferspezies i und M_{Cu} sowie M_i sind die molaren Massen von Kupfer bzw. der Kupferspezies i. In der Reihe Cu, Cu$_2$O, CuO nimmt die Menge an Kupfer auf der Elektrode mit steigender Oxidationszahl der Kupferspezies ab. Die geringere Kupfermenge auf der Elektrode scheint aufgrund einer höheren Aktivität der Cu$_2$O- bzw. CuO-Materialien nicht ausschlaggebend zu sein.

Die Materialien Cat_A bis Cat_J wurden ebenfalls als Katalysatoren in der CO$_2$RR verwendet. Die Produktbildung unterscheidet sich je nach verwendetem Katalysator mitunter beträchtlich (Abbildung 3.8). Über eine Korrelation der Kupferspezies mit dem Anteil von C$_{2+}$-Produkten (η_{C2+}) kann für Materialien Cat_A bis Cat_J keine eindeutige Aussage getroffen werden, da die meisten Materialien Kupfer in der Oxidationsstufe II beinhalten. Die einzigen Materialien, welche Kupfer in den Oxidationsstufen 0 und I enthalten, sind Cat_G und Cat_H. Der Anteil von CuO an den Katalysatormaterialien Cat_G und Cat_H beträgt 36 bzw. 72 %. Auffällig ist dabei, dass das Material mit dem höchsten Anteil von Kupfer in den Oxidationsstufen 0 und I

Tabelle 3.2: Anteil von Produkten mit mehreren Kohlenstoffatomen (C_{2+}) bezogen auf alle ge-bildeten CO_2 Reduktionsprodukte (η_{C2+}) und Wasserstoffentwicklung im CO_2RR Experiment bei $100\,mA\,cm^{-2}$ für Einträge 1–5 und 7[a] und bei $75\,mA\,cm^{-2}$ für Einträge 6–16. x_{Cu} bezeichnet den Anteil von Cu innerhalb aller beinhalteten Kupferspezies ([b] Massenanteil von Cu bei Einbeziehung der Masse an MWCNTs). FE_{C2+} ist die Summe der FE von Produkten mit mehreren Kohlenstoffatomen. CuO_com bezeichnet kommerzielle CuO-Nanopartikel.

	Katalysator	Kupferspezies	x_{Cu} [wt%]	FE_{C2+} [%]	η_{C2+} [%]	$FE(H_2)$ [%]
1	Cu_glycine	Cu	100	3	11	69
2	Cu_threonine	Cu	100	6	23	72
3	Cu2O_citrate	Cu_2O	89	4	27	83
4	Cu2O_oxalate	Cu_2O	89	6	27	77
5	CuO_control	CuO	80	9	30	71
6	Cat_A	$X\,CuCO_3 \cdot Cu(OH)_2$	57	19	36	47
7	Cat_B	CuO	80	21 (31[a])	47 (62[a])	54 (50[a])
8	Cat_C	CuO	80	12	25	51
9	Cat_D	CuO	80	3	11	73
10	Cat_E	CuO	80 (40[b])	3	8	65
11	Cat_F	CuO	80 (40[b])	8	21	61
12	Cat_G	Cu_xO_y	87	1	3	77
13	Cat_H	Cu_xO_y	83	11	47	76
14	Cat_I	CuO	80	15	35	57
15	Cat_J	CuO	80	9	33	73
16	CuO_com	CuO	80	7	18	63

(Cat_G) die geringste Menge von C_{2+}-Produkten hervorbringt. Dabei wurde für Cat_G kein Ethylen und n-Propanol gefunden. Eine höhere Aktivität von Oxid-basierten Katalysatoren wird in der Literatur auf die Bildung einer poröseren Nanostruktur während der Reduktion der Kupferspezies zurückgeführt.[14,91,92] Wird der Massenanteil von Kupfer gegen die erreichte C_{2+}-Effizienz aufgetragen, kann mit steigendem Cu-Gehalt eine Tendenz zu geringerer Aktivität bzgl. der C-C-Bindungsknüpfung erahnt werden (Abbildung 3.9). Des Weiteren wird durch Abbildung 3.9 veranschaulicht, dass die Werte für FE_{C2+} nicht allein von der Oxidationsstufe des Kupfers abhängen können, da große Schwankungen für die getesteten CuO-Materialien existieren. Bemerkenswert ist auch die hohe Aktivität das basischen Kupfercarbonats (Cat_A), da die aufgetragene Katalysatormenge nur zu einem deutlich geringeren Teil aus Kupfer besteht, verglichen mit den anderen Katalysatormaterialien. Für Katalysatoren Cat_A und Cat_B wurde eine vergleichsweise hohe Effizienz für Ethylen (12–14 %) erreicht. Generell wurde bei den beiden Materialien eine hohe Selektivität für die CO_2-Reduktion beobachtet. Dies wird bei Betrachtung der generierten Wasserstoffmenge, welche für Cat_A und Cat_B im Vergleich besonders gering sind, sichtbar (Tabelle 3.2). Möglicherweise ist bei der elektrochemischen Reduktion des basischen Kupfercarbonats die bei Oxid-basierten Katalysatoren beobachtete Bildung von Nanostrukturen besonders ausgeprägt. Bei der thermischen Umwandlung von
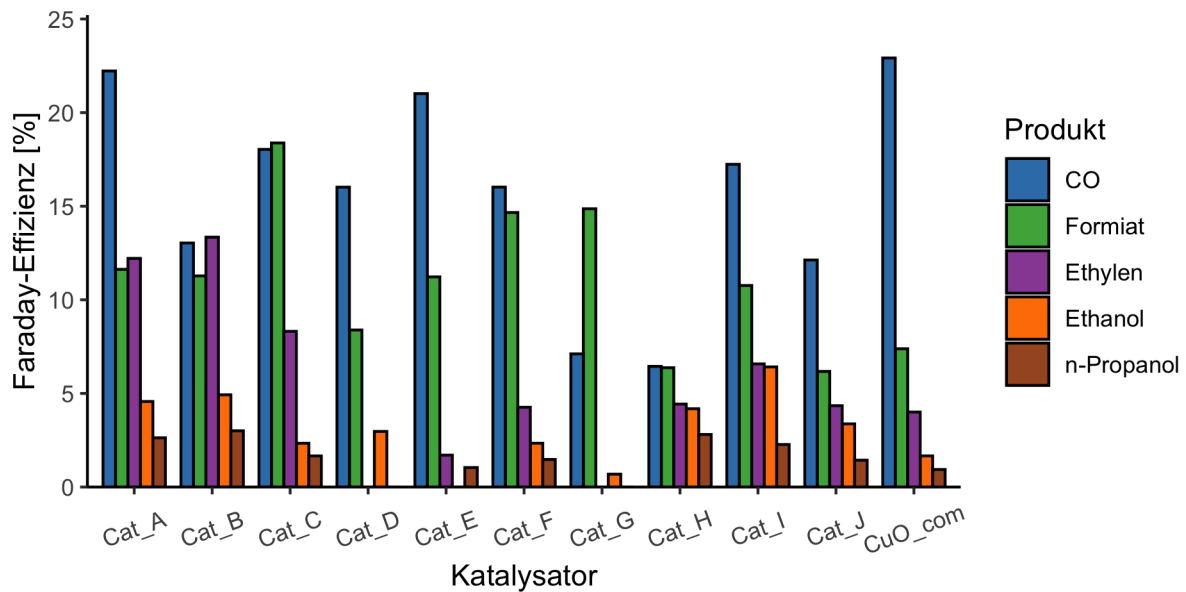
Abbildung 3.8: Faraday-Effizienz bei Verwendung der verschiedenen Katalysatoren im CO_2RR-Experiment. Bedingungen: 1 M KOH, 75 mA cm^{-2}. Die Differenz zu 100 % ergibt sich aus der Wasserstoffentwicklung. CuO_com bezeichnet kommerzielle CuO-Nanopartikel.

Cat_A in Cat_B könnten ebenfalls porösere Strukturen geschaffen werden.

Die drei Materialien Cat_D, Cat_I und Cat_J wurden jeweils auf ähnliche Weise hergestellt. Bei Cat_I und Cat_J wurden ʟ-Alanin bzw. Zitronensäure als Additive in geringen Mengen zugefügt, wobei bei der Charakterisierung der erhaltenen CuO-Partikel keine Unterschiede festgestellt werden konnten. Ein ähnliches Ergebnis in der Produktverteilung während der CO_2-Reduktion zwischen den Materialien Cat_I und Cat_J scheint daher plausibel. Überraschend ist hingegen das Ausbleiben von Ethylen und n-Propanol bei Verwendung des Materials, welches ohne Additive hergestellt wurde (Cat_D). Außerdem wird mithilfe von Cat_I deutlich weniger Wasserstoff generiert, was sich auch in einer höheren Summe der C_{2+}-Produkte manifestiert. Der Anteil an C_{2+}-Produkten an allen C-Produkten (η_{C2+}) ist bei den beiden Materialien Cat_I und Cat_J wiederum gleich. Da alle drei Materialien (Cat_D, Cat_I und Cat_J) ähnliche Eigenschaften (Morphologie, Partikelgröße, Kristallitgröße) aufweisen, können die Unterschiede in der CO_2-Reduktion auf keine Ursache zurückgeführt werden. Generell hat die Partikelgröße der getesteten Katalysatoren keinen eindeutigen Effekt im CO_2RR-Experiment gezeigt. Allgemein wird angenommen, dass eine geringe Größe der Katalysatorpartikel durch die große spezifische Oberfläche der Katalysatoraktivität zuträglich ist. In Versuchen mit Nanopartikeln unterschiedlicher Größe wurde gezeigt, dass bei gleichem Potential eine deutlich größere katalytische Stromdichte entsteht, wenn die Katalysatorpartikel sehr klein sind.[93] Allerdings wurde dabei mit 2–15 nm großen Partikeln hauptsächlich Wasserstoff generiert. Im Vergleichsexperiment mit einer Kupferfolie stieg die Faraday-Effizienz für Ethylen von ≤5 % auf ca. 20 %. Für besonders kleine Nanopartikel wurden hauptsächlich H_2 und CO
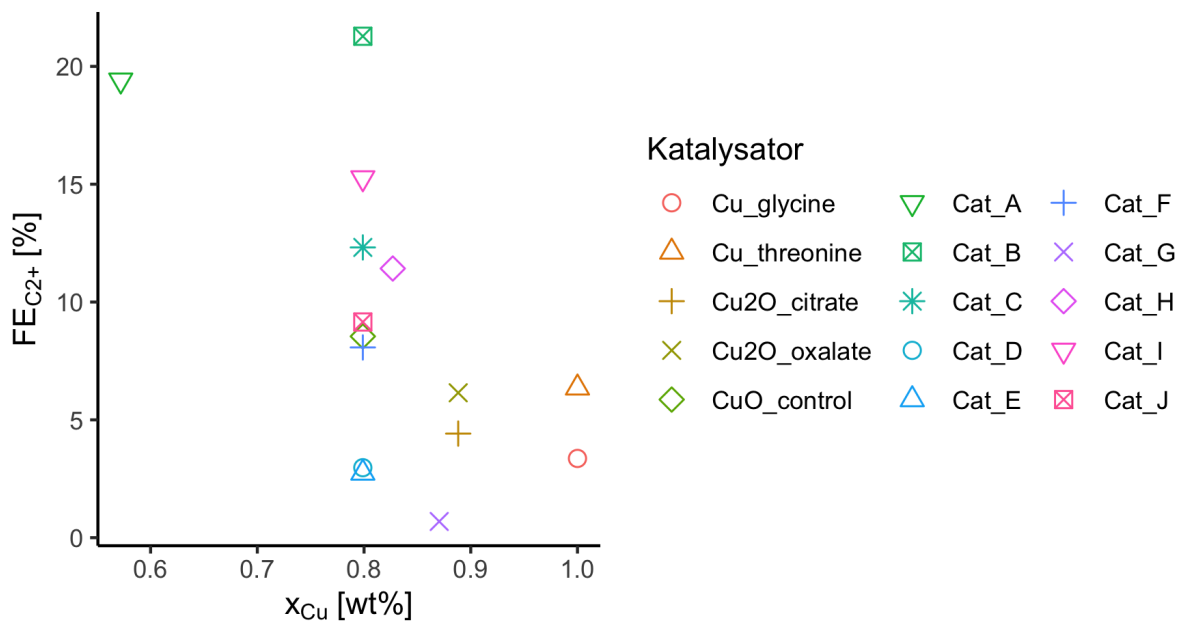
Abbildung 3.9: Faraday-Effizienz für Produkte mit mehreren Kohlenstoffatomen in Abhängigkeit von der Kupfermenge im Katalysator. Bei Materialien Cat_E und Cat_F wurde der Massenanteil relativ zur Kupferspezies gewählt (ohne Einbeziehung der MWCNTs).

detektiert. Als Erklärung wurde eine starke Bindung und verringerte Mobilität von Intermediaten herangeführt, wodurch die Chance der Bildung komplexerer Moleküle sinkt.[93] Bei den hier getesteten Materialien wurde für große Partikel (Cat_C, 30 μm) eine stärkere C_{2+}-Produktbildung beobachtet als für Nanopartikel (CuO_com, ≤100 nm). Auch andere vergleichsweise große CuO-Partikel wie Cat_B haben mitunter eine höhere Effizienz bzgl. der CO_2-Reduktion gezeigt.

Der Effekt von Kohlenstoff-Nanoröhrchen wurde in zwei Katalysatormaterialien getestet: Cat_E und Cat_F. Dabei wurden bei den Materialsynthesen analog zu Cat_D bzw. Cat_C MWCNTs beigemischt. Im Fall von Cat_E haben sich kugelförmige MWCNT-Cluster, dekoriert mit CuO-Partikeln gebildet, während im Material Cat_F eine weitgehend homogen verteilte Mischung aus CuO und Kohlenstoffröhrchen vorliegt. In der Synthese der Partikel Cat_C und Cat_F hat die Beimischung der MWCNTs keinen nennenswerten Effekt auf die Produktverteilung erzielt (Abbildung 3.10). Zu bedenken ist allerdings, dass für alle Materialien die gleiche Katalysatormasse auf der Elektrode immobilisiert wurde. Die Elektroden mit Cat_E und Cat_F besitzen also nur die Hälfte des Kupferoxids, verglichen mit den Materialien Cat_C und Cat_D. Die Partikel aus der anderen Synthesemethode (Cat_D und Cat_E) bringen ähnliche Mengen Formiat und Kohlenstoffmonoxid hervor. In den Mengen gebildeter C_{2+}-Produkte existieren zwar Unterschiede, allerdings ist die Faraday-Effizienz für C_{2+}-Produkte bei beiden Katalysatoren sehr gering (ca. 3 %). Ein signifikanter Einfluss von Kohlenstoff-Nanoröhrchen auf die Produktverteilung in der CO_2RR konnte demnach nicht festgestellt werden.

Wie bereits geschildert, wird Oxid-basierten Kupferkatalysatoren mitunter eine höhere Aktivität
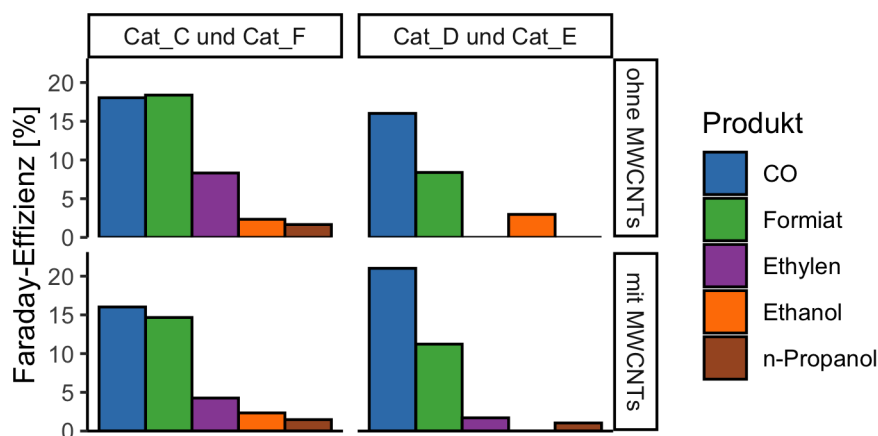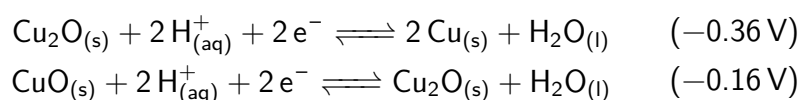
Abbildung 3.10: Produktverteilung bei Verwendung von Katalysatoren mit und ohne Kohlenstoff-Nanoröhrchen (MWCNTs). Bedingungen: 1 M KOH, 75 mA cm^{-2}. Die Differenz zu 100 % ergibt sich aus der Wasserstoffentwicklung. Ein Kontrollversuch mit MWCNTs ohne Kupferspezies ergab keine CO$_2$-Reduktionsprodukte.

bzgl. der C-C-Bindungsbildung attestiert.[91,92] Da die Kupfermaterialien als Kathode verwendet werden, muss die Reduktion von Cu^{2+} und Cu^{1+} in die Überlegung bzgl. der während der Elektrolyse vorliegenden Kupferspezies mit einbezogen werden. Die elektrochemische CO$_2$-Reduktion wurde bei 75 bzw. 100 mA cm^{-2} durchgeführt. Das gemessene Elektrodenpotential bewegte sich dabei im Bereich -2.2 bis -1.7 V *vs.* Ag/AgCl, was etwa -1.2 bis -0.7 V *vs.* RHE entspricht. Die Standardpotentiale für die Reduktion von Kupferoxiden bei pH = 14 liegen deutlich positiver:[94]

$$\text{Cu}_2\text{O}_{(s)} + 2\,\text{H}^+_{(aq)} + 2\,\text{e}^- \rightleftharpoons 2\,\text{Cu}_{(s)} + \text{H}_2\text{O}_{(l)} \qquad (-0.36\,\text{V})$$

$$\text{CuO}_{(s)} + 2\,\text{H}^+_{(aq)} + 2\,\text{e}^- \rightleftharpoons \text{Cu}_2\text{O}_{(s)} + \text{H}_2\text{O}_{(l)} \qquad (-0.16\,\text{V})$$

Daher kann davon ausgegangen werden, dass die vorliegenden Kupferspezies zumindest an deren Oberfläche vollständig zu elementarem Kupfer reduziert werden. Um die vorherrschende Kupferspezies während der Elektrolyse zu bestimmen, wurden verschiedene Materialien als Kathode verwendet und anschließend mittels Pulverdiffraktometrie analysiert. Über Rietveld-Verfeinerung wurden die Massenanteile der einzelnen Kupferspezies bestimmt (Abbildung 3.11). Um die Oxidation des Elektrodenmaterials an der Luft beim Entfernen der Elektrode aus der Zelle so gering wie möglich zu halten, wurde die Elektrode sofort unter Argon getrocknet und ohne Verzögerung im Diffraktometer analysiert. Innerhalb des Diffraktometers lag allerdings kein Schutzgas vor, sodass eine Oxidation nicht vollständig ausgeschlossen werden konnte. Die Stabilität von Kupferoxiden in Elektroden wurde von Lum und Ager mithilfe von ^{18}O-Labeling untersucht.[92] Dabei fanden sie heraus, dass nach der Elektrolyse (ca. 5 h) lediglich weniger als 1 % des ursprünglichen ^{18}O im Katalysatormaterial vorhanden ist. Sie schlussfolgerten, dass die darüber hinausgehende Menge an Oxiden aus der Reoxidation des Materials stammen muss. Weiterhin unterstreichen sie die besonders schnelle Reoxidation des reduzierten Materials und
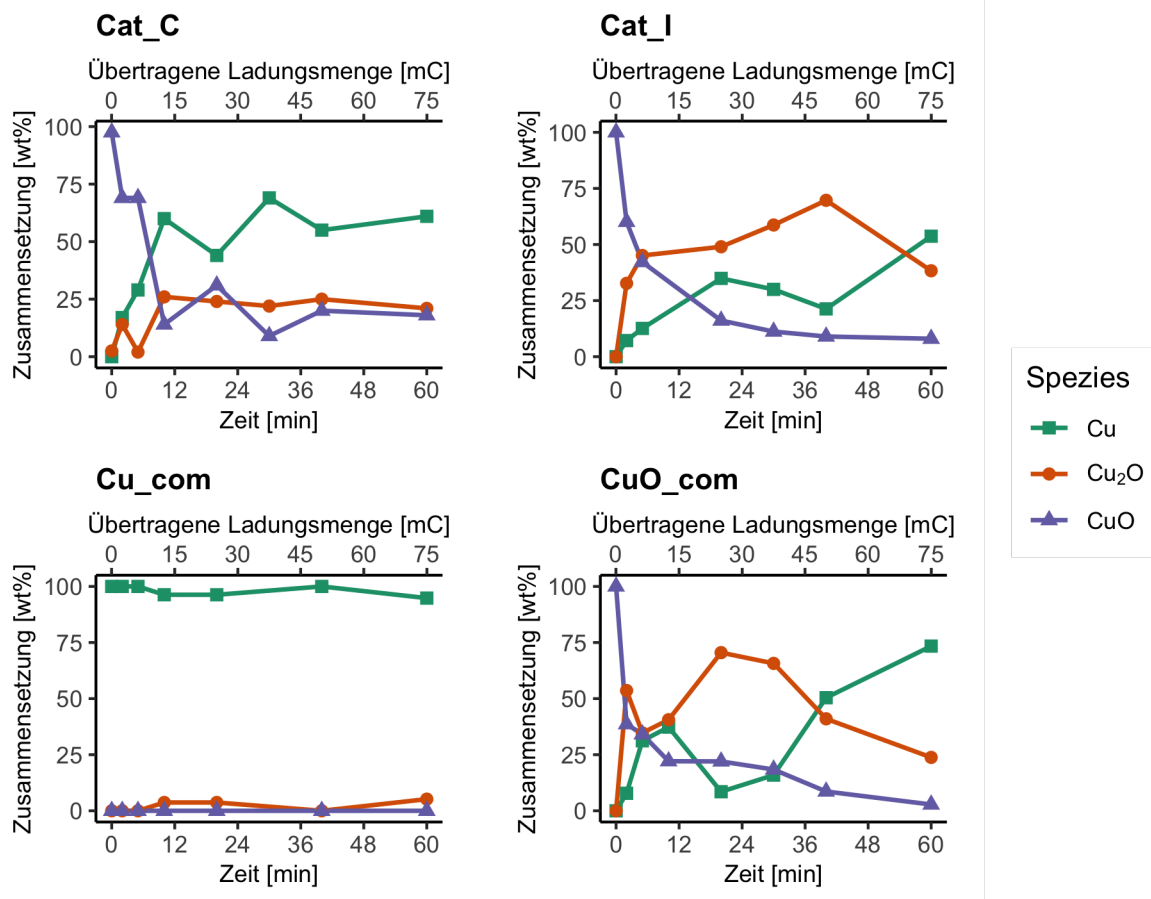
Abbildung 3.11: Veränderung der Katalysatorzusammensetzung während der Elektrolyse bei 75 mA cm^{-2}. Elektrolyt: 1 M KOH. Cu_com und CuO_com sind kommerzielle Nanopartikel.

führen dies auf eine besonders hohe Dichte an Korngrenzen zurück, welche als Keim für die Bildung von Oxiden fungieren. Die Studien von Lum und Ager wurden an Kupfer-Nanofilmen durchgeführt. Die hier untersuchten Partikel sind deutlich größer (mehrere Mikrometer) und daher ist eine langsamere Reoxidierung anzunehmen. Als Kontrollversuch wurden kommerzielle Cu-Nanopartikel (Cu_com, $\leq$100 nm) verwendet (Abbildung 3.11). Der bestimmte Cu-Anteil schwankt dabei leicht zwischen 95 und 100 %, was auf eine relativ geringe Oxidation nach der Elektrolyse schließen lässt. Als oxidierte Spezies wurde lediglich Cu$_2$O gefunden, während keine der untersuchten Proben von Cu_com Kupfer(II)-oxid (CuO) enthält. Die spontane Oxidation an Luft nach Entfernen der Elektrode aus der Zelle scheint sich demnach auf die Bildung von Kupfer(I)-oxid zu beschränken. Im Vergleich der drei übrigen Materialien sinkt der CuO-Anteil für die kleinsten Partikel (CuO_com) auf den niedrigsten Wert (knapp 3 %). Bei den größeren Partikeln Cat_I und Cat_C wurde nach 1 h ein größerer Anteil des ursprünglichen Kupfer(II)-oxids, verglichen mit den Nanopartikeln, bestimmt. Mit der verwendeten Röntgendiffraktometrie werden nicht nur die Spezies an der Oberfläche sondern auch im Partikelinneren analysiert. Da der detektierte Anteil von CuO mit steigender Partikelgröße zunimmt, ist es wahrscheinlich, dass der Anteil von CuO bei größeren Partikeln (wie Cat_C) nicht von der Oberflächenzusammensetzung

Tabelle 3.3: Mittels Rietveld-Verfeinerung bestimmte Korngrößen in Abhängigkeit von der Zeit bei $75\,\mathrm{mA\,cm^{-2}}$ in $1\,\mathrm{M}$ KOH.

		Korngröße [nm]								
		Cu			Cu_2O			CuO		
Zeit [min]	Katalysator	100	010	001	100	010	001	100	010	001
0	Cat_C	–	–	–	27	27	27	16	59	23
2	Cat_C	11	11	11	9	9	9	14	44	26
5	Cat_C	14	14	14	7	7	7	20	20	20
10	Cat_C	12	12	12	4	4	4	31	31	31
20	Cat_C	12	12	12	4	4	4	7	7	7
30	Cat_C	13	13	13	9	9	9	28	28	28
40	Cat_C	13	13	13	7	7	7	28	28	28
60	Cat_C	13	13	13	8	8	8	24	24	24
0	Cat_I	3	3	3	–	–	–	9	13	27
2	Cat_I	7	7	7	19	19	19	7	5	51
5	Cat_I	13	13	13	12	12	12	13	13	13
10	Cat_I	10	10	10	6	6	6	16	16	16
20	Cat_I	13	13	13	10	10	10	13	13	13
30	Cat_I	14	14	14	12	12	12	11	11	11
40	Cat_I	14	14	14	17	17	17	12	12	12
60	Cat_I	10	10	10	4	4	4	18	18	18

herrührt sondern aus dem Inneren der Partikel. Ob die verbliebenen Oxide noch einen Einfluss auf die CO_2-Reduktion besitzen, ist zweifelhaft, da Adsorption und Ladungsübertrag an der Oberfläche der Katalysatoren stattfinden. Letztlich kann der Annahme von Lum und Ager nicht widersprochen werden, da eine vollständige Reduktion an der Oberfläche zu Cu^0 sehr wahrscheinlich erscheint. Dabei ist es unerheblich ob das Startmaterial ein Kupferoxid oder elementares Kupfer ist. Eine höhere Selektivität bzgl. C_{2+}-Produkten von Oxid-basierten Katalysatoren wird in der Literatur auf eine hohe Dichte von Korngrenzen zurückgeführt.[60,91,95] Dabei werden veränderte Adsorptionseigenschaften von CO und weiteren Intermediaten angeführt. Aus den Röntgendiffraktogrammen der Elektroden nach der Elektrolyse wurden die Kristallitgrößen bestimmt (Tabelle 3.3). Eine deutliche Verringerung der Korngröße könnte ein Indikator für die Entstehung vieler Korngrenzen sein. Allerdings wurde keine solche Tendenz beobachtet. Die Kristallitgrößen scheinen unabhängig von der Elektrolysedauer zu sein.

Der Einfluss der Stromdichte (bzw. des angelegten Potentials) wurde untersucht. Dabei hat eine höhere Stromdichte zu einer Verschiebung des Produktspektrums in Richtung der CO_2-Reduktionsprodukte geführt (Abbildung 3.12). Folglich nimmt die Wasserstoffentwicklung mit steigender Stromdichte ab. Da ein hohes Überpotential für die Bildung von komplexeren Molekülen aus CO_2 nötig ist,[96] verschiebt sich innerhalb der kohlenstoffhaltigen Produkte das Verhältnis stark in Richtung der C_{2+}-Produkte bei einem Potential negativ von $-0.9\,\mathrm{V}$ *vs.* RHE. Wird die Stromdichte von $45\,\mathrm{mA\,cm^{-2}}$ auf $100\,\mathrm{mA\,cm^{-2}}$ erhöht, so verdoppelt sich die Effizienz für C_{2+}-Produkte (15 % auf 31 %). Dieser Zuwachs ist vor allem der vermehrten Ethylenbildung

zuzuschreiben, während die Konversion zu Ethanol nur wenig zunimmt und die Bildung von Propanol unabhängig von der Stromdichte war. Die beobachtete Abhängigkeit der Produktbildung vom verwendeten Potential stimmt in etwa mit Literaturdaten[14] überein, wobei die Maxima für CO und Formiat um $-0.9\,\text{V}$ bei dem hier verwendeten Material kaum ausgeprägt sind.
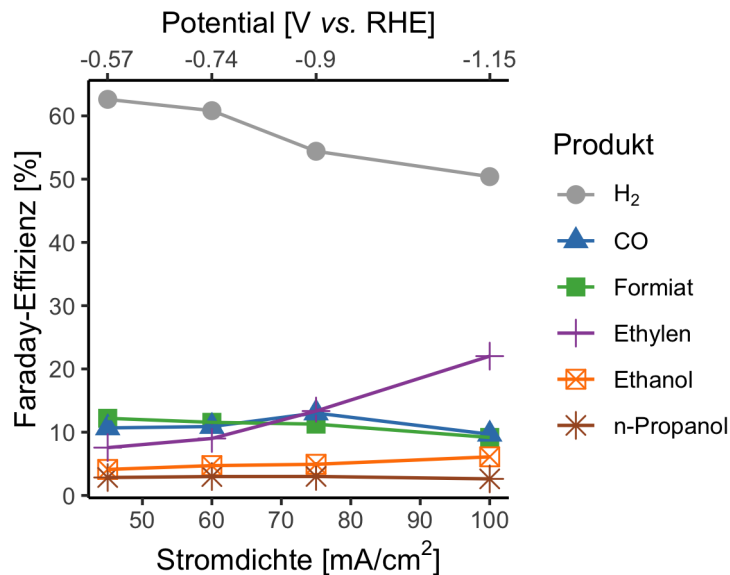

Abbildung 3.12: Produktbildung aus CO_2 in Abhängigkeit von der Stromdichte. Katalysator: Cat_B. Elektrolyt: $1\,\text{M KOH}$.

Die Wasserstoffentwicklung konsumiert bei den getesteten Reaktionsbedingungen mindestens die Hälfte der applizierten Ladung. In einer kleinen Versuchsreihe wurde versucht, die Wasserstoffentwicklung mithilfe von Additiven zu hemmen. In der Literatur existieren bereits Ansätze mit Pyridinium-Additiven, welche als Film auf der Elektrode immobilisiert werden.[97] Die dadurch verringerte Diffusion von Protonen hin zur Kathode wird als Grund für die unterdrückte Wasserstoffbildung genannt. Die Idee bei den hier verwendeten Ammoniumadditiven basiert auf der coulombschen Abstoßung der Ammoniumspezies und der Protonen. Die positiv geladenen Ammoniumspezies lagern an der Kathode an und bilden eine Schicht, welche die direkte Reduktion von H^+ an der Elektrode hemmen. Der Effekt von drei verschiedenen Additiven auf die Produktverteilung wurde getestet (Abbildung 3.13). Der Zusatz von $1\,\text{mM}$ Ammoniumadditiv wirkte sich deutlich auf die generierten Produkte aus. Auffällig ist, dass entgegen der Annahme einer verringerten Wasserstoffproduktion, eine größere Menge H_2 generiert wurde, wenn Additive verwendet wurden (Tabelle 3.4). Für *Additiv A* wurde eine ähnliche Produktverteilung wie im Kontrollversuch ohne Additiv detektiert, wobei die Wasserstoffentwicklung leicht zunahm. Für *Additive B* und *C* wurden deutlichere Abweichungen vom Kontrollversuch beobachtet. Bei Verwendung von *Additiv B* wurde die Produktverteilung zugunsten von C_1-Produkten und Wasserstoff verschoben. Einen besonders großen Effekt hat *Additiv C* gezeigt, wobei die Faraday-Effizienz für C_{2+}-Produkte am niedrigsten war und die Effizienz für Formiat von $9\,\%$ auf

23 % anstieg. Eine mögliche Erklärung für die geringere Effizienz bezüglich der CO_2-Reduktion bei Verwendung von Ammoniumadditiven könnte in einer Blockierung der aktiven Zentren des Katalysators liegen. Durch die Belegung der Elektrodenoberfläche mit den Ammoniumspezies steht weniger Oberfläche für die CO_2-Reduktion zur Verfügung. Alternativ könnte auch eine schlechtere Adsorption von Intermediaten vorliegen. Die Konversion von CO_2 zu Reduktionsprodukten involviert die Adsorption von verschiedenen C_1-Spezies, wie $M-C\equiv O$. In der weiteren Konversion zu C_{2+}-Produkten ist eine Reihe weiterer, komplexer Ad- und Desorptionsvorgänge enthalten.[60] Es ist daher denkbar, dass die Bildung komplexerer Moleküle durch die Anwesenheit von Kationen auf der Elektrodenoberfläche gestört wird. Interessant ist der starke
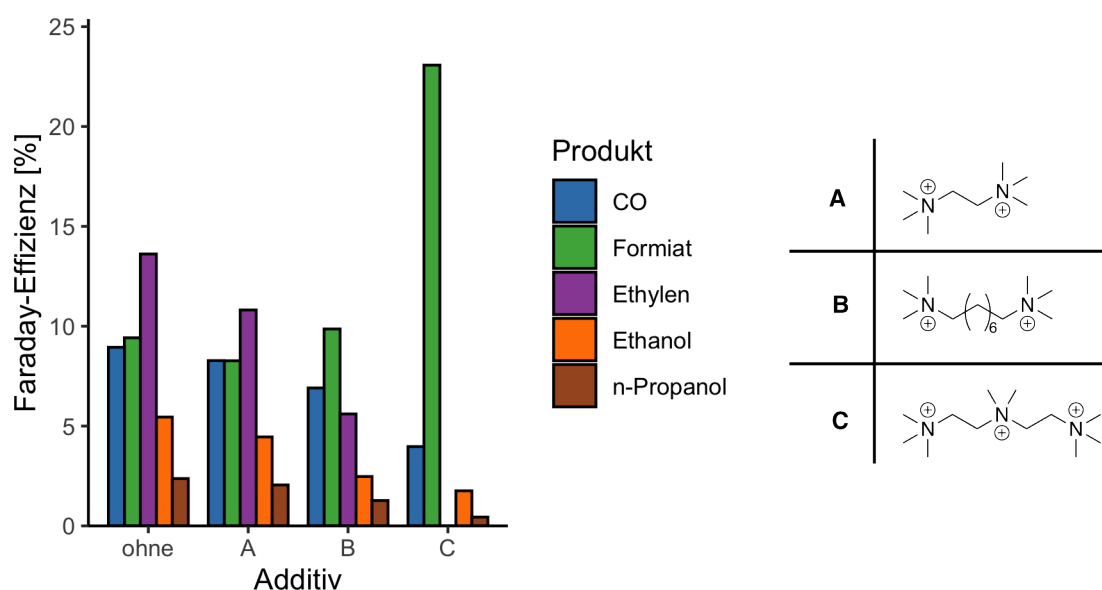

Abbildung 3.13: Produktverteilung in der CO_2RR bei Verwendung von Ammoniumadditiven (Anion: $MeSO_4^-$). Bedingungen: 1 mM Additiv in 1 M KOH, Cat_B′ (Hergestellt wie Cat_B, aber andere Charge), 100 mA cm^{-2}.

Tabelle 3.4: Anteil von Produkten mit mehreren Kohlenstoffatomen (C_{2+}) bezogen auf alle gebildeten CO_2 Reduktionsprodukte (η_{C2+}) und Wasserstoffentwicklung im CO_2RR-Experiment bei 100 mA cm^{-2} bei Verwendung von Ammoniumadditiven. FE_{C2+} ist die Summe der FE von Produkten mit mehreren Kohlenstoffatomen.

	Additiv	FE_{C2+} [%]	η_{C2+} [%]	$FE(H_2)$ [%]
1	ohne	21	54	60
2	A	17	51	66
3	B	9	36	74
4	C	2	8	71

Anstieg der Faraday-Effizienz für Formiat bei Verwendung von *Additiv C*. Generell ist es bei der Herstellung von Carboxylaten (wie Formiat) von Vorteil, wenn Kationen zur Stabilisierung der Carboxylatanionen anwesend sind.[98] Zwar werden bei Zusatz von *Additiven A* und *B* ebenfalls Kationen zur Verfügung gestellt, allerdings bietet *Additiv C* eine zusätzliche Ammoniumfunktion.

Möglicherweise spielt auch der Abstand der zusätzlichen (mittleren) Ammoniumfunktion zur Elektrode (und damit zu den gebildeten Formiatanionen) eine Rolle.

Es kann zusammengefasst werden, dass verschieden generierte Kupferpartikel (und Kupferoxide) teilweise große Unterschiede in der elektrochemischen CO_2-Reduktion bewirken. Für alle generierten Partikel wurde eine hohe Wasserstoffentwicklung ($\geq 50\,\%$) beobachtet. Im Vergleich verschiedener Kupferspezies wurde mit den Verbindungen, welche prozentual weniger Cu enthielten (CuO oder $CuCO_3 \cdot Cu(OH)_2$) tendenziell eine höhere Effizienz für C_{2+}-Produkte beobachtet. Dies ist mit der Literatur im Einklang, in welcher die verstärkte Bildung von C_{2+}-Produkten auf poröse und korngrenzenreiche Strukturen zurückgeführt wird, welche aus der Reduktion von Kupferoxiden entstehen. Bei den hier getesteten Materialien konnte kein konkreter Zusammenhang zwischen weiteren Struktureigenschaften des Materials, wie Partikelgröße oder Morphologie aufgezeigt werden. Zu bedenken ist dabei die Komplexität und die Vielzahl der Einflussfaktoren. Letztlich wird durch die Herstellung zweier Materialien mit unterschiedlicher Morphologie nicht nur die Partikelform verglichen, da sich mit der Synthese zweier Materialien auch Eigenschaften wie Oberflächenrauhigkeit, Porosität, Kristallitgröße, Partikelgröße etc. ändern. Die Effekte all dieser Materialeigenschaften überlagern sich und führen zu einem Ergebnis, welches nicht mehr eindeutig auf einen Ursprung zurückgeführt werden kann. Dennoch konnte gezeigt werden, dass Katalysatoren, deren Herstellungsmethoden sich lediglich durch ein Additiv unterscheiden, teils stark verschiedene Selektivitäten in der elektrochemischen CO_2-Reduktion aufweisen.

3.2 Elektrocarboxylierung mit Kohlenstoffdioxid

Erklärung meines Beitrags:

Personenbezogene Daten

Hintergrund Die Herstellung von α-Hydroxysäuren, wie Mandelsäure (Hydroxyphenylessigsäure) wird häufig über die Cyanierung von Aldehyden und der anschließenden Hydrolyse

des entstandenen Nitrils realisiert.[99,100] Dabei wird hochgiftiges Cyanid eingesetzt. Außerdem entstehen in der Hydrolyse stöchiometrische Mengen des NH_4^+-Salzes. Alternativ können Hydroxycarbonsäuren elektrochemisch hergestellt werden. Dabei werden Ketone oder Aldehyde reduktiv mit Kohlenstoffdioxid (CO_2) verknüpft (Schema 2).
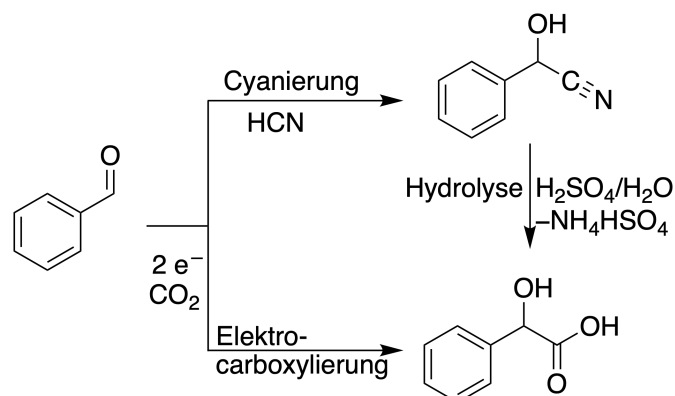
Schema 2: Cyanierung von Benzaldehyd und anschließende Hydrolyse zu Mandelsäure. Eine Alternative ist die direkte Elektrocarboxylierung mit CO_2.

Da das entstandene Carboxylatanion für eine effiziente Reaktion gut stabilisiert werden muss, werden in den meisten einschlägigen Studien zur Elektrocarboxylierung ungeteilte Zellen mit Opferanoden verwendet.[101–110] Die Auflösung der Anode unter Freisetzung von Kationen sorgt für eine Stabilisierung der Carboxylate. Einher gehen allerdings eine starke Kontamination des Elektrolyten mit Metallspezies und eine aufwändige Rückgewinnung des Anodenmaterials. In der aufgeführten Publikation wird die Elektrocarboxylierung in geteilten Zellen mit stabilen Graphit-Anoden durchgeführt. Des Weiteren wird Propylencarbonat als *grünes* Lösungsmittel verwendet und stellt somit eine ungiftigere Alternative zu den für die Carboxylierung meist verwendeten Lösungsmitteln *N,N*-Dimethylformamid und Acetonitril dar.

Ergebnisse Als Testreaktion diente die Carboxylierung von Benzaldehyd zu Mandelsäure. Die Elektrocarboxylierung wurde in polaren aprotischen Lösungsmitteln getestet. Hierfür wurden verschiedene Lösungsmittel miteinander verglichen: Acetonitril (MeCN), *N,N*-Dimethylformamid (DMF), Dimethylsulfoxid (DMSO) und Propylencarbonat (PC). Protische Lösungsmittel scheiden für die Anwendung in der Elektrocarboxylierung aus, da sie Bildung von Nebenprodukten (Alkohol oder Pinacol-Typ) begünstigen.[111] Im Vergleich der getesteten Lösungsmittel wurde mit Propylencarbonat die mit Abstand höchste Ausbeute für Mandelsäure erzielt. Dies war aus mehreren Gründen überraschend: Zum einen ist PC in der Literatur, verglichen mit DMF oder MeCN, eher unterrepräsentiert und zeigt, wenn es verwendet wurde, eher schlechtere Ergebnisse.[98] Zum anderen ist die Löslichkeit von CO_2 in PC deutlich geringer (knapp 60 %) als in MeCN.[112,113] Die Wassergehalte der getesteten Lösungsmittel waren ähnlich und konnten nicht für die Unterschiede in der Ausbeute verantwortlich sein. Letztlich könnte die hohe

Ausbeute für Propylencarbonat auf dessen hohe Dielektrizitätskonstante zurückzuführen sein. Die ausgeprägte Polarität von Propylencarbonat begünstigt die Bildung der ionischen Spezies während der Elektrocarboxylierung. DMSO besitzt zwar ebenso wie PC eine hohe Polarität, könnte allerdings aufgrund seiner Eigenschaften als Oxidationsmittel wirken und entstandene Intermediate abfangen. Dies wurde durch Cyclovoltammetriemessungen unterstützt, bei denen kein dezidierter Reduktionspeak für Benzaldehyd in DMSO auftrat. Neben dem Lösungsmittel wurden weitere Elektrolyseparamter wie Leitsalz, Leitsalzkonzentration, Stromdichte, applizierte Ladungsmenge und Kathodenmaterial untersucht. Einen besonders großen Effekt auf die Mandelsäureausbeute zeigte die Leitsalzkonzentration. Als Leitsalz wurden Tetraalkylammoniumsalze eingesetzt. Wurde die Leitsalzmenge von 1 Äquivalent überschritten, so stieg die Mandelsäureausbeute sprunghaft an und erreichte bei weiterer Zugabe von Leitsalz ein Plateau bei etwa 4 Äquivalenten. Eine plausible Erklärung ist die Stabilisierung der Carboxylatanionen durch die Leitsalzkationen. In Aufbauten mit Opferanode wird die Stabilisierung über die in Lösung gebrachten Metallspezies erreicht. Im hier verwendeten Setup wird diese Funktion vom Leitsalz übernommen. Interessanterweise hat die Länge der Alkylketten der Leitsalze keine Rolle gespielt. Mit Tetraethyl-, -propyl- und -butylammoniumsalzen konnten nahezu identische Produktausbeuten erreicht werden. Ähnlich verhielt es sich mit dem Anion des Leitsalzes wobei allerdings die Verwendung von Chlorid (Bu_4NCl) zu signifikanten Einbußen in der Produktausbeute führte. Ein geringerer Dissoziationsgrad von Bu_4NCl könnte die Carboxylierung negativ beeinflussen, würde aber zu einer höheren Zellspannung führen, was wiederum nicht beobachtet wurde.

Als weiterer Parameter wurde das Kathodenmaterial untersucht. Die für Elektrocarboxylierungen häufig verwendete Nickelkathode[114–117] wurde von mehreren getesteten Materialien in der Produktausbeute deutlich übertroffen. Ein positiver Aspekt ist die sehr gute Performance der kostengünstigen und gut verfügbaren Graphitelektroden (56 % Mandelsäureausbeute). Auch mit anderen, kohlenstoffbasierten Materialien wie Glaskohlenstoff oder Sigracell® konnten höhere Ausbeuten erreicht werden als mit den meisten getesteten Metallkathoden. Lediglich mit der Bleikathode konnten ebenfalls hohe Ausbeuten erreicht werden. In der Literatur wird die Metall-Wasserstoff (M-H) Bindungsstärke als Einflussparameter auf die Carboxylierungseffizienz beschrieben.[111] Unter den getesteten Metallkathoden besitzt Blei die geringste M-H Bindungsstärke,[118] was zu einer geringeren Nebenproduktbildung führt. Für die metallfreie Kathodenserie kann die M-H Bindungsstärke allerdings keine hinreichende Erklärung liefern, da die bor-dotierte Diamantelektrode (BDD) zur niedrigsten Ausbeute unter den C-basierten Materialien führt, obwohl sie von allen Materialien das weiteste Potentialfenster aufweist.[119]

Das Produktspektrum wurde unter den optimierten Elektrolysebedingungen von Mandelsäure auf weitere Hydroxycarbonsäuren erweitert. Die Reaktion zeigte dabei eine Toleranz verschiedener Substituenten, wobei die Anwesenheit zusätzlicher −OH Gruppen einen negativen Einfluss auf die Produktausbeute hatte. Die entsprechenden Edukte agieren vermutlich als Protondonatoren und führen zu vermehrter Nebenproduktbildung. Im Vergleich von Aldehyden

und Ketonen wurden mit letzteren etwas höhere Ausbeuten erreicht (Schema 3). Dies kann mit einer geringeren Reaktivität und sterischen Hinderung der Ketone erklärt werden, welche zu einer verringerten Nebenproduktbildung (z.B. Pinacol-Dimer) führt.[111]
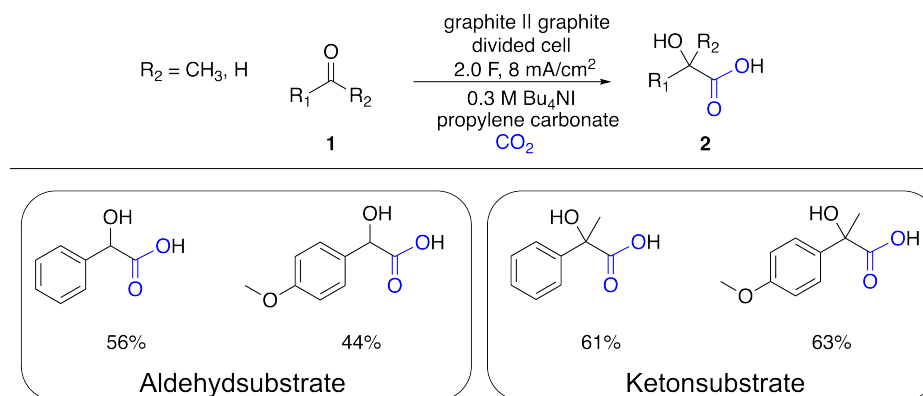
Schema 3: Optimierte Reaktionsbedingungen und Auszug aus dem Produktspektrum. Ketone haben im Vergleich höhere Ausbeuten erbracht als Aldehyde.

Cyclovoltammetriemessungen konnten den grundlegenden, in der Literatur beschriebenen Mechanismus der Elektrocarboxylierung bestätigen. Nach der initialen Reduktion des Edukts zum Ketylradikal wird ein CO_2-Molekül nukleophil addiert. Es folgt eine weitere Reduktion zur Hydroxycarbonsäure. Hinweise auf das in der Literatur aufgeführte Carbonat konnten im Rahmen der vorliegenden Publikation nicht gefunden werden (Schema 4).
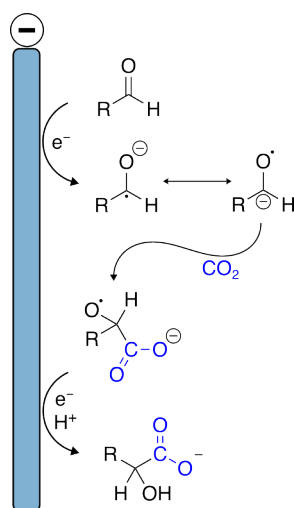
Schema 4: Mechanismus der Elektrocarboxylierung eines Aldehyds. Eine Carboxylierung am Sauerstoff des Ketylradikals und eine daraus folgende Carbonatspezies wurden nicht detektiert.

In der vorgestellten Arbeit konnte erfolgreich auf den Einsatz von Opferanoden verzichtet werden. Hervorzuheben ist die hohe Ausbeute von Mandelsäure bei Verwendung von Propylen-carbonat als *grünes* Lösungsmittel. Insgesamt sind die Ausbeuten mit ca. 60 % etwas niedriger

als bei in der Literatur beschriebenen Reaktionen mit Opferanoden.[103] Dennoch bietet das erarbeitete Protokoll eine attraktive Alternative, da gesundheitsschädliche Lösungsmittel und Metallkontaminationen vermieden werden können.

Electrochemical CO₂ Utilization for the Synthesis of α-Hydroxy Acids

Johannes Seidler, Arne Roth, Luciana Vieira,* and Siegfried R. Waldvogel*

ACCESS | Metrics & More | Article Recommendations | Supporting Information

ABSTRACT: The electrocarboxylation of organic compounds provides a green alternative to the conventional use of cyanides or organometallics. Via a simple electrochemical approach, CO_2 can be directly incorporated into aldehydes or ketones to form α-hydroxy acids using electrical energy as a driving force. In this study, propylene carbonate was used as a "green" solvent. Importantly, the use of sacrificial anodes was avoided; instead, cost-efficient and stable graphite anodes were applied. Voltammetric studies on benzaldehyde carboxylation revealed that the presence of CO_2 significantly changes the reduction behavior of benzaldehyde at potentials more negative than the potential of the ketyl radical formation. Bulk electrolysis was performed in various solvents and supporting electrolyte systems, leading to more than 55% mandelic acid yield in propylene carbonate. Among the tested solvents (acetonitrile, *N,N*-dimethylformamide, dimethyl sulfoxide, and propylene carbonate), propylene carbonate resulted in the highest carboxylate yield. Numerous cathode materials were tested. High carboxylate yields were achieved using graphite, glassy carbon, and lead cathodes. The reaction was successfully carried out for various aromatic aldehydes and ketones as substrates, providing yields of up to 63%.

KEYWORDS: electrocarboxylation, propylene carbonate, green solvent, sacrificial anode-free, solvent control, electrochemical CO₂ utilization, reduction, mandelic acid
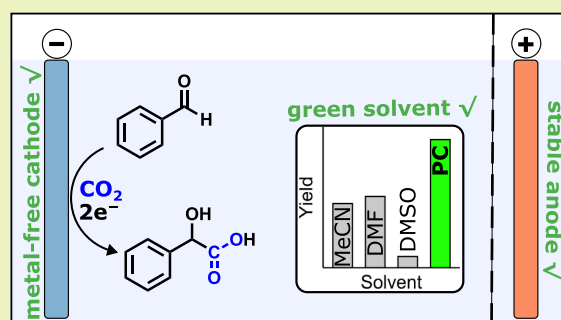
■ INTRODUCTION

Hydroxy acids are widely used compounds with applications in cosmetics[1,2] and food processing and as pharmaceutical precursors.[3] Mandelic acid, one of the most important α-hydroxy acids, has an antibacterial effect, inhibiting, for example, *Staphylococcus aureus*, *Bacillus proteus*, *Escherichia coli*, and *Aerobacter aerogenes*.[4] Moreover, mandelic acid is used in various cosmetics and in the treatment of certain skin conditions such as acne.[5] Derivatives of mandelic acid have also been used for the preparation of ionic liquids.[6]

The chemical synthesis of mandelic acid is usually performed by a two-step reaction starting from benzaldehyde. First, mandelonitrile is prepared by reacting benzaldehyde with highly toxic sodium cyanide. Subsequently, the nitrile is hydrolyzed, for example, under acidic conditions, affording mandelic acid and stoichiometric amounts of NH_4^+ salts.[7] Generally, carboxylic acids could be prepared via the Grignard reaction, which requires stoichiometric amounts of organometallics.[8] Another method for the synthesis of mandelic acid involves chloroform, which is also toxic.[9] In terms of waste minimization and the application of non-hazardous chemicals, the above-mentioned synthetic approaches are undesirable.

Electrochemistry, which has experienced a renaissance in the past decades, can provide alternative synthesis routes avoiding stoichiometric amounts of reducing agents or oxidizers and can pay off as an alternative to conventional synthesis routes.[10−13]

The electrochemical carboxylation approach is appealing as it avoids cyanides and organometallic compounds. In the case of a renewable supply of electricity, the electroreduction becomes an even more sustainable alternative to conventional synthesis. Additionally, the use of CO_2 as a reactant is an important step toward closed carbon cycles. Numerous studies have demonstrated the electrochemical fixation of carbon dioxide into organic compounds generating carboxylic acids.[14−17] For example, the carboxylation of imines affording amino acids has been presented using microreactors.[18,19] However, despite many publications and patents, no medium- to large-scale industrial implementation has been achieved to date.[16]

Electrocarboxylation reactions are usually conducted in aprotic polar solvents such as acetonitrile (ACN)[20−22] or *N,N*-dimethylformamide (DMF),[23−28] whereas the latter is rather undesirable due to its toxicity.[29] Ionic liquids have been studied as alternative solvents for electrocarboxylation reactions because of their good conductivity; they are non-flammable and possess the ability to dissolve high amounts of

A

CO_2. Zhang and co-workers reported 98% yield for the electrocarboxylation of acetophenone in [BMPyrd][TFSI]. However, a magnesium sacrificial anode was applied.[30] Sacrificial anodes such as magnesium or aluminum are used in the vast majority of electrocarboxylation studies.[15,16,20,28,30−35] During electrolysis, these anode materials dissolve, releasing metal ions into the electrolyte. The anodically generated metal ions stabilize the carboxylate product, which is formed at the cathode. Furthermore, any unwanted oxidation processes are avoided as the dissolution of the anode material is the only anodic process taking place. Depending on the compounds involved, the product may precipitate as metal carboxylate facilitating product isolation. However, the main drawback of using sacrificial anodes is the contamination of the electrolyte with large amounts of metal ions requiring laborious and energy-intensive metal recovery. Moreover, the consumption of the electrode material increases cost and restricts applications in simple flow cells for a longer time scale. When stable anode materials, such as platinum, glassy carbon, or boron-doped diamond, are used, reactions are usually carried out in divided cells to avoid unwanted oxidation of the starting material or product of the cathodic process.[36] A typical anodic reaction occurring in systems with inert anodes is the oxidation of the solvent or supporting electrolyte anions.[37] Several approaches have been pursued to avoid sacrificial anodes in electrocarboxylation reactions. Muchez et al. presented an undivided cell setup with a stable anode where the TEMPO (2,2,6,6-tetramethylpiperidinyloxyl)-mediated oxidation of benzyl alcohol to benzaldehyde is the anodic process. A CO_2 pressure of 5 bar was applied. The generated benzaldehyde is carboxylated to mandelic acid. However, the yields for mandelic acid in their setup were below 20%.[21]

Corbin et al. described the carboxylation of organic halides in a divided electrochemical cell with inert Pt anodes. Instead of a sacrificial anode, Mg^{2+} was added as $MgBr_2$ to the electrolyte. DMF served as a solvent. The approach successfully increased selectivity compared to a setup where no Mg^{2+} was present and led to similar yields using sacrificial anodes (24−78%). However, the use of $MgBr_2$ on larger scales may also cause sustainability issues.[38]

Here, a variety α-hydroxy acids were prepared via electrocarboxylation of aldehydes and ketones using CO_2. The carboxylation of benzaldehyde to mandelic acid was studied as test reaction for cyclic voltammetry and the development of the reaction conditions. The presented protocol uses stable, inert, and low-cost graphite anodes in a divided cell setup. Several solvents were tested for the carboxylation, including ACN, DMF, dimethyl sulfoxide (DMSO), and propylene carbonate (PC). In this study, the highest yield was obtained using PC as a solvent. In the literature, PC is strongly underrepresented as a solvent for electrocarboxylation reactions compared to DMF or ACN.[35] Propylene carbonate offers low toxicity, dissolves well supporting electrolytes, has a large electrolytic window, is biodegradable, and can be produced in a large scale with an atom efficiency of 100%.[39] Furthermore, it is synthesized from propylene epoxide and carbon dioxide, thus contributing to the establishment of a closed carbon cycle. Various cathode materials were screened for their activity toward the electrocarboxylation of benzaldehyde. Prior to bulk electrolysis experiments, the electroreduction of benzaldehyde was studied via cyclic voltammetry. Finally, the scope of the electrocarboxylation protocol was

extended to a variety of aldehydes and ketones as starting substances.

■ EXPERIMENTAL SECTION

Chemicals. Propylene carbonate (SOLVAGREEN, >99.7%), supporting electrolytes (tetraalkylammonium salts), and dimethyl sulfoxide were purchased from Carl Roth, Germany. Acetonitrile (LiChrosolv, >99.9%) was purchased from Merck Chemicals. *N,N*-Dimethylformamide and all ketones and aldehydes were purchased from Sigma-Aldrich. The water impurities of the used solvents according to their specifications are <0.01% (ACN), <0.1% (PC), <0.01% (DMSO), and <0.5% (DMF). All solvents were dried over 3 Å molecular sieves for at least 24 h prior to use. Karl-Fischer titrations were performed using Honeywell electrolytes: Hydranal Coulomat CG (catholyte) and Hydranal Coulomat (anolyte). When commercially available, hydroxy acid products were purchased as reference substances from TCI Chemicals or Sigma-Aldrich.

Electrocarboxylation Experiments. Voltammetric studies were performed using an undivided three-electrode setup consisting of a working electrode [graphite, boron-doped diamond (BDD), glassy carbon (GC), and various metals], the counter electrode (graphite), and the reference electrode (leak-less miniature Ag/AgCl reference electrode, eDAQ). Cyclic voltammetry (CV) was carried out using a Metrohm Autolab PGSTAT128N controlled by Nova 2.1 software. The potential was not corrected for the *iR* drop.

Bulk electrolysis was performed in a screening system consisting of three divided Teflon cells equipped with magnetic stirrers (Figure S1). A ceramic filter disk (ROBU, 15 series) was used as a separator between anodic and cathodic compartments. Each cell was operated individually by an R&S NGE103B power supply in the galvanostatic mode. The relevant cathodic electrode area was adjusted to 1.5 cm². Both cell compartments were filled with 5 mL of the electrolyte, and the cathodic compartment was continuously purged with CO_2 (or argon for control experiments) starting at least 30 min prior to electrolysis. The aldehydes or ketones were added to the catholyte, and the electrolysis was started upon the entire substrate has dissolved. The electrolysis duration was controlled via the amount of applied charge. For product isolation, reactions were conducted using Et_4NBr as the supporting electrolyte. After electrolysis, the catholyte (5 mL) was removed from the cell and the pH was adjusted to approx. 1−3 using 0.1 M HCl. The mixture was extracted with ethyl acetate (3× 10 mL). The combined organic fractions were extracted with 0.5 M $NaHCO_3$ (3× 20 mL), and the combined aqueous fractions were acidified using 3 M HCl (pH ≈ 1). The acidic solution was extracted with ethyl acetate (3× 50 mL), and the combined organic fractions were dried over $MgSO_4$. The solvent was removed under reduced pressure, affording the carboxylic acid product.

For quantitative product analysis, the electrolyte was diluted 1:100 in either ACN or H_2O and subjected to a Shimadzu HPLC/MS system equipped with a Phenomenex Luna Omega Polar C18 column. An eluent mixture of ACN and formate/formic acid buffer (10 mM ammonium formate, pH 3) was used. Quantification was performed via calibration curves. ^1H and ^{13}C spectra of products were recorded using a JEOL JNM-ECA 400 MHz spectrometer. Calibration curves and NMR spectra can be found in the Supporting Information.

The CO_2 saturation concentration in propylene carbonate with and without amine additives was determined using a titration method described by Anouti et al. and is further described in the Supporting Information.[40]

For coulometric Karl-Fischer titrations, a Metrohm Titrando instrument with Pt-wire electrode and a generator electrode with a diaphragm was used.

■ RESULTS AND DISCUSSION

The electrocarboxylation of aldehydes using CO_2 was first studied using the test reaction of benzaldehyde to mandelic acid. The electrochemical reaction must be carried out in an aprotic solvent to avoid the reduction to benzyl alcohol and the

formation of pinacol-type species (Scheme 1), which are the main products in aqueous media.[41] Voltammetric studies and

Scheme 1. Electroreduction of Benzaldehyde to Mandelic Acid (a)[a]
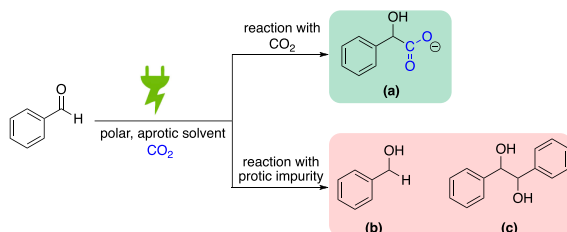
[a]The reaction in aprotic media favors the carboxylation to (a) mandelic acid, whereas the presence of protic species, such as water, leads mainly to (b) benzyl alcohol and the hydrodimer (c) hydrobenzoin.

electrochemical process optimization (current density, electrolyte composition, supporting electrolyte, and cathode material) were first carried out with benzaldehyde as a benchmark substrate. Thereafter, bulk electrolysis with different aldehydes and ketones were performed with the optimized electrochemical conditions.

Voltammetric Experiments. The voltammetric profile of benzaldehyde was investigated in PC in the presence and absence of CO_2. For cyclic voltammograms in the absence of CO_2, the electrolyte was purged with argon prior to the cyclic voltammetry (CV) measurement. In the absence of benzaldehyde, no Faradaic current was observed at potentials of up to approx. −2.7 V versus Ag/AgCl (Figure 1). At potentials more
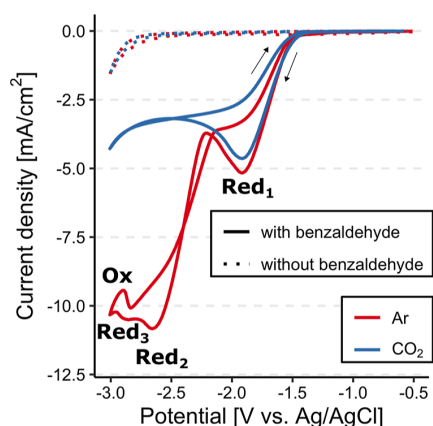

Figure 1. Cyclic voltammogram with and without 50 mM benzaldehyde in 0.1 M Bu_4NBF_4/propylene carbonate purged with argon or CO_2. Cathode material = glassy carbon. Scan rate = 10 mV/s.

negative than −2.7 V versus Ag/AgCl, the current increases considerably regardless of the purging gas (Ar or CO_2) due to electrochemical PC decomposition. The addition of benzaldehyde led to a reduction peak at −1.9 V (Red$_1$), which is slightly more negative in the presence of CO_2. The negative shift of the first reduction event in the presence of CO_2 has been observed in other carboxylation studies and could be a result of the

consecutive reaction.[42,43] A remarkable effect of the purging gas was observed. In the absence of CO_2, a second reduction peak (Red$_2$) accompanied by a third redox event (Red$_3$ and Ox) could be observed, which are not present in the CO_2-saturated electrolyte. The first reduction peak (Red$_1$) can be attributed to the formation of the ketyl radical via a single electron transfer, regardless of the CO_2 presence.[44] Interestingly, the more negative reduction peaks (Red$_2$ and Red$_3$) in CV are not visible in the presence of CO_2. Instead, the back scan exhibits a higher current density than the forward scan, resulting in a curve crossing at approx. −2.4 V versus Ag/AgCl. The higher current during the reverse scan for the CO_2-saturated electrolyte and the lack of a second reduction peak may indicate the generation of active species with a reduction potential more positive than Red$_1$.[45,46] Alternatively, the accumulation of adsorbed species could also lead to the observed curve crossing. The addition of small amounts of water to the electrolyte led to a more pronounced curve crossing (Figure S5), indicating that the event is not linked to the carboxylation reaction.

Common products for the reduction of benzaldehyde involve pinacol-type compounds and benzyl alcohol. The mechanism of the electrocarboxylation of aldehydes has been reported in the literature (Scheme 2).[16,47] After reduction of the aldehyde to the ketyl radical, the latter undergoes protonation and is either further reduced to the alcohol or recombines with another radical to form the pinacol species. In principle, the second reduction peak (Red$_2$) could be a result of the reduction to benzyl alcohol. However, in this study, benzyl alcohol was only detected during bulk electrolysis when water was added to the solvents. Otherwise, only hydrobenzoin was observed when CO_2 was present. Gas chromatography–mass spectrometry (GC–MS) analysis of argon-purged PC electrolytes confirmed the formation of entirely different products (Figure S7). Compound identification was based on fragmentation patterns and comparison with literature data. Interestingly, in the absence of CO_2, only small amounts of hydrobenzoin were found. Instead, the formation of 1,2-diphenylethane and 1,2-diphenylethene seems likely. Furthermore, when propylene carbonate was used as a solvent, a reaction with the solvent took place, which is not the case when CO_2 was present.

Alternatively to the reactions to benzyl alcohol or different diphenyl species, benzaldehyde can react with CO_2 in an ECE mechanism forming mandelic acid.

The first electron transfer to benzaldehyde generates a ketyl radical (electrochemical step), which attacks a CO_2 molecule (chemical step). The thereby produced active species fixates another CO_2 molecule and becomes further reduced at the cathode (electrochemical step). This product is then stabilized by the cations of the supporting electrolyte. The α-hydroxy acid is obtained after acidic workup. The disappearance of reduction events after Red$_1$ upon CO_2 addition has been reported for the carboxylation of acetophenone.[43] An increase in peak current for reduction Red$_1$ was observed for acetophenone in the presence of CO_2 and was linked to a fast reaction with CO_2 and an immediate second reduction at the electrode. For benzaldehyde, we did not observe a higher peak current in the presence of CO_2. If the intermediate is not immediately reduced but requires a more negative potential, the current density for reduction event Red$_1$ would not differ whether CO_2 is present or absent. However, in this case, we would expect another reduction peak in the CV measurement.

C

Scheme 2. Mechanism of the Electrocarboxylation of Aldehydes Using CO_2 and the Electroreduction to the Alcohol and Pinacol-type Products[16,47a]
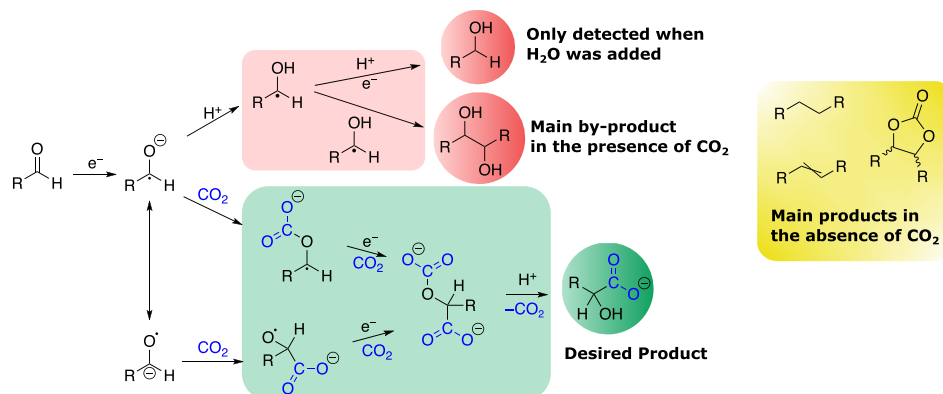
[a]No evidence regarding the presence of the carbonate (ketyl-oxygen attacking the CO_2) was found in this work. Here, the alcohol was only found when water was added to the electrolyte. In the absence of CO_2, different species were obtained (yellow box).

Bulk Electrolysis. The electrocarboxylation of benzaldehyde to mandelic acid was studied in divided Teflon cells. Various electrolysis parameters including solvent, current density, and concentration of the supporting electrolyte were investigated. For product quantification, the electrolyte was diluted and analyzed via HPLC–MS and GC–MS. In addition to mandelic acid, hydrobenzoin diastereomers were detected as side products. Benzyl alcohol was only found when water was added to the electrolyte and absent when anhydrous solvents were used. Among the tested solvents, DMF and ACN provide the best solubility of CO_2.[40,48] DMSO or PC is used in significantly fewer studies, presumably because of their lower solubility of CO_2 compared to ACN and DMF. In this study, however, we observed remarkably higher product yields for mandelic acid when PC was used as a solvent compared to ACN, DMF, and DMSO (Figure 2).
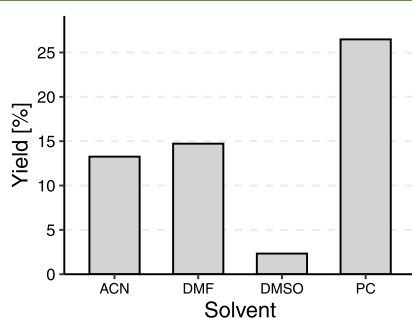

Figure 2. Mandelic acid yield for bulk electrolysis in different solvents. Conditions: BDD cathode, 100 mM benzaldehyde, 0.1 M Bu₄NI, 10 mA/cm², 2F. The terminal cell for each solvent can be found in the Supporting Information.

This is in contrast to the findings by Corbin et al., who studied the carboxylation of halides and observed only poor carboxylate selectivity in propylene carbonate.[38] The amount of water was kept there below 1 mM (approx. 15 ppm). The authors attributed their observations to a higher acidity of propylene carbonate compared with DMF and DMSO. However, in our study, utilization of PC as a solvent resulted

in the highest yield of the carboxylation product. The carboxylation of halides may also require slightly different solvent properties than aldehyde carboxylation. To investigate the source of the superior performance of propylene carbonate, we compared the tested solvents regarding their solvent characteristics. One important solvent property regarding electrocarboxylation is carbon dioxide solubility. Since the CO_2 concentration in the solvent (and the CO_2 to substrate ratio) has an effect on product selectivity,[49] the CO_2 saturation concentrations in the applied solvents were compared (Table 1). Among the tested solvents, acetonitrile provides by far the highest solubility for carbon dioxide.

Table 1. Selected Physical and Chemical Properties of the Applied Solvents[a]

	ACN	DMF	PC	DMSO
$c(CO_2)$ [mmol/L][40,48]	314	194	134	131
$c(H_2O)$ [ppm]	168	305	136	137
$n(H_2O)/n(BA)$ [equiv]	0.09	0.17	0.08	0.08
D [10^{-5} cm²/s]	4.10	1.14	0.40	NA
ε_r [-][50,51]	37.5	36.7	64.9	46.7
AN [ppm][50,52]	18.9	16.0	18.3	19.3
DN [kJ/mol][48,52]	59.0	111.4	63.2	124.8

[a]ε_r = dielectric constant, D = diffusion coefficient. The water concentration after drying over molecular sieves was determined using Karl-Fischer titration. The diffusion coefficients for benzaldehyde were determined at 25 °C. AN = acceptor number, DN = donor number. For DMSO, the diffusion coefficient was not determined since no discrete reduction peak was observed.

Although the solubility of CO_2 was considerably higher in ACN compared to DMF, the carboxylate yields are similar in both solvents (Figure 2). It is also important to remark that the CO_2 saturation concentration was higher than the initial substrate concentration of 100 mmol/L for all solvents. Although the CO_2 solubility is in a similar range for DMSO and PC, only small amounts of the carboxylate product were detected in DMSO, whereas PC showed the highest carboxylate yield compared to all other solvents. Hence, the CO_2 saturation in the electrolyte was not the limiting factor for carboxylation. Nevertheless, increasing the CO_2 concentration
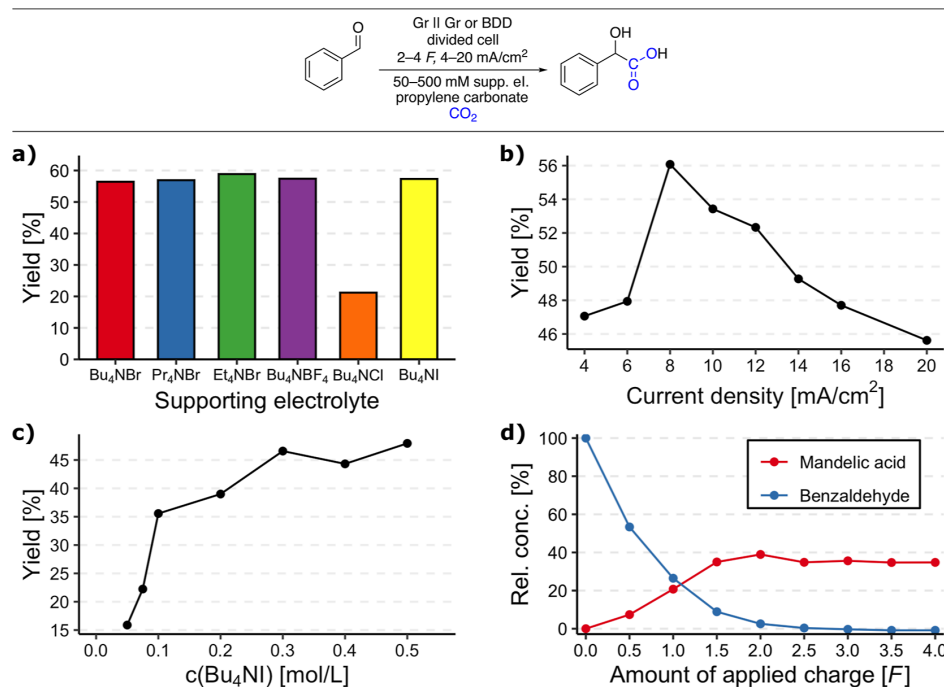
Figure 3. Effect of supporting electrolyte anion (a), current density (b), supporting electrolyte concentration (c), and amount of applied charge (d) on the electrocarboxylation of 100 mM benzaldehyde. Conditions: (a) graphite (Gr) cathode, 10 mA/cm², 2F, 0.5 M supp. electrolyte; (b) graphite (Gr) cathode, 2F, 0.5 M Bu$_4$NI; (c) BDD cathode, 75 mM benzaldehyde, 2F, 10 mA/cm²; and (d) BDD cathode, 0.3 M Bu$_4$NI, 10 mA/cm².

in PC could still improve product selectivity. The CO_2 saturation concentration can be increased by using amine additives instead of higher CO_2 partial pressures.[53] In an experiment series, various amines were added to the electrolyte. The resulting CO_2 saturation concentration was determined via a titration method.[40] The addition of N,N,N′,N′-tetramethylethane-1,2-diamine and triethylamine led to an increase of the CO_2 concentration by 27 and 19%, respectively. However, none of the tested amine additives significantly increased the carboxylate yield (Figure S13).

In addition to the CO_2 concentration, the residual amount of water significantly influences the selectivity of the electrocarboxylation.[49] In the presence of protic media, such as water, there is reduction of the aldehyde or ketone to the corresponding alcohols and pinacol-type products are the dominating products.[16] Therefore, the solvents were dried over activated molecular sieves for at least 24 h prior to the experiment. The final water concentration was determined via coulometric Karl-Fischer titration (Table 1). The lowest water content was found for PC and DMSO. Only slightly higher data were determined for acetonitrile. Addition of small amounts of water to PC led to a lower yield of carboxylate (Figure S14), indicating that water decreases selectivity. However, to decrease the mandelic acid yield by half, an 8-fold increase of the water content would be necessary. Considering the low difference in water content between PC, ACN, and DMSO and comparing the carboxylate selectivity in these electrolytes, we suggest that the water concentration in the electrolyte does not account for the significant difference in the obtained mandelic acid yield; therefore, it is not considered the reason for the better performance of PC.

Diffusion coefficients for benzaldehyde were determined in ACN, DMF, and PC by CV (Figures S15 and S16). For CV measurements, a glassy carbon cathode was used to minimize the error emerging from an inaccurate electrode area. Since the glassy carbon electrode possesses the smoothest and least porous surface of the tested electrodes, its active surface area was assumed to be equal to its geometric surface area. The diffusion coefficient of benzaldehyde is the lowest in PC (4.03 10^{-6} cm² s^{-1}) and the highest in ACN (4.10 10^{-5} cm² s^{-1}). Consistently, the diffusion coefficients in the three solvents are inversely proportional to their viscosities; thus, diffusion is the slowest in the most viscous solvent.[54,55]

A possible rationale for the better performance of PC may arise from its high dielectric constant (Table 1). Based on the Hughes-Ingold rules on solvation, it can be assumed that the higher polarity of PC is beneficial to the carboxylation as charged species are generated during the reaction. DMSO also possesses a high dielectric constant compared to ACN or DMF; however, only small amounts of mandelic acid were detected when DMSO was used. On the other hand, the solvent polarity might not be sufficiently high to even out the effect of the low carbon dioxide solubility in DMSO. Another rationale may arise from DMSO being an oxidizing agent as it may trap intermediates after the reduction of benzaldehyde. Furthermore, DMSO has the highest donor number among the tested solvents, leading to a pronounced solvation of the tetraalkylammonium cations used as supporting electrolytes. These cations are essential for the stabilization of the generated carboxylate species. If the solvation shell is too pronounced, the interaction of the stabilizing cation and the generated carboxylate may interfere, leading to a lower carboxylate efficiency.

E

In addition to the solvent identity, the effect of supporting electrolytes, current density, and amount of applied charge was investigated (Figure 3).

Comparing the supporting electrolyte anions (Figure 3a), a significantly lower carboxylate yield was achieved for Cl^- compared to Br^-, I^-, or BF_4^-. A similar effect was observed in a study with a stainless-steel cathode; however, the reason remains unclear.[56] Studies on anion solvation in PC have shown that the solubility of halide salts increases with the size of the halide anion.[52] A lower degree of dissociation of Bu_4NCl could negatively influence the carboxylation reaction. However, a significantly lower dissociation would increase the terminal cell voltage, which was not higher for Cl^- compared to the other anions (Table S5). The alkyl chain length of the tested supporting electrolytes (ethyl, propyl, butyl) showed no significant effect on the product yield. In contrast to setups with sacrificial anodes, no metal cations are released into the electrolyte during electrolysis. Alternatively, with inert anodes, it is expected that the generated carboxylate anions are stabilized by the cations in the supporting electrolyte. Therefore, properties such as alkyl chain length of the tetraalkylammonium ion could influence the formation of the carboxylate product, as suggested in other studies.[57] However, in this work, only small variations of the product yield were detected for different tetraalkylammonium cations. On the other hand, the concentration of the supporting electrolyte has a strong influence on the carboxylation reaction (Figure 3c). When equimolar amounts of benzaldehyde and the supporting electrolyte are used, the product yield ranges between 20 and 25%. If the supporting electrolyte concentration is slightly increased, the carboxylate yield sharply increases, reaching a plateau at a Bu_4NI excess of 4 equivalents (0.3 M) and a yield of approx. 47%. This increase in product yield indicates an important role of the tetraalkylammonium cation in the stabilization of the generated carboxylate anion.

The electrocarboxylation of benzaldehyde was conducted at different current densities and applied amounts of charge (Figure 3b,d) in PC. A maximum yield of mandelic acid was observed for a current density of 8 mA/cm², which is in the range of current densities reported in the literature.[21,35] Higher current densities may promote the dimerization of benzaldehyde. On the other hand, a considerably lower current density might not be sufficient to either create the ketyl radical or enable the second reduction step. The amount of applied charge of 2F was sufficient to achieve a benzaldehyde conversion of practically 100%.

Electrocarboxylation reactions have been performed on various cathode materials including nickel, lead, silver, stainless steel, platinum, graphite, glassy carbon, and boron-doped diamond.[35] To investigate the effect of the cathode material on product yield within the benzaldehyde/propylene carbonate system, different electrode materials were investigated (Figure 4).

Interestingly, the nickel cathode, which has been used in numerous carboxylation studies, was outperformed by various cathode materials, including all carbon-based electrodes. The highest mandelic acid yield was achieved using a lead cathode, followed by graphite. No cathodic corrosion of the lead cathode was observed.[58] Significantly lower product yields were obtained for all other tested metal cathodes. It was suggested in the literature that the metal−hydrogen (M−H) bond strength can have a significant influence on the carboxylation efficiency.[21] While Pb, Zn, and Sn exhibit low
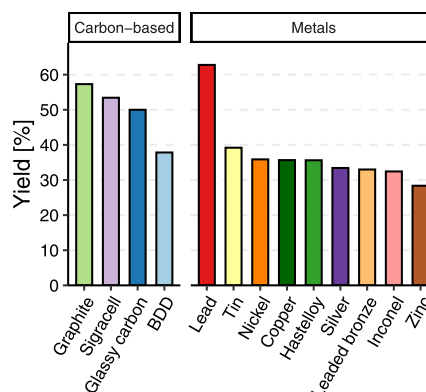

Figure 4. Effect of the cathode material on the electrocarboxylation of benzaldehyde. Conditions: 10 mA/cm², 2F, 75 mM benzaldehyde in 0.3 M Bu_4NI in PC. SIGRACELL = carbon-based bipolar plate, BDD = boron-doped diamond. Hastelloy and Inconel are nickel-based alloys.

M−H bond strength, the other metals used are characterized by an intermediate M−H interaction.[59] Among the tested metals, Pb has the lowest M−H bond strength and consistently led to the highest product yield. However, the carbon series appears puzzling since the BDD electrode has the widest electrochemical potential window of all tested materials[60] and does not perform significantly better than most of the metals or other carbon-based electrodes. Therefore, no clear correlation between the M−H interaction and carboxylation efficiency can be made in this case.

The effect of increasing mass transport was investigated by varying the mechanical electrolyte stirring (Figure 5). No stirring led to low conversion and low product yield. Purging the electrolyte with CO_2 (approx. 6 mL/min) increased the conversion even without mechanical stirring as the gas flow agitated the electrolyte. As expected, the conversion was the
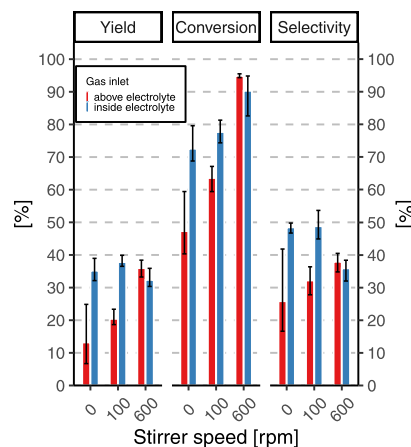

**Figure 5.** Effect of electrolyte stirring and CO_2 gas inlet. Inside electrolyte indicates that the electrolyte was continuously purged with CO_2. Above electrolyte means that only the reactor volume above the liquid was under a continuous CO_2 flow. Error bars denote the minimum and maximum of three experiments. Conditions: BDD-cathode, 100 mM benzaldehyde, 2F, 10 mA/cm².

F

Scheme 3. Scope of the Electrocarboxylation in PC at Graphite Cathodes
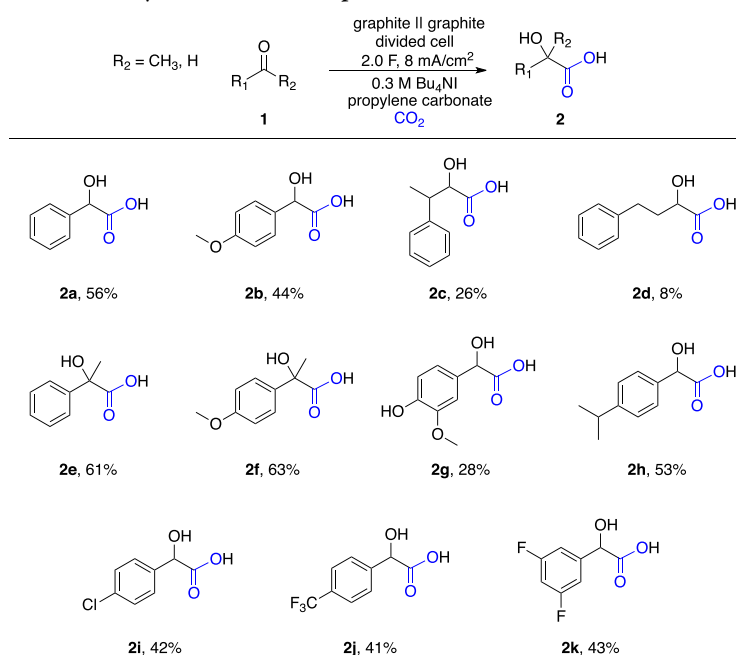
highest when the electrolyte was vigorously stirred (600 rpm). However, the product yield, that is, the selectivity, did not increase regardless of the better conversion rate. Similar mandelic acid yields were obtained for all stirring velocities when the electrolyte was purged with CO_2. However, the conversion was lower for less agitation, leading to higher selectivity at lower stirrer velocities. The strong agitation might impair the second redox process, flushing away unstable intermediates. A distinct effect of mechanical stirring was also observed in other electro−organic reactions.[61,62] However, this would require a rather slow second reduction step, which contradicts the suggestions by Zhang and co-workers, who postulate an immediate second reduction step.[42]

To generalize the electrocarboxylation protocol, various aldehydes and ketones were subjected under conditions optimized for benzaldehyde as a starting material (Scheme 3). Graphite was chosen as a cathode material since it is non-toxic and environmentally benign, and the mandelic acid yield was only slightly smaller compared to lead.

Higher yields for acetophenone and 4-methoxyacetophenone were achieved compared to their aldehyde equivalents (**2a**, **2b** and **2e**, **2f**). This is in line with findings by Muchez et al., who observed higher by-product formation for benzaldehyde compared to acetophenone.[21] Presumably, this is because of the lower reactivity of ketones compared to aldehydes as a result of their higher steric hindrance and the positive inductive effect of the methyl group, which makes the carbonyl carbon less positively charged compared to the aldehyde. As a result, the ketones are less reactive toward side reactions such as the dimerization. The presence of (−OH) substituents appears to have an adverse effect on the product yield (**2g**), most likely because of the potential proton donating ability and increased side product formation. The presence of electron-withdrawing groups such as (−CF₃) or (−F) (**2j**, **2k**) leads to slightly lower product yields. The isopropyl substituent did not alter the

carboxylation efficiency. When the distance of the carbonyl from the aromatic ring increases, the carboxylate yield decreases significantly (**2c** and **2d**). In the case of **2c**, both diastereomers were observed.

■ CONCLUSIONS

In summary, PC was successfully applied as a green alternative to other aprotic, but toxic, solvents, like acetonitrile, and N,N-dimethylformamide for the electrocarboxylation of aldehydes and ketones. Therefore, solvent control in electrosynthesis was observed, which is an important parameter in this technique.[63] Presumably, the high polarity of PC and outstanding redox stability are attributed to the better performance over ACN, DMSO, or DMF. The use of stable and low-cost graphite anodes avoids the tremendous metal contamination of the electrolyte when sacrificial anodes are applied.

Besides the solvent system, other parameters such as supporting electrolyte concentration showed a significant effect on the carboxylate yield. The carboxylate yield increased with a higher concentration of tetraalkylammonium cations, most likely because of better carboxylate stabilization at high cation concentrations. Carbon-based cathodes such as graphite, SIGRACELL, and glassy carbon showed superior performance compared to most tested metal cathodes. For metal-based cathodes, the hydrogen adsorption energy may influence the carboxylation efficiency, resulting in the highest carboxylate yield for the Pb cathode. However, the hydrogen adsorption energy could not account for the carbon electrode series, where the BDD electrode resulted in the lowest carboxylate yield.

Under optimized conditions (graphite cathode, 8 mA/cm², 2F, 0.3 M Bu₄NI/PC), a mandelic acid yield of up to 56% was achieved. For ketones, the carboxylate yield was above 60%. Further optimization, for example, using an elevated CO_2 pressure, gas diffusion electrodes, or a flow-cell setup could

improve the selectivity of the electrocarboxylation if a significant increase of the local CO_2 concentration at the electrode can be achieved.

■ ASSOCIATED CONTENT

Ⓢ Supporting Information

The Supporting Information is available free of charge at https://pubs.acs.org/doi/10.1021/acssuschemeng.2c06046.

> Experimental details, control experiments, results using amine additives, cyclic voltammograms, determination of diffusion coefficients, and NMR spectra (PDF)

■ AUTHOR INFORMATION

Corresponding Authors

Luciana Vieira − *Bio, Electro and Chemocatalysis BioCat, Straubing Branch, Fraunhofer IGB, 94315 Straubing, Germany;* ⦿ orcid.org/0000-0003-1466-6447; Email: luciana.vieira@igb.fraunhofer.de

Siegfried R. Waldvogel − *Department of Chemistry, Johannes Gutenberg University, 55128 Mainz, Germany; ESy-Labs GmbH, 93055 Regensburg, Germany;* ⦿ orcid.org/0000-0002-7949-9638; Email: waldvogel@uni-mainz.de

Authors

Johannes Seidler − *Department of Chemistry, Johannes Gutenberg University, 55128 Mainz, Germany; Bio, Electro and Chemocatalysis BioCat, Straubing Branch, Fraunhofer IGB, 94315 Straubing, Germany; ESy-Labs GmbH, 93055 Regensburg, Germany*

Arne Roth − *Bio, Electro and Chemocatalysis BioCat, Straubing Branch, Fraunhofer IGB, 94315 Straubing, Germany*

Complete contact information is available at:
https://pubs.acs.org/10.1021/acssuschemeng.2c06046

Author Contributions

The manuscript was written through contributions of all authors. All authors have given approval to the final version of the manuscript.

Notes

The authors declare no competing financial interest.

■ ACKNOWLEDGMENTS

■ REFERENCES

(1) Saint-léger, D.; Lévêque, J. L.; Verschoore, M. The Use of Hydroxy Acids on the Skin: Characteristics of C8 -Lipohydroxy Acid. *J. Cosmet. Dermatol.* **2007**, *6*, 59−65.

(2) Smith, W. P. Comparative Effectiveness of ?-Hydroxy Acids on Skin Properties. *Int. J. Cosmet. Sci.* **1996**, *18*, 75−83.

(3) Bhalla, T. C.; Kumar, V.; Bhatia, S. K. Hydroxy Acids: Production and Applications. *Advances in Industrial Biotechnology*; IK International Publishing House Pvt Ltd, 2011; Chapter 4, pp 56−76.

(4) Taylor, M. B. Summary of Mandelic Acid for the Improvement of Skin Conditions. *Cosmet. Dermatol.* **1999**, *12*, 26−28.

(5) Dayal, S.; Kalra, K. D.; Sahu, P. Comparative Study of Efficacy and Safety of 45% Mandelic Acid versus 30% Salicylic Acid Peels in Mild-to-moderate Acne Vulgaris. *J. Cosmet. Dermatol.* **2020**, *19*, 393−399.

(6) Prydderch, H.; Haiβ, A.; Spulak, M.; Quilty, B.; Kümmerer, K.; Heise, A.; Gathergood, N. Mandelic Acid Derived Ionic Liquids: Synthesis, Toxicity and Biodegradability. *RSC Adv.* **2017**, *7*, 2115−2126.

(7) Miltenberger, K. Hydroxycarboxylic Acids, Aliphatic. *Ullmann's Encyclopedia of Industrial Chemistry*; Wiley-VCH Verlag GmbH & Co. KGaA: Weinheim, Germany, 2000.

(8) Faba, L.; Rapado, P.; Ordóñez, S. Carboxylation Reactions for Integrating CO2 Capture with the Production of Renewable Monomers. *Greenhouse Gases: Sci. Technol.* **2022**, *18*, 1−18.

(9) Xu, H.; Chen, Y. An Efficient and Practical Synthesis of Mandelic Acid by Combination of Complex Phase Transfer Catalyst and Ultrasonic Irradiation. *Ultrason. Sonochem.* **2008**, *15*, 930−932.

(10) Pollok, D.; Waldvogel, S. R. Electro-Organic Synthesis − a 21 St Century Technique. *Chem. Sci.* **2020**, *11*, 12386.

(11) Möhle, S.; Zirbes, M.; Rodrigo, E.; Gieshoff, T.; Wiebe, A.; Waldvogel, S. R. Modern Electrochemical Aspects for the Synthesis of Value-Added Organic Products. *Angew. Chem., Int. Ed.* **2018**, *57*, 6018−6041.

(12) Wiebe, A.; Gieshoff, T.; Möhle, S.; Rodrigo, E.; Zirbes, M.; Waldvogel, S. R. Electrifying Organic Synthesis. *Angew. Chem., Int. Ed.* **2018**, *57*, 5594−5619.

(13) Seidler, J.; Strugatchi, J.; Gärtner, T.; Waldvogel, S. R. Does Electrifying Organic Synthesis Pay off? The Energy Efficiency of Electro-Organic Conversions. *MRS Energy Sustain.* **2020**, *7*, 42.

(14) Lu, Y.; Zou, Y.; Zhao, W.; Wang, M.; Li, C.; Liu, S.; Wang, S. Nanostructured Electrocatalysts for Electrochemical Carboxylation with CO 2. *Nano Sel.* **2020**, *1*, 135−151.

(15) Senboku, H.; Katayama, A. Electrochemical Carboxylation with Carbon Dioxide. *Curr. Opin. Green Sustainable Chem.* **2017**, *3*, 50−54.

(16) Matthessen, R.; Fransaer, J.; Binnemans, K.; De Vos, D. E. Electrocarboxylation: Towards Sustainable and Efficient Synthesis of Valuable Carboxylic Acids. *Beilstein J. Org. Chem.* **2014**, *10*, 2484−2500.

(17) Tateno, H.; Matsumura, Y.; Nakabayashi, K.; Senboku, H.; Atobe, M. Development of a Novel Electrochemical Carboxylation System Using a Microreactor. *RSC Adv.* **2015**, *5*, 98721−98723.

(18) Naito, Y.; Kondo, M.; Nakamura, Y.; Shida, N.; Ishikawa, K.; Washio, T.; Takizawa, S.; Atobe, M. Bayesian Optimization with Constraint on Passed Charge for Multiparameter Screening of Electrochemical Reductive Carboxylation in a Flow Microreactor. *Chem. Commun.* **2022**, *58*, 3893−3896.

(19) Naito, Y.; Nakamura, Y.; Shida, N.; Senboku, H.; Tanaka, K.; Atobe, M. Integrated Flow Synthesis of α-Amino Acids ByIn SituGeneration of Aldimines and Subsequent Electrochemical Carboxylation. *J. Org. Chem.* **2021**, *86*, 15953−15960.

(20) Singh, K.; Sohal, H. S.; Singh, B. Synthesis of α-Hydroxycarboxylic Acids from Various Aldehydes and Ketones by Direct Electrocarboxylation: A Facile, Efficient and Atom Economy Protocol. *Asian J. Chem.* **2021**, *33*, 839−845.

(21) Muchez, L.; De Vos, D. E.; Kim, M. J. Sacrificial Anode-Free Electrosynthesis of α-Hydroxy Acids via Electrocatalytic Coupling of Carbon Dioxide to Aromatic Alcohols. *ACS Sustain. Chem. Eng.* **2019**, *7*, 15860−15864.

(22) König, M.; Lin, S.-H.; Vaes, J.; Pant, D.; Klemm, E. Integration of the Aprotic CO2 Reduction to Oxalate at a Pb Catalyst into a GDE Flow Cell Configuration. *Faraday Discuss.* **2021**, *230*, 360.

(23) Yuan, G.; Li, Z.; Jiang, H. Electrosyntheses of α-Hydroxycarboxylic Acids from Carbon Dioxide and Aromatic Ketones Using Nickel as the Cathode. *Chin. J. Chem.* **2009**, *27*, 1464−1470.

(24) Hoppe, C.-F.; Nordschild, A.; Harald, J.; Christoph, W.; Roth, P.; Moussallem, I. Verfahren zur Herstellung von Alpha-Hydroxycarbonsäure durch Elektrochemische Carboxylierung von Aldehyden oder Ketonen. DE 102011078468 A1, 2013.

(25) Reufer, C.; Hateley, M.; Lehmann, T.; Weckbecker, C.; Sanzenbacher, R.; Bilz, J. Process for the Preparation of α-Substituted Carboxylic Acids from the Series Comprising α-Hydroxycarboxylic Acids and n-Substituted-α-Aminocarboxylic Acids. U.S. Patent 7,332,067 B2, 2008.

H

(26) Lehmann, T.; Schneider, R.; Weckbecker, C.; Dunach, E.; Olivero, S. Process for the Production of 2-Hydroxy-4-Methylmercaptobutyric Acid. ES 2528383 T3, 2002.

(27) Yang, D. T.; Zhu, M.; Schiffer, Z. J.; Williams, K.; Song, X.; Liu, X.; Manthiram, K. Direct Electrochemical Carboxylation of Benzylic C-N Bonds with Carbon Dioxide. ACS Catal. 2019, 9, 4699−4705.

(28) Senboku, H.; Sakai, K.; Fukui, A.; Sato, Y.; Yamauchi, Y. Efficient Synthesis of Mandel Acetates by Electrochemical Carboxylation of Benzal Diacetates. ChemElectroChem 2019, 6, 4158−4164.

(29) Joshi, D. R.; Adhikari, N. An Overview on Common Organic Solvents and Their Toxicity. J. Pharm. Res. Int. 2019, 28, 1.

(30) Zhao, S. F.; Horne, M.; Bond, A. M.; Zhang, J. Electrocarboxylation of Acetophenone in Ionic Liquids: The Influence of Proton Availability on Product Distribution. Green Chem. 2014, 16, 2242−2251.

(31) Matthessen, R.; Fransaer, J.; Binnemans, K.; Vos, D. E. De. Electrochemical Dicarboxylation of Conjugated Fatty Acids as an Efficient Valorization of Carbon Dioxide. RSC Adv. 2013, 3, 4634.

(32) Saravanan, K. R.; Chandrasekaran, M.; Suryanarayanan, V. Efficient Electrocarboxylation of Benzophenone on Silver Nanoparticles Deposited Boron Doped Diamond Electrode. J. Electroanal. Chem. 2015, 757, 18−22.

(33) Yang, H. P.; Lin, Q.; Zhang, H. W.; Li, G. D.; Fan, L. D.; Chai, X. Y.; Zhang, Q. L.; Liu, J. H.; He, C. X. Platinum/Nitrogen-Doped Carbon/Carbon Cloth: A Bifunctional Catalyst for the Electrochemical Reduction and Carboxylation of CO2 with Excellent Efficiency. Chem. Commun. 2018, 54, 4108−4111.

(34) Zhang, K.; Xiao, Y.; Lan, Y.; Zhu, M.; Wang, H.; Lu, J. Electrochemical Reduction of Aliphatic Conjugated Dienes in the Presence of Carbon Dioxide. Electrochem. Commun. 2010, 12, 1698−1702.

(35) Liu, X.-F.; Zhang, K.; Tao, L.; Lu, X.-B.; Zhang, W.-Z. Recent Advances in Electrochemical Carboxylation Reactions Using Carbon Dioxide. Green Chem. Eng. 2022, 3, 125−137.

(36) Yang, N.; Waldvogel, S. R.; Jiang, X. Electrochemistry of Carbon Dioxide on Carbon Electrodes. ACS Appl. Mater. Interfaces 2016, 8, 28357−28371.

(37) Klein, M.; Waldvogel, S. R. Counter Electrode Reactions − Important Stumbling Blocks on the Way to a Working Electro-Organic Synthesis. Angew. Chem., Int. Ed. 2022, 61, No. e202204140.

(38) Corbin, N.; Yang, D.-T.; Lazouski, N.; Steinberg, K.; Manthiram, K. Suppressing Carboxylate Nucleophilicity with Inorganic Salts Enables Selective Electrocarboxylation without Sacrificial Anodes. Chem. Sci. 2021, 12, 12365.

(39) Bello Forero, J. S. B.; Hernández Muñoz, A. J.; Jones Junior, J.; da Silva, M. F. Propylene Carbonate in Organic Synthesis: Exploring Its Potential as a Green Solvent. Curr. Org. Synth. 2016, 13, 834−846.

(40) Anouti, M. M.; Dougassa, Y. R.; Tessier, C.; El Ouatani, L.; Jacquemin, J. Low Pressure Carbon Dioxide Solubility in Pure Electrolyte Solvents for Lithium-Ion Batteries as a Function of Temperature. Measurement and Prediction. J. Chem. Thermodyn. 2012, 50, 71−79.

(41) Kunkel, R.; Schmidt, V. M.; Cremers, C.; Müller, D.; Schmiedl, D.; Tübke, J. Electrochemical Synthesis of Biobased Polymers and Polymer Building Blocks from Vanillin. RSC Adv. 2021, 11, 8970−8985.

(42) Zhang, K.; Liu, X.-F.; Zhang, W.-Z.; Ren, W.-M.; Lu, X.-B. Electrocarboxylation of N -Acylimines with Carbon Dioxide: Access to Substituted α-Amino Acids. Org. Lett. 2022, 24, 3565−3569.

(43) Zhang, L.; Xiao, L.-P.; Niu, D.-F.; Luo, Y.-W.; Lu, J.-X. Electrocarboxylation of Acetophenone to 2-Hydroxy-2-Phenylpropionic Acid in the Presence of CO2. Chin. J. Chem. 2008, 26, 35−38.

(44) Péter, Á.; Agasti, S.; Knowles, O.; Pye, E.; Procter, D. J. Recent Advances in the Chemistry of Ketyl Radicals. Chem. Soc. Rev. 2021, 50, 5349−5365.

(45) Lee, K. J.; McCarthy, B. D.; Dempsey, J. L. On Decomposition, Degradation, and Voltammetric Deviation: The Electrochemist's Field Guide to Identifying Precatalyst Transformation. Chem. Soc. Rev. 2019, 48, 2927−2945.

(46) Amatore, C.; Pinson, J.; Savéant, J. M.; Thiebault, A. Trace Crossings in Cyclic Voltammetry and Electrochemic Electrochemical Inducement of Chemical Reactions. Aromatic Nucleophilic Substitution. J. Electroanal. Chem. 1980, 107, 59−74.

(47) Scialdone, O.; Amatore, C.; Galia, A.; Filardo, G. CO2 as a C1-Organic Building Block: Electrocarboxylation of Aromatic Ketones. A Quantitative Study of the Effect of the Concentration of Substrate and of Carbon Dioxide on the Selectivity of the Process. J. Electroanal. Chem. 2006, 592, 163−174.

(48) König, M.; Vaes, J.; Klemm, E.; Pant, D. Solvents and Supporting Electrolytes in the Electrocatalytic Reduction of CO2. iScience 2019, 19, 135−160.

(49) Scialdone, O.; Galia, A.; Isse, A. A.; Gennaro, A.; Sabatino, M. A.; Leone, R.; Filardo, G. Electrocarboxylation of Aromatic Ketones: Influence of Operative Parameters on the Competition between Ketyl and Ring Carboxylation. J. Electroanal. Chem. 2007, 609, 8−16.

(50) Mayer, U.; Gutmann, V.; Gerger, W. The Acceptor Number - A Quantitative Empirical Parameter for the Electrophilic Properties of Solvents. Monatsh. Chem. 1975, 106, 1235−1257.

(51) Barthel, J.; Neueder, R.; Roch, H. Density, Relative Permittivity, and Viscosity of Propylene Carbonate + Dimethoxyethane Mixtures from 25 °C to 125 °C. J. Chem. Eng. Data 2000, 45, 1007−1011.

(52) Peruzzi, N.; Lo Nostro, P.; Ninham, B. W.; Baglioni, P. The Solvation of Anions in Propylene Carbonate. J. Solution Chem. 2015, 44, 1224−1239.

(53) Chowdhury, F. A.; Yamada, H.; Higashii, T.; Goto, K.; Onoda, M. CO2 Capture by Tertiary Amine Absorbents: A Performance Comparison Study. Ind. Eng. Chem. Res. 2013, 52, 8323−8331.

(54) Pires, J.; Timperman, L.; Jacquemin, J.; Balducci, A.; Anouti, M. Density, Conductivity, Viscosity, and Excess Properties of (Pyrrolidinium Nitrate-Based Protic Ionic Liquid + Propylene Carbonate) Binary Mixture. J. Chem. Thermodyn. 2013, 59, 10−19.

(55) Aminabhavi, T. M.; Gopalakrishna, B. Density, Viscosity, Refractive Index, and Speed of Sound in Aqueous Mixtures of N,N-Dimethylformamide, Dimethyl Sulfoxide, N,N-Dimethylacetamide, Acetonitrile, Ethylene Glycol, Diethylene Glycol, 1,4-Dioxane, Tetrahydrofuran, 2-Methoxyethanol, and 2-Ethoxyethanol at 298.15 K. J. Chem. Eng. Data 1995, 40, 856−861.

(56) Zhao, S. F.; Wang, H.; Lan, Y. C.; Liu, X.; Lu, J. X.; Zhang, J. Influences of the Operative Parameters and the Nature of the Substrate on the Electrocarboxylation of Benzophenones. J. Electroanal. Chem. 2012, 664, 105−110.

(57) Luo, P.-P.; Zhang, Y.-T.; Chen, B.-L.; Yu, S.-X.; Zhou, H.-W.; Qu, K.-G.; Kong, Y.-X.; Huang, X.-Q.; Zhang, X.-X.; Lu, J.-X. Electrocarboxylation of Dichlorobenzenes on a Silver Electrode in DMF. Catalysts 2017, 7, 274.

(58) Wirtanen, T.; Prenzel, T.; Tessonnier, J.; Waldvogel, S. R. Cathodic Corrosion of Metal Electrodes—How to Prevent It in Electroorganic Synthesis. Chem. Rev. 2021, 121, 10241.

(59) Conway, B. E.; Jerkiewicz, G. Relation of Energies and Coverages of Underpotential and Overpotential Deposited H at Pt and Other Metals to the 'volcano Curve' for Cathodic H2 Evolution Kinetics. Electrochim. Acta 2000, 45, 4075−4083.

(60) McLaughlin, M. H. S.; Corcoran, E.; Pakpour-Tabrizi, A. C.; de Faria, D. C.; Jackman, R. B. Influence of Temperature on the Electrochemical Window of Boron Doped Diamond: A Comparison of Commercially Available Electrodes. Sci. Rep. 2020, 10, 15707.

(61) Beil, S. B.; Breiner, M.; Schulz, L.; Schüll, A.; Müller, T.; Schollmeyer, D.; Bomm, A.; Holtkamp, M.; Karst, U.; Schade, W.; Waldvogel, S. R. About the Selectivity and Reactivity of Active Nickel Electrodes in C-C Coupling Reactions. RSC Adv. 2020, 10, 14249−14253.

(62) Beil, S. B.; Pollok, D.; Waldvogel, S. R. Reproducibility in Electroorganic Synthesis—Myths and Misunderstandings. Angew. Chem., Int. Ed. 2021, 60, 14750.

(63) Schulz, L.; Waldvogel, S. Solvent Control in Electro-Organic Synthesis. Synlett 2019, 30, 275−286.

Supporting Information

Electrochemical CO_2 utilization for the synthesis of α-hydroxy acids

Johannes Seidler,[a,b,c] Arne Roth,[b] Luciana Vieira,[b] and Siegfried R. Waldvogel*[a,c]*

[a] Department of Chemistry, Johannes Gutenberg University, Duesbergweg 10–14, 55128 Mainz, Germany. E-mail: waldvogel@uni- mainz.de

[b] Fraunhofer IGB, Bio, Electro and Chemocatalysis BioCat, Straubing Branch, Schulgasse 11a, 94315 Straubing, Germany.E-mail: luciana.vieira@igb.fraunhofer.de

[c] ESy-Labs GmbH, Siemensstrasse 7, 93055 Regensburg, Germany.

Content

Number of pages: 36
Number of figures: 29
Number of tables: 6

1　Electrolysis cells and electrode materials

Bulk electrolysis experiments were performed in divided cells made of Teflon (**Figure S1**).[1] Anolyte and catholyte were separated by a ceramic filter disk. Stirring bars were used in each half-cell during electrolysis. The described screening systems are commercially available (IKA Screening System Package, IKA® Werke GmbH & Co. KG, Staufen, Germany). Each compartment was filled with 5 mL electrolyte. The catholyte was bubbled continuously with carbon dioxide.
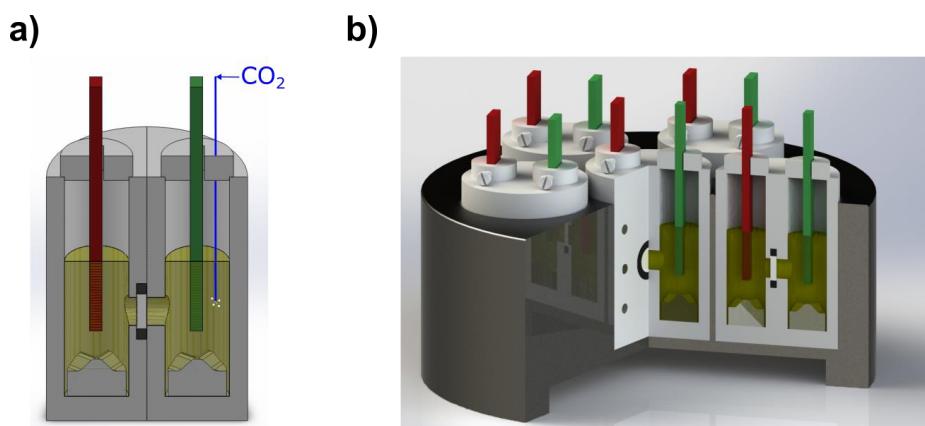

Figure S1. Teflon cells used for bulk electrolysis: a) cross-section of one divided cell, b) arrangement of multiple cells in a stainless-steel block.

The cells were equipped with different cathode materials (**Table S1**). The relevant active electrode area was adjusted to 1.5 cm^2.

S2

Table S1. List of investigated cathode materials.

	Entry	Cathode material	Quality/Vendor
Carbon-based	1	Graphite	IKA-Werke GmbH & Co. KG
	2	Sigracell (bipolar plate)	sgl carbon
	3	Glassy carbon	HTW GmbH, GER
	4	Boron-doped diamond	Condias GmbH, GER
Metals	5	Lead	Pb, >99.9%, GoodFellow
	6	Tin	Sn, >99.9%, GoodFellow
	7	Zinc	Zn, >99.9%, GoodFellow
	8	Nickel	Ni, >99.9%, GoodFellow
	9	Hastelloy	GoodFellow
	10	Inconel	GoodFellow
	11	Copper	Cu, >99.9%, GoodFellow
	12	Silver	Ag, >99.9%, GoodFellow
	13	Leaded bronze	CuSn7Pb15

2   Calibration curves for product quantification using HPLC

a)

Mandelic acid

b)
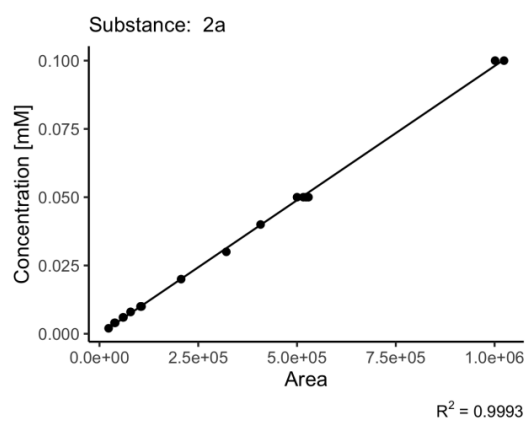
4-Methoxymandelic acid

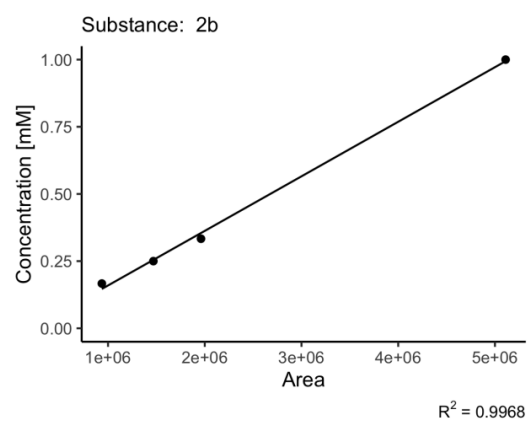

c)

2-Hydroxy-3-phenylbutanoic acid

d)
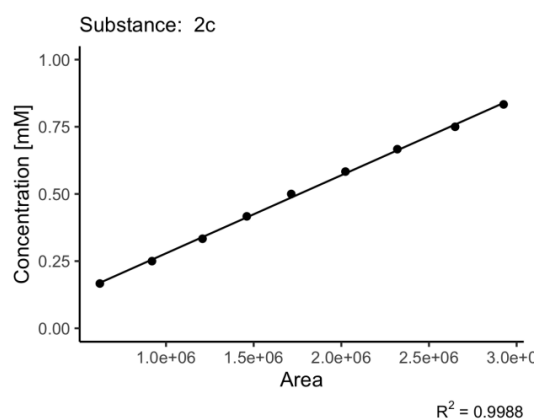
2-Hydroxy-4-phenylbutanoic acid
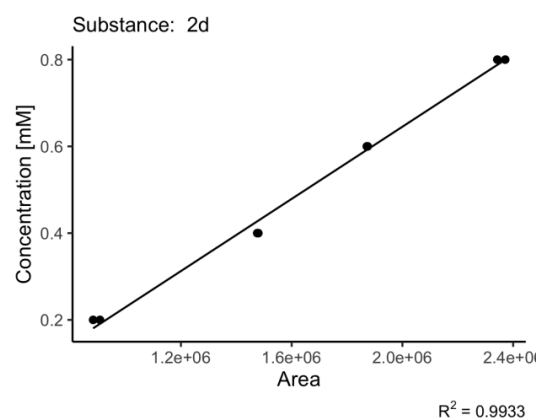
Figure S2. Calibration curves for quantification via HPLC. Mandelic acid (a, substance a), 4-Methoxymandelic acid (b, substance b), 2-Hydroxy-3-phenylbutanoic acid (c, substance c), 2-Hydroxy-4-phenylbutanoic acid (d, substance d).

.

S4

a)

2-Hydroxy-2-phenylpropanoic acid
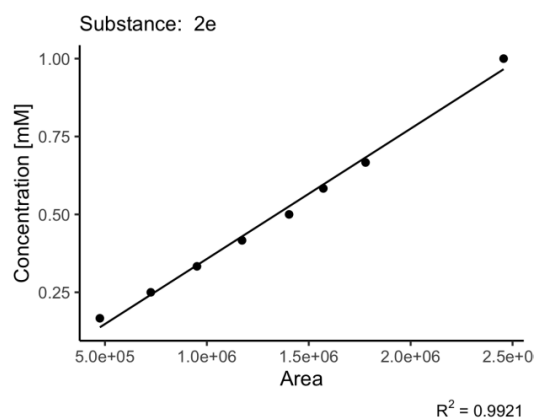
b)

2-Hydroxy-2-(4-methoxyphenyl)propanoic acid
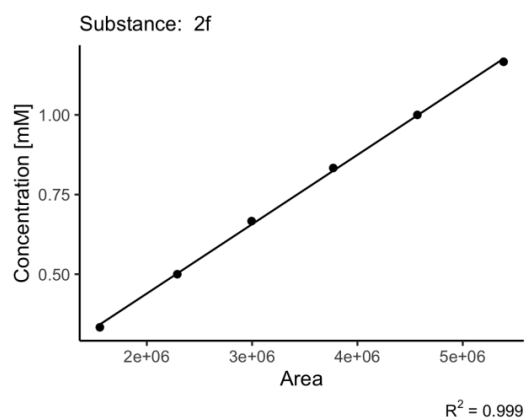
c)

4-Hydroxy-3-methoxymandelic acid
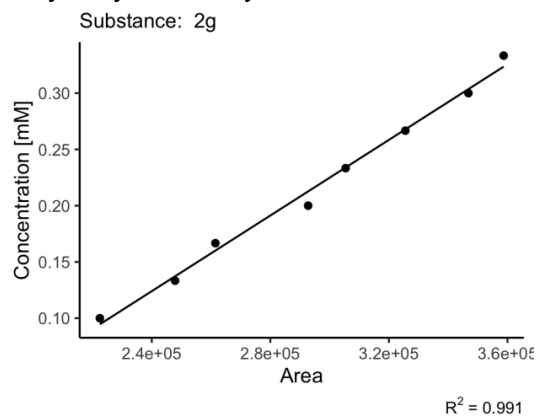
d)

4-Isopropylmandelic acid
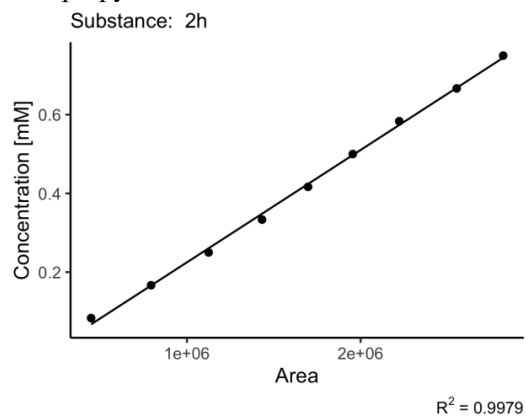
Figure S3. Calibration curves for quantification via HPLC. 2-Hydroxy-2-phenylpropanoic acid (a, substance e), 2-Hydroxy-2-(4-methoxyphenyl)propanoic acid (b, substance f), 4-Hydroxy-3-methoxymandelic acid (c, substance g), 4-Isopropylmandelic acid (d, substance h).
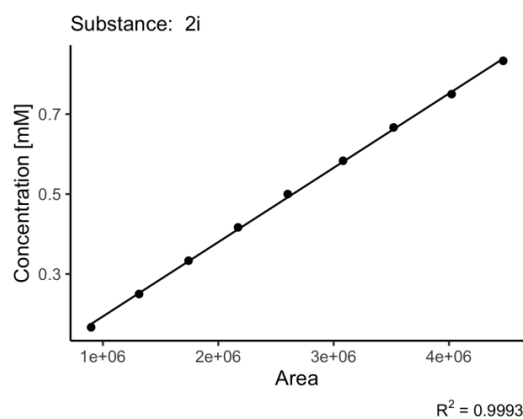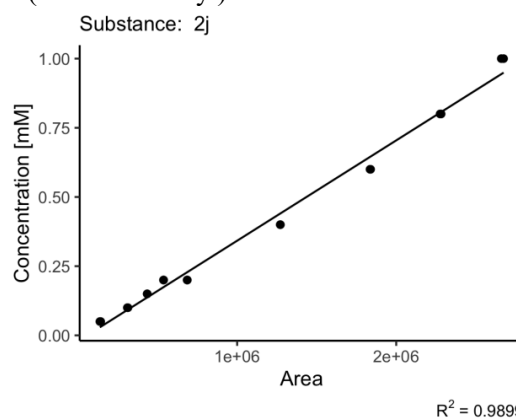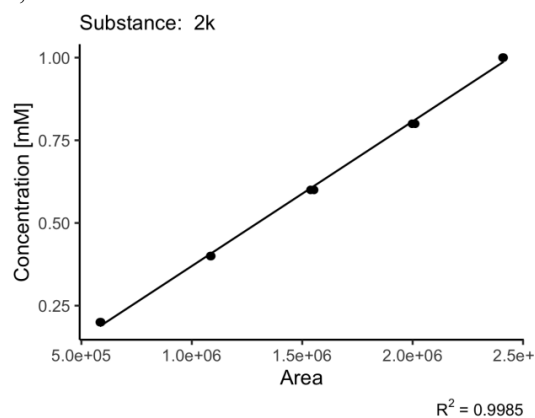
Figure S4. Calibration curves for quantification via HPLC. 4-Chloromandelic acid (a, substance i), 4-(Trifluoromethyl)mandelic acid (b, substance j), 3,5-Difluoromandelic acid (c, substance k).

S6

3 CV analysis with different water content
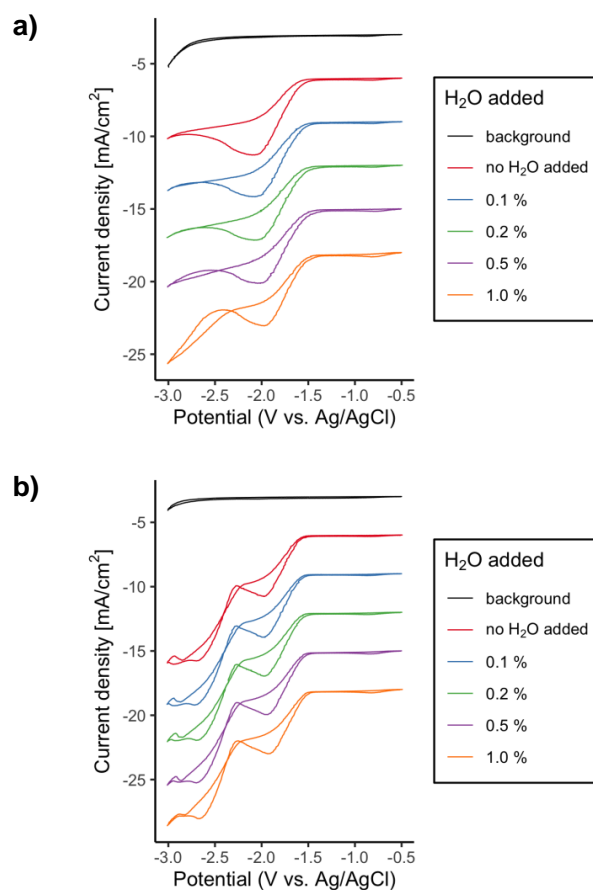
Figure S5. CV measurements for 50 mM benzaldehyde in 0.1 M Bu₄NBF₄ in propylene carbonate at 10 mV/s in the presence (a) and absence (b) of CO_2. Cathode = glassy carbon. Reference electrode = leak-less miniature Ag/AgCl reference electrode, eDAQ.

4   Cyclic voltammetry at different cathode materials
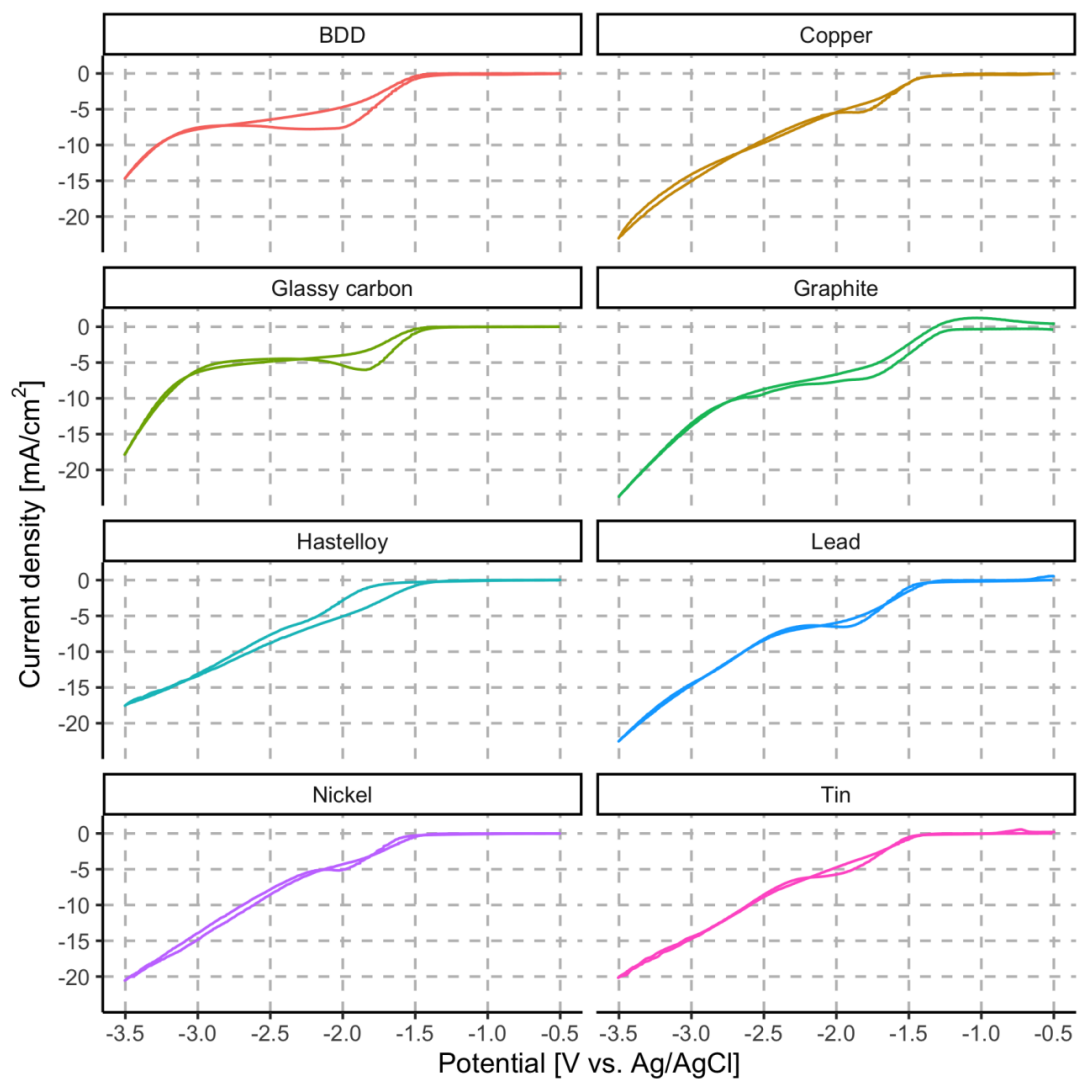
Figure S6. Cyclic voltammograms of 100 mM benzaldehyde in CO_2 saturated 0.1 M Bu_4NBF_4/propylene carbonate using different cathode materials. Scan rate = 10 mV/s. Reference electrode = leak-less miniature Ag/AgCl reference electrode, eDAQ.

Table S2. Reduction potentials and associated peak currents for different cathode materials. 100 mM benzaldehyde in 0.1 M Bu$_4$NBF$_4$/propylene carbonate.

Cathode material	Reduction potential (Peak potential) [V vs. Ag/AgCl]	Peak current [mA/cm^2]
BDD	-2.25	-7.8
Copper	-1.83	-5.4
Glassy carbon	-1.84	-6.0
Graphite	-1.81	-7.3
Hastelloy	NA	NA
Lead	-1.95	-6.5
Nickel	-2.03	-5.2
Tin	-2.09	-6.0

5 By-product formation in the presence and absence of CO₂
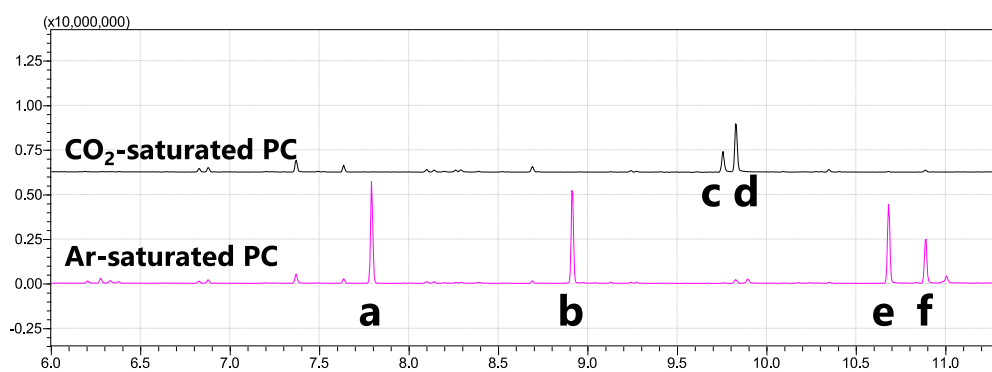
Figure S7. Total ion chromatograms (EI) for reaction mixtures with and without CO2. Same MS patterns were obtained for peaks c+d and e+f.
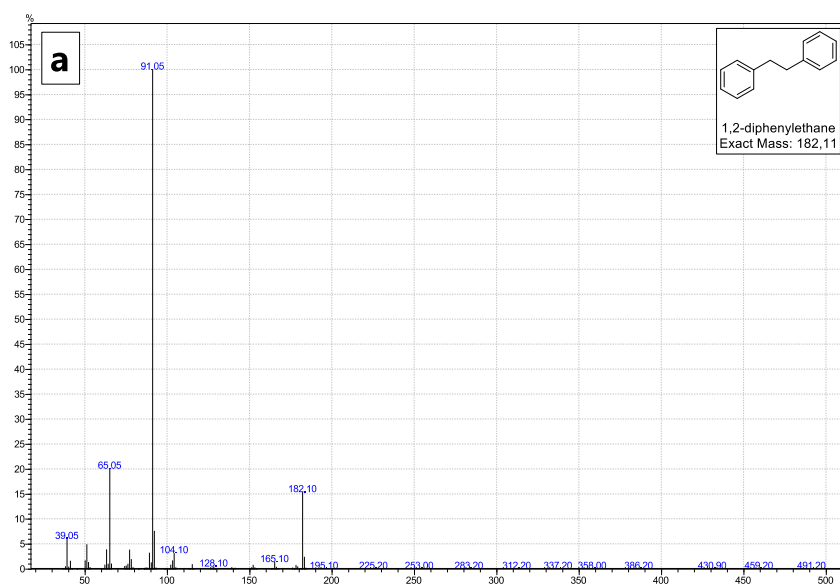
Figure S8. Mass spectrum (EI) for peak (a). The spectrum is in conformance with literature.[2]
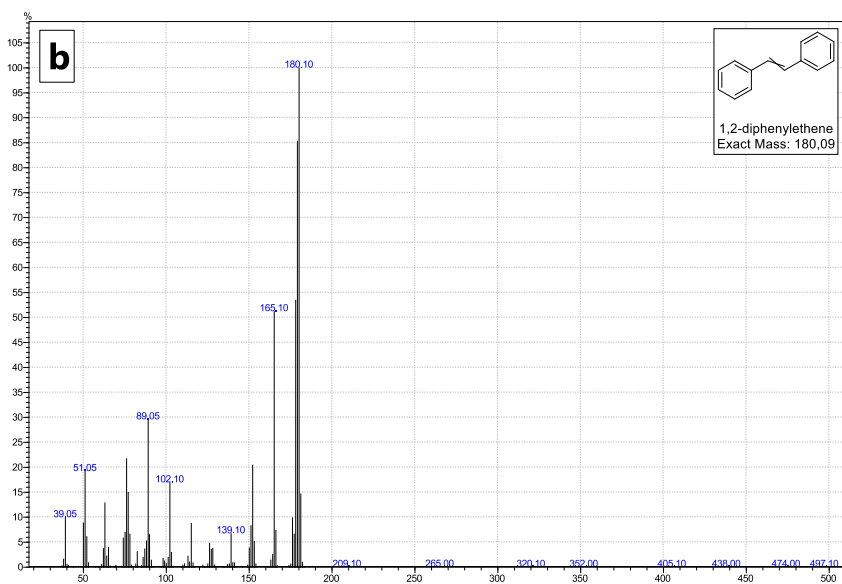
Figure S9. Mass spectrum (EI) for peak (b). The spectrum is in conformance with literature.[3,4]
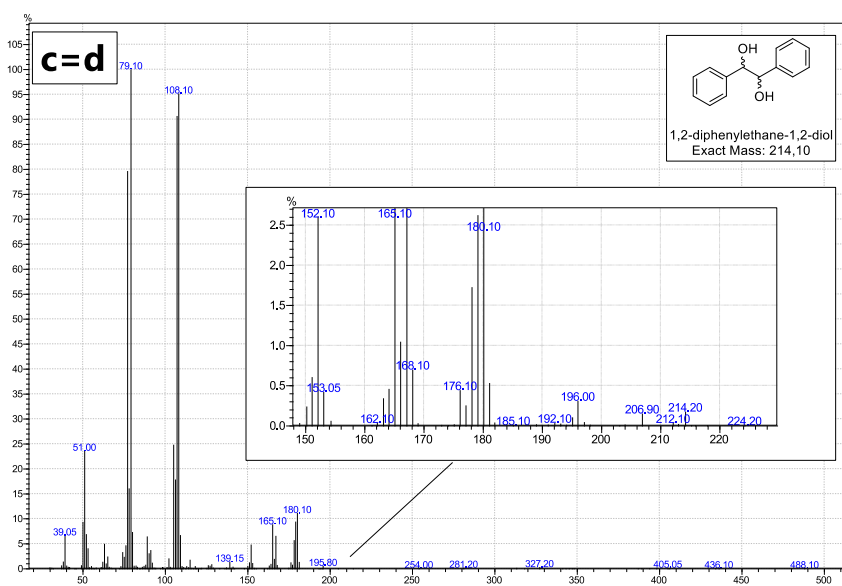
Figure S10. Mass spectrum (EI) for peaks (c) and (d). The spectrum is in conformance with literature.[5]

S11
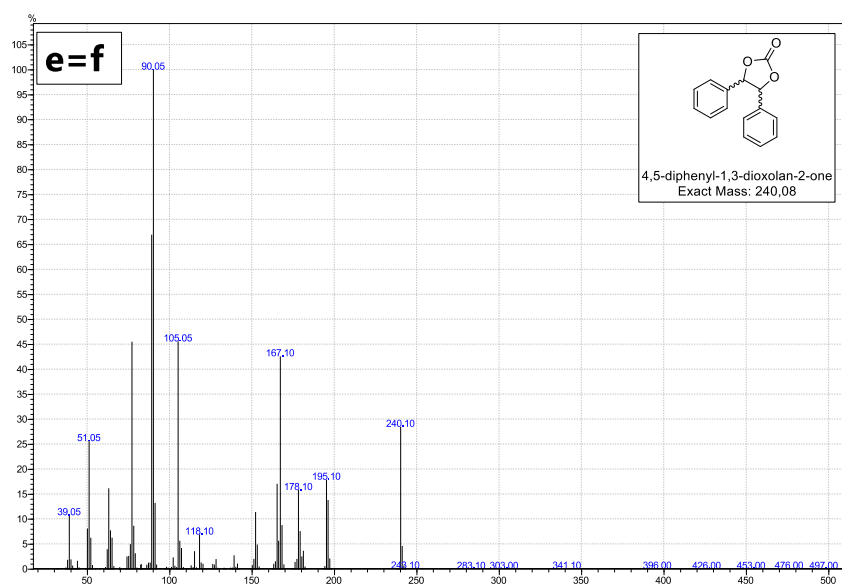
Figure S11. Mass spectrum (EI) for peaks (e) and (f). The spectrum is in conformance with literature.[6]

6   Terminal cell voltage and cell resistance for different solvents

Table S3. Mandelic acid yield and terminal cell voltage and cell resistance using different solvents. Conditions: BDD cathode, 0.1 M Bu$_4$NI in propylene carbonate, 100 mM benzaldehyde, 10 mA/cm^2, 2 F.

	Solvent			
	ACN	DMF	DMSO	PC
Mandelic acid yield	13%	15%	2%	27%
Terminal cell voltage	7 V	11 V	15 V	16 V
Cell resistance	0.5 kΩ	0.7 kΩ	1.0 kΩ	1.1 kΩ

7   Amine additives and determination of CO₂ saturation concentration

The CO_2 saturation concentration was determined using a titration technique reported by Anouti et al.[7] A known quantity of solvent (or solvent + additive) was placed in a glass cell equipped with a septum and held at a constant temperature of 25 °C. The liquid was purged with CO_2 for 1 h to reach saturation. Then, an argon gas flow was used instead of CO_2 to displace the carbon dioxide in solution. The gas outlet of the cell was bubbled into an NaOH solution of known concentration. The carbon dioxide reacts with NaOH to Na_2CO_3. The obtained solution was titrated back with an HCl standard solution. The difference between the two equivalence points was used to determine the HCl consumption (**Figure S12**).
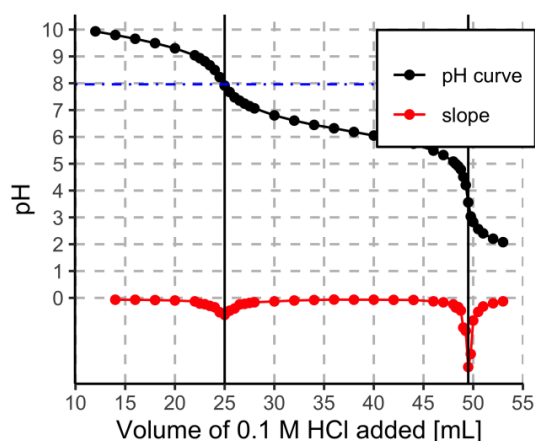
Figure S12. Exemplified titration curve and for the titration of a Na_2CO_3 solution.

The effect of various amine additives on the CO_2 saturation concentration in propylene carbonate was investigated (**Table S4**). Using *N,N,N',N'*-tetramethylethan-1,2-diamine (TMEDA) and *N,N*-diethylethanamine the CO_2 saturation concentration in propylene carbonate was increased compared to the control.

S14

Table S4. CO_2 saturation concentration in propylene carbonate using amine additives.

Amine additive	CO_2 saturation concentration [mmol/L] (deviation from control)
None (control)	119.8 (0%)
TMEDA	152.5 (+27.3%)
TEA	143.2 (+19.5%)
Ethanolamine	128.8 (+7.6%)
Urotropin	119.6 (-0.1%)
DABCO	106.4 (-11.2%)

Various amines were added to the reaction mixture (**Scheme S1**) and their effect on the mandelic acid yield was determined. Although some of the amines increased the CO_2 saturation concentration, none of the tested additives increased the mandelic acid yield remarkably.

Scheme S1. Benzaldehyde carboxylation using different amine additives.
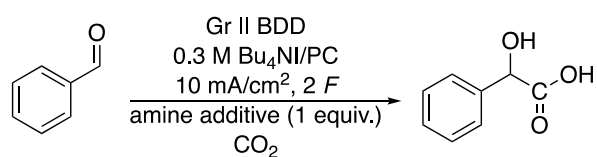
Figure S13. Yield of mandelic acid (HPLC) using different amine additives.

8　Influence of the water content onto electrolysis

To evaluate magnitude of the effect of water presence, the amount of water in the electrolyte was systematically varied. Even a small increase of the water concentration lowers the product yield to some extent.
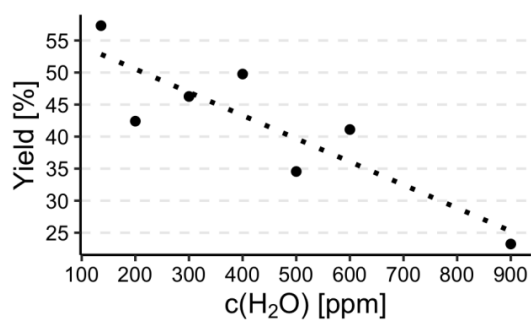
Figure S14. Effect of the water content of the electrolyte onto yield of mandelic acid. The initial amount of water was determined via Karl-Fischer titration (136 ppm). J = 10 mA/cm^2, 2 F, 100 mM benzaldehyde in 0.3 M Bu$_4$NI/propylene carbonate.

S17

95

9   Determination of diffusion coefficients

Diffusion coefficients for benzaldehyde in different solvents were determined using the Randles-Sevcik equation:

$$I_{peak} = \pm 0.436 nFAC \sqrt{\frac{nDv}{RT}} \qquad (S1)$$

Peak currents were measured using cyclic voltammograms at various scan rates (**Figure S15**) and plotted against the square root of the scan rate (**Figure S16**). The slope the lines were inserted into equation 1, which were the solved for the diffusion coefficients.
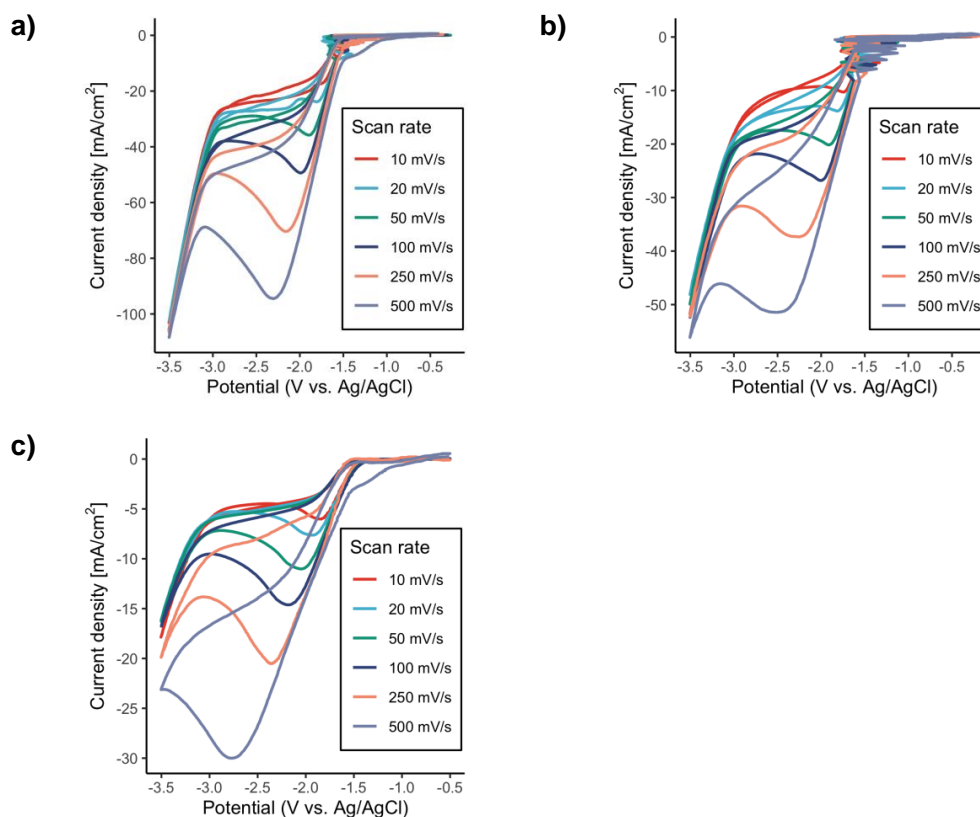
Figure S15. Cyclic voltammograms at different scan rates for 50 mM benzaldehyde in 100 mM Bu$_4$NBF$_4$ in a) acetonitrile, b) *N,N*-dimethylformamide, and c) propylene carbonate. Cathode: glassy carbon.

S18
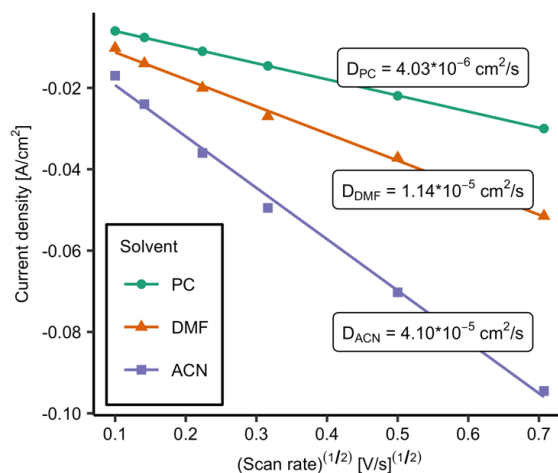
Figure S16. Randles-Sevcik plot for 100 mM benzaldehyde in different solvents and the according diffusion coefficients at 25 °C. PC = propylene carbonate, DMF = *N*,*N*-dimethylformamide, ACN = acetonitrile.

CVs were recorded for benzaldehyde in different solvents. For DMSO no reduction peak was observed (**Figure S17**).
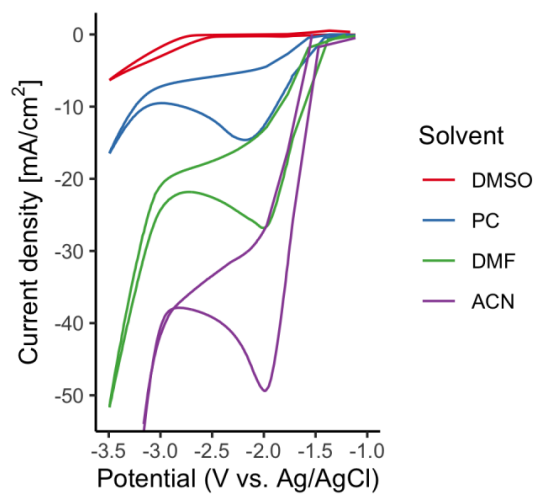
Figure S17. Cyclic voltammograms of 100 mM benzaldehyde in different CO_2 saturated solvents at 10 mV/s.

S19

10 Comparison of supporting electrolytes

Table S5. Mandelic acid yield and terminal cell voltage using different supporting electrolytes. Conditions: Graphite cathode, 0.5 M supporting electrolyte in propylene carbonate, 100 mM benzaldehyde, 10 mA/cm^2, 2 F.

	Supporting electrolytes					
	Bu$_4$NBr	Pr$_4$NBr	Et$_4$NBr	Bu$_4$NBF$_4$	Bu$_4$NCl	Bu$_4$NI
Mandelic acid yield	56%	57%	59%	57%	21%	57%
Terminal cell voltage	16.1 V	15.8 V	15.2 V	17.8 V	16.9 V	15.7 V

11 NMR spectra

For product isolation, the catholyte (5 mL) was removed from the cell and the pH was adjusted to approx. 1–3 using 0.1 M HCl. The mixture was extracted with ethyl acetate (3x 10 mL). The combined organic fractions were extracted with 0.5 M $NaHCO_3$ (3x 20 mL), and the combined aqueous fractions were acidified using 3 M HCl (pH ≈ 1). The acidic solution was extracted with ethyl acetate (3x 50 mL) and the combined organic fractions were dried over $MgSO_4$. The solvent was removed under reduced pressure affording the carboxylic acid product.

The chemical shifts were referenced using the solvent peaks of the deuterated solvents for ^{1}H and ^{13}C spectra. For ^{19}F spectra, trifluoroacetic acid was added as reference. To adjust the chemical shift.

Where available, the NMR spectra were compared to literature data, confirming the obtained structures.

Table S6. Comparison of measured NMR spectra with literature data.

	Product	Reference
2a	Mandelic acid	Baker et al. [8]
2b	4-Methoxymandelic acid	Poterata et al. [9]
2c	2-Hydroxy-3-phenylbutanoic acid	-
2d	2-Hydroxy-4-phenylbutanoic acid	Furukawa et al. [10]
2e	2-Hydroxy-2-phenylpropanoic acid	Qu et al. [11]
2f	2-Hydroxy-2-(4-methoxyphenyl)propanoic acid	Qu et al. [11]
2g	4-Hydroxy-3-methoxymandelic acid	Cardinal et al. [12]
2h	4-Isopropylmandelic acid	Poterata et al. [9]
2i	4-Chloromandelic acid	Gonzalez-Alvarez et al. [13]
2j	4-(Trifluoromethyl)mandelic acid	Okumura and Uozumi [14]
2k	3,5-Difluoromandelic acid	Li et al. [15]

S21

2a Mandelic acid

Solvent: DMSO-d$_6$

^{1}H
400 MHz

12.0 11.0 10.0 9.0 8.0 7.0 6.0 5.0 4.0 3.0 2.0 1.0 0 -1.0 -2.0

7.388
7.370
7.321
7.303
7.285
7.261
7.243
7.186

4.991

X : parts per Million : Proton

^{13}C
100 MHz

220.0 210.0 200.0 190.0 180.0 170.0 160.0 150.0 140.0 130.0 120.0 110.0 100.0 90.0 80.0 70.0 60.0 50.0 40.0 30.0 20.0 10.0 0 -10.0 -20.0

174.633

140.702

128.667
128.199
127.160

72.907

X : parts per Million : Carbon13
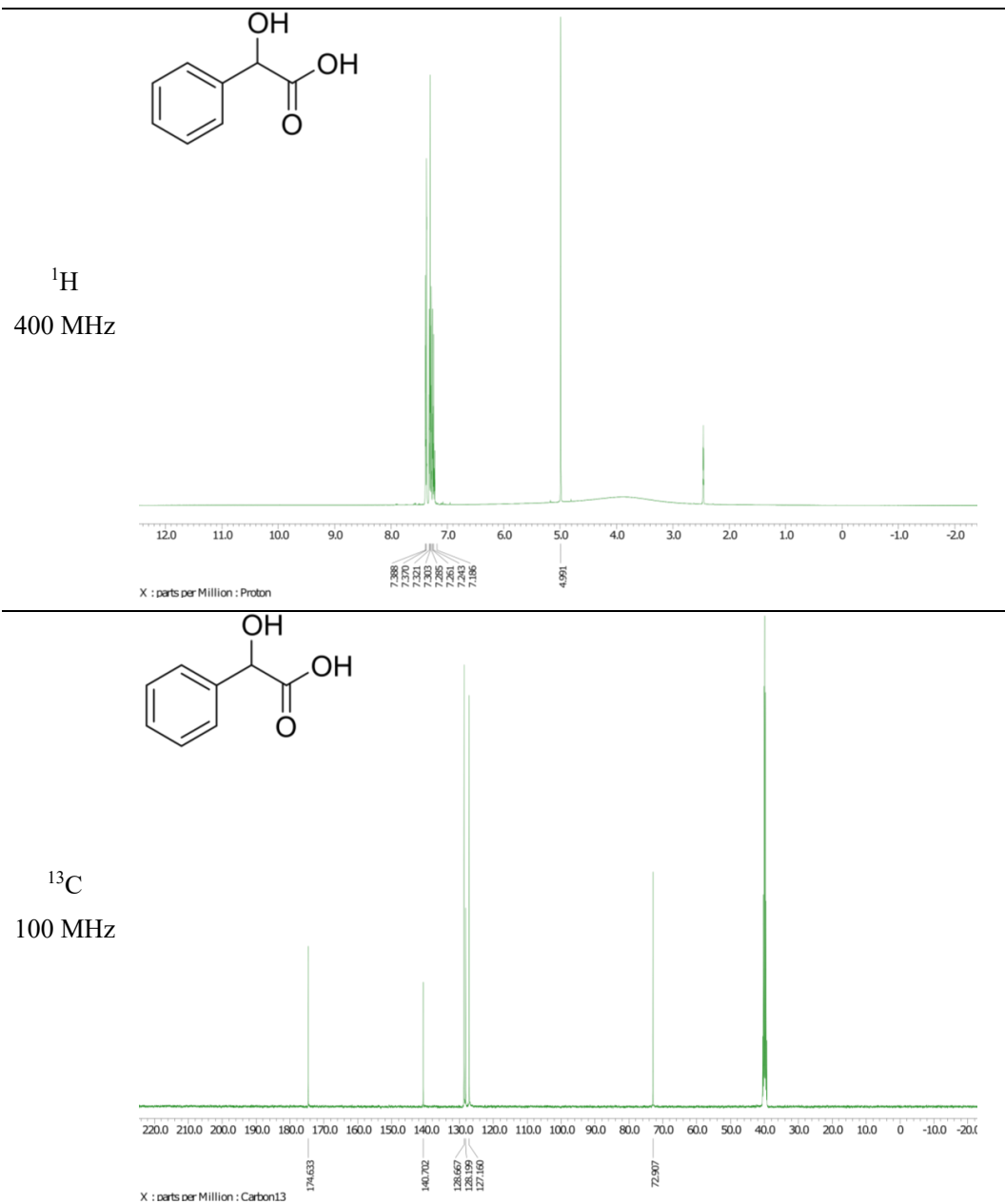
Figure S18. ^{1}H and ^{13}C NMR spectra for Mandelic acid.

S22

100

2b 4-Methoxymandelic acid

Solvent: DMSO-d$_6$

^{1}H
400 MHz

7.287
7.265
6.865
6.843

4.911

3.690

X : parts per Million : Proton

^{13}C
100 MHz

174.871
159.327
132.786
128.419
114.057
72.411
55.598

X : parts per Million : Carbon13
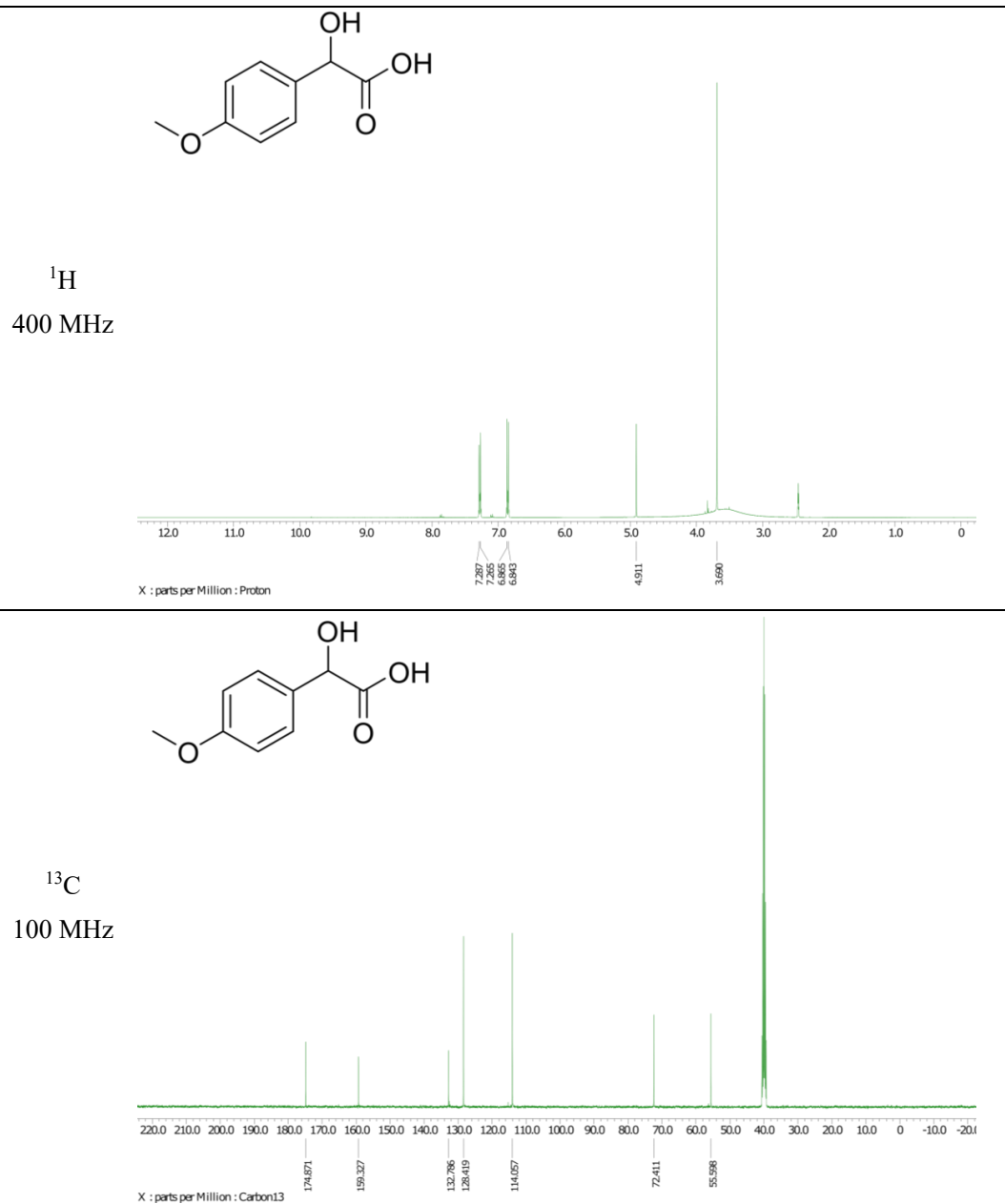
Figure S19. ^{1}H and ^{13}C NMR spectra for 4-Methoxymandelic acid.

S23

2c 2-Hydroxy-3-phenylbutanoic acid

Solvent: DMSO-d_6

^{1}H
400 MHz

X : parts per Million : Proton

7.232
7.220
7.206
7.195
4.042
4.027
3.996
3.985
3.071
3.058
3.052
3.040
3.028
3.025
3.010
1.201
1.184
1.160
1.142

^{13}C
100 MHz

X : parts per Million : Carbon13

175.300
144.259
143.391
128.733
128.524
128.352
126.731
75.119
43.006
42.905
18.873
15.898
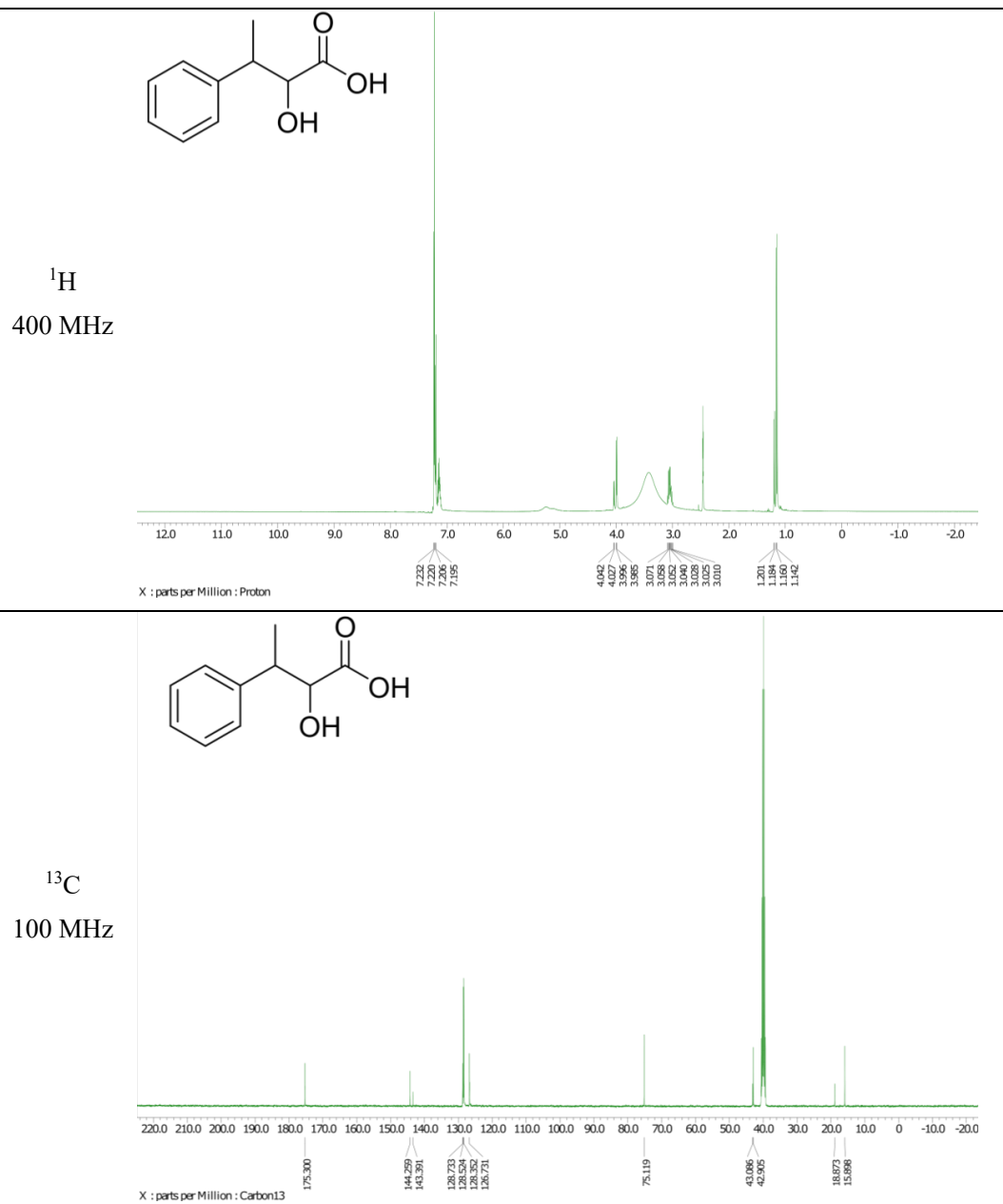
Figure S20. ^{1}H and ^{13}C NMR spectra for 2-Hydroxy-3-phenylbutanoic acid.

2d 2-Hydroxy-4-phenylbutanoic acid

Solvent: DMSO-d$_6$

^{1}H
400 MHz

7.234 7.216 7.156 7.138
3.886 3.876 3.866 3.855
2.631 2.611 2.591
1.889 1.877 1.865 1.845 1.771 1.753 1.739 1.719

X : parts per Million : Proton

^{13}C
100 MHz

176.282
142.065
128.857 126.321
69.474
36.325 31.404

X : parts per Million : Carbon13
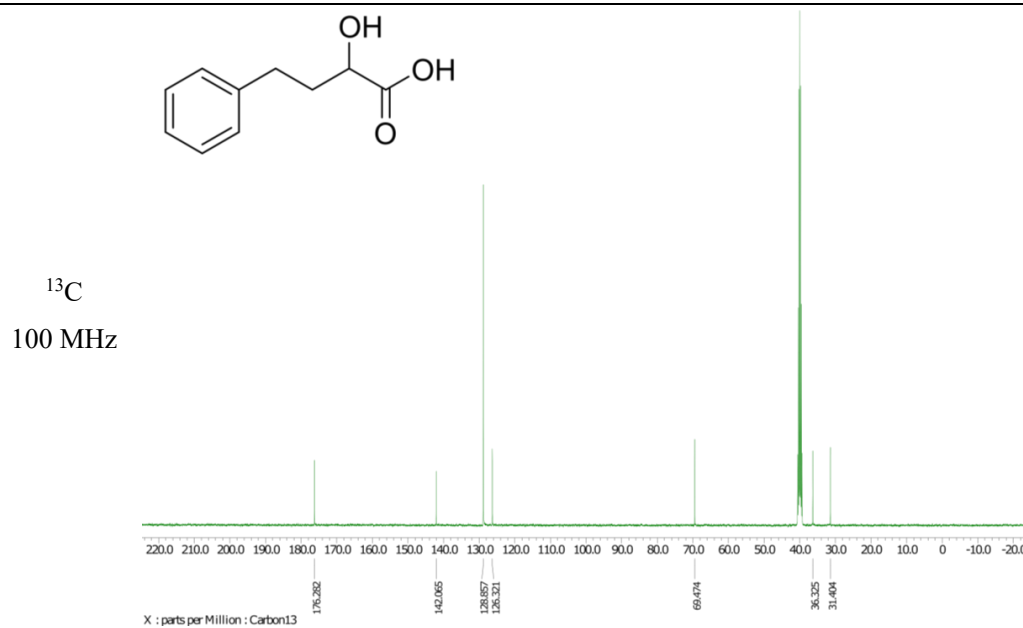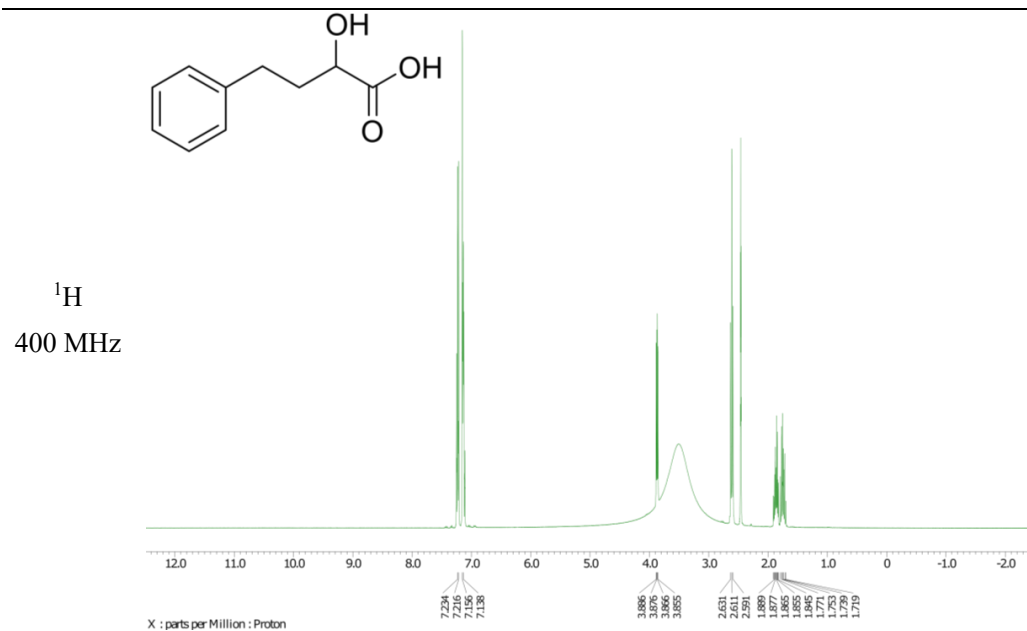
Figure S21. ^{1}H and ^{13}C NMR spectra for 2-Hydroxy-4-phenylbutanoic acid.

2e 2-Hydroxy-2-phenylpropanoic acid

Solvent: MeCN-d$_3$
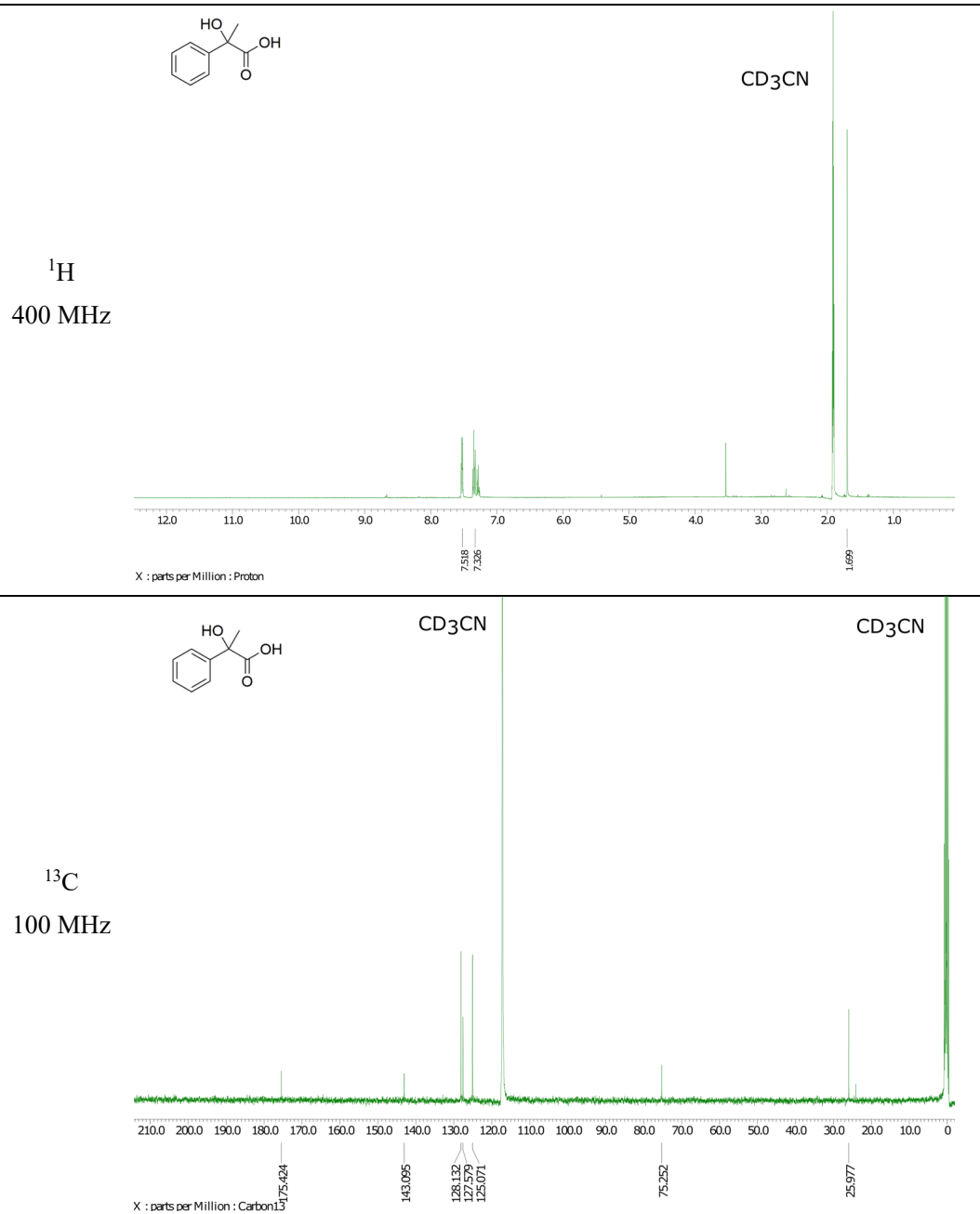
Figure S22. ^{1}H and ^{13}C NMR spectra for 2-Hydroxy-2-phenylpropanoic acid.

S26

2f 2-Hydroxy-2-(4-methoxyphenyl)propanoic acid

Solvent: DMSO-d$_6$

^{1}H

400 MHz

7.385
7.364
6.851
6.830

3.690

1.547

X : parts per Million : Proton

^{13}C

100 MHz

176.836

136.925
126.950
113.704

74.957

55.569

27.799

X : parts per Million : Carbon13
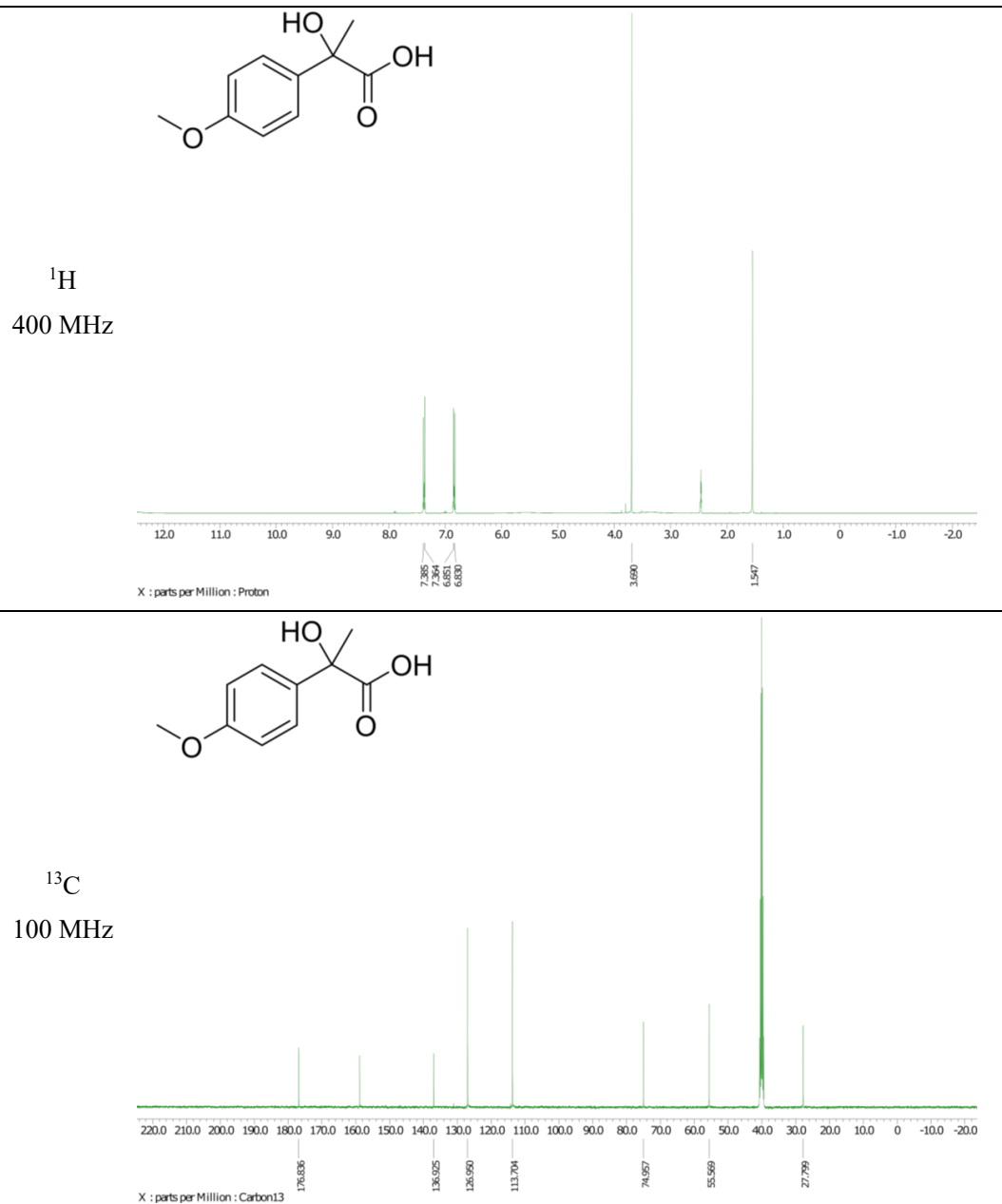
Figure S23. ^{1}H and ^{13}C NMR spectra for 2-Hydroxy-2-(4-methoxyphenyl)propanoic acid.

S27

2g 4-Hydroxy-3-methoxymandelic acid
Solvent: DMSO-d$_6$

^{1}H

400 MHz

X : parts per Million : Proton

6.916
6.766
6.740
6.689
6.669
4.848
3.703

^{13}C

100 MHz

X : parts per Million : Carbon13

174.928
147.787
146.653
131.642
119.865
115.544
111.310
72.735
56.084
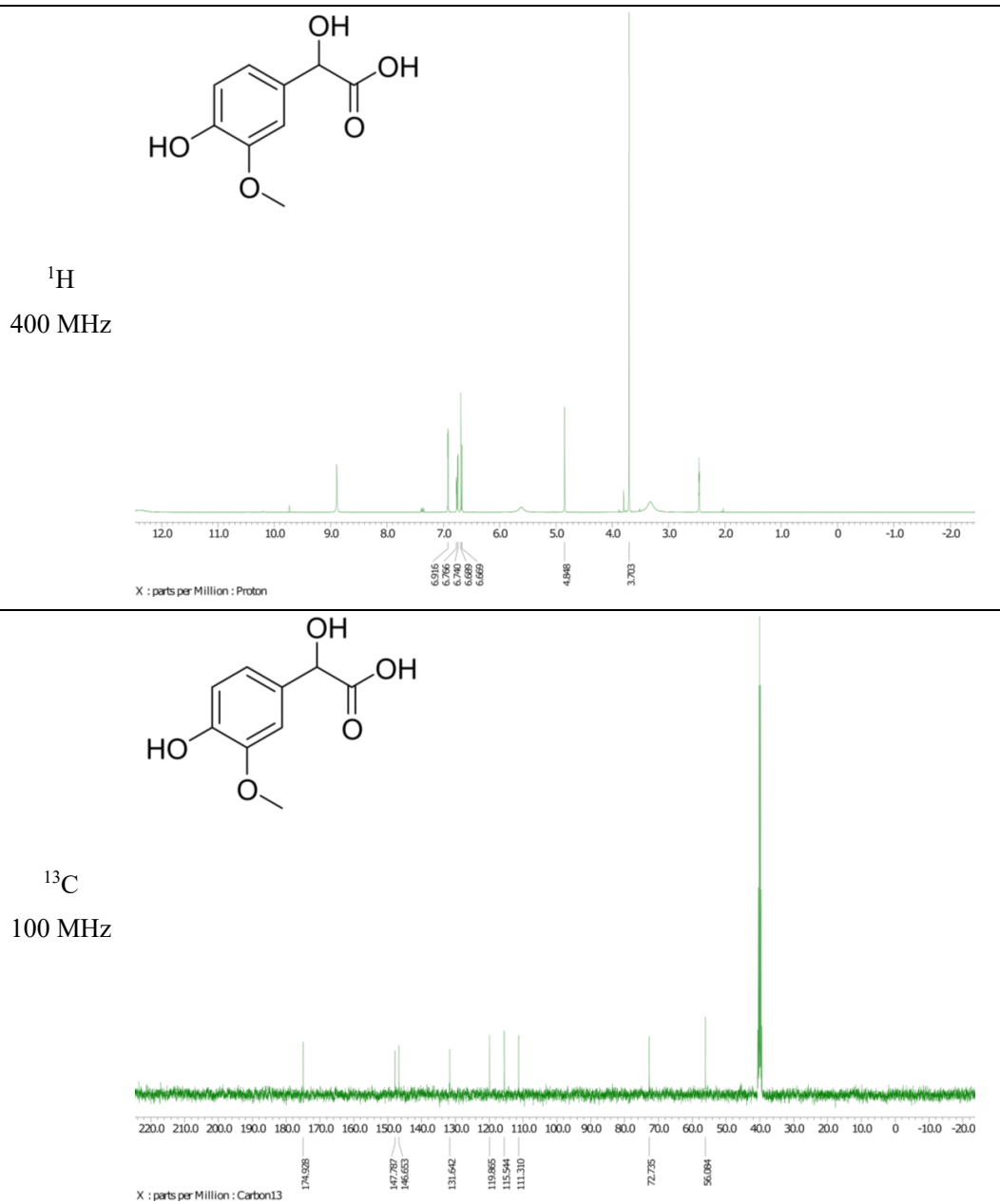
Figure S24. ^{1}H and ^{13}C NMR spectra for 4-Hydroxy-3-methoxymandelic acid.

2h 4-Isopropylmandelic acid

Solvent: MeCN-d₃

^{1}H
400 MHz

7.311
7.290
7.240
7.219

5.071

2.921
2.903
2.886
2.869
2.852

1.209
1.192

X : parts per Million : Proton

^{13}C
100 MHz

173.650

149.237

136.811

126.836
126.597

72.296

33.683

23.298

X : parts per Million : Carbon13
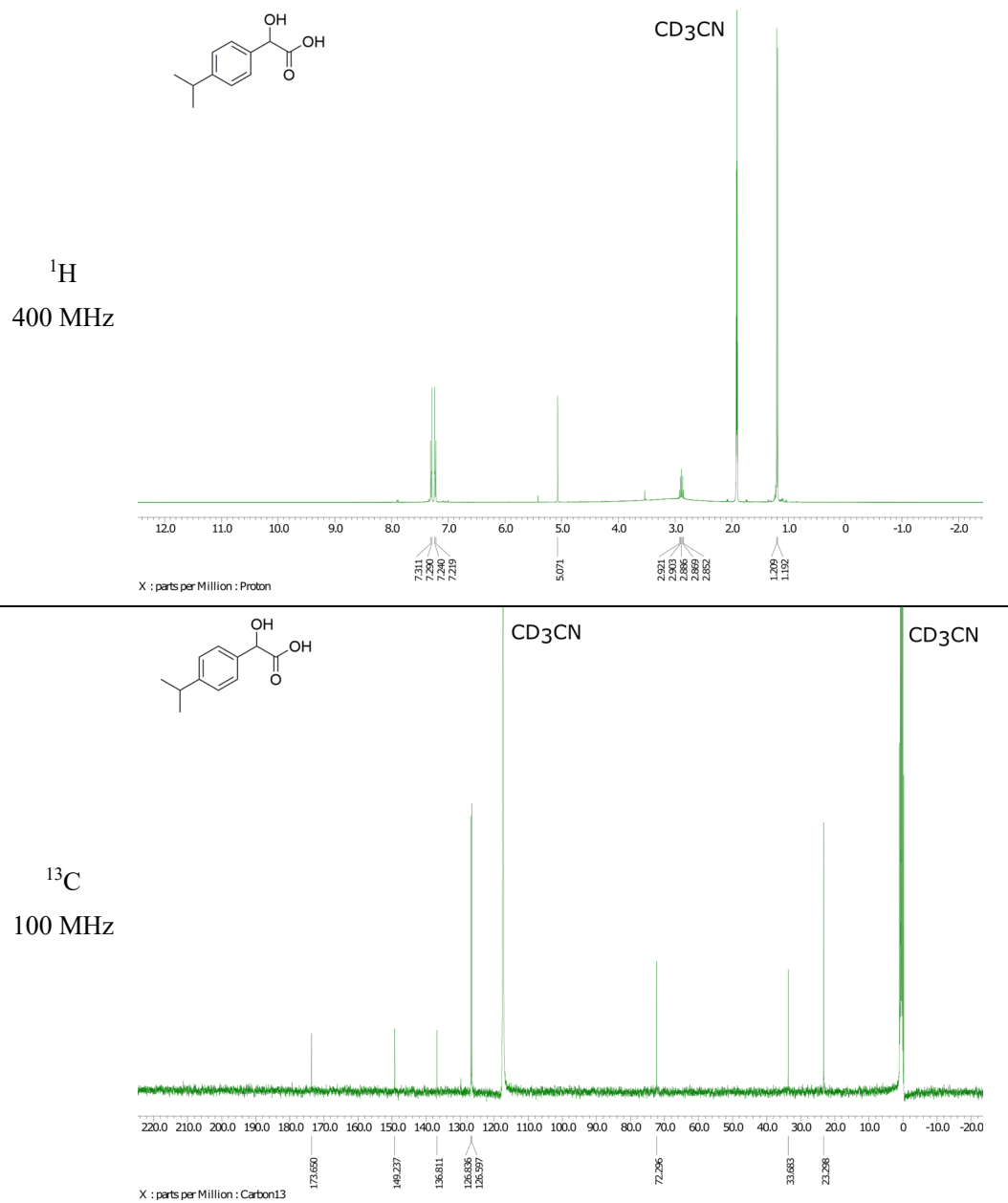
Figure S25. ^{1}H and ^{13}C NMR spectra for 4-Isopropylmandelic acid.

S29

2i 4-Chloromandelic acid

Solvent: DMSO-d$_6$

^{1}H
400 MHz

7.409
7.388
7.375
7.352

5.009

X : parts per Million : Proton

^{13}C
100 MHz

174.261

139.758
132.739
128.972
128.648

72.163

X : parts per Million : Carbon13
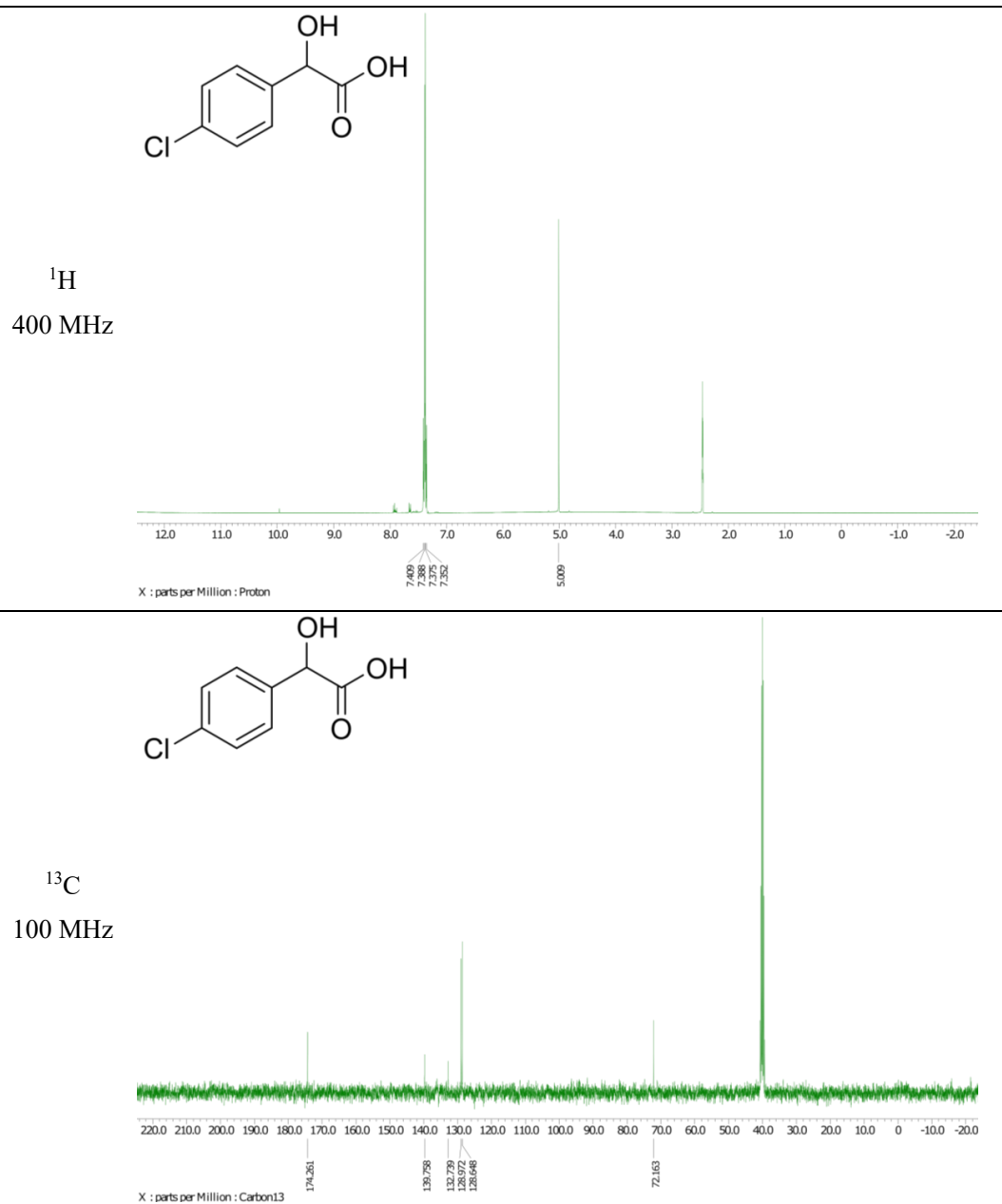
Figure S26. ^{1}H and ^{13}C NMR spectra for 4-Chloromandelic acid.

2j 4-(Trifluoromethyl)mandelic acid

Solvent: DMSO-d$_6$

^{1}H
400 MHz

7.687
7.666
7.617
7.595

5.124

X : parts per Million : Proton

^{13}C
100 MHz

173.956

145.298
128.934
128.619
127.875
126.120
125.586
125.548
123.412

72.354

X : parts per Million : Carbon13
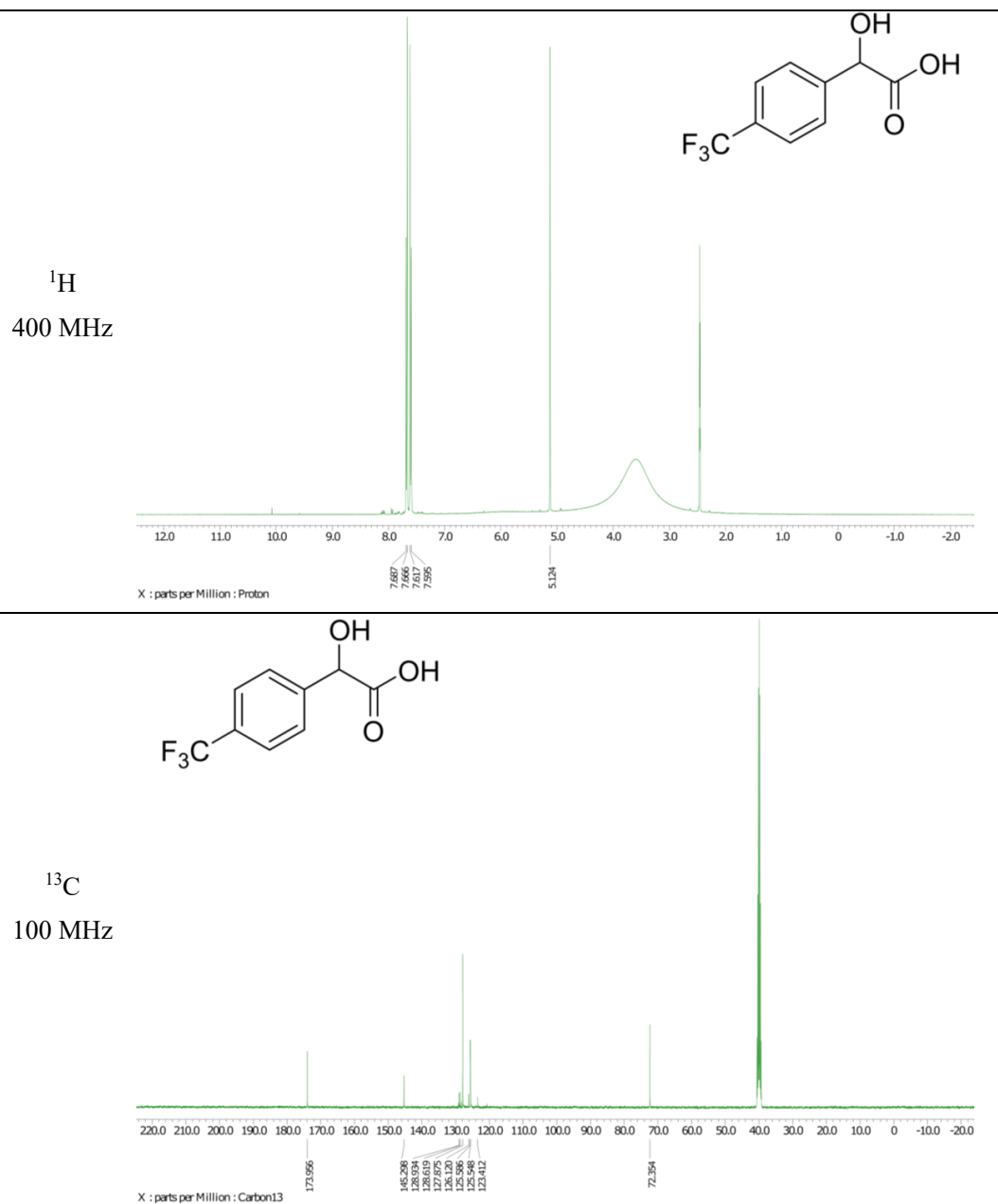
Figure S27. ^{1}H and ^{13}C NMR spectra for 4-(Trifluoromethyl)mandelic acid.

2k 3,5-Difluoromandelic acid

Solvent: DMSO-d$_6$

^{1}H

400 MHz

X : parts per Million : Proton

7.129
7.123
7.117
7.100
7.096
7.082
7.065

5.068

^{13}C

100 MHz

X : parts per Million : Carbon13

173.593

163.952
163.828
161.510
161.377

145.346
145.260
145.165

110.261
110.004
103.736
103.548
103.290

71.896
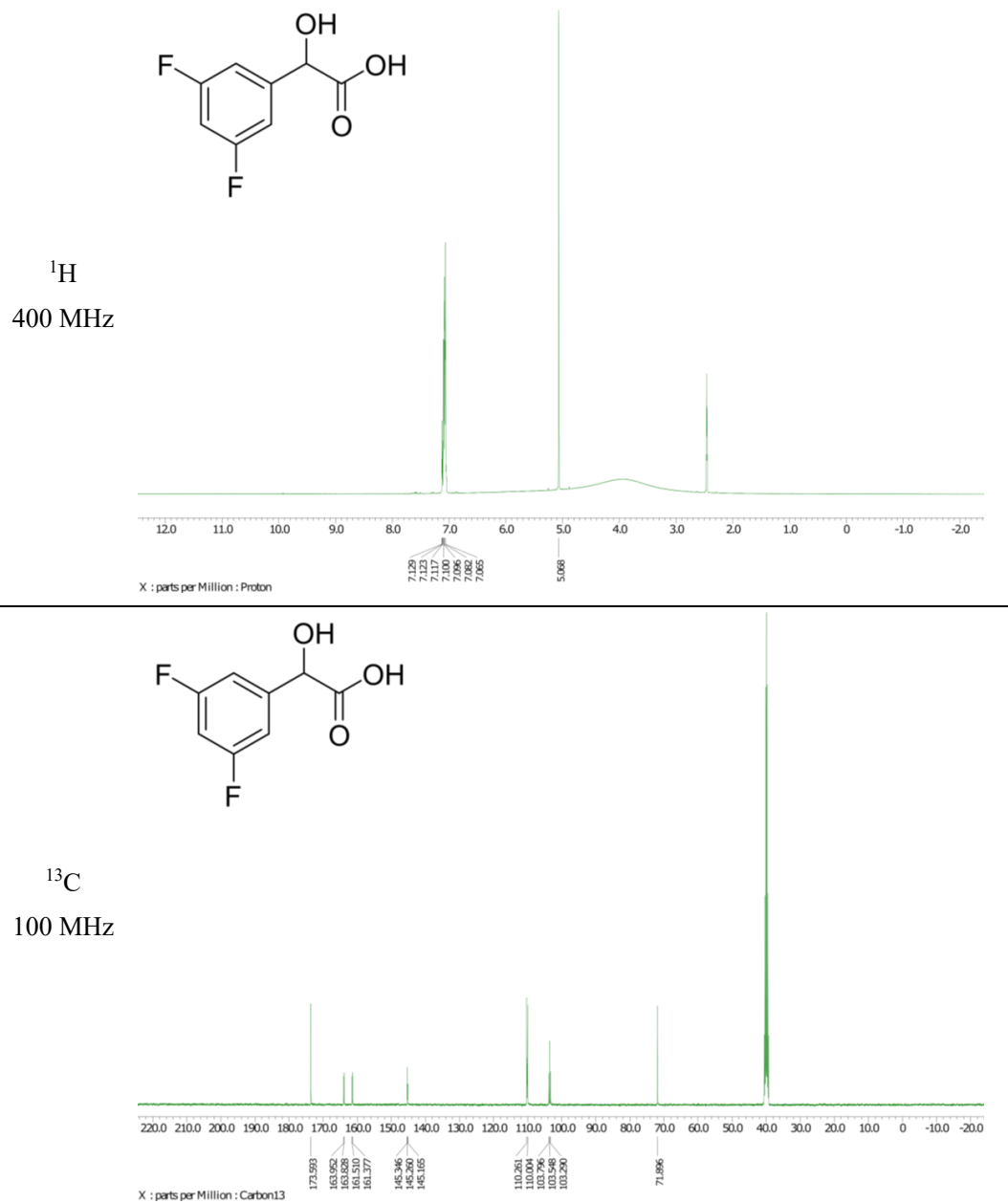
Figure S28. ^{1}H and ^{13}C NMR spectra for 3,5-Difluoromandelic acid.

S32

^{19}F spectra (376 MHz)
Solvent: DMSO-d$_6$

2j 4-(Trifluoromethyl)mandelic acid

trifluoroacetic acid

-62.381

-76.550
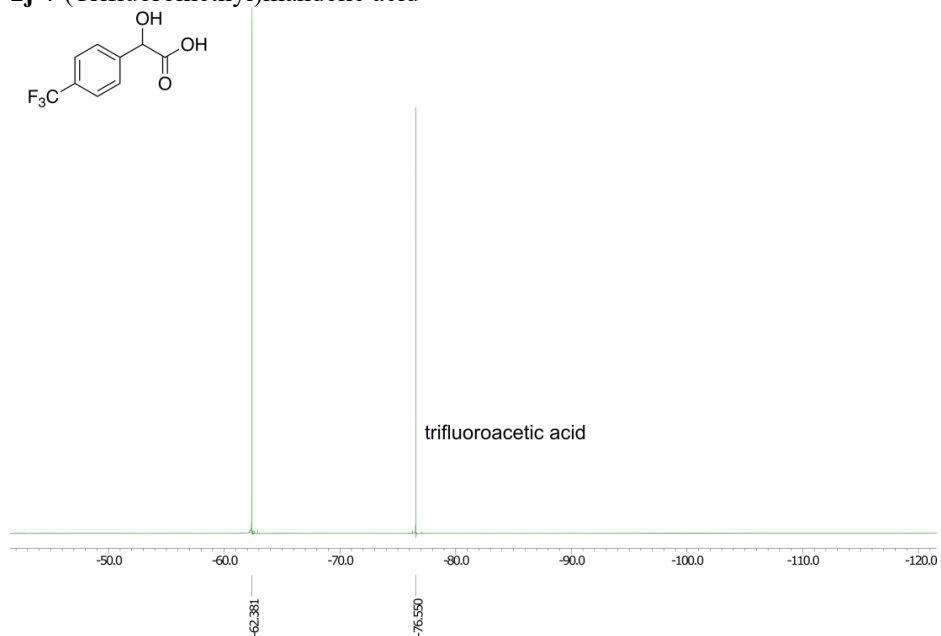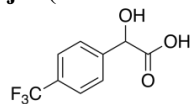
X : parts per Million : Fluorine19

2j 4-(Trifluoromethyl)mandelic acid

trifluoroacetic acid

-76.550

-111.366
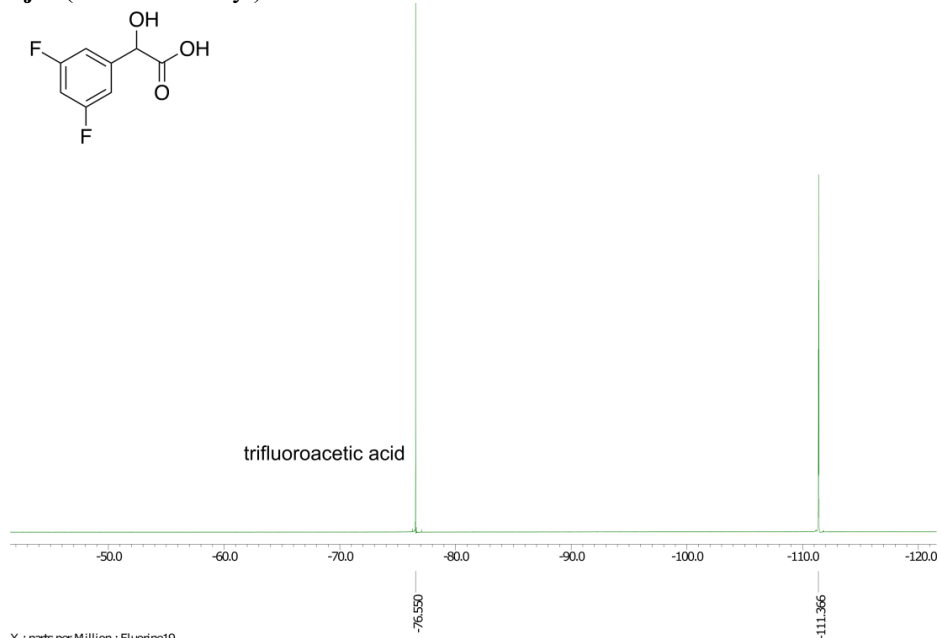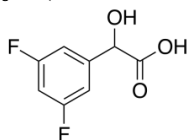
X : parts per Million : Fluorine19

Figure S29. ^{19}F NMR spectra for 4-(Trifluoromethyl)mandelic acid and 4-(Trifluoromethyl)mandelic acid.

S33

References

(1)   Gütz, C.; Klöckner, B.; Waldvogel, S. R. Electrochemical Screening for Electroorganic Synthesis. *Org. Process Res. Dev.* **2016**, *20* (1), 26–32, DOI 10.1021/acs.oprd.5b00377.

(2)   Smith, A. J.; Young, A.; Rohrbach, S.; O'Connor, E. F.; Allison, M.; Wang, H.-S.; Poole, D. L.; Tuttle, T.; Murphy, J. A. Electron-Transfer and Hydride-Transfer Pathways in the Stoltz-Grubbs Reducing System (KO t Bu/Et 3 SiH). *Angew. Chemie Int. Ed.* **2017**, *56* (44), 13747–13751, DOI 10.1002/anie.201707914.

(3)   Pitzer, L.; Sandfort, F.; Strieth-Kalthoff, F.; Glorius, F. Carbonyl–Olefin Cross-Metathesis Through a Visible-Light-Induced 1,3-Diol Formation and Fragmentation Sequence. *Angew. Chemie Int. Ed.* **2018**, *57* (49), 16219–16223, DOI 10.1002/anie.201810221.

(4)   Sperger, T.; Stirner, C.; Schoenebeck, F. Bench-Stable and Recoverable Palladium(I) Dimer as an Efficient Catalyst for Heck Cross-Coupling. *Synthesis (Stuttg).* **2016**, *49* (01), 115–120, DOI 10.1055/s-0036-1588318.

(5)   Castellanos-Blanco, N.; Arévalo, A.; García, J. J. Nickel-Catalyzed Transfer Hydrogenation of Ketones Using Ethanol as a Solvent and a Hydrogen Donor. *Dalt. Trans.* **2016**, *45* (34), 13604–13614, DOI 10.1039/C6DT02725C.

(6)   Gabriele, B.; Mancuso, R.; Salerno, G.; Veltri, L.; Costa, M.; Dibenedetto, A. A General and Expedient Synthesis of 5- and 6-Membered Cyclic Carbonates by Palladium-Catalyzed Oxidative Carbonylation of 1,2- and 1,3-Diols. *ChemSusChem* **2011**, *4* (12), 1778–1786, DOI 10.1002/cssc.201100250.

(7)   Anouti, M. M.; Dougassa, Y. R.; Tessier, C.; El Ouatani, L.; Jacquemin, J. Low Pressure Carbon Dioxide Solubility in Pure Electrolyte Solvents for Lithium-Ion Batteries as a Function of Temperature. Measurement and Prediction. *J. Chem. Thermodyn.* **2012**, *50*

S34

(2012), 71–79, DOI 10.1016/j.jct.2012.01.027.

(8)   Baker, S. I.; Yaghoubi, M.; Bidwell, S. L.; Pierce, S. L.; Hratchian, H. P.; Baxter, R. D. Enhanced Reactivity for Aromatic Bromination via Halogen Bonding with Lactic Acid Derivatives. *J. Org. Chem.* **2022**, *87* (13), 8492–8502, DOI 10.1021/acs.joc.2c00611.

(9)   Poterała, M.; Dranka, M.; Borowiecki, P. Chemoenzymatic Preparation of Enantiomerically Enriched (R)-(−)-Mandelic Acid Derivatives: Application in the Synthesis of the Active Agent Pemoline. *European J. Org. Chem.* **2017**, *2017* (16), 2290–2304, DOI 10.1002/ejoc.201700161.

(10)   Furukawa, K.; Shibuya, M.; Yamamoto, Y. Chemoselective Catalytic Oxidation of 1,2-Diols to α-Hydroxy Acids Controlled by TEMPO–ClO 2 Charge-Transfer Complex. *Org. Lett.* **2015**, *17* (9), 2282–2285, DOI 10.1021/acs.orglett.5b01003.

(11)   Qu, S.; Smith, S. M.; Laina-Martín, V.; Neyyappadath, R. M.; Greenhalgh, M. D.; Smith, A. D. Isothiourea-Catalyzed Acylative Kinetic Resolution of Tertiary A-Hydroxy Esters. *Angew. Chemie Int. Ed.* **2020**, *59* (38), 16572–16578, DOI 10.1002/anie.202004354.

(12)   Cardinal, S.; Azelmat, J.; Grenier, D.; Voyer, N. Anti-Inflammatory Properties of Quebecol and Its Derivatives. *Bioorg. Med. Chem. Lett.* **2016**, *26* (2), 440–444, DOI 10.1016/j.bmcl.2015.11.096.

(13)   González-Álvarez, A.; Alfonso, I.; Gotor, V. An Azamacrocyclic Receptor as Efficient Polytopic Chiral Solvating Agent for Carboxylic Acids. *Tetrahedron Lett.* **2006**, *47* (36), 6397–6400, DOI 10.1016/j.tetlet.2006.06.154.

(14)   Okumura, S.; Uozumi, Y. Photocatalytic Carbinol Cation/Anion Umpolung: Direct Addition of Aromatic Aldehydes and Ketones to Carbon Dioxide. *Org. Lett.* **2021**, *23* (18), 7194–7198, DOI 10.1021/acs.orglett.1c02592.

(15) Li, G.-W.; Wang, X.-J.; Cui, D.-D.; Zhang, Y.-F.; Xu, R.-Y.; Shi, S.-H.; Liu, L.-T.; Wang,
M.-C.; Liu, H.-M.; Lei, X.-X. Azaheterocyclic Diphenylmethanol Chiral Solvating Agents
for the NMR Chiral Discrimination of Alpha-Substituted Carboxylic Acids. *RSC Adv.* **2020**,
10 (57), 34605–34611, DOI 10.1039/D0RA06312F.

3.3 Skalierbare und industriell relevante Elektro-Reduktionen

3.3.1 Optimierung der elektrochemischen Reduktion von L-Cystin

Zu diesem Kapitel wurde ein Manuskript veröffentlicht:

Erklärung meines Beitrags:

Personenbezogene Daten

Hintergrund Die Produktion von L-Cystein aus L-Cystin ist von großer industrieller Bedeutung. Anwendungsfelder von L-Cystein finden sich in der Lebensmittelindustrie (z.B. als Zusatzstoff in Backwaren um deren Elastizität zu verbessern), in Arzneimitteln (z.B. als S-Carboxymethyl-L-cystein oder N-Acetylcystein), in Kosmetika und Futtermitteln.[120] Des Weiteren ist L-Cystein eine wichtige Verbindung für die (Bio-)Synthese von Methionin oder Proteinen. Im technischen Maßstab wird L-Cystein aus keratinhaltigen tierischen Quellen, wie Haaren oder Federn gewonnen. Das L-Cystein wird dabei meist über chemische oder enzymatische Hydrolyse gewonnen.[121] Alternativ können pflanzenbasierte Materialien fermentativ umgesetzt werden um auf tierische Rohstoffe zu verzichten.[122,123] Eine zentrale Herausforderung bei der Konversion von Disulfiden zu den entsprechenden Thiolen ist die aufwändige Produktisolation. Häufig genutzte Reduktionsmittel sind Mercapto-Spezies, welche vollständig abgetrennt werden müssen. Während der Aufreinigung kann es leicht zur Re-oxidation des gewünschten Thiols kommen.[124] Alternativ können Disulfide elektrochemisch reduziert werden, wobei keine zusätzlichen Reduktionsmittel benötigt werden (Schema 5).
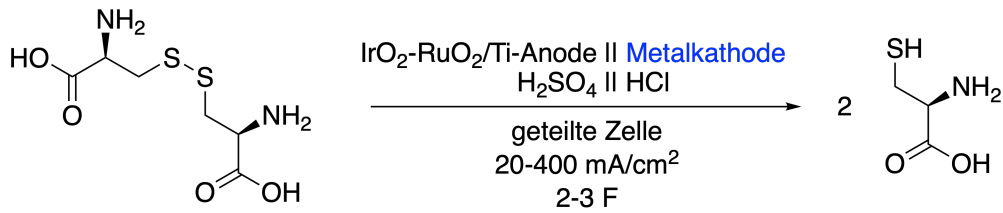
Schema 5: Elektroreduktion von L-Cystin zu L-Cystein. Edukt und Produkt liegen im sauren Elektrolyten als Ammoniumspezies vor.

Mithilfe von statistischen Methoden kann die Optimierung elektrochemischer Methoden besonders effizient umgesetzt werden.

Ergebnisse   Betrachtet wurde die Reaktion von L-Cystin zu L-Cystein (Schema 5). Zunächst wurden zahlreiche Kathodenmaterialien in geteilten Topfzellen (Elektrodenfläche $= 1\,\mathrm{cm}^2$) getestet. Die höchste Ausbeute (über $90\,\%$) wurde dabei mit Zink-, Zinn- und Bleielektroden erreicht. Selbst hohe Stromdichten von bis zu $400\,\mathrm{mA\,cm}^{-2}$ wurden bei Verwendung der Zn-, Sn-, oder Pb-Kathoden toleriert. Besonders die Zinkkathoden schienen völlig unabhängig von der angelegten Stromdichte zu arbeiten. Die getesteten Bleibronzekathoden besitzen zwar im Vergleich zum weichen Blei eine bessere chemische und mechanische Stabilität,[20] schnitten allerdings deutlich schlechter ab als die Bleikathoden. Sowohl bei der Zink- als auch bei der Zinnkathode kam es während der Elektrolyse zu einer deutlichen Korrosion und Materialabtrag. Bei Verwendung der Zinkelektrode konnten Feststoffpartikel im Elektrolyten beobachtet werden, welche sich unter Gasbildung auflösten. Das abgelöste Zink sorgte für eine zusätzliche Aktivität, da es parallel zur Elektroreduktion weitere Disulfide spaltet.[124] Wegen der starken Desintegration der Zink- und Zinnelektroden und der hohen Kontamination des Elektrolyten mit Metallspezies, wurde die Bleikathode für die weiteren Untersuchungen gewählt.

Im nächsten Schritt wurde die Reaktion auf ein Setup mit Flusszelle (Elektrodenfläche $=$ $10.5\,\mathrm{cm}^2$) transferiert und der Effekt der Elektrolyseparameter untersucht. Hierfür wurde ein zweistufiger teilfaktorieller Versuchsplan mit 2^{n-1} Versuchen verwendet wobei n die Anzahl der Experimente darstellt. Im Einzelnen wurden folgende Parameter variiert: *(i)* Stromdichte, *(ii)* applizierte Ladung, *(iii)* Elektrolyttemperatur, *(iv)* Eduktkonzentration und *(v)* Abstand zwischen Kathode und Membran. Im initialen Versuchsplan wurde der Elektrolyt nur einmal durch die Zelle gepumpt (single-pass mode) und die gesamte Ladungsmenge während eines Zelldurchgangs übertragen. Die Ergebnisse des Teilfaktorplans wurden verwendet um ein lineares Beschreibungsmodell zu bedienen. Dabei wurden zunächst alle Wechselwirkungen der Parameter mit aufgenommen:

$$Y = \beta_0 + \sum_{i=1}^{n_f} \beta_i x_i + \sum_{i=1}^{n_f-1} \sum_{j=i+1}^{n_f} \beta_{ij} x_i x_j + \epsilon$$

Dabei ist Y die Systemantwort (Produktausbeute), β_n die Modellkonstanten, x_n die Eingangsgrößen und ϵ der Fehlerterm der Regression. Als statistisch signifikante Parameter haben sich

dabei die applizierte Ladungsmenge, die Stromdichte und Kathodenraumquerschnitt herausgestellt. Des Weiteren wurde eine signifikante Wechselwirkung zwischen ʟ-Cystinkonzentration und Kathodenraumquerschnitt gefunden. Der berechneten Wechselwirkung zufolge steigt die Ausbeute mit höherer Eduktkonzentration in Kombination mit einem geringen Kathodenraumquerschnitt. Auffällig bei der Übertragung der Reaktion aus der Topfzelle in die Flusszelle war die deutlich verringerte Ausbeute (ca. 75 % statt 94 %). Die Reaktion wurde daraufhin mit im Kreis laufendem Katholyten durchgeführt, anstatt die gesamte Ladungsmenge während eines Zelldurchgangs zu applizieren. Dies führte zu einer deutlichen Steigerung der Ausbeute auf über 92 %. Die Erklärung der höheren Ausbeute im *batch-recycle mode* ist der bessere Massentransport aufgrund stärkerer Durchmischung des Elektrolyten.

Da die Reaktion vom Ladungstransfer angetrieben wird, steigt die Ausbeute mit steigender applizierter Ladungsmenge. Allerdings sinkt gleichzeitig die Effizienz des Ladungstransfers (Faraday-Effizienz), da aufgrund der geringen Eduktkonzentration vermehrt Wasserstoff an der Kathode gebildet wird. Als Konsequenz existiert eine optimale Ladungsmenge, für die die Ausbeute zwar hoch ist, aber die Faraday-Effizienz noch nicht unter ein toleriertes Minimum sinkt. Zur Berechnung und Visualisierung wurden die Produktausbeute (Y) und die Faraday-Effizienz (FE) in einer sogenannten *Wunschfunktion* kombiniert und Grenzen für die jeweilige Systemantwort definiert (Abbildung 3.14).
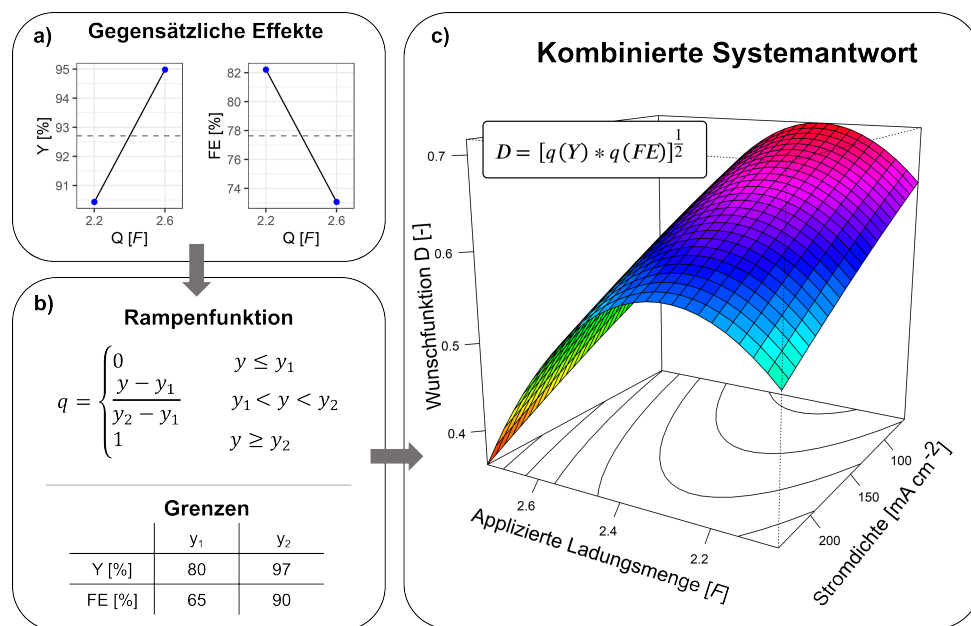
Abbildung 3.14: *Multiple-response optimization* für die Systemantworten Produktausbeute (Y) und Faraday-Effizienz (FE). Die resultierende Wunschfunktion (D) kombiniert beide Systemantworten in einer Gleichung und kann mithilfe eines Oberflächendiagramms visualisiert werden.

Das Oberflächendiagramm illustriert, dass die Wunschfunktion zunächst mit steigender Ladungsmenge zunimmt. Dies ist der Effekt der steigenden Produktausbeute. Nach einer kritischen Ladungsmenge von ca. 2.3 F nimmt die Wunschfunktion aufgrund der sinkenden Faraday-

Effizienz ab. Im Zuge der Optimierung wurde mit einer hohen Stromdichte von $100\,\mathrm{mA\,cm^{-2}}$ eine Ladungsmenge von $2.3\,F$ appliziert um einen zügigen Reaktionsfortschritt zu erzielen. Im Anschluss wurde die Stromdichte auf $10\,\mathrm{mA\,cm^{-2}}$ reduziert, um die Wasserstoffproduktion auf einem geringen Niveau zu halten. Auf diese Weise konnte eine L-Cysteinausbeute von über $99\,\%$ bei einer Ladungsmenge von $2.65\,F$ erreicht werden. Im finalen Schritt wurden die optimierten Bedingungen auf eine $100\,\mathrm{cm^2}$ Flusszelle übertragen. Dabei konnten die Ergebnisse der kleineren Flusszelle reproduziert und die exzellente Skalierbarkeit aufgezeigt werden.

From Screening to Scale-Up: The DoE-Based Optimization of Electrochemical Reduction of L-Cystine at Metal Cathodes

Johannes Seidler, Rebecca Bernhard, Stefan Haufe,* Caroline Neff, Tobias Gärtner,* and Siegfried R. Waldvogel*

ACCESS | 📊 Metrics & More | 📖 Article Recommendations | 🔵 Supporting Information

ABSTRACT: Design of experiment (DoE) is a powerful statistical tool in establishing improved chemical processes. An optimization and scale-up of the electrochemical reduction of L-cystine to L-cysteine is presented. Subsequent to an electrode screening of 17 metals and alloys in divided batch-type cells, the lead electrode was selected for a systematic optimization in flow cells with a geometric cathodic surface area ranging from 10 to 100 cm². Using two consecutive factorial designs, parameters like substrate concentration, current density, electrode gap, amount of applied charge, and number of cell passages were screened for significant effects onto the L-cystine conversion. A multiresponse optimization combining the product conversion and Faradaic efficiency was performed to account for economic considerations.

KEYWORDS: reduction, disulfides, cathodes, cysteine, design of experiment

■ INTRODUCTION

As the ecological footprint of chemical processes and aspects of green chemistry become more important,[1,2] electrifying organic synthesis has experienced a renaissance.[3,4] This method is recognized as a future key technology for value-added products[5,6] and can pay off.[7] The direct use of electricity to drive a chemical reaction reduces reagent waste, is inherently safe, and enables reactions under mild conditions.[8−13] Additionally, electroorganic synthesis is a superior technique, compared to the use of stoichiometric amounts of reducing agents or oxidizers. This electrosynthetic approach can also lead to a shortcut of several steps.[14−17] In recent years, electroorganic conversions have attracted steadily growing attention. However, only few electrochemically driven organic reactions are performed on an industrial scale.[18] Translating an electroorganic conversion from lab scale to technical relevance can be challenging, as numerous factors and parameter interactions are involved in these electrochemical reactions.

In the development and implementation of industrial processes, design of experiment (DoE) is a powerful statistical tool, which ideally provides deep insight into the desired chemical reaction with a minimum number of experiments. In particular, electrochemical conversions are associated with a large number of parameters such as electrode material (e.g., composition, surface morphology, and topography), electrolyte, temperature, current density, amount of applied charge, and interelectrode, gap which are often well documented[19] and might be dependent on each other.[20] Due to the complexity of such a system, the *one variable at a time* (OVAT) approach has a rather low efficiency.[21,22] The application of DoE onto the electrochemical optimization of lab-scale processes enabled tremendous advances in establishing suitable conditions.[21−25]

The production of L-cysteine is of large technical significance. L-Cysteine is a nonessential, sulfur-containing amino acid, with applications in the food industry (bread improver), in pharmaceuticals (*S*-carboxymethyl-L-cysteine or *N*-acetylcysteine), in cosmetics, or in animal feed.[26] L-Cysteine also has a key function in the synthesis of proteins, lipoic acid, and methionine, as well as a precursor for coenzyme A or taurine. The commercial production of L-cysteine is mainly based on chemical or enzymatic hydrolysis of animal materials like hair or feathers. The thiols generated provide issues with oxidative stability, and moreover, the purification of the complex reaction mixtures remains a challenge.[27] Alternatively, there is a trend using plant-based materials for vegan products. Since the late 1990s, synthetic routes for L-cystine/L-cysteine production with a bacterial-based fermentative process are known. The fermentative production of amino acids like L-cystine/L-cysteine with microorganisms has been described in detail in various patents. In particular, Wacker Chemie AG is active in this field of research and holds several patents on the fermentative production of said amino acids and derivatives with microorganisms.[28−31]

Non-natural L-cysteine is mainly produced electrochemically from the dimer L-cystine (which is, e.g., produced via fermentation) by reductive cleavage of the disulfide bond. The electrochemical reduction of L-cystine to L-cysteine and the potential scale-up of the reaction has been the subject of various studies.[32−35] In the review of Walsh and co-workers, numerous results, including the usage of different cathodes and current density, are summarized.[32] It was pointed out that the

A

Scheme 1. Electroreduction of L-Cystine to L-Cysteine at Metal Cathodes[a]
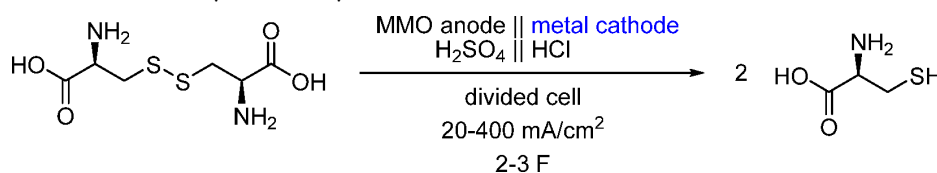
[a]O$_2$ evolution takes place at the MMO (mixed metal oxide: IrO$_2$−RuO$_2$/Ti) anode.
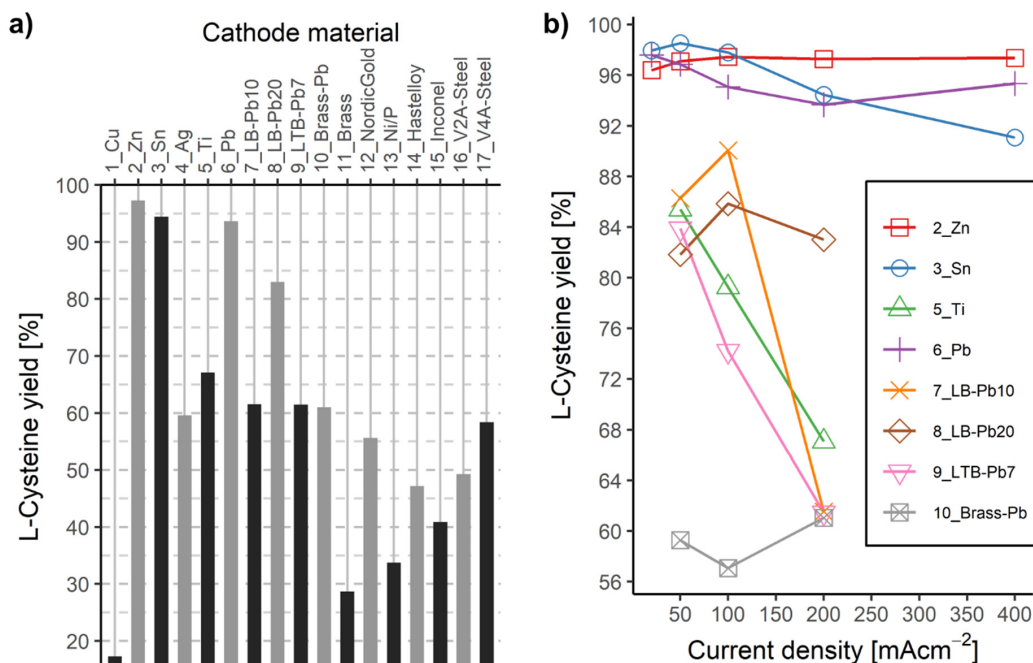
Figure 1. Product yield for (a) different cathode materials at 200 mA/cm^2 and (b) different current densities. Amount of charge: 2 F. LB = leaded bronze, LTB = leaded tin bronze. For detailed specifications of the materials, see the Supporting Information.

efficiency of the conversion largely depends on the nature of the cathode material and that high current densities promote the parasitic hydrogen evolution reaction. The resulting trade-off between a high area−time yield and a high current efficiency was recognized. Extensive work on the reduction of L-cystine was done by Walsh and co-workers between 1994 and 2005.[32,33,35] Fritz-Langhals found an electrochemically deposited lead cathode for the reduction of L-cystine to L-cysteine exhibiting a high overpotential for hydrogen evolution and better figures of merit compared to planar electrodes in 2000.[36] However, a procedure for a strategic optimization of this electroreduction has been missing.

Here, we illustrate how the electrochemical reduction of L-cystine to L-cysteine can be optimized at metal cathodes, using DoE as an efficient statistical tool for the screening of parameters and subsequent reaction optimization. Furthermore, we propose a method for the optimization of both product yield and Faradaic efficiency in a multiresponse approach to tackle the compromise between area−time yield and efficiency of the conversion.

■ EXPERIMENTAL SECTION

Detailed descriptions of the experiments as well as applied methods and calculations can be found in the Supporting Information.

■ RESULTS AND DISCUSSION

The electroreduction of L-cystine to L-cysteine was performed in divided cells in constant current mode using Nafion membranes as a separator (Scheme 1). It is noteworthy that the substrate and product will be protonated and will be in the electrolyte as corresponding ammonium species.

The cathode material screening was conducted in batch-cells.[37] The screening of electrolysis parameters as well as the scale-up were performed in flow cells.[38]

Screening of Cathode Materials in Batch-Type Cells. Seventeen metals and metal alloys were tested for their suitability for the reduction of L-cystine. The electroconversion was performed in divided batch-type cells with a 5 mL catholyte volume. Among the tested materials, cathodes of zinc, tin, and lead showed the highest yield for the desired product, whereas more than 90% yield was achieved for all tested current densities using the three cathode materials (Figure 1). Using lead-containing alloys (leaded bronze, leaded

tin bronze, and brass with lead content), product yields of 60−90% were achieved. Leaded bronzes represent a mechanically and chemically more resistant alternative to soft lead electrodes.[39] These alloys have been successfully used in other cathodic processes.[40−42] The tested leaded bronze materials with 10% and 7% Pb yield a similar amount of product. Increasing the Pb content to 20% leads to a significantly higher product yield, whereas less product is formed using brass with a low lead content (2% Pb). The high activity of Pb cathodes toward the reduction of disulfides has already been described for L-cysteine[32] as well as D,L-homocystine,[43] which is hereby confirmed. The lowest product yield was obtained using a copper cathode. Apparently, replacing Cu with Pb within the alloy has a stronger influence on the product yield than replacing Cu with another, well-performing metal (e.g., Zn). Brass (Cu63Zn37) exhibits a lower activity than LB-Pb10 (Cu80Sn10Pb10), although the copper content is much higher. Product yields for Nordic gold and different nickel-based alloys like Hastelloy or Inconel and different stainless-steel types are between only 35% and 60%.

As expected, the product yield decreases for most cathode materials when the current density is increased (Figure 1b). This is a result of the hydrogen evolution reaction (HER) becoming the dominant reaction at a high current density. This effect is favored by the acidic, aqueous electrolyte. Nevertheless, comparatively high current densities such as 400 mA/cm^2 could be applied using Zn, Sn, and Pb cathodes without an excessive drop of the yield in product. In most electroorganic conversions, current densities below 100 mA/cm^2, typically in the range 1−10 mA/cm^2, are applied.[3,6]

Interestingly, using the Zn electrode, the same product yield is obtained, regardless of the current density applied. Quantitative conversion using a Zn electrode was already described by Walsh and co-workers.[32] The Zn as well as the Sn cathodes suffered from serious corrosion during electrolysis. Whereas the Sn electrode only degraded during the reaction, the Zn electrode already decomposes under hydrogen evolution without current. No protective voltage could be found to avoid the electrode degradation of Zn. As a result of the corrosion, zinc particles could be observed in the catholyte, followed by a rapid dissolution of these solids. For homocysteine, the reduction via a classical chemical route using Zn is a known procedure.[43] We suggest that the electroreduction of L-cystine may be accompanied by the simultaneous reduction by the disintegrated Zn metal. In that case, it is plausible that the obtained product yield is largely independent of the applied current density when Zn is used as a cathode material.

As the corrosion of the Zn and Sn electrodes was too severe, the Pb cathode was chosen for the following investigations in flow cells.

Relevance of Continuous Electrolysis Parameters. As result of the screening of electrode materials, the lead cathode was chosen for a DoE-based parameter optimization. Besides lead, zinc as well as tin electrodes showed an outstanding performance in the reduction of L-cystine. However, the corrosion of both materials zinc and tin and the resulting electrolyte contamination were too high to be considered in subsequent experiments.

To enable the continuous production of L-cysteine, all of the following experiments were performed in divided flow cells, with a Nafion 424 membrane as a separator and with an adjustable electrode gap. In a two-level fractional factorial design (2^{5-1}) the parameters current density (j), amount of applied charge (Q), temperature (T), L-cystine concentration (c), and interelectrode gap within the cathodic compartment (d) were evaluated for statistical significance. In this configuration, the flow rate of the electrolyte represents a function of the amount of applied charge, current density, and concentration of L-cystine. Therefore, the flow rate could not serve as an independent variable. The product yield, which was easily determined from the specific optical rotation measurements of the reaction mixture, was taken as the response of the system.

Strikingly, the obtained product yield using the flow cell was on average much lower, compared to the batch-type cells which were used for the cathode screening (Figure 2a).
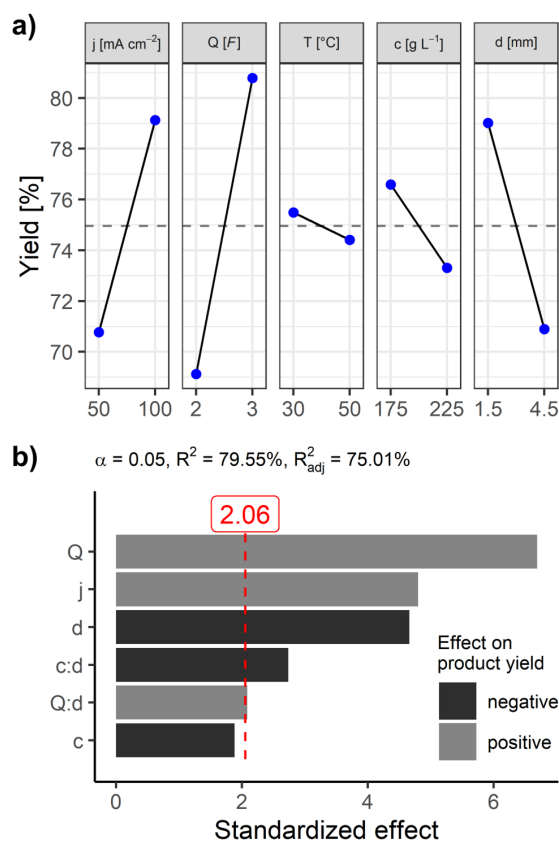
Figure 2. Main effect plots for the screened parameters (a) and the Pareto chart of the reduced model, showing the effects in descending order (b). The p-value for nonlinearity is 0.2 and therefore not significant. The temperature was removed from the model as it showed no significant effect and no involvement in significant parameter interactions. The red line indicates the significance level based on the alpha criterion. Q = amount of applied charge, j = current density, d = interelectrode gap, c = L-cystine concentration.

A plausible rationale is based on the operation mode of the cell: The flow cell was operated in single-pass mode; i.e., the entire amount of charge was applied during one passage of the electrolyte. Most likely, the flow regime did not provide sufficient agitation within the cell, since flow velocities were much lower in single-pass mode. Consequently, the impaired

C
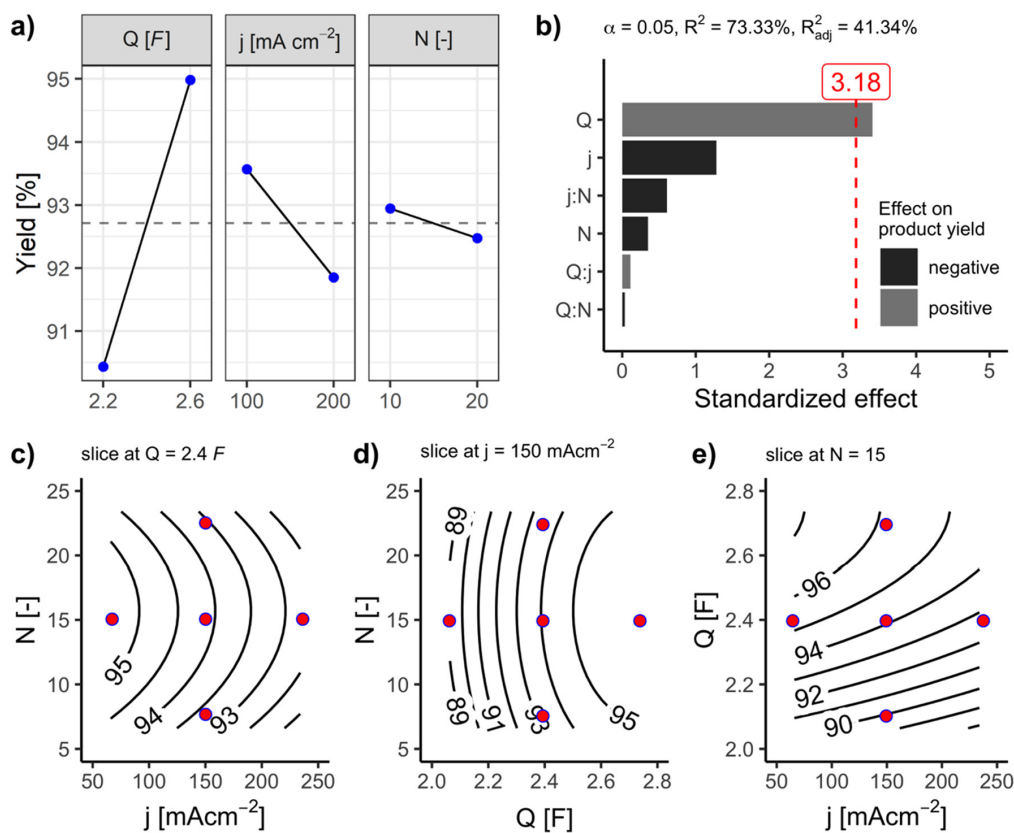
Figure 3. Main effect plot (a) and Pareto chart (b) for the second factorial design. The red line indicates the significance level based on the α criterion. (c–e) The contour plots visualize the effect of the parameters on the product yield. The colored points in the contour plots denote the star points and the center point of the central composite design. For a list of all experiments, see the Supporting Information. Q = amount of applied charge, j = current density, N = number of cell passages.

mass transport of L-cystine to the electrode surface limited the product yield.

Among the tested parameters, current density, amount of applied charge, and the electrode gap have significant effects on the product yield, whereas no significance was found for temperature and substrate concentration (Figure 2). Increasing the amount of applied charge from the theoretical minimum 2 F (where all of the applied charge would be used for the conversion of L-cystine) to 3 F leads to a drastic increase of produced L-cysteine. This is intuitive, as the reaction is driven by electric charge transfer. Furthermore, the longer residence time, which comes along with higher amounts of charge, leads to a higher chance of L-cystine molecules reaching the electrode surface. When a smaller electrode gap is used in the cathodic compartment, the product yield increases significantly, since the electrode surface to volume ratio is increased within the cell.

The L-cystine concentration as well as the electrolyte temperature showed no significant main effects. However, the concentration was involved in a significant interaction with the electrode gap. According to the interaction, the product yield increases for the following configuration: a high concentration of L-cystine and a small interelectrode gap. This is convenient since the main effect of the electrode gap suggests minimizing the distance. The interaction effect

encourages the use of the higher substrate concentration, which yields a higher throughput. Alternatively, a smaller substrate concentration together with a larger interelectrode gap would also be beneficial for the product yield. However, this configuration would interfere with the main effect of the electrode gap.

Interestingly, a higher current density increases the product yield within the tested range. This seems counterintuitive, as a stronger HER would be expected in an acidic aqueous electrolyte at these current densities. Also, this contradicts the results of the cathode screening in batch-type cells, where decreasing the current density led to higher yields using the Pb cathode (Figure 1). However, regarding the product yield, the difference between the tested current densities was rather low for the Pb cathode. The effect of the current density could be attributable to the flow rates in single-pass operation mode: When the applied current density is increased, the flow rate has to be adjusted. Higher current densities are accompanied by higher flow rates, which in turn improve the convection within the cell. As a result, an increased product yield could be obtained. However, in all single-pass experiments, no significant correlation was found between product yield and flow rate (see the Supporting Information).

In the following optimization, the significant parameters current density and amount of applied charge were optimized.
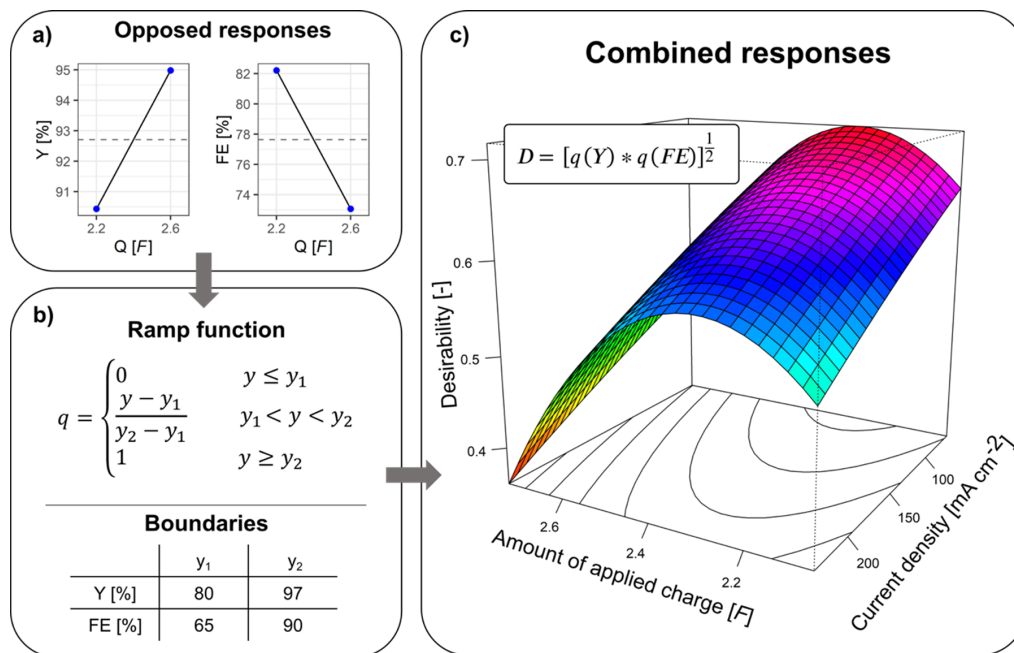
Figure 4. Multiple response optimization for product yield (Y) and Faradaic efficiency (FE). The obtained desirability function (D) combines the system responses into one equation, which is visualized by the surface plot.

The electrode gap was left constant at 1.5 mm, since no smaller gaps could be realized using the setup. The L-cystine concentration 225 g/L was chosen, as higher concentrations were not feasible due to limitations in the solubility of the substrate.

Optimization. Based on the investigations on the flow electrolysis parameters, another factorial design was applied, followed by a central composite design to improve the understanding of the system. As an increase of the current density showed a positive effect on the product yield in the first set of experiments (50−100 mA/cm^2), higher values were tested in the second factorial design (100−200 mA/cm^2). The amount of applied charge was not increased, although this would be suggested by the previous set of experiments. A higher amount of charge will lead to a higher product yield since the reaction is driven by charge transfer. For an economical conversion, the amount of applied charge was targeted between 2.2 and 2.6 F.

Establishing a good mass transport of L-cystine to the electrode is viable for an efficient reaction.[33] When the system was transferred from batch-type cells to the flow cell, the product yield dropped, which was a result of the single-pass operation mode. Therefore, the operational mode was changed to a multipass (or recycling) mode. The outlet of the cell was cycled into the feed vessel, whereby the electrolyte in this reservoir was stirred. The amount of charge was applied over the course of all cell passages. The number of cell passages N was added to the investigated parameters. It is important to note that changing the operation mode from single-pass to recycling can potentially have an influence on the parameter effects. As the flow regime differs, the effect of, e.g., the interelectrode gap might be of a different magnitude. Nevertheless, it is anticipated that a smaller interelectrode gap is beneficial to the conversion, regardless of the operation mode. Furthermore, changing from single-pass to batch-recycle results in a batch process instead of a continuous process.

Compared to the single-pass operation mode, the average yield increased significantly from roughly 75% to approximately 92.5% when the cycling mode was used (Figure 3a).

In the tested range, only the amount of applied charge exhibited a significant effect on the product yield. The L-cysteine yield decreased with higher current density. However, this effect was far below the significance level (Figure 3b). Likewise, no significant effect was observed for the number of cell passages in the tested range (10−20 cycles), although performing the process in cycling mode was superior to the single-pass approach. When the experimental design was extended to a central composite design (CCD), it appears that 15 cell passages is an optimal value, which is illustrated by the contour plots (Figure 3c,d). For fewer or more electrolysis cycles, the product yield decreased slightly. However, in the tested range, this effect showed no statistical significance. The contour plot, combining effects of the amount of applied charge and current density, illustrates that, for a relatively large current density range, a similar product yield can be obtained (Figure 3e). This is in accordance with the findings of the cathode screening in batch-type cells, where the Pb cathode exhibited a similar performance at different current densities (Figure 1b).

In the tested range of the amount of applied charge, the product yield increases with the amount of charge. To maximize the amount of produced L-cysteine, the amount of applied charge must be increased. However, when most of the substrate is reduced, the efficiency of the conversion rate drops due to the lower substrate concentration at the electrode, and the hydrogen evolution reaction becomes the dominant process. This becomes apparent when comparing the main effect plots for the applied charge for product yield and
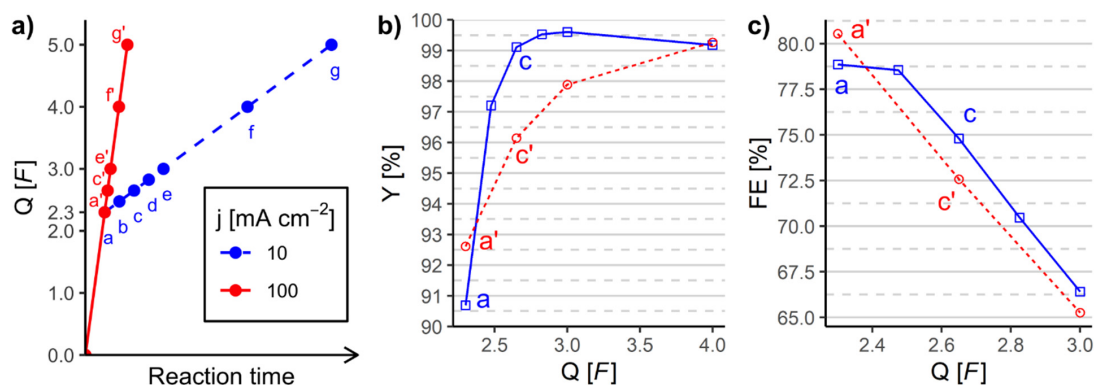
Figure 5. Electrolysis under optimized reaction conditions. The current density (j) was lowered from 100 mA/cm^2 after 2.3 F had passed. Samples were collected during the reaction (reading points a−g). In the control experiment, the current density was not lowered (reading points a′−g′). Y = product yield, Q = amount of applied charge, FE = Faradaic efficiency.

Faradaic efficiency (FE), which show opposite behaviors (Figure 4a). The trade-off between high product yield and conversion efficiency is a common challenge in electroorganic conversions and was also recognized for the reduction of L-cystine.[32] In the present study, a strategy for finding a compromise between yield and efficiency is targeted.

In a multiple response optimization approach, the product yield and the Faradaic efficiency were combined in a desirability function. The desirability function D was constructed using the ramp functions $q(Y)$ and $q(FE)$ with lower and upper boundaries y_1 and y_2 (Figure 4b). The boundaries denote the desired upper and lower limits for the responses Y and FE. For values lower than or equal to y_1, the ramp function is defined as 0; for values greater than or equal to y_2, it is defined as 1. In between, the ramp function increases linearly.

The surface plot illustrates that the desirability function D first increases when the applied charge rises (Figure 4c). This is a result of the higher product yield that is obtained with higher charge (Q): The higher the applied charge, the more product is formed. However, when a critical value $Q = 2.3$ F is reached, the desirability function decreases. The high amount of charge leads to a small Faradaic efficiency, which in turn lowers D as it outweighs the positive contribution of the higher product yield. Within the tested range, D increases with smaller current densities for all amounts of applied charge.

Based on the desirability function and the obtained critical value for the applied charge, the process conditions could be adjusted. Using a current density of 100 mA/cm^2, the amount of 2.3 F was applied. This was considered an optimal amount of charge in the compromise between high product yield and high Faradaic efficiency. After 2.3 F was applied, the current density was lowered to 10 mA/cm^2 to minimize losses attributed to hydrogen evolution. Catholyte samples were collected at regular intervals (Figure 5a). As a control experiment, up to 4 F was applied using 100 mA/cm^2, without lowering the current density after 2.3 F. For an efficient downstream processing, product yields higher than 99% are required. When the current density was lowered to 10 mA/cm^2 after 2.3 F, more than 99% yield was obtained after 2.65 F (Figure 5, reading point c). When the current density remained at 100 mA/cm^2, only 96% yield was achieved (Figure 5, reading point c′), and it takes 4 F in total to reach a 99% L-cysteine yield.

Adjusting the current density after 2.3 F (Figure 5, reading point a) to 10 mA/cm^2 enabled a conversion with lower losses attributed to the HER. After 2.65 F (Figure 5, reading point c), a product yield as high as 99% and an overall Faradaic efficiency of approximately 75% were achieved. In comparable studies on homocysteine, optimized conditions led to 96% yield and 64% Faradaic efficiency using a *one variable at a time* approach,[43] which is a higher experimental effort and provides less information about the system. The 1.5-fold theoretical amount of charge was applied in the homocysteine study; here, only 1.325-fold of the theoretical amount of charge was applied, leading to an electric energy consumption of approximately 0.6 kWh/kg$_{product}$ (L-cysteine hydrochloride monohydrate, M = 175.6 g/mol, which is equivalent to 0.87 kWh/kg L-cysteine with M = 121 g/mol). In the study by Walsh and co-workers on L-cystine reduction, an electric energy consumption of 3.3 kWh/kg$_{product}$ was reported to reach a conversion of 99% at Pb cathodes.[35]

Scale-Up. The optimized conditions were transferred to a flow cell from an ElectroCell cell (Electro MP cell). Based on the results shown in Figure 5, the same experiments were performed on a larger scale to show the translation of calculated parameters. The electrode surface of the cathode (lead metal) had an active area of 100 cm^2. The gap between the electrode and membrane was set to 8 mm.

A constant current density of 100 mA/cm^2 was applied to the L-cystine-containing catholyte feed (for details, see the Experimental Section in the Supporting Information) until 2.3 F was transferred. After that, the current density was lowered to 10 mA/cm^2 (reaction time in total, 11.5 h). Furthermore, two control experiments up to 4 F were performed using (i) a constant current density of 100 mA/cm^2 (reaction time in total, 8.5 h) and (ii) a constant current density of 200 mA/cm^2 (reaction time in, total 4.3 h; see the Supporting Information).

Comparing the obtained yield from a 10 cm^2 cell and a 100 cm^2 cell shows that the optimized conditions were well transferable to the larger cell (Figure 6). Using the larger cell (100 cm^2), the product yield of 99% was reached with an even lower amount of charge compared to the smaller cell.

Comparing electrolyses with and without an adjustment of the current density after 2.3 F on the 100 cm^2 cell shows the beneficial effect of the lower current density (Table 1). Up to 2.3 F, a similar Faradaic efficiency (FE), electric energy
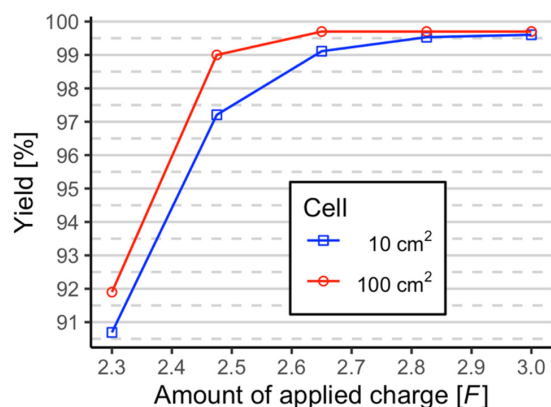
Figure 6. Size effect of the electrolyzer. Results show an excellent transferability of the optimized conditions. Operation mode: 0−2.3 F, 100 mA/cm^2; 2.3−3 F, 10 mA/cm^2.

consumption (EEC), and area−time yields are achieved in the two operation modes. However, when the current density is reduced from 100 to 10 mA/cm^2 after 2.3 F, a high efficiency of the electrolysis can be maintained, whereas the efficiency decreases when the current density remains constant. When the current density is lowered after 2.3 F, another 0.17 F can be applied with no notable change in the overall efficiency. Interestingly, a 99% yield could be achieved even prior to 2.65 F being applied. With the adjustment of the current density, 2.47 F was already sufficient. Without the adjustment, the product yield remained below 99% even when 4 F was applied. Similar to the runs on a smaller scale, the electric energy consumption under optimized conditions is well below 1 kWh/kg, which we attribute to the strategic DoE-based approach.

CONCLUSIONS

The electrochemical reduction of L-cystine was examined at different metal and metal alloy cathodes. Among all tested materials, zinc, tin, and lead cathodes showed the highest substrate conversion. Using the theoretical amount of charge of 2 F, a product yield above 90% can be reached with those materials at a wide range of current density. However, the zinc and tin electrodes suffered from serious corrosion during the process. The DoE-based investigations on flow electrolysis parameters using Pb as a cathode revealed that the amount of applied charge, the interelectrode gap, and the current density

have significant effects on the product yield. Moreover, the yield increased drastically when the cell operation mode was changed from single-pass to cycling. In a multiresponse optimization approach, the product yield and the Faradaic efficiency were combined in a desirability function. 2.3 F was determined as an optimal amount of charge to tackle the trade-off between high current efficiency and high product yield. Applying 100 mA/cm^2 until 2.3 F and 10 mA/cm^2 from 2.3 to 2.65 F yields more than 99% L-cysteine with an electric energy consumption of 0.6 kWh/kg (L-cysteine hydrochloride monohydrate). Apart from the high energy efficiency of the optimized process, inexpensive electrolytes along with a cost-effective cathode material were employed. The MMO anode as well as the Nafion membrane represent rather expensive parts of the setup; however, they showed promising durability and were not replaced in the entire set of experiments. Future investigations on membrane and electrode stability would complement this study.

The translation of optimized parameters from 10 cm^2 flow cells to a 100 cm^2 flow electrolyzer showed excellent reproducibility as the results from the DoE calculations were fully transferable. By the DoE approach, 6 parameters could be examined and optimized with an experimental effort of 34 runs (without replicates), which highlights the efficiency of this experimental design.

We conclude that DoE is a powerful tool to optimize figures of merit of an electrochemical reaction like the reduction of L-cystine to L-cysteine hydrochloride monohydrate even for larger scales using a minimum of experiments.

ASSOCIATED CONTENT

Supporting Information

The Supporting Information is available free of charge at https://pubs.acs.org/doi/10.1021/acs.oprd.1c00153.

> Detailed descriptions of electrochemical cells used and setup of experiments, a list of equations used in the experimental design, a list of all experiments and parameter settings for DoE calculations, and a list of cathode materials applied in the electrode screening (PDF)

AUTHOR INFORMATION

Corresponding Authors

Stefan Haufe − *Wacker Chemie AG, Consortium für elektrochemische Industrie, 81379 München, Germany*; Email: stefan.haufe@wacker.com

Table 1. Figures of Merit[a] of Electrolysis Using a 100 cm^2 Flow Cell under Optimized Conditions

		yield [%]	FE [%][b]	U_{cell}[c] [V]	EEC[b] [kWh/kg]	area−time yield[d] [kg/(m^2 h)]
0−4 F, 100 mA/cm^2	1 F	47.0	92.7 (92.7)	3.92	0.66	5.89 (5.89)
	2.3 F	91.6	79.6 (69.2)	4.06	0.80	4.40 (5.06)
	2.65 F	94.7	72.4 (19.9)	4.09	0.88	1.26 (4.60)
	4 F	98.7	49.6 (5.8)	4.16	1.31	0.37 (3.15)
0−2.3 F, 100 mA/cm^2; 2.3−2.65 F 10 mA/cm^2	1 F	47.8	95.7 (95.7)	3.92	0.65	6.06 (6.06)
	2.3 F	91.9	79.9 (68.5)	4.05	0.79	4.39 (5.13)
	2.47 F	99.0	80.1 (85.9)	2.67	0.78	0.55 (3.22)
	2.65 F	99.7	75.3 (10.4)	2.77	0.80	0.07 (2.38)

[a]For the calculation of the figures of merit, see the Experimental Section in the Supporting Information. FE = Faradaic efficiency, EEC = electric energy consumption per product L-cysteine hydrochloride monohydrate. [b]Cumulative values (the interval value is shown in parentheses). [c]Terminal cell voltage. [d]Value for each interval (the cumulative value is shown in parentheses).

Tobias Gärtner − *ESy-Labs GmbH, 93055 Regensburg, Germany*; Email: tobias.gaertner@esy-labs.de

Siegfried R. Waldvogel − *ESy-Labs GmbH, 93055 Regensburg, Germany; Department of Chemistry, Johannes Gutenberg University, 55128 Mainz, Germany;* ● orcid.org/0000-0002-7949-9638; Email: waldvogel@uni-mainz.de

Authors

Johannes Seidler − *ESy-Labs GmbH, 93055 Regensburg, Germany; Department of Chemistry, Johannes Gutenberg University, 55128 Mainz, Germany*

Rebecca Bernhard − *Wacker Chemie AG, Consortium für elektrochemische Industrie, 81379 München, Germany*

Caroline Neff − *ESy-Labs GmbH, 93055 Regensburg, Germany*

Complete contact information is available at:
https://pubs.acs.org/10.1021/acs.oprd.1c00153

Notes

The authors declare no competing financial interest.

■ REFERENCES

(1) Anastas, P.; Eghbali, N. Green Chemistry: Principles and Practice. *Chem. Soc. Rev.* **2010**, *39* (1), 301−312.

(2) Yuan, Y.; Lei, A. Is Electrosynthesis Always Green and Advantageous Compared to Traditional Methods? *Nat. Commun.* **2020**, *11* (1), 802.

(3) Wiebe, A.; Gieshoff, T.; Möhle, S.; Rodrigo, E.; Zirbes, M.; Waldvogel, S. R. Electrifying Organic Synthesis. *Angew. Chem., Int. Ed.* **2018**, *57* (20), 5594−5619.

(4) Waldvogel, S. R.; Janza, B. Renaissance of Electrosynthetic Methods for the Construction of Complex Molecules. *Angew. Chem., Int. Ed.* **2014**, *53* (28), 7122−7123.

(5) Pollok, D.; Waldvogel, S. R. Electro-Organic Synthesis − a 21 St Century Technique. *Chem. Sci.* **2020**, *11* (46), 12386−12400.

(6) Möhle, S.; Zirbes, M.; Rodrigo, E.; Gieshoff, T.; Wiebe, A.; Waldvogel, S. R. Modern Electrochemical Aspects for the Synthesis of Value-Added Organic Products. *Angew. Chem., Int. Ed.* **2018**, *57* (21), 6018−6041.

(7) Seidler, J.; Strugatchi, J.; Gärtner, T.; Waldvogel, S. R. Does Electrifying Organic Synthesis Pay off? The Energy Efficiency of Electro-Organic Conversions. *MRS Energy Sustain.* **2020**, 7, No. E42.

(8) Kärkäs, M. D. Electrochemical Strategies for C−H Functionalization and C−N Bond Formation. *Chem. Soc. Rev.* **2018**, *47* (15), 5786−5865.

(9) Horn, E. J.; Rosen, B. R.; Baran, P. S. Synthetic Organic Electrochemistry: An Enabling and Innately Sustainable Method. *ACS Cent. Sci.* **2016**, *2* (5), 302−308.

(10) Little, R. D.; Moeller, K. D. Introduction: Electrochemistry: Technology, Synthesis, Energy, and Materials. *Chem. Rev.* **2018**, *118* (9), 4483−4484.

(11) Waldvogel, S. R.; Lips, S.; Selt, M.; Riehl, B.; Kampf, C. J. Electrochemical Arylation Reaction. *Chem. Rev.* **2018**, *118* (14), 6706−6765.

(12) Yan, M.; Kawamata, Y.; Baran, P. S. Synthetic Organic Electrochemical Methods since 2000: On the Verge of a Renaissance. *Chem. Rev.* **2017**, *117* (21), 13230−13319.

(13) Röckl, J. L.; Pollok, D.; Franke, R.; Waldvogel, S. R. A Decade of Electrochemical Dehydrogenative C,C-Coupling of Aryls. *Acc. Chem. Res.* **2020**, *53* (1), 45−61.

(14) Blum, S. P.; Schollmeyer, D.; Turks, M.; Waldvogel, S. R. Metal- and Reagent-Free Electrochemical Synthesis of Alkyl Arylsulfonates in a Multi-Component Reaction. *Chem. - Eur. J.* **2020**, *26* (38), 8358−8362.

(15) Blum, S. P.; Karakaya, T.; Schollmeyer, D.; Klapars, A.; Waldvogel, S. R. Metal-Free Electrochemical Synthesis of Sulfonamides Directly from (Hetero)Arenes, SO2, and Amines. *Angew. Chemie - Int. Ed.* **2021**, *60*, 5056.

(16) Arndt, S.; Grill, B.; Schwab, H.; Steinkellner, G.; Pogorevčnik, U.; Weis, D.; Nauth, A. M.; Gruber, K.; Opatz, T.; Donsbach, K.; Waldvogel, S. R.; Winkler, M. The Sustainable Synthesis of Levetiracetam by an Enzymatic Dynamic Kinetic Resolution and an: Ex-Cell Anodic Oxidation. *Green Chem.* **2021**, *23* (1), 388−395.

(17) Elsler, B.; Schollmeyer, D.; Dyballa, K. M.; Franke, R.; Waldvogel, S. R. Metal- and Reagent-Free Highly Selective Anodic Cross-Coupling Reaction of Phenols. *Angew. Chemie Int. Ed.* **2014**, *53* (20), 5210−5213.

(18) Tanbouza, N.; Ollevier, T.; Lam, K. Bridging Lab and Industry with Flow Electrochemistry. *iScience* **2020**, *23* (11), 101720.

(19) Beil, S. B.; Pollok, D.; Waldvogel, S. R. Reproducibility in Electroorganic Synthesis—Myths and Misunderstandings. *Angew. Chem., Int. Ed.* **2021**, in press. DOI: 10.1002/anie.202014544.

(20) Dörr, M.; Hielscher, M.; Proppe, J.; Waldvogel, S. R. Electrosynthetic Screening and Modern Optimization Strategies for Electrosynthesis of Highly Value-added Products. *ChemElectroChem* **2021**, in press. DOI: 10.1002/celc.202100318.

(21) Dörr, M.; Röckl, J. L.; Rein, J.; Schollmeyer, D.; Waldvogel, S. R. Electrochemical C−H Functionalization of (Hetero)Arenes— Optimized by DoE. *Chem. - Eur. J.* **2020**, *26* (45), 10195−10198.

(22) Hielscher, M. M.; Gleede, B.; Waldvogel, S. R. Get into Flow: Design of Experiments as a Key Technique in the Optimization of Anodic Dehydrogenative C,C Cross-Coupling Reaction of Phenols in Flow Electrolyzers. *Electrochim. Acta* **2021**, *368*, 137420.

(23) Arndt, S.; Weis, D.; Donsbach, K.; Waldvogel, S. R. Die "Grüne" Elektrochemische Synthese von Periodat. *Angew. Chem.* **2020**, *132* (21), 8112−8118.

(24) Santi, M.; Seitz, J.; Cicala, R.; Hardwick, T.; Ahmed, N.; Wirth, T. Memory of Chirality in Flow Electrochemistry: Fast Optimisation with DoE and Online 2D-HPLC. *Chem. - Eur. J.* **2019**, *25* (71), 16230−16235.

(25) Möckel, R.; Hille, J.; Winterling, E.; Weidemüller, S.; Faber, T. M.; Hilt, G. Electrochemical Synthesis of Aryl Iodides by Anodic Iododesilylation. *Angew. Chem., Int. Ed.* **2018**, *57* (2), 442−445.

(26) Hashim, Y.; Ismail, N.; Jamal, P.; Othman, R.; Salleh, H. Production of Cysteine: Approaches, Challenges and Potential Solution. *Int. J. Biotechnol. Wellness Ind.* **2014**, *3* (3), 95−101.

(27) Takumi, K.; Ziyatdinov, M. K.; Samsonov, V.; Nonaka, G. Fermentative Production of Cysteine by Pantoea Ananatis. *Appl. Environ. Microbiol.* **2017**, *83* (5), 1−14.

(28) Brunner, M.; Dassler, T.; Reutter-Maier, A. *Method for the Fermentative Production of L-Cysteine and Derivates of Said Amino Acid*. US Patent US2014141474AA, 2012.

(29) Böhm, A. *Process for Purifying L-Cysteine*. US Patent US2008190854AA, 2007.

(30) Maier, T.; Winterhalter, C. *Method for Production of L-Cysteine or l-Cystine Derivatives by Fermentation*. WO0127307A1, 1999.

(31) Leinfelder, C.; Winterhalter, C. *Microorganisms and Processes for the Fermentative Preparation of L-Cystine, L-Cysteine, N-Acetylserine or Thiazolidine Derivatives*. US Patent US5972663A, 1998.

(32) Ralph, T. R.; Hitchman, M. L.; Millington, J. P.; Walsh, F. C. The Electrochemistry of L-Cystine and l-Cysteine Part 2: Electrosynthesis of l-Cysteine at Solid Electrodes. *J. Electroanal. Chem.* **1994**, *375* (1−2), 17−27.

(33) Ralph, T. R.; Hitchman, M. L.; Millington, J. P.; Walsh, F. C. The Electrochemistry of L-Cystine and l-Cysteine Part 1: Thermodynamic and Kinetic Studies. *J. Electroanal. Chem.* **1994**, *375* (1−2), 1−15.

(34) Thirunavukkarasu, P. Effect of Cathode Materials on the Electrochemical Reduction of L-Cystine to L-Cysteine. *Bull. Electrochem.* **1999**, *15* (7−8), 286−288.

H

(35) Ralph, T. R.; Hitchman, M. L.; Millington, J. P.; Walsh, F. C. The Importance of Batch Electrolysis Conditions during the Reduction of L-Cystine Hydrochloride. *J. Electrochem. Soc.* **2005**, *152* (3), D54.

(36) Fritz-Langhals, E. *Cathode for Electrolysis Cells*. US Patent US 2002/0027083 A1, 2001.

(37) Gütz, C.; Klöckner, B.; Waldvogel, S. R. Electrochemical Screening for Electroorganic Synthesis. *Org. Process Res. Dev.* **2016**, *20* (1), 26−32.

(38) Gütz, C.; Stenglein, A.; Waldvogel, S. R. Highly Modular Flow Cell for Electroorganic Synthesis. *Org. Process Res. Dev.* **2017**, *21* (5), 771−778.

(39) Gütz, C.; Grimaudo, V.; Holtkamp, M.; Hartmer, M.; Werra, J.; Frensemeier, L.; Kehl, A.; Karst, U.; Broekmann, P.; Waldvogel, S. R. Leaded Bronze: An Innovative Lead Substitute for Cathodic Electrosynthesis. *ChemElectroChem* **2018**, *5* (2), 247−252.

(40) Gálvez-Vázquez, M. de J.; Moreno-García, P.; Guo, H.; Hou, Y.; Dutta, A.; Waldvogel, S. R.; Broekmann, P. Leaded Bronze Alloy as a Catalyst for the Electroreduction of CO2. *ChemElectroChem* **2019**, *6* (8), 2324−2330.

(41) Gütz, C.; Selt, M.; Bänziger, M.; Bucher, C.; Römelt, C.; Hecken, N.; Gallou, F.; Galvão, T. R.; Waldvogel, S. R. A Novel Cathode Material for Cathodic Dehalogenation of 1,1-Dibromo Cyclopropane Derivatives. *Chem. - Eur. J.* **2015**, *21* (40), 13878−13882.

(42) Gütz, C.; Bänziger, M.; Bucher, C.; Galvão, T. R.; Waldvogel, S. R. Development and Scale-Up of the Electrochemical Dehalogenation for the Synthesis of a Key Intermediate for NS5A Inhibitors. *Org. Process Res. Dev.* **2015**, *19* (10), 1428−1433.

(43) Sánchez-Cano, G.; Montiel, V.; García, V.; Aldaz, A.; Elías, E. From Voltammetry to Industrial Plant: Electrochemical Synthesis of DL-Homocysteine from DL-Homocystine — An Example of Scale-Up. *Electrochem. Eng. Energy* **1995**, *2*, 151−158.

127

From Screening to Scale-up: The DoE-based Optimization of Electrochemical Reduction of L-Cystine at Metal Cathodes

Johannes Seidler,[†][§] Rebecca Bernhard,[#] Stefan Haufe,[#],* Caroline Neff,[†] Tobias Gärtner,[†],*

Siegfried R. Waldvogel[†,§,]*

[†]ESy-Labs GmbH, Siemensstraße 7, 93055 Regensburg, Germany

[§]Department of Chemistry, Johannes Gutenberg University, Duesbergweg 10–14, 55128 Mainz,

Germany

[#]Wacker Chemie AG, Consortium für elektrochemische Industrie, Zielstattstraße 20, 81379

München, Germany

E-mail: waldvogel@uni-mainz.de, tobias.gaertner@esy-labs.de and stefan.haufe@wacker.com

General. Hydrochloric acid and sulfuric acid were purchased from Carl Roth. L-cystine as well as L-cysteine were obtained from Wacker Chemie AG. All chemicals were used without further purification. For all experiments, an aqueous 3.2 M HCl solution was used as catholyte and an aqueous 3.2 M H_2SO_4 solution was used as anolyte. If not stated otherwise, the L-cystine concentration in the catholyte was 225 g/L (0.94 M). The current density was calculated based on the geometric surface area of the cathode.

Conversion in divided batch cells. Cathode material screening was performed in divided Teflon cells. In the applied setup, six simultaneous runs could be performed. Each compartment was filled with 5 mL electrolyte. Nafion™ 424 proton exchange membranes (EUT GmbH, Germany) were used as separators. Mixed metal oxide anodes (MMO) consisting of an IrO_2-RuO_2/Ti mesh (Jentner Plating Technology GmbH, Germany) served as counter electrodes. The geometric cathode surface area was 1.5 cm^2.

Conversion in flow cells. An IKA ElectraSyn flow electrochemical cell with an electrode surface of 10.5 cm^2 was used for DoE-based parameter screening and optimization. A lead metal sheet was used as cathode material and an MMO anode served as anode. Nafion™ 424 proton exchange membranes (EUT GmbH, Germany) were used as separators. An Ismatec REGLO

2

Digital peristaltic pump was used. Before entering the cell, the electrolyte was heated to the desired temperature. In single-pass mode, the amount of charge was transferred during one passage of the electrolyte. To ensure steady-state conditions, the samples were collected several minutes after start of the electrolysis. In multi-pass operation mode (batch recycle), a reaction volume of 10 mL was used. In the case of batch recycle mode, the entire batch served as sample volume.

For electrolysis experiments on a larger scale an Electro MP Cell (ElectroCell, Denmark) with an active electrode surface of 100 cm^2 was used. Nafion^{TM} type N324 was used a separator. A standard DSA$^®$ electrode (Ir/Ru-MMO, supplied by ElectroCell) served as an anode and a lead metal sheet as cathode. In the standard cell configuration, the electrode/membrane gap was 8.0 mm and the flow rate for the electrolyte was 2.4 L/h for a 15-times multi-pass operation mode. Electrolyses were run galvanostatically using 200 mA/cm^2 as well as between 100 mA/cm^2 and 10 mA/cm^2 for staggered measurements. The used volume for catholyte was 0.84 L of a 0.95 M L-cystine solution in 3.2 M HCl. The feed vessels were cooled to 23 °C during reaction. Hydrogen evolution was quantified on-line with a gas meter during the whole electrolysis process. This allows the calculation of current efficiency and educt conversion per time-step.

3

Electrolyte contamination with lead. For various experiments, the electrolyte was tested for its Pb content via ICP analysis. For experiments using a the 10 cm^2 flow-cell with an electrolyte volume of 10 mL, a lead contamination between 45 and 140 ppm at approx. 217 C/cm^2 was measured. For experiments using the 100 cm^2 flow cell and 840 mL electrolyte volume, between 1 and 13 ppm lead were recorded at 350-1800 C/cm^2. It was observed, that with longer usage of the Pb cathode, the contamination of the electrolyte decreased. In other words, using a freshly polished lead cathode resulted in a higher contamination than using the same cathode after multiple experiment runs.

Product analysis. Product concentrations were obtained via the optical rotation of the reaction mixtures using calibration curves. The optical rotation was determined at 20 ˚C using a Schmidt+Haensch VariPol B101P-NMPVS polarimeter. Rotation angles were measured three times and the average data was used for calculation of the product yield. A calibration curve was used for the conversion between rotation angle and product concentration. For experiments in 100 cm^2 flow-cells, the educt conversion was analyzed after electrolysis by HPLC (high performance liquid chromatography) or mercury titration.

4

The pure product can be obtained using the following procedure: By concentrating the solution under reduced pressure to about 1/3 of the original volume, a solution is obtained from which L-cysteine hydrochloride precipitates in easily filterable crystals. To achieve a higher yield, room temperature and temperatures below are recommended. After filtration, these solid crystals are dried under mild conditions (60°C and reduced pressure) to obtain pure L-cysteine hydrochloride monohydrate. The purity can be checked e.g. using HPLC.

Data analysis and DoE calculations. The entire data processing and visualization was performed using the free statistical software R.[1] RStudio was used as integrated development environment.[2] The R packages ggplot2 and FrF2 were used for data visualization and DoE-specific calculations, respectively.[3,4] Results from the fractional factorial designs were fed into a general linear model:

$$Y = \beta_0 + \sum_{i=1}^{n_f} \beta_i x_i + \sum_{i=1}^{n_f-1} \sum_{j=i+1}^{n_f} \beta_{ij} x_i x_j + \varepsilon$$

Where Y is the response, β_n are regression coefficients, x_n is the predictor, n_f is the number of factors (parameters) and ε is the random error term.[5] For contour plots, the design was extended to a central composite design, therefore quadratic terms were added to the model:

5

$$Y = \beta_0 + \sum_{i=1}^{n_f} \beta_i x_i + \sum_{i=1}^{n_f} \beta_{ii} x_i^2 + \sum_{i=1}^{n_f-1} \sum_{j=i+1}^{n_f} \beta_{ij} x_i x_j + \varepsilon$$

The Faradaic efficiency *FE* was calculated using the amount of applied charge Q_{appl}, the theoretically minimal charge (which is $2\,F$ for the reduction of L-cystine to L-cystine), and the product yield:

$$FE = \frac{2F}{Q_{appl}} * \text{Yield}$$

In the multiple response optimization, ramp functions q_i for the response variables yield *Y* and Faradaic efficiency *FE* were constructed:

$$q = \begin{cases} 0 & \forall\, y \leq y_1 \\ \dfrac{y - y_1}{y_2 - y_1} & \forall\, y_1 < y < y_2 \\ 1 & \forall\, y \geq y_2 \end{cases}$$

Where y_1 and y_2 denote lower and upper boundaries for the responses. The ramp functions were combined to obtain the desirability function *D*:[5]

$$D = [q(FE) * q(Y)]^{\frac{1}{2}}$$

The electric energy consumption of the electrolysis was calculated using the following equation:

$$EEC = \frac{z * F * U_{cell}}{FE * M} * 100\%$$

Where z is the number of electrons needed for the reduction of each mole of substrate, F is

Faraday constant, U_{cell} is the terminal cell voltage, FE is the Faradic efficiency and M is the molar

mass of the product L-cysteine hydrochloride monohydrate.

The area-time-yield was calculated by dividing the produced mass of L-cysteine hydrochloride

monohydrate by the electrode surface area and the time of the electrolysis:

$$\text{AreaTimeYield} = \frac{\text{m}_{\text{product}}}{A_{cathode} * t_{electrolysis}} * 100\%$$

Table S1. First optimization round using a 2^{5-1} factorial design.

Run no.	Run no. in standard order	j [mA cm^{-2}]	Q [F]	T [°C]	c [g L^{-1}]	d [mm]	Yield [%]
1	8.1	100	3	50	175	3	86.19
2	15.1	50	3	50	225	3	80.61
3	3.1	50	3	30	175	3	77.31
4	5.1	50	2	50	175	3	74.38
5	14.1	100	2	50	225	3	79.81
6	12.1	100	3	30	225	3	88.34
7	2.1	100	2	30	175	3	77.06
8	9.1	50	2	30	225	3	72.95
9	12.2	100	3	30	225	3	88.07
10	15.2	50	3	50	225	3	80.93
11	9.2	50	2	30	225	3	70.30
12	2.2	100	2	30	175	3	75.27
13	3.2	50	3	30	175	3	76.65
14	14.2	100	2	50	225	3	77.01
15	5.2	50	2	50	175	3	73.22
16	8.2	100	3	50	175	3	86.09
17	0.1	75	2.5	40	200	4.5	76.41
18	13.1	50	2	50	225	6	48.55
19	16.1	100	3	50	225	6	82.17
20	1.1	50	2	30	175	6	63.32
21	7.1	50	3	50	175	6	75.33
22	10.1	100	2	30	225	6	60.57
23	11.1	50	3	30	225	6	69.79
24	4.1	100	3	30	175	6	85.51
25	6.1	100	2	50	175	6	57.39
26	4.2	100	3	30	175	6	90.52
27	6.2	100	2	50	175	6	81.96

28	10.2	100	2	30	225	6	70.89
29	16.2	100	3	50	225	6	79.29
30	7.2	50	3	50	175	6	74.84
31	11.2	50	3	30	225	6	70.90
32	1.2	50	2	30	175	6	70.46
33	13.2	50	2	50	225	6	52.79
34	0.2	75	2.5	40	200	4.5	83.51
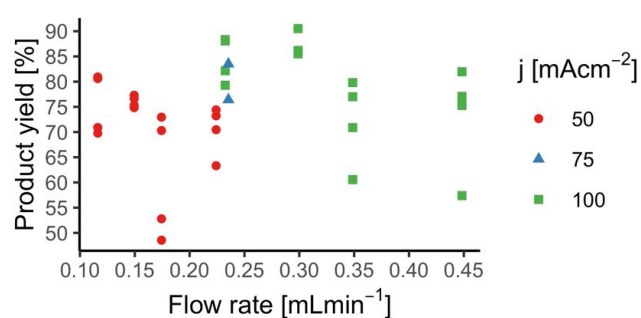
Figure S1. Product yield vs. flow rate for all single-pass experiments. Higher applied current densities are accompanied by higher flow rates. However, no significant correlation between product yield and flow rate was observed.

Table S2. Second optimization round using a 2^3 factorial design followed by central composite design.

Run no.	Run no. in standard order	Q [F]	j [mA cm^{-2}]	N [/]	Yield [%]
1	1	2.4	150	15	96.64
2	1	2.4	150	15	94.06
3	3	2.6	100	10	96.00
4	4	2.2	200	10	90.51
5	6	2.2	100	20	91.95
6	5	2.6	200	10	94.48
7	1	2.4	150	15	91.72
8	9	2.6	200	20	93.92
9	2	2.2	100	10	90.78
10	7	2.6	100	20	95.53
11	8	2.2	200	20	88.50
12	1	2.4	150	15	93.40
13	S2.1	2.064	150	15	90.58
14	S2.2	2.736	150	15	96.00
15	S2.3	2.4	66	15	95.88
16	S2.4	2.4	234	15	93.74
17	S2.5	2.4	150	6.6	93.10
18	S2.6	2.4	150	23.4	94.92
19	S2.7	2.4	150	15	94.56

10

Table S3. Cathode materials used.

Electrode identifier	Material	Composition	DIN EN	ASTM / UNS
1_Cu	Copper	Cu >99.9	CW004A	C11000
2_Zn	Zinc	Zn >99.9		
3_Sn	Tin	Sn >99.9		
4_Ag	Silver	Ag >99.9		B413
5_Ti	Titanium	Ti >99.9	17850 (DIN)	B265
6_Pb	Lead	Pb >99.9	12659 (EN)	B29-03
7_LB-Pb10	Leaded bronze	CuSn10Pb10	CC495K	C93700
8_LB-Pb20	Leaded bronze	CuSn5Pb20	CC497K	C94100
9_LTB-Pb7	Leaded tin bronze	CuSn7Zn4Pb7	CC493K	C93200
10_Brass-Pb	Leaded brass	CuZn39Pb2	CW612N	C37700
11_Brass	Brass	CuZn37	CW508L	C27200
12_NordicGold	Nordic gold	Cu89Al5Zn5Sn1	NA	NA
13_Ni/P	Phosphorous nickel alloy	NiP (approx. 8% P)	4527 (ISO)	B-733
14_Hastelloy	Nickel alloy	Ni57Mo17Cr16FeWMn	2.4819 (DIN)	N10276
15_Inconel	Nickel alloy	Ni72Cr16Fe8	2.4816 (DIN)	N06600
16_V2A-Steel	Stainless steel V2A	FeCr18Ni8	1.4305 (DIN)	AISI 303
17_V4A-Steel	Stainless steel V4A	FeCr18Ni10Mo3	1.4571 (DIN)	AISI 316

Table S4. Figures of merit of electrolysis using a 100 cm^2 flow-cell. FE = Faradaic efficiency, EEC = electric energy consumption per product L-cysteine hydrochloride monohydrate.

		Yield [%]	FE [%]^a	U_{cell} [V]^b	EEC [kWh/kg]^a	Area-time-yield [kg/m^{2}h]^c
	1 *F*	46.4	92.9	4.62	0.77	11.91
0-4 *F*	2.3 *F*	87.6	74.8	4.86	0.97	8.07
200 mA/cm^2	2.65 *F*	91.4	68.9	4.99	1.05	3.18
	4 *F*	97.5	48.0	4.95	1.53	1.13

^{a}cumulative values, ^{b}terminal cell voltage, ^{c}value for each interval (the cumulative value is shown in parenthesis)

References

(1)   R Core Team. R: A Language and Environment for Statistical Computing. Vienna, Austria 2021.

(2)   RStudio Team. RStudio: Integrated Development Environment for R. Boston, MA 2021.

(3)   Wickham, H. *Ggplot2: Elegant Graphics for Data Analysis*; Springer-Verlag New York, 2016.

(4)   Grömping, U. R Package FrF2 for Creating and Analyzing Fractional Factorial 2-Level Designs. *J. Stat. Softw.* **2014**, *56* (1), 1–56. https://doi.org/10.18637/jss.v056.i01.

(5)   Siebertz, K.; van Bebber, D.; Hochkirchen, T. *Statistische Versuchsplanung*; Springer Berlin Heidelberg: Berlin, Heidelberg, 2017; Vol. 158. https://doi.org/10.1007/978-3-662-55743-3.

12

3.3.2 Elektrochemische Reduktion von Nitro-Verbindungen zu Aminen

Zu diesem Kapitel wurde ein Manuskript veröffentlicht:

C. M. Kisukuri[†], J. Seidler[†], T. Gärtner, D. F. Rohrmann and S. R. Waldvogel, *Scalable Electrochemical Reduction of Nitrobenzotrifluorides to 3-Trifluoromethylanilines*, Org. Process Res. Dev. **2023**, Article ASAP. [DOI: 10.1021/acs.oprd.3c00067]

[†]Diese Autoren haben gleichermaßen zum Manuskript beigetragen.

Erklärung meines Beitrags:

Personenbezogene Daten

Hintergrund Anilin-Derivate mit einer 3-ständigen Trifluoromethyl-Gruppe sind wichtige Vorläufer in der Synthese von Arzneistoffen und Pflanzenschutzmitteln.[125–127] Simple, nachhaltige und sichere Syntheserouten für die Herstellung von 3-Trifluoromethylanilinen besitzen daher große industrielle Relevanz. Die Herstellung von Anilin-Derivaten mit 3-Trifluoromethyl-Gruppe erfolgt üblicherweise über die entsprechenden Nitro-Verbindungen, da die $-NO_2$-Gruppe dabei sehr regioselektiv eingeführt werden kann.[128] Für die Reduktion der Nitro-Gruppe zum Amin können Metalle oder eine katalytische Hydrierung genutzt werden.[129–131] Bei den meisten Techniken werden hohe Temperaturen, Drücke, kostenintensive Katalysatoren oder Abfall verursachende Metallspezies verwendet. Eine nachhaltige Methode stellt die elektrochemische Reduktion von Nitro-Verbindungen dar. Für eine industrielle Implementierung sind Skalierbarkeit und eine möglichst simple Produktisolation besonders wichtig. In der vorliegenden Veröffentlichung konnte die elektrochemische Reduktion erfolgreich skaliert werden und das Produkt als Amminiumsalz ausgefällt werden, wodurch die Produktaufarbeitung stark vereinfacht werden konnte.

Ergebnisse Als Testsubstanz für die elektrochemische Nitroreduktion diente 3-Nitrobenzotrifluorid. Als Elektrolyt wurde eine H_2SO_4/MeOH-Mischung verwendet. Das saure Milieu führt nach der Bildung der Aminoverbindung zum Ausfallen des entsprechenden Amminiumsalzes aus der Elektrolytlösung (Schema 6). Zunächst wurde eine Reihe von Kathodenmaterialien getestet: Glaskohlenstoff, Bor-dotierte Diamantelektrode, Graphit, Platin, Edelstahl, Blei und Bleibronze (CuSn7Pb15). Unter den verwendeten Materialien konnten mit Blei- und Bleibronzeelektroden die höchsten Ausbeuten erreicht werden. Der saure protische Elektrolyt

begünstigt die kathodische Wasserstoffentwicklung. Daher ist plausibel, dass die Materialien mit hohem Überpotential für die Wasserstoffentwicklung bessere Ausbeuten bezügliche der Nitroreduktion zeigen. Da an der Bleielektrode eine kathodische Korrosion beobachtet wurde, wurde Bleibronze als Kathodenmaterial für weitere Untersuchungen ausgewählt. Die initialen Versuche in Topfzellen ergaben eine Ausbeute des Aminiumsalzes von 13 %. Die applizierte Ladungsmenge betrug mit $12\,F$ das doppelte der theoretischen Ladungsmenge. Die Elementaranalyse des ausfallenden Salzes bestätigte die Bildung des Aminiumhydrogensulfats $(R-NH_3^+\,HSO_4^-)$.
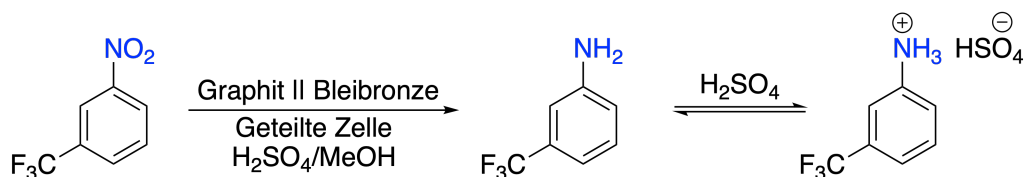

Schema 6: Elektroreduktion von 3-Nitrobenzotrifluorid zu 3-Aminobenzotrifluorid und anschließender Präzipitation in saurem Milieu.

Um die Ausbeute des Präzipitats zu steigern, wurden Stromdichte, Eduktkonzentration und das $H_2O/MeOH$-Verhältnis variiert. Dabei wurde festgestellt, dass die Reaktion vergleichsweise hohe Stromdichten von $30\,mA\,cm^{-2}$ toleriert. Eine höhere Eduktkonzentration steigerte die Ausbeute, da somit die Sättigungskonzentration des Produkts effektiver erreicht wurde. Die Veränderung des $H_2O/MeOH$-Verhältnisses zugunsten von Methanol konnte die Fällung des Produkts ebenfalls verbessern. Entscheidender Schritt für die Erhöhung der Ausbeute des Aniliniumsalzes war die späte Zugabe von konzentrierter Schwefelsäure, wodurch das in Schema 6 gezeigte Gleichgewicht stark zum entsprechenden Salz verschoben wurde. Dies steigerte die Ausbeute von 36 % auf 69 %.

Die in den Topfzellen ($A_{Kathode} = 2\,cm^2$) verwendeten Bedingungen konnten erfolgreich auf eine Flusszelle ($A_{Kathode} = 12\,cm^2$) übertragen werden. Dabei konnten Ausbeuten bis zu 85 % erreicht werden. Um die Skalierbarkeit der Reaktion zu demonstrieren, wurde eine noch größere Flusszelle ($A_{Kathode} = 48\,cm^2$) verwendet. Auf diese Weise konnte das Aniliniumsalz von 3-Aminobenzotrifluorid mit ca. 76 % isolierter Ausbeute dargestellt werden. In einem Ansatz mit 800 mL Reaktionsvolumen wurden 107 g des Aniliniumsalzes mit einer Rate von $21\,mg\,h^{-1}\,cm^{-2}$ hergestellt.

Das erarbeitete Protokoll wurde neben 3-Nitrobenzotrifluorid auf weitere Verbindungen angewendet (Schema 7). Dabei wurden die eingesetzten hohen Eduktkonzentrationen weitgehend toleriert.
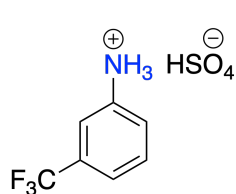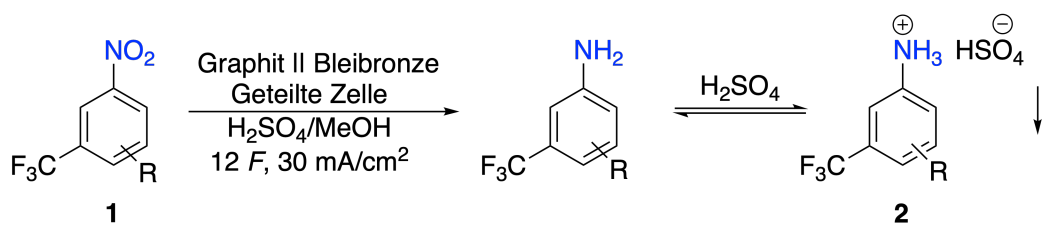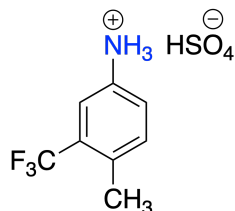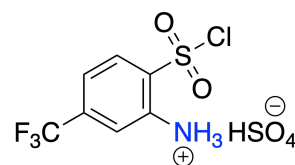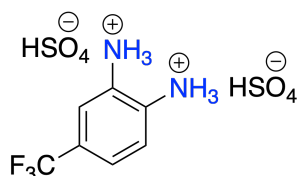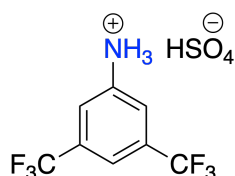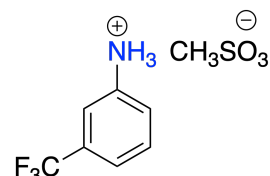
Schema 7: Produktspektrum mit isolierten Ausbeuten für die Reaktion in Topfzellen. Die Ausbeute für Versuche in der Flusszelle sind in Klammern angegeben. Die Nitrokomponente wurde jeweils in einer Konzentration von 0.4 mM eingesetzt.

Die in der Studie vorgestellten Reaktionsbedinungen zeigen die Skalierbarkeit der elektrochemischen Reduktion der Nitro- zur Aminogruppe. Die Präzipitation des Produkts als Aminiumhydrogensulfat vereinfacht die Produktisolation dramatisch, was besonders vorteilhaft für eine industrielle Anwendung ist.

Scalable Electrochemical Reduction of Nitrobenzotrifluorides to 3-Trifluoromethylanilines

Camila M. Kisukuri,[||] Johannes Seidler,[||] Tobias Gärtner, Denis F. Rohrmann,
and Siegfried R. Waldvogel*

Cite This: https://doi.org/10.1021/acs.oprd.3c00067

Read Online

ACCESS | | Metrics & More | | Article Recommendations | | Supporting Information

ABSTRACT: The scalability of electrochemical methods remains one of the biggest reasons for their scarce implementation in manufacturing synthetic routes as well as pharmaceutical and agrochemical industry. To bridge this gap, we designed a robust and safe electrochemical workflow route for the synthesis of a collection of various 3-trifluoromethylanilines. The 3-trifluoromethylanilines are important intermediates for preparing agrochemicals and active pharmaceutical ingredients. The agent-free conversion could be easily scaled beyond the decagram scale. The cathodic conversion of nitroarenes in sulfuric acid/methanolic media was used to generate the 3-trifluoromethylanilinium bisulfates. During the reductive process, H_2SO_4 formed the corresponding bisulfates, which precipitated and facilitated downstream processing. The translation of a small-scale batch electrochemical reduction to forge the 3-trifluoromethylanilinium bisulfates in a continuous flow electrolysis allowed the target compound to be obtained in quantities of up to 107 g per run. The molecular composition of 3-trifluoromethylanilinium bisulfate was confirmed by elemental analysis. In addition, we demonstrated that the methodology can be extended to a broader scope. In total, eight different 3-trifluoromethylnitrobenzenes were applicable in batch, and six of them were translated to flow conditions.

KEYWORDS: nitroarenes, flow electrochemistry, reduction, gram scale, 3-trifluoromethylanilines

■ INTRODUCTION

The urgency to develop greener and more cost-efficient synthetic methods has prompted chemists to look for new approaches to important building blocks.[1−3] Among them, electrosynthesis is one of the most attractive, since it is possible to perform redox reactions without the need of any toxic chemical reagents.[3−5] However, many of the methodologies published involve the electrochemical production of building blocks, usually on milligram scale.[6] This is an ironic fact since the multigram-scale regime is precisely where electrosynthesis originally started.[7,8] Up to now, only a few electrosynthetic examples reported more than a decagram scale.[9−22]

The 3-trifluoromethylaniline derivatives are major products and well-known precursors to other valuable organic products. In general, several 3-trifluoromethylanilines are important intermediates for preparing agrochemicals and active pharmaceutical ingredients (Figure 1).[23−25] This particular benzotrifluoride moiety with amino substitution is found in many important commercial drugs and pesticides, independent of its area for application. Consequently, it can be considered as a privileged molecular entity for bioactive compounds.

Therefore, protocols for the preparation of 3-trifluoromethylanilines in simple, safe, and economical processes with good yields and purities are desired. The preparation usually employs the pathway via 3-nitro derivatives, since the nitration reaction is here outstandingly regioselective.[26−28] The existing synthetic routes to 3-trifluoromethylanilines include metal-based and metal-free routes (Scheme 1).[28−38] Most of the methods are not suitable for implementation on a technical scale or have other disadvantages such as costly reagents,

toxicity, low yield, and formation of byproducts.[32,39,40] Other methodologies to synthesize 3-trifluoromethylanilines on a larger scale involve expensive catalysts, heating, and high pressure.[41−44] In general, the catalytic hydrogenation of nitrobenzene is the main route for the commercial production of such anilines on a large scale.[45] Traditionally, nitrobenzene compounds are still reduced in aqueous solutions using reductive metal powders. This method leads to the formation of large quantities of metal oxides and hydroxides and will contain residual amines, whose disposal is becoming increasingly difficult in an environmentally conscious society.[39]

Recently, more effort has been focused on the nitro-reductive approaches, such as electrochemical reduction.[39,46−48] Electrochemical reduction has received significant attention because it is cleaner and more efficient and the costs are comparable with other cutting-edge techniques.[49,50] In electrosynthesis it is not necessary to use excess of reducing agents, rare and expensive catalyst (e.g., Pd), high pressures, or elevated temperatures since the activation by electrons occurs under mild and usually ambient conditions.[46] In contrast to reduction by dissolving metals, compatibility with strong acids is given.[51,49] The high tolerance to acids stems from the fact that common cathode materials (e.g., leaded bronze) have low
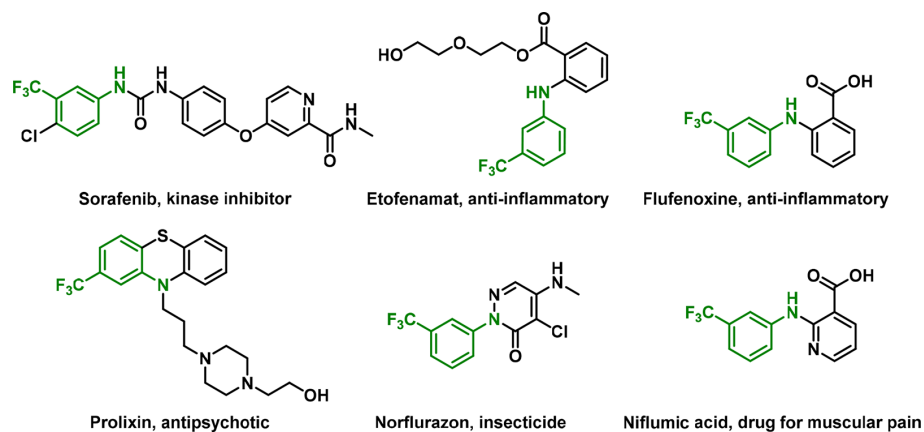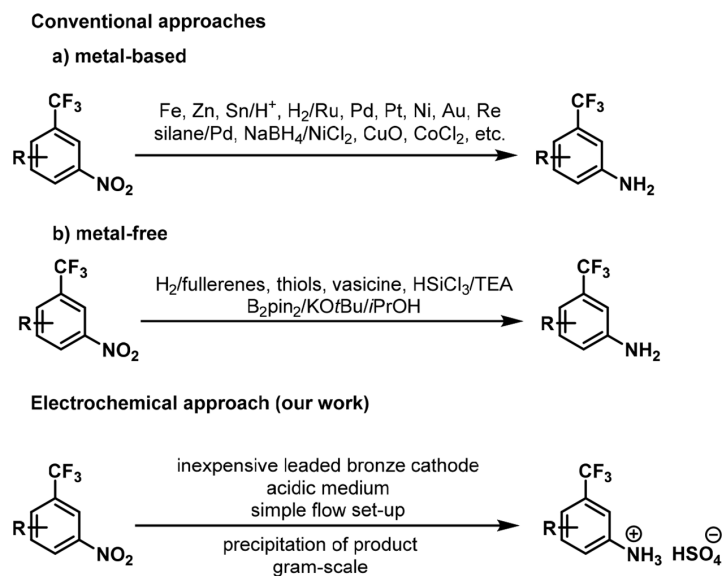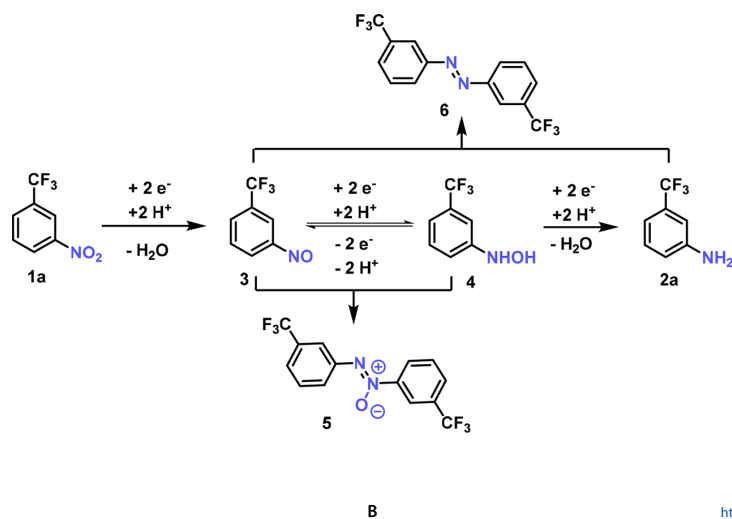
Figure 1. Examples of commercial molecules involving 3-trifluoromethylaniline moiety.

Scheme 1. Synthetic Strategies Leading to 3-Trifluoromethylanilines

Scheme 2. Reduction of Nitroarenes and Some Possible Reaction Pathways

B

exchange current densities for proton reduction. As a consequence, substrates with relatively high negative reduction potentials can be reduced selectively in the presence of various proton donors, such as common acidic conditions.[20,21]

However, the reduction of nitroaryls with electricity can lead to different products (Scheme 2). The electrolysis can yield nitroso compounds, hydroxylamines, and anilines as potential products.[46] As the nitroso group is more easily reducible than the nitro group, obtaining nitroso derivatives (3) by directly reducing a nitro group is difficult and requires, for example, specific electrolyzers which reoxidize the intermediate.[48,52,53] In contrast, hydroxylamines (4) usually are formed straight from the nitro reduction. Moreover, nitroso intermediates and hydroxylamines can condense to afford azoxybenzenes (5), which can be subsequently electroreduced to azobenzenes (6) or further to hydrazobenzenes. Analogously, the nitroso and aniline species can condense to azobenzene derivatives.[54,55] Furthermore, hydrazobenzenes can be electroreduced to anilines under acidic conditions. The reduction potentials of nitroarenes may vary significantly since they depend on the solvent, pH, electrode material, electrocatalyst, and substitution pattern at the aryl moiety.[46,48]

Given the importance of 3-trifluoromethylaniline building blocks and the challenges that remain for their synthesis, we propose the development of the electrochemical workflow to scale the production of 3-trifluoromethylanilinium bisulfate (2a) (Scheme 3). The cathodic process should be simple to

conduct and facilitate downstream processing in order to establish a novel multigram-scale electrosynthesis. Since the formed anilines are very prone to oxidation, the electrolysis has to be carried out in a divided electrolysis cell. Employment of a strong acidic electrolyte fulfills several requirements: the product can be handled at ambient conditions and might be crystallized as the final product. The use of electrocatalytic continuous recirculating mode can facilitate obtaining the desired product since the byproducts shown in Scheme 2 can be easily reduced in the process.

■ RESULTS AND DISCUSSION

All the experiments for the electroreduction of 3-nitro-benzotrifluoride derivatives (1a–h) to 3-trifluoromethylanilinium bisulfate derivatives (2a–h) were performed in divided cells using a Nafion membrane as a separator. The electrolysis was performed in constant-current mode for simplicity and subsequent scalability experiments.[56,57] The cathode material screening was conducted in divided batch-type cells. CV experiments were performed to assist in the choice of the working electrode. The screening of the other electrochemical parameters (anode, substrate concentration, and solvent) was also conducted in divided batch-type cells.[58,59] Divided flow cells using a Nafion membrane as a separator were used to scale up the production of the desired product.[60,61] The results are shown in relation to the formation of 2a. Since 2a precipitates in solution and can be collected by simple filtration, the isolated yield is easy to determine. Crystallography, NMR, ESI, and elemental analysis were employed to characterize the product.

Electrode Considerations (Cathode). Commonly, when electro-organic reduction is performed, strong negative potentials are required to replace hydrogen gas or hydrides as reducing reagents. Therefore, cathode materials with a high overpotential for the hydrogen evolution reaction (HER) must be applied. Carbon allotropes[62] and metal electrodes such as lead,[63] stainless steel,[64] and others are prominent materials for electro-organic reductions in protic media since they have high overpotential for HER. Bearing this in mind, we selected seven different materials as cathodes for the reduction of 3-nitrobenzotrifluoride (1a): lead (Pb), leaded bronze (CuSn7Pb15), graphite (C_{gr}), glassy carbon (GC), boron-

Scheme 3. Envisioned Electrochemical Synthesis of 3-Trifluoromethylanilinium Bisulfate
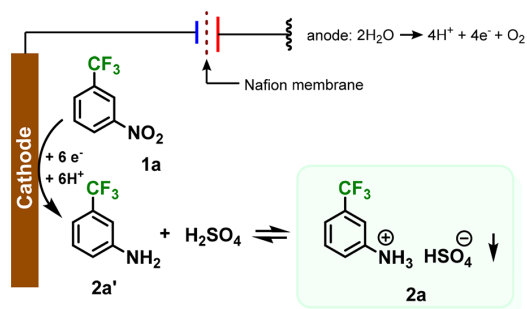
Table 1. Cathode Screening Experiments for Electrosynthesis of 3-Trifluoromethylanilinium Bisulfate (2a) in Batch-Type Cell[a]

Entry	Cathode	Yield of 2a [%][b]
1	GC	4
2	BDD	6
3	C_{gr}	5
4	Pt	7
5	Stainless Steel	11
6	Pb	14
7	**CuSn7Pb15**	**13**

[a]Reaction conditions: batch electrolyzer (anode|Nafion membrane|cathode, cathode area = 2 cm²), $j = 4$ mA cm⁻², $Q = 12F$, 2 × 6 mL of solvent (formed by a solution of 1:1 H_2O/MeOH), 2 M H_2SO_4(aq), room temperature. 2a′ yields were calculated by ¹⁹F NMR using ethyl trifluoroacetate as internal standard, and the values are reported in the SI. [b]Isolated yields of 2a.

C

Table 2. Selected Results of Screening Experiments for Synthesis of 2a in Batch-Type Cell (For More Details, See SI Section 5)[a]

Entry	Conc. of **1a** [mM][b]	j [mA cm^{-2}]	Anode	H$_2$O/MeOH[c]	Yield of **2a** [%][d]
1	80	4	GC	1:1	11
2	80	4	C$_{gr}$	1:1	12
3	80	4	BDD	1:1	−
4	80	4	C$_{gr}$	1:1	−
5	80	30	C$_{gr}$	1:1	14
6	80	40	C$_{gr}$	1:1	12
7	80	60	C$_{gr}$	1:1	7
8[e]	80	30	C$_{gr}$	1:1	15
9	320	30	C$_{gr}$	1:1	28
10	400	30	C$_{gr}$	1:1	32
11	400	30	C$_{gr}$	1:3	36
12[f]	**400**	**30**	**C$_{gr}$**	**1:3**	**69**

[a]Reaction conditions: batch electrolyzer (anode|Nafion membrane|CuSn7Pb15, cathode area = 2 cm^2), Q = 12F, 2 × 6 mL of solvent (formed by a solution of H$_2$O/MeOH at the indicated ratio), 2 M H$_2$SO$_{4(aq)}$, room temperature. **2a′** yields were calculated by ^{19}F NMR using ethyl trifluoroacetate as internal standard, and the values are reported in the SI. [b]The concentration is equivalent to the concentration of **1a** in catholyte. [c]Ratio of the amounts of H$_2$O and methanol solution. [d]Isolated yields of **2a**. [e]3 M H$_2$SO$_{4(aq)}$ was used. [f]100 μL of H$_2$SO$_4$ (96%) was added in catholyte compartment at the end of the reaction.

doped diamond (BDD), and stainless steel. Although platinum (Pt) has a low overpotential for HER, due to the catalytic features, it was also tested.

Batch-type electrolyses were performed in a divided cell setup using the previously mentioned cathodes (Table 1). The electrosynthetic experiments were conducted using 80 mM **1a**. C$_{gr}$ was employed as counter electrode, H$_2$O/MeOH (1:1) was used as solvent, and 2 M H$_2$SO$_{4(aq)}$ was used as electrolyte. The current density was set to 4 mA cm^{-2}, and a charge of 12F was applied. Initially, a low current density was applied to minimize the hydrogen evolution reaction. A charge of 12F was applied to achieve full conversion and to account for the HER, which could not be entirely avoided.

The metal-free electrodes (glassy carbon, BDD, and C$_{gr}$) showed a very low conversion resulting in only little precipitation of the salt **2a** (4, 6, and 5%, respectively; Table 1, entries 1−3), whereas Pt, stainless steel, lead, and leaded bronze showed 7, 11, 14, and 13% yield of **2a**, respectively (Table 1, entries 4−7).

In general, platinum, lead, and stainless steel showed promising results, whereas Pt, as expected, exhibits a very low overpotential for the parasitic HER at the given conditions. Furthermore, during the reactions, carbon allotropes and stainless steel electrodes exhibited corrosion (Figure S27). Lead could be a prominent material for electro-organic reductions in protic media since it has the high overpotential for HER. However, the corrosion can result in the toxic organolead compounds that are difficult to remove. Therefore, a cathode material that combines the performance of lead with a high mechanical and chemical stability is highly desired. Leaded bronze—a copper matrix alloy with tin and lead—is commercially available at low costs (approximately 10 € kg^{-1}). Also, it ensures a high selectivity and reactivity combined with a high chemical and mechanical stability.[65−69]

Among the tested cathode materials, the lead cathode resulted in the highest yield for **2a**, closely followed by the leaded bronze material. As described, the lead cathode is prone to cathodic corrosion.[49] In this study, we also observed alteration on the cathode surface when lead was used. Since the leaded bronze (CuSn7Pb15) exhibits a higher mechanical and chemical stability and considering the promising results achieved when leaded bronze was used as cathode, it was chosen as working electrode, which is of particular interest for flow cells.

Screening for the Electrosynthesis of 2a in Batch-Type Cells. Initially, batch-type experiments were carried out to improve the electrochemical synthesis of **2a** (Table 2 and Supporting Information (SI) Section 5). First, experiments to evaluate the effect of the anode material were performed using 80 mM **1a** in a solution of 1:1 H$_2$O/MeOH at room temperature employing CuSn7Pb15 as cathode. The methanol was used to improve the solubility of starting material. The electrolyte was 2 M H$_2$SO$_{4(aq)}$. A divided-beaker-type cell with a Nafion membrane was employed, and the electro-chemical parameters were adjusted to 4 mA cm^{-2} and 12F. The use of a divided cell is necessary to avoid the oxidation of the final product. Besides being necessary for the conversion and precipitation of **2a**, the acid is necessary to keep the pH constant in order to supply H$^+$ for the final product and promote the nitro reduction. GC, C$_{gr}$, BDD, and Pt were tested as anode materials.

When GC and C$_{gr}$ were employed, the formation of small amounts of pale-yellow solid (11 and 12%, respectively) was observed. The solid was filtered off, washed with cold water, and characterized by NMR analysis, confirming the formation of **2a**. On other hand, when platinum was employed as anode, it was not possible to obtain the desired salt **2a** as precipitate (Table 2, entry 3). The dissolved species of **2a′** amounts to a yield of 63%. Also, the formation of 1,2-bis(3-(trifluoromethyl)phenyl)diazene (**6**) in 8% yield was observed. For the azobenzene formation, the conversion of the nitro group in **1** to the nitroso group in **3** is most likely the key step

Table 3. Selected Results of Screening Experiments for Synthesis of 2a in Flow (For More Details, See SI Section 7)[a]

Entry	j [mA cm^{-2}]	Flow Rate [L h^{-1}]	C(H$_2$SO$_4$) [M][b]	Yield of 2a [%][c]
1	30	3.5	2	75 (709 mg)
2	30	4.0	2	79 (751 mg)
3	30	4.5	2	80 (759 mg)
4[d]	30	4.5	2	58 (825 mg)
5[e]	30	4.5	2	70 (661 mg)
6[f]	**30**	**4.5**	**2**	**85 (803 mg)**
7	30	4.5	3	77 (734 mg)
8	40	4.5	3	79 (756 mg)
9[g]	30	4.5	2	55 (8.4 g)

[a]Reaction conditions: flow electrolyzer (anode|Nafion membrane|CuSn7Pb15, cathode area = 12 cm^2), 400 mM **1a**, $Q = 12F$, 2 × 8 mL of solvent (formed by a solution of 1:1 H$_2$O/MeOH), room temperature. **2a′** yields were calculated by ^{19}F NMR using ethyl trifluoroacetate as internal standard, and the values are reported in the SI. [b]Equal to concentration of H$_2$SO$_4$(aq) added to the H$_2$O/MeOH solution. [c]Isolated yields of **2a**. [d]600 mM **1a** was used. [e]2 mL of 2 M H$_2$SO$_4$(aq) was added in catholyte compartment at 6F. [f]200 μL of H$_2$SO$_4$ (96%) was added in catholyte compartment at the end of the reaction. [g]The reaction was scaled up to 0.052 mol using a catholyte solution of 96 mL: 400 mm **1a**, 1:1 H$_2$O/MeOH, and 2 M H$_2$SO$_4$(aq).

of this transformation. As shown in Scheme 2, **1a** is converted to nitrosobenzene **3**, which reacts with a molecule of phenylhydroxylamine **4** to give azoxybenzene **5**, which is then further reduced to azobenzene **6**.[70,71]

Next, BDD was employed as the anode, and using the mentioned conditions no **2a** precipitation was observed (Table 2, entry 4). The dissolved species **2a′** amounts in this case to 75% yield. To our delight, within the carbon-based electrode materials screened, glassy carbon and graphite, the latter and most inexpensive material gave superior results.

After the variation of the anode material, the effect of different current densities was investigated. The current density j was screened from 4 to 60 mA cm^{-2} (Table 2, entries 5−7, and Table S3). Current density of 30 mA cm^{-2} favors the yield of **2a**, whereas higher current densities lead to inferior results. In order to minimize electrolysis time, a current density of 30 mA cm^{-2} (Table 2, entry 5) was chosen for the following experiments. The next screening experiments investigated the concentration of H$_2$SO$_4$(aq) in the reaction solution of H$_2$O/MeOH; a range from 1.5 to 5 M was tested. Up to 2 M the results for the formation of **2a** were similar (Table 2, entry 8, and Table S4). We also investigated the concentration of **1a**, applying concentrations in the range of 80−400 mM. Increasing the concentration of **1a** to 320 and 400 mM gave the precipitate **2a** in yields of 28 and 32%, respectively (Table 2, entries 9 and 10, and Table S5). Using a higher concentration of starting material, the saturation concentration of **2a** is easily reached, leading to an increased precipitation of **2a**.

As another parameter, the amount of methanol in the solution was investigated (Table S6). When a H$_2$O/MeOH ratio of 1:3 was employed in the reaction, a 36% yield of **2a** was obtained (Table 2, entry 11, and Table S6). Different alcohols, such as ethanol and butanol, were also tested as cosolvents (Table S7). When ethanol was used, we did not observe the formation of **2a**; instead, the dissolved product **2a′** remained in solution. When butanol was used, an 11% yield of salt **2a** was formed along with high amounts of an azo-type

byproduct (product **6**, Scheme 2). These and additional experiments are presented in detail in SI Section 5.

Considering that H$_2$SO$_4$ is consumed during the process (by precipitation of the bisulfate salt), a further increase in acid concentration finally led to better results for the precipitation of the salt in the reaction (Table 2, entry 12, and Table S8). After 2 h, it was possible to recover **2a** in 69% isolated yield. Here, the amount of the added acid supplies the theoretical amount of acid necessary for reduction and formation of salt.

Subsequently, a suitable single crystal of the product was analyzed by crystallography. For the crystallography analysis it was possible to observe the formation of the 3-trifluoromethylanilinium sulfate in an equivalence of 2:1 of the cation 3-trifluoromethylanilinium and the anion sulfate (SI Section 14). However, elemental analysis (SI Section 15) was used to confirm the product structure as 3-trifluoromethylanilinium bisulfate **2a**. The composition found by elemental analysis equals C$_7$H$_7$F$_3$N(HSO$_4$)·2H$_2$O. The identified composition was used to calculate all isolated yields.

Scale-Up of the Electrosynthesis of 3-Trifluoromethylanilinium Bisulfate. Since this work aimed to address the scale-up of the 3-trifluoromethylanilinium bisulfate electrosynthesis, the reaction was then transferred to a flow cell. Flow electrolysis is particularly well suited for scale-up, since the electrode to cell volume (interelectrode gap) can be constant over a wide range of scales. In batch-type cells, electrolyte agitation may become less effective.[69,72,73] In flow electrosynthesis three key parameters can be optimized to help increase the productivity of a transformation: electrode surface area, current density, and Faradaic efficiency. The electrode surface area is a reactor-specific parameter that can be maximized upon scale-up by employing larger or multiple electrodes. In contrast, optimal current density and Faradaic efficiency are reaction attributes that depend on the reaction conditions employed (e.g., electrode material, solvent, electrolyte, and concentration of the substrate).[6]

To start scale-up experiments, a modular flow cell based on Teflon casing was used for the reduction of **1a** (cathode area = 12 cm^2).[60,69] The system is commercially available as

E

Scheme 4. Electrosynthesis of 3-Trifluoromethylanilinium Bisulfate (2a) in Flow Conditions
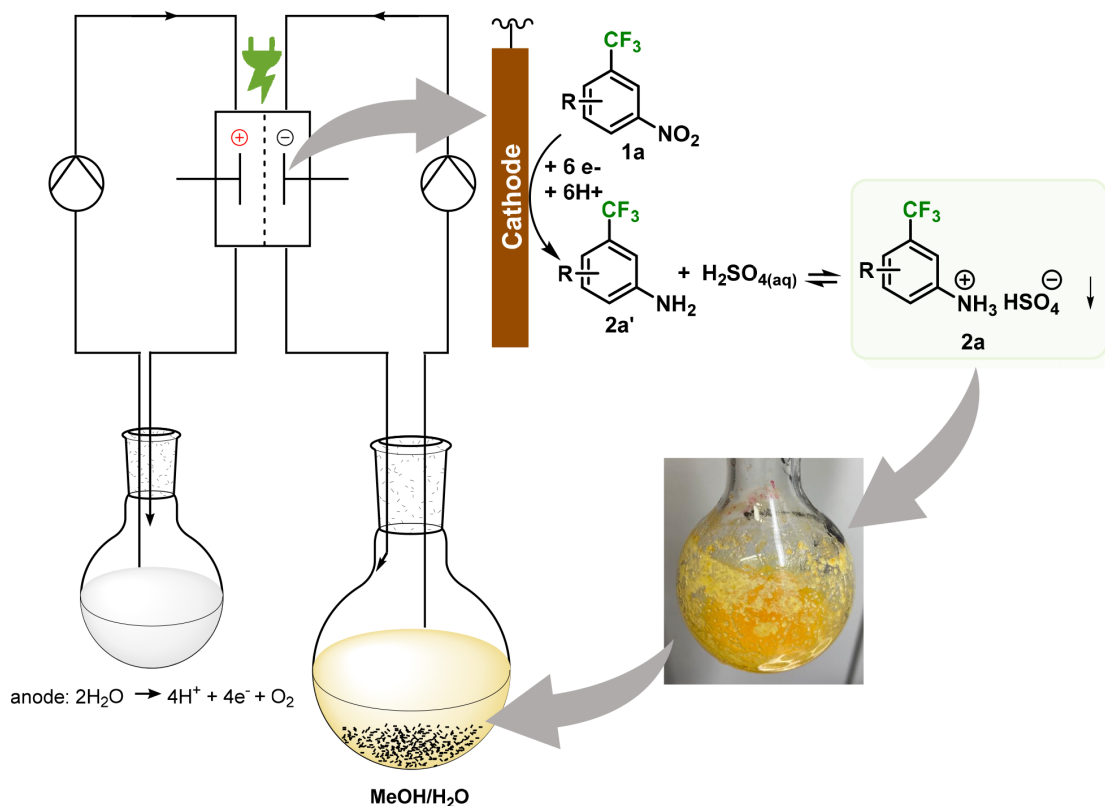
ElectraSyn flow (IKA Werke GmbH & Co. KG, Staufen, Germany). C_{gr} was used as the anode and CuSn7Pb15 as the cathode. The cell was divided by Nafion, and both electrolytes (V = 6 mL) were pumped in two independent cycles. Accordingly, all flow experiments described in this study were performed under continuous recirculating mode. When performing the reaction in flow under these conditions, we were able to drive the reaction to full conversion with a similar purity profile and yield compared to those using batch-type cells. Initially, the electrochemical parameters applied were $12F$, 30 mA cm^{-2}, 400–800 mM **1a**, and 2–5 M H_2SO_4(aq) using 1:1 H_2O/MeOH as solvent. A yield of **2a** up to 23% was obtained using the following conditions: 400 mM **1a**, 2.5 L h^{-1}, $12F$, 30 mA cm^{-2}, and 3 M H_2SO_4(aq). These experiments and additional experiments are presented in detail in SI Section 6.

However, in most previous experiments clogging issues were observed. The problem could be circumvented by increasing the reaction volume and the flow rate. These changes made it possible to expel the formed salt **2a** faster from the cell, avoiding clogging. The results of the optimization using the new setup are illustrated in Table 3 and SI Section 7. An illustration of the flow setup can be found in Figure S28. By increasing the flow rate and volume it was possible to obtain the **2a** salt in 75% yield (Table 3, entry 1), representing a significant increase compared to the previous result of 23% yield.

Parameter variation of the **1a** concentration (400–600 mM), current density (30–40 mA cm^{-2}), H_2SO_4(aq)
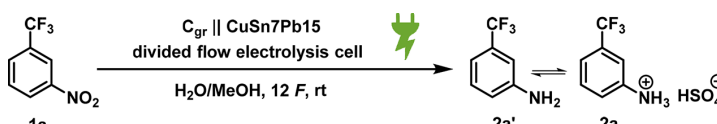
concentration (2–3 M), and flow rate (3.5–4.5 L h^{-1}) were investigated. The following reaction conditions were identified by optimization studies: 400 mM concentration of **1a**, a current density of 30 mA cm^{-2}, 2 M H_2SO_4(aq) in a solution of 1:1 H_2O/MeOH, an applied charge of $12F$, and 4.5 L h^{-1} (Table 3, entry 3). Utilizing the aforementioned conditions, it was possible to obtain the **2a** in 80% yield. During electrolysis, the cathodic solution had a pale-yellow color that changed to yellow at around $3F$. At $7F$ a light-yellow solid precipitated and formed a suspension. Also, an increase in hydrogen evolution can be observed after $7F$. Scheme 4 illustrates the electrosynthesis of **2a** in continuous flow.

Similar to the batch experiments, a further increase in acid concentration finally led to better results for the precipitation of the salt **2a** (Table 3, entry 6). After 2 h, it was possible to recover **2a** in 85% of isolated yield.

Guided by the good results, the next step was scaling up the reaction, considering the substrate mass. The reaction was scaled up from 0.0032 to 0.052 mol. Thus, 96 mL of 0.4 M **1a** (0.052 mol) in H_2O/MeOH and 2 M H_2SO_4(aq) was prepared and added to the catholyte compartment (Table 3, entry 9). The same electrochemical conditions as shown in Table 3, entry 6 were employed. After electrolysis, **2a** was isolated by simple filtration and washed with cold water and hexane, obtaining 55% yield (8.4 g). The decrease in the formation of **2a** could be associated with a low solubility of **1a** in the reaction medium. The low homogenization of the solution hinders the constant entry of the starting material. Finally, **1a** was found in 17% yield.

Table 4. Selected Results of Scale-Up Experiments for Synthesis of 2a in Flow (For More Details, See Table S15)[a]

Entry	Conc. of 1 [mM][b]	j [mA cm^{-2}]	Flow Rate [L h^{-1}]	C(H$_2$SO$_4$) [M][c]	V [mL]	Yield of 2a [%][d]
1	400	30	4.5	2	50	8 (0.5 g)
2	400	30	5.0	2	50	20 (1.2 g)
3	400	30	7.5	2	50	49 (2.9 g)
4	400	40	7.5	2	50	37 (2.2 g)
5	400	60	7.5	2	50	23 (1.4 g)
6	600	30	7.5	2	50	78 (6.9 g)
7	600	30	7.5	3	50	74 (6.6 g)
8	600	30	7.5	5	50	80 (7.1 g)
10	**600**	**30**	**7.5**	**5**	**100**	**81 (14.1 g)**
11	600	30	7.5	5	200	76 (27.0 g)
12	600	30	7.5	5	500	73 (64.6 g)
13	600	30	7.5	5	800	76 (107.0 g)

[a]Reaction conditions: flow electrolyzer (anode|Nafion membrane|CuSn7Pb15, cathode area = 48 cm^2), Q = 12F, H$_2$O/MeOH solvent ratio 1:1–1:3 (50–200 mL), room temperature. 2a′ yields were calculated by ^{19}F NMR using ethyl trifluoroacetate as internal standard, and the values are reported in the SI. [b]The concentration is equivalent to the concentration of 1a in catholyte. [c]Equal to concentration of H$_2$SO$_4$ added to the H$_2$O/MeOH solution. [d]Isolated yields of 2a.

Scheme 5. Scope of Nitro Reduction in Batch Conditions
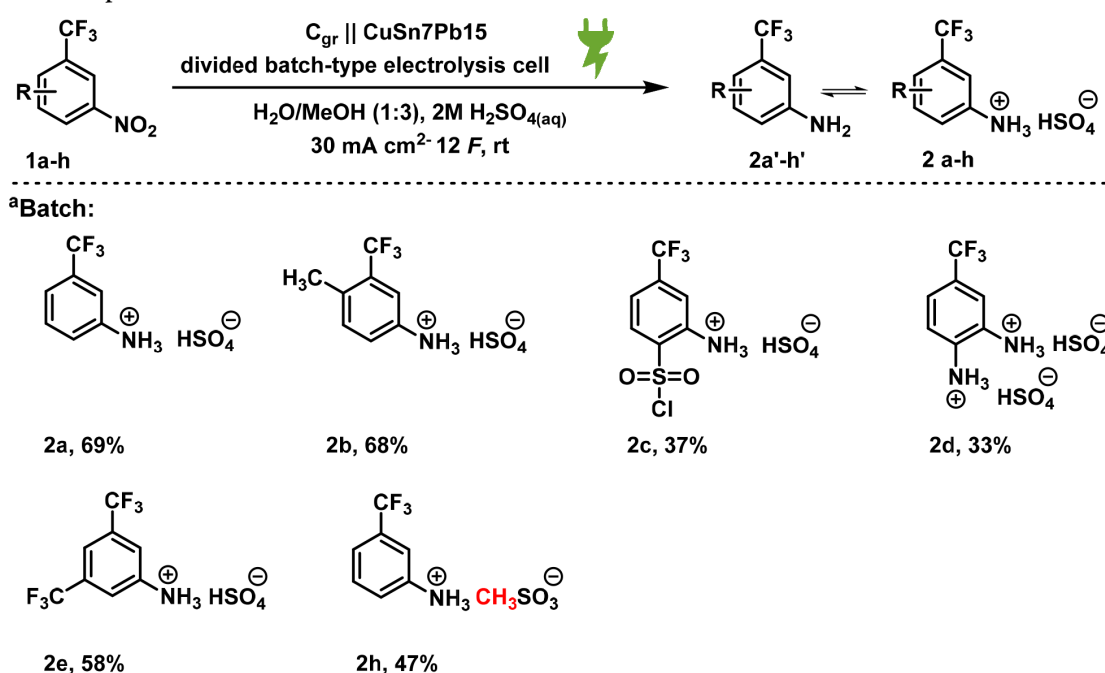
[a]Reaction conditions: batch electrolyzer (anode|Nafion membrane|CuSn7Pb15, cathode area = 2 cm^2), 400 mM 1a, Q = 12F, j = 30 mA cm^{-2}, 6 mL of 1:1 H$_2$O/MeOH, 2 M H$_2$SO$_4$(aq), room temperature. 2′ yields were calculated by ^{19}F NMR using ethyl trifluoroacetate as internal standard, and the values are reported in the SI. Isolated yields of 2 are reported. [b]2 M methanesulfonic acid was used.

In further scale-up, the cathode area was increased. A modular flow cell based on Teflon casing with the cathode area of 48 cm^2 developed by our group was employed first.[74] Notably, conditions were applied similar to the ones presented in Table 3, entry 6. However, using a 50 mL reaction solution, clogging was exceedingly observed due to the precipitation of 2a. The clogging required disassembly and cleaning of the cell, which resulted in significant maintenance efforts. To avoid this problem, a second modular flow cell based on Teflon casing with cathode area of 48 cm^2 developed by our group was employed. In this case, the cell has a different design at the exit and feed—not using microchannels but using a single channel for the outlet and inlet. These favor expelling the suspension

Scheme 6. Substrate Scope Study Using Flow Conditions
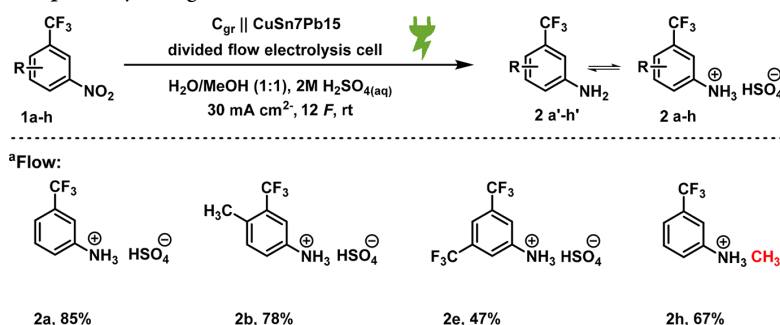
[a]Reaction conditions: flow electrolyzer (anode|Nafion membrane|CuSn7Pb15, cathode area = 12 cm^2), 400 mM **1a**, Q = 12F, j = 30 mA cm^{-2}, 2 × 6 mL 1:1 H$_2$O/MeOH, 2 M H$_2$SO$_4$(aq), room temperature. **2'** yields were calculated by ^{19}F NMR using ethyl trifluoroacetate as internal standard, and the values are reported in the SI. Isolated yields of **2** are reported. ^{b}2 M methanesulfonic acid was used.

containing the formed salt more easily (see Figures S31 and S32 for details,).[75,76]

Comparable results were obtained in terms of isolated yield as a function of charge for the cathode areas of 12 and 48 cm^2 (Table 4 and SI Section 7.7). Salt **2a** was produced in up to 78% yield in the screening of the concentration (Table 4, entry 6), which improved slightly to 81% when the volume was increased 2-fold and 5 M acid was used (Table 4, entry 10). With the increase in the reaction volume, it was possible to obtain larger amounts of **2a** per run (Table 4, entries 11−13). When the reaction volume was increased to 800 mL, it was possible to obtain 107.0 g of **2a** per run (∼1 g h^{-1}) (Table 4, entry 13). It is important to note that using this flow cell no clogging was observed.

Additionally, ICP-OES experiment showed that in the 200 mL volume experiment 5.61 ppm lead was found in the crude solution and 0.21 ppm in the final product. Current tolerable lead limits in pharmaceutical substances in some cases exceed 10 ppm according to the United States Pharmacopeia (USP).[77]

Scope Elucidation. With the optimized conditions for batch and flow experiments, attention was turned toward examining the compatibility of other 3-nitrobenzotrifluoride substrates with the developed reaction conditions. It is noteworthy that these experiments were performed using the IKA flow cell with a relevant electrode active surface area of 12 cm^2. For this 1-methyl-4-nitro-2-(trifluoromethyl)benzene (**1b**), 2-nitro-4-(trifluoromethyl)benzenesulfonyl chloride (**1c**), 4-trifluoromethyl-2-nitroaniline (**1d**), 1-nitro-3,5-bis-(trifluoromethyl)benzene (**1e**), 4-(trifluoromethyl)-2-nitro-benzaldehyde (**1f**), and 2-nitro-1,4-bis(trifluoromethyl)-benzene (**1g**) were used.

In experiments using batch-type cells, five different trifluoromethyl nitro compounds (**1a–e**) were successfully converted to the desired products with yields between 33 and 69%. When **1f** and **1g** were used as substrates, the desired salt was not observed. Also, methanesulfonic acid could be used as acid source, giving the formation of **2h** from **1a**. Scheme 5 displays the results for the reduction of nitro compounds **1a−e** to the corresponding 3-trifluoromethylanilinium bisulfate derivatives **2a−e** and **2h**.

The compounds that were successfully converted to the desired product in batch were then tested using the optimized flow conditions (Scheme 6). In this case, three trifluoromethyl nitro compounds formed the desired salts (**1a**, **1b**, and **1e**) in

81, 78, and 47% yield, respectively. The syntheses of **2c** and **2d** were not possible in flow, as the low solubility of the solid starting materials led to clogging of the continuous flow system.

■ CONCLUSION

We have surveyed a new approach to the electrochemical synthesis of 3-trifluoromethylanilinium bisulfate derivatives by batch-type and flow conditions. The presented protocol allows precipitation in a reservoir, leading to easy downstream processing, which is highly advantageous from an industrial point of view. For obtaining the pure product, inexpensive electrodes were used, graphite as anode and leaded bronze alloy as cathode. In the batch experiments, it was possible to obtain the desired product in 69% isolated yield, while in flow conditions the product was obtained in 81% isolated yield. When the flow conditions were scaled up, it was possible to obtain the desired product at a rate of ∼1 g h^{-1}, summing up to 107 g per run. In addition, we demonstrated that the methodology could be extended to a broader scope. In total, six different 3-trifluoromethylanilinium bisulfates were synthesized in batch, and four of them were translated to flow conditions. The developed electrochemical protocol can be considered an example for the sustainable use of electric current as reagent and might inspire other process development projects given the demonstrated scalability of the electrochemical reaction conditions coupled with the inherent advantages of continuous chemistry.

■ EXPERIMENTAL SECTION

General Information. All reagents were used in analytical or sufficiently pure grades. All reactions were carried out at ambient pressure and temperature unless otherwise stated. Reactions were monitored by TLC (silica gel 60 F254, Merck KGaA, Darmstadt, Germany). ^{1}H, ^{13}C, and ^{19}F NMR spectra were acquired on a Bruker Avance III HD 300, Avance II 400, or Avance III HD 400 spectrometer (Bruker, Karlsruhe, Germany) in DMSO-d_6 at 25 °C. Mass spectra via electrospray ionization (ESI±) or atmospheric-pressure chemical ionization (APCI±) mass spectrometry were recorded using an Agilent G6545A QTOF-MS (Agilent, Santa Clara, CA, USA). For the electrolysis, electrodes were obtained from commercial suppliers: boron-doped diamond (DIACHEM, 15 μm diamond layer on silicon support, CONDIAS GmbH, Itzehoe,

Germany), glassy carbon (SIGRADUR G, HTW, Thierhaupten, Germany), platinum (Ögussa, Vienna, Austria), isostatic graphite (Sigrafine V2100, SGL Carbon, Bonn, Germany), CuSn7Pb15 (Metallwerke Langenau GmbH, Langenau, Germany), and stainless steel (type EN1.4401, Montanstahl GmbH, Oelde, Germany). Nafion N324 from DuPont was used as membrane. A galvanostatic HMP4040 power source from Rohde & Schwarz was used. Detailed and comprehensive descriptions of the analytical experimentation can be found in the SI.

General Protocol for Batch-Type Electrolysis. Batch-type screening experiments were conducted in divided Teflon electrolysis cells.[58,59] This batch-type cell is commercially available as IKA Screening system package (IKA Werke GmbH & Co. KG, Staufen, Germany). In the batch-type cell (Figure S2) divided through Nafion N324 membrane (DuPont, Wilmington, DE, United States), both compartments were filled with 1:3 H_2O/MeOH (2×6 mL) and 2 M H_2SO_4(aq). The molarity of H_2SO_4(aq) equals the concentration of the acid added to H_2O/MeOH solution. The 3-nitrobenzotrifluoride derivative (**1a−g**) (2.4 mmol, 400 mM) was added to the cathode compartment, and the electrolysis was started with graphite as anode and CuSn7Pb15 as cathode. Both electrodes have an active surface of 2 cm^2 and were arranged in 2 cm distance relative to each other. Each cell compartment was equipped with a round magnetic stir bar. A given amount of applied charge (12F), and a given current density (30 mA cm^{-2}) were set. The reaction was performed at room temperature. After electrolysis, 100 μL of H_2SO_4 (96%) was added to the catholyte. After 2 h the content of the cathode compartment was collected. The solid was filtered. The liquid phase of the filtration was used to determine the yields of starting material **1a−g** and dissolved product by ^{19}F NMR spectroscopy, using as standard ethyl trifluoroacetate. The solid part was washed with cold water and cyclohexane. After, the solid was dried under reduced pressure, and the isolated yield for the 3-trifluoromethylanilinium bisulfate derivative was determined. In the case of **2h** synthesis, methanesulfonic acid (2 M) was used instead of sulfuric acid.

General Protocol for Flow Electrolysis (2 cm × 6 cm Cathode Surface). Flow electrolyses were performed in a modular flow cell based on Teflon that was designed by the Waldvogel research group (Figure S3)[60,61] and is commercially available as ElectraSyn flow (IKA Werke). The cell consists of two Teflon half-cells. Each half-cell contains an electrode with an active surface of 12 cm^2. A Nafion N324 membrane (DuPont) was used as separator, tethered with Teflon spacers (0.5 mm). Two Ritmo R033 pumps from Fink were used to propel the anolyte and catholyte into the cell. Graphite was used as anode, and CuSn7Pb15 was used as cathode. The 3-nitrobenzotrifluoride derivative (**1a−e**) (3.2 mmol, 400 mM) was dissolved in 1:1 H_2O/MeOH (2×8 mL) solution, and 2 M H_2SO_4(aq) was used as electrolyte. The molarity of H_2SO_4(aq) equals the concentration of the acid added to H_2O/MeOH solution. A given amount of applied charge (12F), a given current density (30 mA cm^{-2}), and a given flow rate were set. After electrolysis, 200 μL of H_2SO_4 (96%) was added to the catholyte. After 2 h the content of the cathode compartment was collected. The solid was filtered. The liquid phase of the filtration was used to determine the yields of starting material **1a−e** and dissolved product by ^{19}F NMR spectroscopy, using as standard ethyl trifluoroacetate. The solid part was washed with cold water and cyclohexane. After,

the solid was dried under reduced pressure, and the isolated yield for the 3-trifluoromethylanilinium bisulfate derivative **2a−e** was determined. In the case of **2h** synthesis, methanesulfonic acid (2 M) was used instead of sulfuric acid.

General Protocol for Flow Electrolysis (4 cm × 12 cm Cathode Surface). Flow electrolyses were performed in electrolysis cells that were designed by the Waldvogel research group.[75,76] Each half-cell contains an electrode with an active surface of 48 cm^2. A Nafion N324 membrane (DuPont) was used as a separator tethered with ethylene propylene diene monomer (EPDM) spacers (1.0 mm). Two Ritmo R033 pumps from Fink were used to propel the anolyte and catholyte into the cell. Graphite was used as anode, and CuSn7Pb15 was used as cathode. The 3-nitrobenzotrifluoride (**1a**) (400−800 mM) was dissolved in 1:1−1:3 H_2O/MeOH solution, and 2−5 M H_2SO_4(aq) was used as electrolyte. The molarity of H_2SO_4(aq) equals the concentration of the acid added to H_2O/MeOH solution. A given amount of applied charge, a given current density, and a given flow rate were set. After electrolysis, the content of the cathode compartment was collected. The solid was filtered. The liquid phase of the filtration was used to determine the yields of starting material **1a** and dissolved product **2a′** by ^{19}F NMR spectroscopy, using as standard ethyl trifluoroacetate. The solid part was washed with cold water and cyclohexane. After, the solid was dried under reduced pressure, and the isolated yield for 3-trifluoromethylanilinium bisulfate **2a** was determined.

■ ASSOCIATED CONTENT

Ⓢ Supporting Information

The Supporting Information is available free of charge at https://pubs.acs.org/doi/10.1021/acs.oprd.3c00067.

> Used equipment supported by pictures and explosion drawings, used chemicals, preliminary experiments, representative procedures, monitoring results, calculation of yields, analytical spectra, electrode screening supported by pictures, and flow experiments supported by pictures (PDF)
>
> Crystallographic data for **2a** (CIF)

■ AUTHOR INFORMATION

Corresponding Author

Siegfried R. Waldvogel − *Department of Chemistry, Johannes Gutenberg University Mainz, 55128 Mainz, Germany; ESy-Laboratories GmbH, 93055 Regensburg, Germany; Institute of Biological and Chemical Systems—Functional Molecular Systems (IBCS-FMS), 76344 Eggenstein-Leopoldshafen, Germany;* ⊙ orcid.org/0000-0002-7949-9638; Email: waldvogel@uni-mainz.de

Authors

Camila M. Kisukuri − *Department of Chemistry, Johannes Gutenberg University Mainz, 55128 Mainz, Germany*

Johannes Seidler − *Department of Chemistry, Johannes Gutenberg University Mainz, 55128 Mainz, Germany; ESy-Laboratories GmbH, 93055 Regensburg, Germany*

Tobias Gärtner − *ESy-Laboratories GmbH, 93055 Regensburg, Germany*

Denis F. Rohrmann − *Department of Chemistry, Johannes Gutenberg University Mainz, 55128 Mainz, Germany*

Complete contact information is available at:
https://pubs.acs.org/10.1021/acs.oprd.3c00067

■ ACKNOWLEDGMENTS

■ ABBREVIATIONS

CV, cyclic voltammetry; NMR, nuclear magnetic resonance; ESI, electrospray ionization; GC, glassy carbon; BDD, boron-doped diamond; C_{gr}, graphite; V, volts; HER, hydrogen evolution reaction; F, Faraday

■ REFERENCES

(1) Yan, M.; Kawamata, Y.; Baran, P. S. Synthetic Organic Electrochemical Methods Since 2000: On the Verge of a Renaissance. *Chem. Rev.* **2017**, *117*, 13230−13319.

(2) Tay, N. E. S.; Lehnherr, D.; Rovis, T. Photons or Electrons? A Critical Comparison of Electrochemistry and Photoredox Catalysis for Organic Synthesis. *Chem. Rev.* **2022**, *122*, 2487−2649.

(3) Leech, M. C.; Garcia, A. D.; Petti, A.; Dobbs, A. P.; Lam, K. Organic Electrosynthesis: From Academia to Industry. *React. Chem. Eng.* **2020**, *5*, 977−990.

(4) Wiebe, A.; Gieshoff, T.; Möhle, S.; Rodrigo, E.; Zirbes, M.; Waldvogel, S. R. Electrifying Organic Synthesis. *Angew. Chem., Int. Ed.* **2018**, *57*, 5594−5619.

(5) Möhle, S.; Zirbes, M.; Rodrigo, E.; Gieshoff, T.; Wiebe, A.; Waldvogel, S. R. Modern Electrochemical Aspects for the Synthesis of Value-added Organic Products. *Angew. Chem., Int. Ed.* **2018**, *57*, 6018−6041.

(6) Bottecchia, C.; Lehnherr, D.; Lévesque, F.; Reibarkh, M.; Ji, Y.; Rodrigues, V. L.; Wang, H.; Lam, Y.; Vickery, T. P.; Armstrong, B. M.; Mattern, K. A.; Stone, K.; Wismer, M. K.; Singh, A. N.; Regalado, E. L.; Maloney, K. M.; Strotman, N. A. Kilo-Scale Electrochemical Oxidation of a Thioether to a Sulfone: A Workflow for Scaling up Electrosynthesis. *Org. Process Res. Dev.* **2022**, *26*, 2423−2437.

(7) Lund, H. A Century of Organic Electrochemistry. *J. Electrochem. Soc.* **2002**, *149*, S21−S33.

(8) Wang, J. *Analytical Electrochemistry*, 3rd ed.; Wiley-VCH: Weinheim, Germany, 2006; pp 1−28.

(9) Malkowsky, I. M.; Rommel, C. E.; Fröhlich, R.; Griesbach, U.; Pütter, H.; Waldvogel, S. R. Novel Template-Directed Anodic Phenol-Coupling Reaction. *Chem. - Eur. J.* **2006**, *12*, 7482−7488.

(10) Gütz, C.; Bänziger, M.; Bucher, C.; Galvão, T. R.; Waldvogel, S. R. Development and Scale-Up of the Electrochemical Dehalogenation for the Synthesis of a Key Intermediate for NS5A Inhibitors. *Org. Process Res. Dev.* **2015**, *19*, 1428−1433.

(11) Ding, H.; DeRoy, P. L.; Perreault, C.; Larivée, A.; Siddiqui, A.; Caldwell, C. G.; Harran, S.; Harran, P. G. Electrolytic Macro-cyclizations: Scalable Synthesis of a Diazonamide-Based Drug Development Candidate. *Angew. Chem., Int. Ed.* **2015**, *54*, 4818−4822.

(12) Horn, E. J.; Rosen, B. R.; Chen, Y.; Tang, J.; Chen, K.; Eastgate, M. D.; Baran, P. S. Scalable and Sustainable Electrochemical Allylic C-H Oxidation. *Nature* **2016**, *533*, 77−81.

(13) Kawamata, Y.; Vantourout, J. C.; Hickey, D. P.; Bai, P.; Chen, L.; Hou, Q.; Qiao, W.; Barman, K.; Edwards, M. A.; Garrido Castro, A. F.; DeGruyter, J. N.; Nakamura, H.; Knouse, K.; Qin, C.; Clay, K. J.; Bao, D.; Li, C.; Starr, J. T.; Garcia-Irizarry, C.; Sach, N.; White, H. S.; Neurock, M.; Minteer, S. D.; Baran, P. S. Electro Chemically Driven, Ni-Catalyzed Aryl Amination: Scope, Mechanism, and Applications. *J. Am. Chem. Soc.* **2019**, *141*, 6392−6402.

(14) Gnaim, S.; Takahira, Y.; Wilke, H. R.; Yao, Z.; Li, J.; Delbrayelle, D.; Echeverria, P.-G.; Vantourout, J. C.; Baran, P. S. Electrochemically Driven Desaturation of Carbonyl Compounds. *Nat. Chem.* **2021**, *13*, 367−372.

(15) Cai, C.-Y.; Shu, X.-M.; Xu, H.-C. Practical and Stereoselective Electrocatalytic 1,2-Diamination of Alkenes. *Nat. Commun.* **2019**, *10*, 4953.

(16) Peters, B. K.; Rodriguez, K. X.; Reisberg, S. H.; Beil, S. B.; Hickey, D. P.; Kawamata, Y.; Collins, M.; Starr, J.; Chen, L.; Udyavara, S.; Klunder, K.; Gorey, T. J.; Anderson, S. L.; Neurock, M.; Minteer, S. D.; Baran, P. S. Scalable and Safe Synthetic Organic Electroreduction Inspired by Li-Ion Battery Chemistry. *Science* **2019**, *363*, 838−845.

(17) Teresh Chenko, O. D.; Perebiynis, M. Y.; Knysh, I. V.; Vasylets, O. V.; Sorochenko, A. A.; Slobodyanyuk, E. Y.; Rusanov, E. B.; Borysov, O. V.; Kolotilov, S. V.; Ryabukhin, S. V.; Volochnyuk, D. M. Electrochemical Scaled-up Synthesis of Cyclic Enecarbamates as Starting Materials for Medicinal Chemistry Relevant Building Blocks. *Adv. Synth. Catal.* **2020**, *362*, 3229−3242.

(18) Zhong, X.; Hoque, M. A.; Graaf, M. D.; Harper, K. C.; Wang, F.; Genders, J. D.; Stahl, S. S. Scalable Flow Electrochemical Alcohol Oxidation: Maintaining High Stereochemical Fidelity in the Synthesis of Levetiracetam. *Org. Process Res. Dev.* **2021**, *25*, 2601−2607.

(19) Barton, L. M.; Chen, L.; Blackmond, D. G.; Baran, P. S. Electrochemical Borylation of Carboxylic Acids. *Proc. Natl. Acad. Sci. U. S. A.* **2021**, *118*, e2109408118.

(20) Zhang, H.-J.; Chen, L.; Oderinde, M. S.; Edwards, J. T.; Kawamata, Y.; Baran, P. S. Chemoselective, Scalable Nickel-Electrocatalytic O-Arylation of Alcohols. *Angew. Chem., Int. Ed.* **2021**, *60*, 20700−20705.

(21) Shono, T.; Matsumura, Y.; Tsubata, K. Anodic Oxidation of N-Carbomethoxypyrrolidine: 2-Methoxy-N Carbomethoxypyrrolidine. *Org. Synth.* **1985**, *63*, 206.

(22) Egbert, J. D.; Thomsen, E. C.; O'Neill-Slawecki, S. A.; Mans, D. M.; Leitch, D. C.; Edwards, L. J.; Wade, C. E.; Weber, R. S. Development and Scale up of Continuous Electrocatalytic Hydrogenation of Functionalized Nitro Arenes, Nitriles, and Unsaturated Aldehydes. *Org. Process Res. Dev.* **2019**, *23*, 1803−1812.

(23) Yang, W.; Chen, Y.; Zhou, X.; Gu, Y.; Qian, W.; Zhang, F.; Han, W.; Lu, T.; Tang, W. Design, Synthesis and Biological Evaluation of Bis-Aryl Ureas and Amides Based on 2-Amino-3-Purinylpyridine Scaffold as DFG-out B-Raf Kinase Inhibitors. *Eur. J. Med. Chem.* **2015**, *89*, 581−596.

(24) Wang, Q.; Tang, B.; Sun, D.; Dong, Y.; Ji, Y.; Shi, H.; Zhou, L.; Yang, Y.; Luo, M.; Tan, Q.; Chen, L.; Dong, Y.; Li, C.; Xie, R.; Zang, Y.; Shen, J.; Xiong, B.; Li, J.; Chen, D. Discovery of 4-Cyclopropyl-3-(2-((1-cyclopropyl-1*H*-pyrazol-4-yl)amino)quinazolin-6-yl)-*N*-(3-(trifluoromethyl)phenyl)benzamides as Potent Discoidin Domain Receptor Inhibitors for the Treatment of Idiopathic Pulmonary Fibrosis. *Acta Pharm. Sin. B* **2022**, *12*, 1943−1962.

(25) Lamberth, C. Organic Isocyanates and Isothiocyanates: Versatile Intermediates in Agrochemistry. *Synthesis* **2022**, *54*, 1250−1260.

(26) Knighton, W. B.; Grimsrud, E. P. Gas-Phase Electron-Transfer Reactions between Selected Molecular Anions and Halogenated Methanes. *J. Am. Chem. Soc.* **1992**, *114*, 2336−2342.

(27) Paul, G. J. C.; Kebarle, P. Stabilities of complexes of bromide with substituted benzenes (SB) based on determinations of the gas-phase equilibria Br⁻ + SB = (BrSB)⁻. *J. Am. Chem. Soc.* **1991**, *113*, 1148−1154.

(28) Ung, S.; Falguières, A.; Guy, A.; Ferroud, C. Ultrasonically Activated Reduction of Substituted Nitrobenzenes to Corresponding N-Arylhydroxylamines. *Tetrahedron Lett.* **2005**, *46*, 5913−5917.

(29) Benkeser, R. A.; Buting, W. E. The Preparation of Aromatic Amines with Sodium Amide in Liquid Ammonia. *J. Am. Chem. Soc.* **1952**, *74*, 3011−3014.

(30) Roberts, J. D.; Vaughan, C. W.; Carlsmith, L. A.; Semenow, D. A. Orientation in Animations of Substituted Halobenzenes1. *J. Am. Chem. Soc.* **1956**, *78*, 611−614.

(31) Rahaim, R. J., Jr.; Maleczka, R. E., Jr. Palladium-Catalyzed Silane/Siloxane Reductions in the One-Pot Conversion of Nitro Compounds into Their Amines, Hydroxylamines, Amides, Sulfon Amides, and Carbamates. *Synthesis* **2006**, *2006*, 3316−3340.

(32) Tordeux, M.; Wakselman, C. The Bamberger Reaction in Hydrogen Fluoride: The Use of Mild Reductive Metals for the Preparation of Fluoroaromatic Amines. *J. Fluorine Chem.* **1995**, *74*, 251−254.

(33) Belley, M.; Sauer, E.; Beaudoin, D.; Duspara, P.; Trimble, L. A.; Dubé, P. Synthesis and Reactivity of *N*-Hydroxy-2-Aminoindoles. *Tetrahedron Lett.* **2006**, *47*, 159−162.

(34) Guan, X.; Zhu, H; Driver, T. G. Cu-Catalyzed Cross-Coupling of Nitroarenes with Aryl Boronic Acids to Construct Diarylamines. *ACS Catal.* **2021**, *11*, 12417−12422.

(35) González-Lainez, M.; Jiménez, M. V.; Passarelli, V.; Pérez-Torrente, J. J. Effective N-Methylation of Nitroarenes with Methanol Catalyzed by a Functionalized NHC-Based Iridium Catalyst: A Green Approach to *N*-Methyl Amines. *Catal. Sci. Technol.* **2020**, *10*, 3458−3467.

(36) Robic, N.; Noël, J.-P Synthesis of [Trifluoromethyl-[$^{14}C_6$]-Phenyl]-SR 57746A. *J. Labelled Compd. Radiopharm.* **1999**, *42*, 109−119.

(37) Longsheng, Z.; Liang, Z.; Dong, F.; Qi, L.; Fuxiang, L. Method for processing fluoride ions in aminobenzotrifluoride. Patent CN106431936A, 2017. https://worldwide.espacenet.com/patent/search/family/058181854/publication/CN106431936A?q=pn%3DCN106431936A

(38) Hartwig, J. F.; Shekhar, S.; Shen, Q.; Barrios-Landeros, F. Synthesis of Anilines. In *Patai's Chemistry of Functional Groups*; John Wiley & Sons: Chichester, U.K., 2009; pp 1−82.

(39) Noel, M.; Ravichandran, C.; Anantharaman, P. N. An Electrochemical Technique for the Reduction of Aromatic Nitro-compounds in H_2SO_4 Medium on Thermally Coated Ti/TiO$_2$ Electrodes. *J. Appl. Electrochem.* **1995**, *25*, 690−698.

(40) Layer, R. W. The Chemistry of Imines. *Chem. Rev.* **1963**, *63*, 489−510.

(41) Jinan Wutong Biotechnology. Synthetic Method for 2-Methyl-3-trifluoromethylaniline. CN 201810930549 A, 2020.

(42) Suli Pharmaceutical Tech Jiangyin. Synthesis Process of 2,2′-Bis(trifluoromethyl)diaminobiphenyl. CN 115124430 A, 2022.

(43) Zhejiang Weihua New Mat. Co. Ltd. Preparation Method of *m*-Trifluoromethylphenol. CN 201910831538 A, 2020.

(44) Zhejiang Weihua New Mat. Co. Ltd. Method for Preparing *m*-Trifluoromethylphenol. WO 2021042721 A1, 2021.

(45) Kirk, R. E.; Othmer, D. F. *Encyclopedia of Chemical Technology*; Wiley Interscience: New York, 1978; Vol. 2, pp 355−376.

(46) Wirtanen, T.; Rodrigo, E.; Waldvogel, S. R. Recent Advances in the Electrochemical Reduction of Substrates Involving N-O Bonds. *Adv. Synth. Catal.* **2020**, *362*, 2088−2101.

(47) Chen, Z.; Wang, Z.; Wu, D.; Ma, L. Electrochemical Study of Nitrobenzene Reduction on Galvanically Replaced Nanoscale Fe/Au Particles. *J. Hazard. Mater.* **2011**, *197*, 424−429.

(48) Winter, J.; Prenzel, T.; Wirtanen, T.; Schollmeyer, D.; Waldvogel, S. R. Direct Electrochemical Synthesis of 2,3-Disubstituted Quinoline *N*-Oxides by Cathodic Reduction of Nitro Arenes. *Chem. - Eur. J.* **2023**, *29*, No. e202203319.

(49) Wirtanen, T.; Prenzel, T.; Tessonnier, J.-P.; Waldvogel, S. R. Cathodic Corrosion of Metal Electrodes-How to Prevent It in Electroorganic Synthesis. *Chem. Rev.* **2021**, *121*, 10241−10270.

(50) Kisukuri, C. M.; Fernandes, V. A.; Delgado, J. A. C.; Häring, A. P.; Paixão, M. W.; Waldvogel, S. R. Electrochemical Installation of CFH$_2$-, CF$_2$H-, CF$_3$-, and Perfluoroalkyl Groups into Small Organic Molecules. *Chem. Rec.* **2021**, *21*, 2502−2525.

(51) Utley, J. H. P.; Little, R. D.; Nielsen, M. F. Reductive Coupling. In *Organic Electrochemistry*, 4th ed.; Hammerich, O., Lund, H., Eds.; CRC Press: Boca Raton, FL, 2000; pp 621−704.

(52) Hammerich, O. Reduction of Nitro Compounds and Related Substrates. In *Organic Electrochemistry*, 5th ed.; Hammerich, O., Speiser, B., Eds.; CRC Press: Boca Raton, FL, 2015; pp 1149−1200.

(53) Rodrigo, E.; Waldvogel, S. R. Simple Electrochemical Reduction of Nitrones to Amines. *Chem. Sci.* **2019**, *10*, 2044−2047.

(54) Sassykova, L. R.; Aubakirov, Y. A.; Sendilvelan, S.; Tashmukhambetova, Z. K.; Zhakirova, N. K.; Faizullaeva, M. F.; Batyrbayeva, A. A.; Ryskaliyeva, R. G.; Tyussyupova, B. B.; Abildin, T. S. Studying the Mechanisms of Nitro Compounds Reduction (A-Review). *Orient. J. Chem.* **2019**, *35*, 22−38.

(55) Priewisch, B.; Rück-Braun, K. Efficient Preparation of Nitrosoarenes for the Synthesis of Azobenzenes. *J. Org. Chem.* **2005**, *70*, 2350−2352.

(56) Beil, S. B.; Pollok, D.; Waldvogel, S. R. Reproducibility in Electroorganic Synthesis—Myths and Misunderstandings. *Angew. Chem., Int. Ed.* **2021**, *60*, 14750−14759.

(57) Seidler, J.; Strugatchi, J.; Gärtner, T.; Waldvogel, S. R. Does Electrifying Organic Synthesis Pay off? The Energy Efficiency of Electro-Organic Conversions. *MRS Energy Sustainability* **2020**, *7*, 42.

(58) Dörr, M.; Hielscher, M. M.; Proppe, J.; Waldvogel, S. R. Electrosynthetic Screening and Modern Optimization Strategies for Electrosynthesis of Highly Value-added Products. *ChemElectroChem* **2021**, *8*, 2621−2629.

(59) Gütz, C.; Klöckner, B.; Waldvogel, S. R. Electrochemical Screening for Electroorganic Synthesis. *Org. Process Res. Dev.* **2016**, *20*, 26−32.

(60) Gütz, C.; Stenglein, A.; Waldvogel, S. R. Highly Modular Flow Cell for Electroorganic Synthesis. *Org. Process Res. Dev.* **2017**, *21*, 771−778.

(61) Gleede, B.; Selt, M.; Gütz, C.; Stenglein, A.; Waldvogel, S. R. Large, Highly Modular Narrow-Gap Electrolytic Flow Cell and Application in Dehydrogenative Cross-Coupling of Phenols. *Org. Process Res. Dev.* **2020**, *24*, 1916−1926.

(62) Yang, N.; Waldvogel, S. R.; Jiang, X. Electrochemistry of Carbon Dioxide on Carbon Electrodes. *ACS Appl. Mater. Interfaces* **2016**, *8*, 28357−28371.

(63) Gütz, C.; Grimaudo, V.; Holtkamp, M.; Hartmer, M.; Werra, J.; Frensemeier, L.; Kehl, A.; Karst, U.; Broekmann, P.; Waldvogel, S. R. Leaded Bronze: An Innovative Lead Substitute for Cathodic Electrosynthesis. *ChemElectroChem* **2018**, *5*, 247−252.

(64) Kim, M.; Ha, J.; Kim, Y.-T.; Choi, J. Stainless Steel: A High Potential Material for Green Electrochemical Energy Storage and Conversion. *Chem. Eng. J.* **2022**, *440*, 135459−135465.

(65) Edinger, C.; Kulisch, J.; Waldvogel, S. R. Stereoselective cathodic synthesis of 8-substituted (1R,3R,4S)-menthylamines. *Beilstein J. Org. Chem.* **2015**, *11*, 294−301.

(66) Kulisch, J.; Nieger, M.; Stecker, F.; Fischer, A.; Waldvogel, S. R. Efficient and Stereodivergent Electrochemical Synthesis of Optically-Pure Menthylamines. *Angew. Chem., Int. Ed.* **2011**, *50*, 5564−5567.

(67) Griesbach, U.; Waldvogel, S. R.; Kulisch, J.; Malkowsky, I. M. Electrochemical Production of Sterically Hindered Amines. Patent WO 2008/003620 A2, 2007.

(68) Edinger, C.; Grimaudo, V.; Broekmann, P.; Waldvogel, S. R. Stabilizing Lead Cathodes with Diammonium Salt Additives in the Deoxygenation of Aromatic Amides. *ChemElectroChem* **2014**, *1*, 1018−1021.

(69) Gütz, C.; Bänziger, M.; Bucher, C.; Galvão, T. R.; Waldvogel, S. R. Development and Scale-Up of the Electrochemical Dehalogenation for the Synthesis of a Key Intermediate for NS5A Inhibitors. *Org. Process Res. Dev.* **2015**, *19*, 1428−1433.

(70) Pothula, K.; Tang, L.; Zha, Z.; Wang, Z. Bismuth Nano-particles: An Efficient Catalyst for Reductive Coupling of Nitroarenes to Azo-Compounds. *RSC Adv.* **2015**, *5*, 83144−83148.

(71) Smith, M. B.; March, J. *March's Advanced Organic Chemistry: Reactions, Mechanisms, and Structure*, 7th ed.; John Wiley & Sons: Hoboken, NJ, 2013; pp 902−912.

153

(72) Noël, T.; Cao, Y.; Laudadio, G. The Fundamentals Behind the Use of Flow Reactors in Electrochemistry. *Acc. Chem. Res.* **2019**, *52*, 2858−2869.

(73) Selt, M.; Franke, R.; Waldvogel, S. R. Supporting-Electrolyte-Free and Scalable Flow Process for the Electrochemical Synthesis of 3,3′,5,5′-Tetramethyl-2,2′-Biphenol. *Org. Process Res. Dev.* **2020**, *24*, 2347−2355.

(74) Gleede, B.; Selt, M.; Gütz, C.; Stenglein, A.; Waldvogel, S. R. Waldvogel. Large, Highly Modular Narrow-Gap Electrolytic Flow Cell and Application in Dehydrogenative Cross-Coupling of Phenols. *Org. Process Res. Dev.* **2020**, *24*, 1916−1926.

(75) Arndt, S.; Rücker, R.; Stenglein, A.; Waldvogel, S. R. Reactor Design for the Direct Electrosynthesis of Periodate. *Org. Process Res. Dev.* **2022**, *26*, 2447−2455.

(76) Waldvogel, S. R.; Arndt, S.; Weis, D.; Donsbach, K. Method for preparing periodates. WO 2021110928 A1, 2021.

(77) *USP 29-NF 24, U.S. Pharmacopeia and National Formulary*; U.S. Pharmacopeial Convention: Rockville, MD, 2006.

Scalable Electrochemical Reduction of Nitrobenzo-trifluorides to 3-Trifluoromethyl-anilines

Camila M. Kisukuri[a‡], Johannes Seidler[a,b‡], Tobias Gärtner[b], Denis F. Rohrmann[a] and Siegfried R. Waldvogel[a,b,c]*

*Email: waldvogel@uni-mainz.de

[a] *Department of Chemistry, Johannes Gutenberg University Mainz, 55128 Mainz, Germany.*

[b] *ESy-Labs GmbH, Siemensstrasse 7, 93055 Regensburg, Germany.*

[c] *Institute of Biological and Chemical Systems –Functional Molecular Systems (IBCS-FMS), Hermann-von-Helmholtz-Platz 1, 76344 Eggenstein-Leopoldshafen, Germany.*

Number of pages: 49

Number of figures: 35

Number of tables: 24

Table of Contents

1. General Information

All reagents were used in analytical or sufficiently pure grades. Solvents were purified by standard methods.[1] All reactions were carried out at ambient atmosphere and temperature unless otherwise stated. Electrodes were obtained from commercial suppliers: Boron-doped diamond (BDD, DIACHEM®, 15 μm diamond layer on silicon support, CONDIAS GmbH, Itzehoe, Germany), glassy carbon (SIGRADUR® G, HTW, Thierhaupten, Germany), platinum (OEGUSSA, Vienna, Austria), isostatic graphite (Sigrafine™ V2100, SGL Carbon, Bonn, Germany), CuSn7Pb15 (Metallwerke Langenau GmbH, Langenau, Germany) and stainless steel (type EN1.4401, Montanstahl GmbH, Oelde, Germany). Nafion™ N324 from DuPont was used as membrane. A galvanostatic HMP4040 power source from Rohde&Schwarz was used.

Gas Chromatography: Gas chromatography was performed on a Shimadzu GC-2010 device (Shimadzu, Kyoto Japan) with a ZB-5 quartz capillary column (Phenomenex, Torrance, USA) with the specifications: dimensions 30 m x 0.25 mm x 0.25 μm, carrier gas: helium, injection temperature 250 °C; detector temperature 310 °C, 50 °C as start temperature for 1 minute, heating rate of 15 °C/min, 290 °C as end temperature for 8 minutes, temperature at ion source: 200 °C) coupled with a GCMS-QP2010 (Shimadzu, Kyoto, Japan) mass detector.

NMR Spectroscopy: ^{1}H NMR, ^{13}C NMR, and ^{19}F NMR spectra were recorded at 25 °C by using a Bruker Avance II 300 or a Bruker Avance III HD 400 (Bruker BioSpin GmbH, Rheinstetten, Germany). Chemical shifts (δ) are reported in parts per million (ppm). For quantification by ^{19}F spectra were recorded without ^{1}H decoupling and Ethyl trifluoroacetate served as external standard (δ = -74.777 ppm).

Crystallographic Analysis: A suitable crystal was selected and mounted on a MITIGEN holder with oil on a GV50, TitanS2 diffractometer. The crystal was kept at 122.9(3) K during data collection. Using Olex2,[2] the structure was solved with the ShelXT 2018/3 (Sheldrick, 2015) structure solution program using Intrinsic Phasing and refined by Least Squares using version 2018/3 of ShelXL 2018/3 (Sheldrick, 2015).

High Resolution Mass Spectra: were obtained using a G6545A Q-ToF (Agilent GmbH, Waldbronn, Germany) with dual AJS electrospray ion source (Dual AJS ESI).

MS parameters were as follows: Mass rage: 80–3200 m/z, Scan rate: 1 spectrum s^{-1}, Nebulizer pressure: 25 psi, Capillary Voltage: 3500 V, Fragmentor: 50 V, Skimmer: 45 V, Dry gas temperature: 275°C, Dry gas flow: 10 L min^{-1}, Sheath gas temperature: 350°C, Sheath gas flow: 10 L min^{-1}. Mass calibration was performed on the day of measurement using an external standard. The mass accuracy of the measurement results is better than 5 ppm. Chromatographic separation was carried out on a 1260 Infinity II HPLC system (Agilent GmbH, Waldbronn, Germany) with G7111B 1260 Quaternary Pump, G7129A 1260 Vialsampler, and G7116A 1260 Multicolumn Thermostat equipped with an Agilent EclipsePlus C18 RRHP (2.1 x 50 mm, 2.1 µm particle size) analytical column. Eluents were 98% H_2O with 2% ACN and 0.05% formic acid (Eluent A) and 2% H_2O with 98% ACN and 0.05% formic acid (Eluent B). The following gradient elution was applied for separation at flow rate of 200 µL min^{-1}: Starting at 10% B for 1 min, followed by a linear increase to 95% B at 10 min, maintaining 95% B until 30 min, before going back to 10% B at 33 min. The column was equilibrated at 10% B for 15 min before the next measurement. Injection volume was 2 µL. Data was recorded using Agilent MassHunter Workstation LC/MS software version 11.0 and data analysis was performed using Agilent MassHunter Workstation Qualitative Analysis software version 10.0.

Cyclovoltammetry: Cyclic voltammetry was performed in a 10 mL snap-cap vial equipped with an Autolab PGSTAT101 potentiostat (Metrohm AG, Herisau, Switzerland). The CV was performed using 3-nitrobenzotrifluoride 1a in a solution of 1 M $H_2SO_{4(aq)}$, CuSn7Pb15 as cathode, Pt-wire as reference electrode, and Pb as anode. A sweep rate of 100 mV/s was used.

Inductively Coupled Plasma Optical Emission Spectroscopy (ICP-OES): ICP-OES measurements were performed with an ICP-OES 5800 VDV (Agilent Technologies Inc., Santa Clara, United States) and ICP multi-element standard solution IV Certipur® (Merck KGaA, Darmstadt, Germany) dissolved in 1% (m/v) nitric acid Suprapur® (Merck KGaA, Darmstadt, Germany). The calibration data was obtained using a dilution series of 0 ppb, 5 ppb, 50 ppb, 200 ppb, 600 ppb and 800 ppb. The measured concentration of lead was obtained by measuring at a wavelength of λ = 283.305 nm. The wavelength was chosen based on the lowest interference by other metals. All measurements were performed without matrix adaptation.

S5

Elemental Analysis (CHN): Elemental analysis was measured on an Elementar vario EL cube elemental analyzer machine (vario EL cube, Elementar Analysensysteme GmbH, Langenselbold, Germany). The CHN elemental analysis was performed on triplicates for each sample (2 mg).

2. Used Chemicals

Methanol [67-56-1] ROTISOLV®, ≥99%

Sulfuric acid [7664-93-9] ROTIPURAN®Supra, 96%

Methanesulfonic acid [75-75-2] Alfa Aesar, ≥98%

3-Nitrobenzotrifluoride [98-46-4] TCI, ≥96%

1-Methyl-4-nitro-2-(trifluoromethyl)benzene [89976-12-5] TCI, ≥96%

2-Nitro-4-(trifluoromethyl)benzenesulfonyl chloride [837-95-6] TCI, ≥97%

4-Trifluoromethyl-2-nitroaniline [400-98-6] TCI, ≥98%

1-Nitro-3,5-bis(trifluoromethyl)benzene [328-75-6] TCI, ≥98%

2-Nitro-4-(trifluoromethyl)benzaldehyde [109466-87-7] TCI, ≥97%

2-Nitro-1,4-bis(trifluoromethyl)benzene [320-88-7] TCI, ≥98%

3. Cyclic Voltammetry

Cyclic voltammetry was performed in 1M $H_2SO_{4(aq)}$ to determine the potential for the reduction of 3-nitrobenzotrifluoride (**1a**) at various electrode materials (**Figure S1**). Among the tested electrodes, the copper-tin-lead alloy (leaded bronze) shows the lowest potential for the reduction reaction. The leaded bronze had a potential for the reduction of **1a** to **2a** reaction of the E = -0.48 V, followed by Pt (E = -0.50 V), stainless steel (E = -0.55 V), BDD (E = -0.62 V), GC (E = -0.92 V), graphite (E = -1.25 V) ad Pb (E = -1.35 V).
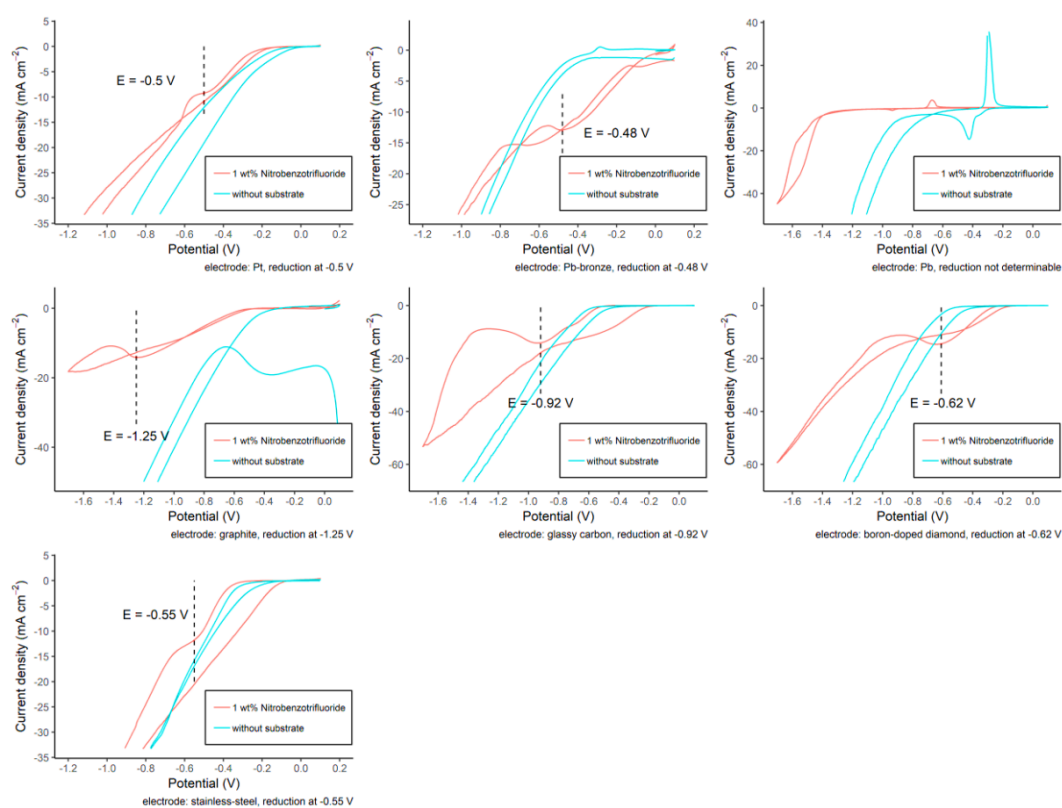
Figure S1. Cyclic voltammetry of 3-nitrobenzotrifluoride (**1a**) at different electrode materials.

4. Protocols

4.1. General Protocol for Batch-Type Electrolysis (GP1)

Batch-type screening experiments were conducted in divided Teflon™ electrolysis cells (Figure S2).[3] This batch-type cell is commercially available as IKA Screening

system package (IKA®-Werke GmbH & Co. KG, Staufen, Germany). In the batch-type cell (Figure S2) divided through Nafion[TM] N324 membrane (DuPont, Wilmington, United States) both compartments were filled with H_2O/MeOH (1:3, 2 x 6 mL) and 2M $H_2SO_{4(aq)}$. The molarity of $H_2SO_{4(aq)}$ equals the concentration of the acid added to H_2O/MeOH solution. The 3-nitrobenzotrifluoride derivate (**1a-h**) (2.4 mmol, 400 mM) was added to the cathodic compartment and the electrolysis was started with graphite as anode and CuSn7Pb15 as cathode. Both electrodes have an active surface of 2 cm[2] and were arranged in 2 cm distance relative to each other. Each cell compartment was equipped with a round magnetic stir bar. A given amount of applied charge, and a given current density was set. The reaction was performed at room temperature. After electrolysis, the content of the cathode compartment was collected. The solid was filtered. The liquid phase of the filtration was used to determine the yields of start material (**1a-h**) and dissolved product by ^{19}F NMR spectroscopy, using as standard ethyl trifluoroacetate. The solid part was washed with cold water and cyclohexane. After, the solid was dried under reduced pressure and the isolated yield for the 3-trifluoromethylanilinium bisulfate derivative **2a-h** was determined.
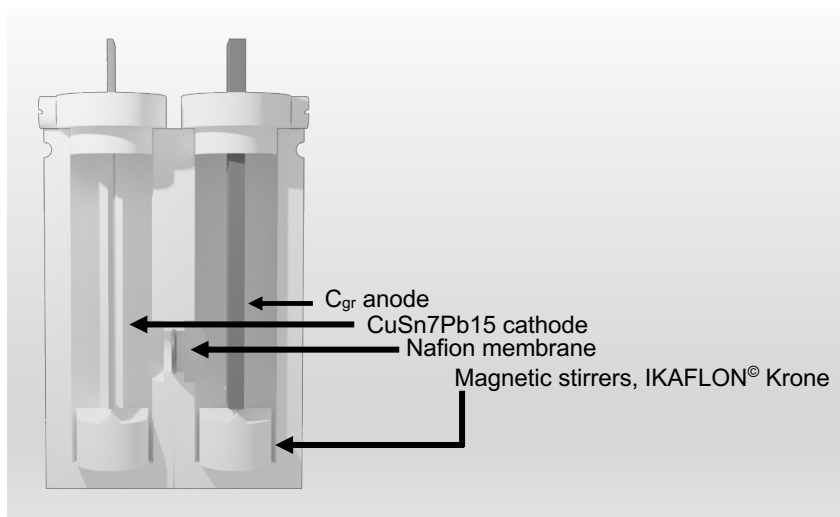
Figure S2. Batch-type Teflon[TM] divided cell equipped with Nafion[TM] N324 membrane, two electrodes, and magnetic stirrers.[3]

4.2. Flow Electrolysis (2 x 6 cm^2 Cathodic Surface) (GP2)

Flow electrolysis were performed in a modular flow cell based on Teflon^{TM}, that were designed by the Waldvogel research group (**Figure S3**),[4–6] and is commercially available as ElectraSyn flow (IKA®-Werke GmbH & Co. KG, Staufen, Germany). The cell consists of two Teflon^{TM} half cells. Each half cell contains an electrode with an active surface of 12 cm^2. A Nafion^{TM} N324 membrane (DuPont, Wilmington, United States) was used as a separator, tethered with Teflon^{TM} spacers (0.25-0.5 mm). One Ismatec® pump (with independent channel control) was used to propel the anolyte and catholyte into the cell. Graphite was used as anode and CuSn7Pb15 was used as cathode. The 3-nitrobenzotrifluoride (**1a**) (2.4-4.8 mmol, 400-800 mM) was dissolved in H$_2$O/MeOH (1:1-1:3, 2 x 6 mL) solution. 2-5 M of H$_2$SO$_{4(aq)}$ was used as electrolyte. The molarity of H$_2$SO$_{4(aq)}$ equals the concentration of the acid added to H$_2$O/MeOH solution. A given amount of applied charge, a given current density, and a given flow rate was set. After electrolysis, the content of the cathodic compartment was collected. The solid was filtered. The liquid phase of the filtration was used to determine the yields of start material (**1a**) and dissolved product by ^{19}F NMR spectroscopy, using as standard ethyl trifluoroacetate. The solid part was washed with cold water and cyclohexane. After, the solid was dried under reduced pressure and the isolated yield for the 3-trifluoromethylanilinium bisulfate **2a** derivative was determined.

Figure S3. Technical drawings of flow electrolysis cell: a) Cross-section of the Teflon piece with connection for tubing, inlet, outlet and free space for electrodes. b) Complete half-cell containing Teflon piece. c) Half-cell with gasket/ spacer on top. d) Exploded drawing of a complete divided flow electrolysis cell. For the undivided mode, the Nafion™ N324 membrane and one gasket/spacer is omitted.[5]

4.3. Flow Electrolysis (2 x 6 cm² Cathodic Surface) (GP3)

Flow electrolyses were performed in a modular flow cell based on Teflon™, that were designed by the Waldvogel research group (**Figure S3**),[4–6] and is commercially available as ElectraSyn flow (IKA®-Werke GmbH & Co. KG, Staufen, Germany). The cell consists of two Teflon™ half cells. Each half cell contains an electrode with an active surface of 12 cm². A Nafion™ N324 membrane (DuPont, Wilmington, United States) was used as separator, tethered with Teflon™ spacers (0.25-0.5 mm). Two Ritmo R033 pumps from Fink were used to propel the anolyte and catholyte into the cell. Graphite was used as anode and CuSn7Pb15 was used as cathode. The 3-nitrobenzotrifluoride (**1a**) (3.2-6.4 mmol, 400-800 mM) was dissolved in H_2O/MeOH (1:1-1:3, 2 x 8 mL) solution. 2-5 M of $H_2SO_{4(aq)}$ was used as electrolyte. The molarity of

H$_2$SO$_{4(aq)}$ equals the concentration of the acid added to H$_2$O/MeOH solution. A given amount of applied charge, a given current density and a given flow rate was set. After electrolysis, the content of the cathodic compartment was collected. The solid was filtered. The liquid phase of the filtration was used to determine the yields of start material (**1a**-**h**) and dissolved product by ^{19}F NMR spectroscopy, using as standard ethyl trifluoroacetate. The solid part was washed with cold water and cyclohexane. After, the solid was dried under reduced pressure and the isolated yield for the 3-trifluoromethylanilinium bisulfate derivative **2a**-**h** was determined.
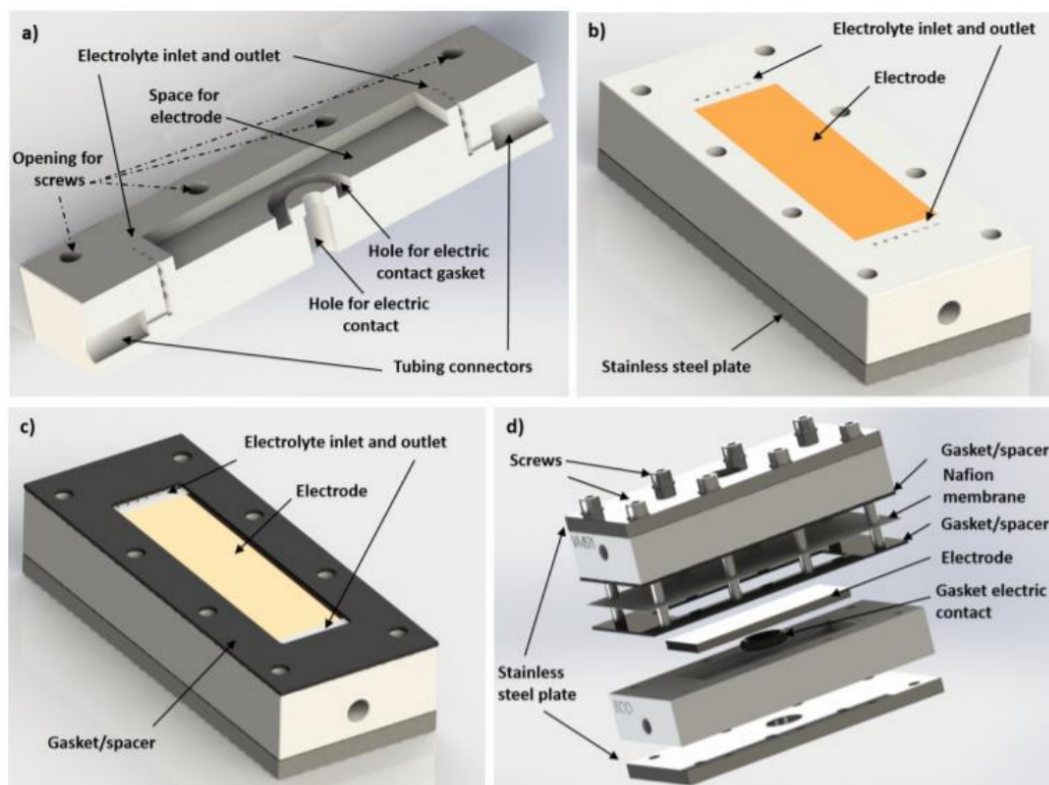
4.4. Flow Electrolysis (4 x 12 cm^2 Cathodic Surface) (GP 4)

Flow electrolyses were performed in a modular flow cell based on Teflon^{TM}, that were designed by the Waldvogel research group (**Figure S4**).[6] The cell consists of two Teflon^{TM} half cells. Each half cell contains an electrode with an active surface of 48 cm^2. A Nafion^{TM} N324 membrane (DuPont, Wilmington, United States) was used as a separator, tethered with Teflon^{TM} spacers (0.5 mm). Two Ritmo R033 pumps from Fink were used to propel the anolyte and catholyte into the cell. Graphite was used as anode and CuSn7Pb15 was used as cathode. The 3-nitrobenzotrifluoride (**1a**) (3.2 mmol, 400 mM) was dissolved in H$_2$O/MeOH (1:1 2 x 8 mL) solution. 2 M of H$_2$SO$_{4(aq)}$ was used as electrolyte. The molarity of H$_2$SO$_{4(aq)}$ equals the concentration of the acid added to H$_2$O/MeOH solution. A given amount of applied charge (12 F), a given current density (30 mA cm^{2-}) and a given flow rate (3.5 L h^{1-}) was set. Due to several clogging issues it was not possible to obtain yield for the desired product when this set-up was used. In this case, the product formed was trapped in the microchannels of the cell.

Figure S4. Views of assembled flow-electrolysis cell and partly exploded drawing of the full-featured 4x12 cm^2 cathodic area flow cell.[6]

4.5. Flow Electrolysis (4 x 12 cm^2 Cathodic Surface) (GP 5)

Flow electrolyses were performed in electrolysis cells, that were designed by the Waldvogel research group (**Figure S3**).[7–9] Each half cell contains an electrode with an active surface of 48 cm^2. A Nafion^{TM} N324 membrane (DuPont, Wilmington, United States) was used as a separator, tethered with EPDM (ethylene propylene diene monomer) spacers (1.0 mm). Two Ritmo R033 pumps from Fink were used to propel the anolyte and catholyte into the cell. Graphite was used as anode and CuSn7Pb15 was used as cathode. The 3-nitrobenzotrifluoride (**1a**) (400-800 mM) was dissolved in H$_2$O/MeOH (1:1-1:3) solution. 2-5 M of H$_2$SO$_{4(aq)}$ was used as electrolyte. The molarity of H$_2$SO$_{4(aq)}$ equals the concentration of the acid added to H$_2$O/MeOH solution. A given amount of applied charge, a given current density and a given flow rate was set. After electrolysis, the content of the cathodic compartment was collected. The solid was filtered. The liquid phase of the filtration was used to determine the yields of start

S12

166

material (**1a-h**) and dissolved product by ^{19}F NMR spectroscopy, using as standard ethyl trifluoroacetate. The solid part was washed with cold water and cyclohexane. After, the solid was dried under reduced pressure and the isolated yield for the 3-trifluoromethylanilinium bisulfate **2a** was determined.
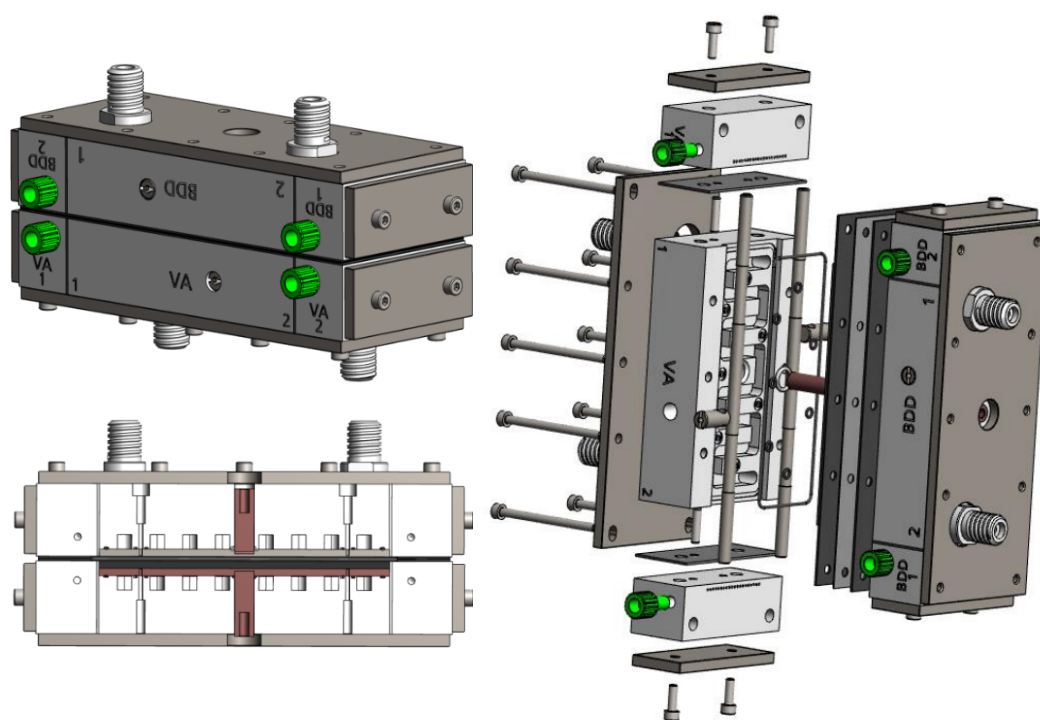

Figure S5. Views of assembled flow-electrolysis cell and partly exploded drawing of the full-featured 4x12 cm^2 cathodic area flow cell.[7–9]

5. Optimizations for Batch-Type Electrolysis

The screening for optimized reaction conditions in a divided batch-type electrolysis cell was conducted according to general protocol 4.1 (GP1). The reaction conditions were subjected to One-Variation-At-Time approach to maximize product formation. The electrode materials, current density, solvent system, applied charge, and substrate concentration **1a** were screened. It is important to note that the same Nafion™ N324 (DuPont, Wilmington, United States) membrane was used for all experiments.

5.1. Variation of Cathode Material

Table S1. Electrochemical synthesis of 3-trifluoromethylanilinium bisulfate (**2a**) under variation of the cathode material.[a]

Entries	Cathode	Yield (1a)/ %	Yield (2a')/ %	Yield (2a)/ %	Yield (6)/ %
1	Glassy Carbon	8	83	4	-
2	BDD	15	75	6	
3	Graphite	22	69	5	-
4	Pt	18	56	7	8
5	Stainless steel	-	85	11	-
6	Pb	-	82	14	-
7	**CuSn7Pb15**	**-**	**83**	**13**	**-**

[a]**Electrolysis parameters:** applied charge: 555.76 C (12 F); current density: 4 mA·cm^{-2}; temperature: room temperature; anode: C$_{gr}$ (cathodic area: 2 cm^2); c(substrate): 80 mM; separator: Nafion™ N324 (0.5 mm); 2 x 6 mL of solvent (formed by a solution of H$_2$O/MeOH; 1:1); electrolyte: 2 M H$_2$SO$_{4(aq)}$; 2a corresponds to the precipitated product in the salt form. The difference between the yields corresponds to the product that is dissolved in the solution. Yields of 1a, dissolved product 2a', and 6 were determined via ^{19}F NMR spectroscopy using ethyl trifluoroacetate as internal standard.

5.2. Variation of Anode Material

Table S2. Electrochemical synthesis of 3-trifluoromethylanilinium bisulfate (**2a**) under variation of the anode material.[a]

Entries	Anode	Yield (1a)/ %	Yield (2a')/ %	Yield (2a)/ %	Yield (6)/ %
8	**Graphite**	**18**	**65**	**12**	**-**
9	Glassy Carbon	20	64	11	-
10	Platinum	14	63	-	8
11	BDD	23	75	-	-

[a]**Electrolysis parameters**: applied charge: 555.76 C (12 F); current density: 4 mA·cm^{-2}; temperature: room temperature; cathode: CuSn7Pb15 (cathodic area: 2 cm^2); c(substrate): 80 mM; separator: Nafion^{TM} N324 (0.5 mm); 2 x 6 mL of solvent (formed by a solution of H_2O/MeOH; 1:1); electrolyte: 2 M $H_2SO_{4(aq)}$; 2a corresponds to the precipitated product in the salt form. Yields of 1a, dissolved product 2a', and 6 were determined via ^{19}F NMR spectroscopy using ethyl trifluoroacetate as internal standard.

5.3. Variation of Current Density

Table S3. Electrochemical synthesis of 3-trifluoromethylanilinium bisulfate (**2a**) under variation of the current density.[a]

Entries	j (mA/cm^2)	Yield (1a)/ %	Yield (2a')/ %	Yield (2a)/ %	Yield (6)/ %
12	16	-	85	13	-
13	24	-	86	11	-
14	**30**	**-**	**83**	**14**	**-**
15	40	-	82	12	-
16	60	-	63	7	12

[a]**Electrolysis parameters:** applied charge: 555.76 C (12 F); current density: 16-60 mA·cm^{-2}; temperature: room temperature; anode: C_{gr}; cathode: CuSn7Pb15 (cathodic area: 2 cm^2); c(substrate): 80 mM; separator: Nafion^{TM} N324 (0.5 mm); 2 x 6 mL of solvent (formed by a solution of H_2O/MeOH; 1:1); electrolyte: 2 M $H_2SO_{4(aq)}$; 2a corresponds to the precipitated product in the salt form. The difference between the yields corresponds to the product that is dissolved in the solution. Yields of 1a, dissolved product 2a', and 6 were determined via ^{19}F NMR spectroscopy using ethyl trifluoroacetate as internal standard.

5.4. Variation of the H_2SO_4 Concentration

Table S4. Electrochemical synthesis of 3-trifluoromethylanilinium bisulfate (**2a**) under variation of the H_2SO_4 concentration.[a]

Entries	H_2SO_4 [M]	Yield (1a)/ %	Yield (2a')/ %	Yield (2a)/ %
17	1.5	-	93	-
18	3.0	-	82	15
19	5.0	-	89	4

[a]Electrolysis parameters: applied charge: 555.76 C (12 F); current density: 30 mA·cm^{-2}; temperature: room temperature; anode: C_{gr}; cathode: CuSn7Pb15 (cathodic area: 2 cm^2); c(substrate): 80 mM; separator: Nafion^{TM} N324 (0.5 mm); 2 x 6 mL of solvent (formed by a solution of H_2O/MeOH; 1:1); electrolyte: 1.5-5 M $H_2SO_{4(aq)}$; 2a corresponds to the precipitated product in the salt form. The difference between the yields corresponds to the product that is dissolved in the solution. Yields of 1a, and dissolved product 2a' were determined via ^{19}F NMR spectroscopy using ethyl trifluoroacetate as internal standard.

5.5. Variation of 3-Nitrobenzotrifluoride (1a) Concentration

Table S5. Electrochemical synthesis of 3-trifluoromethylanilinium bisulfate (**2a**) under variation of the 3-nitrobenzotrifluoride (**1a**) concentration.[a]

Entries	c of 1a [mM]	Yield (1a)/ %	Yield (2a')/ %	Yield (2a)/ %
20	160	-	83	15
21	240	-	76	19
22	320	-	68	28
23	**400**	**-**	**65**	**32**
24	600	-	70	25

[a]Electrolysis parameters: applied charge: 1111.51-4168.16 C (12 F); current density: 30 mA·cm^{-2}; temperature: room temperature; anode: C_{gr}; cathode: CuSn7Pb15 (cathodic area: 2 cm^2); c(substrate): 160-600 mM; separator: Nafion^{TM} N324 (0.5 mm); 2 x 6 mL of solvent (formed by a solution of H_2O/MeOH; 1:1); electrolyte: 2 M $H_2SO_{4(aq)}$; 2a corresponds to the precipitated product in the salt form. The difference between the yields corresponds to the product that is dissolved in the solution. Yields of 1a, and dissolved product 2a' were determined via ^{19}F NMR spectroscopy using ethyl trifluoroacetate as internal standard.

5.6. Variation of H₂O/MeOH Ratio

Table S6. Electrochemical synthesis of 3-trifluoromethylanilinium bisulfate (**2a**) under variation of the H$_2$O/MeOH ratio.[a]

Entries	H$_2$O/MeOH	Yield (1a)/ %	Yield (2a')/ %	Yield (2a)/ %
25	1:2	-	59	35
26	**1:3**	**-**	**60**	**36**

[a]**Electrolysis parameters**: applied charge: 2778.78 C (12 F); current density: 30 mA·cm^{-2}; temperature: room temperature; anode: C$_{gr}$; cathode: CuSn7Pb15 (cathodic area: 2 cm^2); c(substrate): 400 mM; separator: Nafion™ N324 (0.5 mm); 2 x 6 mL of solvent (formed by a solution of H$_2$O/MeOH; 1:1-1:3); electrolyte: 2 M H$_2$SO$_{4(aq)}$; 2a corresponds to the precipitated product in the salt form. The difference between the yields corresponds to the product that is dissolved in the solution. Yields of 1a, and dissolved product 2a' were determined via ^{19}F NMR spectroscopy using ethyl trifluoroacetate as internal standard.

5.7. Variation of Organic Solvent

Table S7. Electrochemical synthesis of 3-trifluoromethylanilinium bisulfate (**2a**) under variation of the organic solvent.[a]

Entries	ROH	Yield (1a)/ %	Yield (2a')/ %	Yield (2a)/ %	Yield (6)/ %
27	EtOH	-	93	-	
28	BuOH	-	22	11	30

[a]**Electrolysis parameters**: applied charge: 2778.78 C (12 F); current density: 30 mA·cm^{-2}; temperature: room temperature; anode: C$_{gr}$; cathode: CuSn7Pb15 (cathodic area: 2 cm^2); c(substrate): 400 mM; separator: Nafion™ N324 (0.5 mm); 2 x 6 mL of solvent (formed by a solution of H$_2$O and selected alcohol; 1:3); electrolyte: 2 M H$_2$SO$_{4(aq)}$; 2a corresponds to the precipitated product in the salt form. The difference between the yields corresponds to the product that is dissolved in the solution. Yields of 1a, dissolved product 2a', and 6 were determined via ^{19}F NMR spectroscopy using ethyl trifluoroacetate as internal standard.

5.8. Variation of H₂SO₄ Addition in the Final of Reaction

Table S8. Electrochemical synthesis of 3-trifluoromethylanilinium bisulfate (**2a**) under addition of acid in the final of reaction.[a]

Entries	H$_2$SO$_4$ (µL)	Yield (1a)/ %	Yield (2a')/ %	Yield (2a)/ %
29	**100**	**-**	**25**	**69**
30	200	-	29	68
31	300	-	29	67

[a]**Electrolysis parameters:** applied charge: 2778.78 C (12 F); current density: 30 mA·cm^{-2}; temperature: room temperature; anode: C$_{gr}$; cathode: CuSn7Pb15 (cathodic area: 2 cm^2); c(substrate): 400 m$_M$; separator: Nafion^{TM} N324 (0.5 mm); 2 x 6 mL of solvent (formed by a solution of H$_2$O/MeOH; 1:3); electrolyte: 2 $_M$ H$_2$SO$_{4(aq)}$. The acid was added at the end of the reaction. After 2 hours, 2a was isolated and washed with cold water and cyclohexane. The difference between the yields corresponds to the product that is dissolved in the solution. Yields of 1a, and dissolved product 2a' were determined via ^{19}F NMR spectroscopy using ethyl trifluoroacetate as internal standard.

6. Optimizations for Flow Electrolysis (Setup GP2)

We started the screening for reaction optimization using a divided flow electrolysis indicated in the protocol 3.2 (GP2). Initially, solvent system, substrate concentration of **1a**, molarity of acid, and space between the cells were investigated, Table S9.

Table S9. Preliminary results for the reaction optimization using a divided flow electrolysis indicated in the protocol 3.2 (GP2).[a]

Entries	d (Spacer) / mm	c of 1a [mM]	H_2SO_4 [M]	H_2O/MeOH	Yield (2a')/ %	Yield (2a) / %
1	0.25	400	2	1:1	85	13
2	0.25	400	2	1:2	83	13
3	0.25	400	2	1:3	89	5
4	0.25	400	3	1:1	-	clogging
5	0.25	600	2	1:1	-	clogging
6	0.25	800	2	1:1	-	clogging
7	**0.50**	**400**	**3**	**1:1**	**71**	**23**
8	0.50	600	3	1:1	-	clogging
9	0.50	400	5	1:1	75	22

[a]**Electrolysis parameters:** applied charge: 2778.78-5557.55 C (12 F); current density: 30 mA·cm^{-2}; temperature: room temperature; anode: C_{gr}; cathode: CuSn7Pb15 (cathodic area: 12 cm^2); c(substrate): 400-800 mM; separator: Nafion™ N324 (0.5 mm); 2 x 6 mL of solvent (formed by a solution of H_2O/MeOH; 1:1-1:3); electrolyte: 2-5 M $H_2SO_{4(aq)}$. The flow rate adopted in this case was 0.99 L h^{-1}. 2a corresponds to the precipitated product in the salt form. The difference between the yields corresponds to the product that is dissolved in the solution. Yields of 1a, and dissolved product 2a' were determined via ^{19}F NMR spectroscopy using ethyl trifluoroacetate as internal standard.

Due to problems faced by system clogging, some parameters have been changed. Optimization proceeded using general protocol 3.3 (GP4).

7. Optimizations for Flow Electrolysis (GP3)

We stared the screening for optimized reaction condition in a divided flow electrolysis cell using general protocol 3.3 (GP3). Initially, Flow rate, space between the cells, solvent system, substrate concentration **1a**, and molarity of acid and were investigated. It is important to note that the same Nafion™ N324 (DuPont, Wilmington, United States) membrane was used for all experiments.

S19

173

7.1. Variation of Flow Rate

Table S10. Electrochemical synthesis of 3-trifluoromethylanilinium bisulfate (**2a**) under flow conditions (GP3) - flow rate variation.[a]

Entries	d (Spacer) / mm	Fr [L h^{-1}]	Yield (2a')/ %	Yield (2a) / %
1	0.25	2.5	-	clogging
2	0.25	3.5	40	56
3	0.25	4.0	43	51
4	0.25	4.5	42	54
5	0.50	2.5	43	51
6	0.50	3.5	21	75
7	0.50	4.0	18	79
8	**0.50**	**4.5**	**15**	**80**

[a]**Electrolysis parameters**: applied charge: 3705.04 C (12 F); current density: 30 mA·cm^{-2}; temperature: room temperature; anode: graphite; C_{gr}: CuSn7Pb15 (cathodic area: 12 cm^2); c(substrate): 400 mM; separator: Nafion^{TM} N324 (0.5 mm); 2 x 8 mL of solvent (formed by a solution of H_2O/MeOH; 1:1); electrolyte: 2 M $H_2SO_{4(aq)}$. The flow rate adopted varied between 2.5-4.5 L h^{-1}. 2a corresponds to the precipitated product in the salt form. The difference between the yields corresponds to the product that is dissolved in the solution. Yields of 1a, and dissolved product 2a' were determined via ^{19}F NMR spectroscopy with ethyl trifluoroacetate as internal standard.

7.2. Variation of Current Density and Sulfuric Acid Concentration

Table S11. Electrochemical synthesis of 3-trifluoromethylanilinium bisulfate (**2a**) under flow conditions (GP3) - current density and sulfuric acid concentration variation.[a]

Entries	j / mA cm^{-2}	H_2SO_4 [M]	Yield (2a')/ %	Yield (2a) / %
9	40	2	15	79
10	60	2	30	67
11	30	3	19	77
12	40	3	20	79
13	60	3	24	73

[a]**Electrolysis parameters**: applied charge: 3705.04 C (12 F); current density: 40-60 mA·cm^{-2}; temperature: room temperature; anode: C_{gr}; cathode: CuSn7Pb15 (cathodic area: 12 cm^2); c(substrate): 400 mM; separator: Nafion^{TM} N324 (0.5 mm); 2 x 8 mL of solvent (formed by a solution of H_2O/MeOH; 1:1); electrolyte: 2-3 M $H_2SO_{4(aq)}$. Flow rate adopted 4.5 L h^{-1}. 2a corresponds to the precipitated product in the salt form. The difference between the yields corresponds to the product that is dissolved in the solution. Yields of 1a, and dissolved product 2a' were determined via ^{19}F NMR spectroscopy with ethyl trifluoroacetate as internal standard.

7.3. Variation of Substrate Concentration 1a

Table S12. Electrochemical synthesis of 3-trifluoromethylanilinium bisulfate (**2a**) under flow conditions (GP3) – variation of substrate concentration (**1a**).[a]

Entries	c of 1a [M]	Yield (2a')/ %	Yield (2a) / %
14	600	37	58
15	800	40	56

[a]**Electrolysis parameters**: applied charge: 5557.55-7410.07 C (12 F); current density: 30 mA·cm^{-2}; temperature: room temperature; anode: C$_{gr}$; cathode: CuSn7Pb15 (cathodic area: 12 cm^2); c(substrate): 400-800 mM; separator: Nafion™ N324 (0.5 mm); 2 x 8 mL of solvent (formed by a solution of H$_2$O/MeOH; 1:1); electrolyte: 2 M H$_2$SO$_{4(aq)}$. Flow rate adopted 4.5 L h^{-1}. 2a corresponds to the precipitated product in the salt form. The difference between the yields corresponds to the product that is dissolved in the solution. Yields of 1a, and dissolved product 2a' were determined via ^{19}F NMR spectroscopy with ethyl trifluoroacetate as internal standard.

7.4. Variation of H$_2$O/MeOH Ratio

Table S13. Electrochemical synthesis of 3-trifluoromethylanilinium bisulfate (**2a**) under flow conditions (GP3) – variation of H$_2$O/MeOH Ratio.[a]

Entries	H$_2$O/MeOH	Yield (2a')/ %	Yield (2a) / %
16	1:2	30	65
17	1.3	45	51

[a]**Electrolysis parameters**: applied charge: 3705.04 C (12 F); current density: 30 mA·cm^{-2}; temperature: room temperature; anode: C$_{gr}$; cathode: CuSn7Pb15 (cathodic area: 12 cm^2); c(substrate): 400 mM; separator: Nafion™ N324 (0.5 mm); 2 x 8 mL of solvent (formed by a solution of H$_2$O/MeOH; 1:1-1:3); electrolyte: 2 M H$_2$SO$_{4(aq)}$. Flow rate adopted 4.5 L h^{-1}. 2a corresponds to the precipitated product in the salt form. The difference between the yields corresponds to the product that is dissolved in the solution. Yields of 1a, and dissolved product 2a' were determined via ^{19}F NMR spectroscopy with ethyl trifluoroacetate as internal standard.

7.5. Variation of Sulfuric Acid Addition

Table S14. Electrochemical synthesis of 3-trifluoromethylanilinium bisulfate (**2a**) under flow conditions (GP3) – addition of acid.[a]

Entries	Addition of H_2SO_4	Yield (2a')/ %	Yield (2a) / %
18	2 mL of the 2M $H_2SO_{4(aq)}$	28	70
19[b]	**200 µL (96%)**	**12**	**85**

[a]**Electrolysis parameters**: applied charge: 3705.04 C (12 F); current density: 30 mA·cm^{-2}; temperature: room temperature; anode: C_{gr}; cathode: CuSn7Pb15 (cathodic area: 12 cm^2); c(substrate): 400 mM; separator: Nafion™ N324 (0.5 mm); 2 x 8 mL of solvent (formed by a solution of H_2O/MeOH; 1:1-1:3); electrolyte: 2 M $H_2SO_{4(aq)}$. Flow rate adopted 4.5 L h^{-1}. 2a corresponds to the precipitated product in the salt form. The difference between the yields corresponds to the product that is dissolved in the solution. Yields of 1a, and dissolved product 2a' were determined via ^{19}F NMR spectroscopy with ethyl trifluoroacetate as internal standard; [b]The product was isolated after two hours of acid addition.

7.6. Mass Production Scale-Up (GP3)

The flow electrolysis was scaled-up with respect to the amount of mass of the substrate (from 0.0032 mol to 0.052 mol). Thus, 96 mL of 0.4 M **1a** (0.052 mol) was prepared and added to the catholyte compartment formed by H_2O/MeOH (1:1) and 2M of $H_2SO_{4(aq)}$. Both compartments, catholyte and anolyte, were pumped separately into the cell (Fr = 4.5 L h^{-1}). Electrochemical conditions: 44460.43 C (12 F); current density: 30 mA cm^{-2}; temperature: room temperature; anode: C_{gr}; cathode: CuSn7Pb15 (cathodic area: 12 cm^2); separator: Nafion™ N324 (0.5 mm). After electrolysis, the content of the cathodic compartment was collected. The solid was filtered. The liquid phase of the filtration was used to determine the yields of start material (**1a**) and dissolved product by ^{19}F NMR spectroscopy, using as standard ethyl trifluoroacetate. The solid part was washed with cold water and cyclohexane. After, the solid was dried under reduced pressure and the isolated yield for the 3-trifluoromethylanilinium bisulfate **2a** was determined. It is important to note that the same Nafion™ N324 (DuPont, Wilmington, United States) membrane was used for all experiments.

7.7. Cathode Area Scale-Up (GP5)

We stated the cathodic area scale-up using the general protocol 4.5 (GP5). Initially, flow rate, solvent system, substrate concentration (**1a**), and molarity of acid were

investigated (**Table S15**). It is important to note that the same Nafion™ N324 (DuPont, Wilmington, United States) membrane was used for all experiments.

Table S15. Results for the reaction optimization using a divided flow electrolysis indicated in the protocol 3.2 (GP5) – cathode area scale-up.[a]

Entries	c of 1a [mM]	j [mA cm^{-2}]	c (H$_2$SO$_4$) [M]	H$_2$O/ MeOH	V [mL]	F [L h^{-1}]	Q [F]	(2a') / %	(2a) / %
1	400	30	2	1:1	16	7.5	12	79	17
2	400	30	2	1:3	16	7.5	12	85	< 5
3	400	30	2	1:3	16	7.5	14	89	-
4	400	30	2	1:3	16	7.5	16	91	< 5
5	400	30	3	1:2	16	7.5	14	58	39
6	400	30	2	1:1	16	5.0	14	85	12
7	400	30	2	1:1	16	5.0	14	70	26
8	400	30	2	1:1	16	5.0	16	64	31
9	**600**	**30**	**2**	**1:1**	**16**	**7.5**	**12**	**15**	**81**
10	500	60	2	1:1	16	7.5	12	75	25
11	500	30	2	1:1	16	5.0	12	83	15
12	500	30	2	1:1	16	7.5	16	92	< 5
13	400	30	2	1:1	50	4.5	12	89	8
14	400	30	2	1:1	50	7.5	12	48	49
15	400	30	2	1:1	50	5.0	12	75	20
16	600	30	2	1:1	50	7.5	12	17	78
17	600	30	3	1:1	50	7.5	12	22	74
18	400	40	2	1:1	50	7.5	12	60	37
19	400	60	2	1:1	50	7.5	12	71	23
20	**600**	**30**	**5**	**1:1**	**50**	**7.5**	**12**	**15**	**80**
21	**600**	**30**	**5**	**1:1**	**100**	**7.5**	**12**	**18**	**81**
22	600	30	5	1:1	200	7.5	12	20	76
23	600	30	5	1:1	500	7.5	12	21	73
24	600	30	5	1:1	800	7.5	12	18	76

[a]**Electrolysis parameters**: applied charge: 12 F; current density: 30-60 mA·cm^{-2}; temperature: room temperature; anode: C$_{gr}$; cathode: CuSn7Pb15 (cathodic area: 48 cm^2); c(substrate): 400-600 mM; separator: Nafion™ N324 (0.5 mm); 16-800 mL of solvent (formed by a solution of H$_2$O/MeOH; 1:1-1:3); electrolyte: 2-5 M H$_2$SO$_{4(aq)}$. Flow rate adopted varied 4.5-7.5 L h^{-1}. 2a corresponds to the precipitated product in the salt form. The difference between the yields corresponds to the product that is dissolved in the solution. Yields of 1a, and dissolved product 2a' were determined via ^{19}F NMR spectroscopy with ethyl trifluoroacetate as internal standard; [b]The product was isolated after two hours of acid addition.

8. Synthesis of 3-Trifluoromethylanilinium Bisulfate Derivates (2a-h)

3-Trifluoromethylanilinium bisulfate (2a)
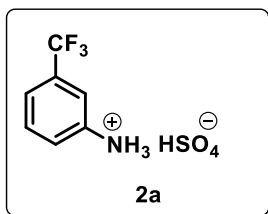
Prepared according to the general protocol described in the section 3.1. (GP1) from 3-nitrobenzotrifluoride **1a** (320 µL, 2.4 mmol, 400 mм). The product 2a was obtained by filtration using a sintered glass funnel after washing with cold water and cyclohexane. A light-yellow solid (491 mg, 1.9 mmol, 69%).

**1H NMR** (400 MHz, DMSO-D6): δ [ppm] = 7.46 (td, *J* = 8.1. 1.1 Hz, 1H), 7.26-7.20 (m, 3H), 6.98 (s, 3H).

13C NMR (101 MHz, CDCl₃): δ [ppm] = 139.19, 131.21, 130.96, 130.64, 130.32, 130.01, 128.38, 125.67, 124.51, 122.96, 120.73, 116.83.

19F NMR (376 MHz, CDCl₃): δ [ppm] = -61.43 (s, 3H).

HRMS for $C_7H_6F_3N$ (ESI⁺) [M+H]⁺: calc.: 162.0525, found:162.0523.

Elemental analysis for $C_7H_7F_3N(HSO_4)\cdot 2H_2O$ calc.: C: 28.48; H: 4.10; N: 4.74, found: C: 28.88; H: 3.67; N: 4.90.

3-(Trifluoromethyl)-4-methylanilinium bisulfate (2b)
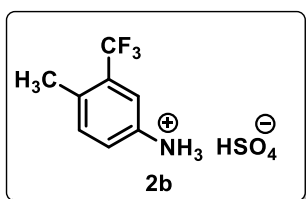
Prepared according to the general protocol described in the section 3.1. (GP1) from 1-methyl-4-nitro-2-(trifluoromethyl)benzene **1b** (492 mg, 2.4 mmol, 400 mм). The product **2b** was obtained by filtration using a sintered glass funnel after washing with cold water and cyclohexane. A light-yellow solid (452.13 mg, 1.65 mmol, 68%).
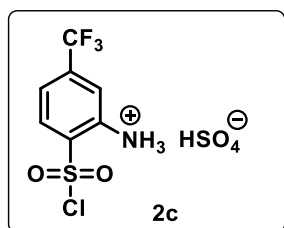
1H NMR (400 MHz, DMSO-D6): δ [ppm] = 8.34 (dd, *J* = 8.5, 2.5 Hz, 1H), 8.28 (d, *J* = 2.4 Hz, 1H), 7.72 (d, *J* = 8.4 Hz, 1H), 7.31 (s, 3H), 2.51 (s, 4H).

¹³C NMR (101 MHz, CDCl₃): δ [ppm] = 146.02, 144.72, 134.40, 129.23, 128.92, 128.61, 128.30, 127.73, 127.44, 124.99, 122.27, 121.16, 121.10, 121.05, 120.99, 19.25, 19,23.

¹⁹F NMR (376 MHz, CDCl₃): δ [ppm] = -60.70 (s, 3H).

HRMS for $C_8H_8F_3N$ (ESI⁺) [M+H]⁺: calc.: 176.0682; found: 176.0681.

5-Trifluoromethyl-2-sulfochloride-anilinium bisulfate (2c)

Prepared according to the general protocol described in the section 3.1. (GP1) from 2-nitro-4-(trifluoromethyl)benzenesulfonyl chloride **1c** (695.08 mg, 2.4 mmol, 400 mм). The product **2c** was obtained by filtration using a sintered glass funnel after washing with cold water and cyclohexane. A light-yellow solid (314.09 mg, 0.88 mmol, 37%).
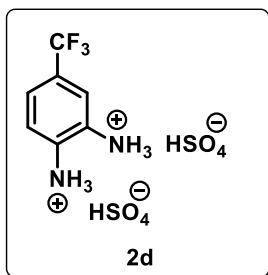
¹H NMR (400 MHz, DMSO-D6): δ [ppm] = 7.71 (d, *J* = 7.2 Hz, 1H), 7.16 (d, *J* = 1.9 Hz, 1H), 7.08 (dd, *J* = 7.7, 1.4 Hz, 1H), 5.83 (s, 3H).

¹³C NMR (101 MHz, CDCl₃): δ [ppm] = 140.86, 137.13, 131.03, 130.72, 130.41, 130.09, 128.85, 125.75, 123.04, 115.45, 114.91, 114.87.

¹⁹F NMR (376 MHz, CDCl₃): δ [ppm] = -61.46 (s, 3H).

HRMS for $C_7H_7ClF_3NO_2S$ (ESI⁺) [M+H]⁺: calc.: 259.9754; found: 259.9697.

4-(Trifluoromethyl)-1,2-phenylenediaminium bisulfate (2d)

Prepared according to the general protocol described in the section 3.1. (GP1) from 4-trifluoromethyl-2-nitroaniline **1d** (566.65 mg, 2.4 mmol, 400 mM). The product **2d** was obtained by filtration using a sintered glass funnel after washing with cold water and cyclohexane. A purple solid (293.87 mg, 0.79 mmol, 33%).
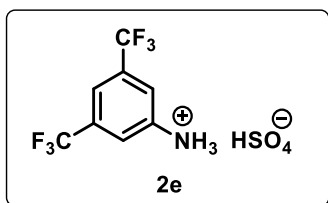
¹H NMR (400 MHz, DMSO-D6): δ [ppm] = 7.16 (d, J = 2.1 Hz, 1H), 7.10 (dd, J = 8.3, 2.5 Hz, 1H), 6.85 (d, J = 8.3 Hz, 1H), 5.70 (s, 6H).

¹³C NMR (101 MHz, CDCl₃): δ [ppm] = 140.28, 129.28, 127.08, 126.59, 123.91, 120.22, 118.80, 118.48, 118.16, 117.80, 116.39.

¹⁹F NMR (376 MHz, CDCl₃): δ [ppm] = -59.53 (s, 3H).

HRMS for $C_7H_8F_3NO_4S$ (ESI⁺) [M+H]⁺: calc.: 178.0707; found: 178.0696.

3,5-Bis(trifluoromethyl)anilinium bisulfate (2e)

Prepared according to the general protocol described in the section 3.1. (GP1) from 1-nitro-3,5-bis(trifluoromethyl)benzene **1e** (621 mg, 2.4 mmol, 400 mM). The product **2e** was obtained by filtration using a sintered glass funnel after washing with cold water and cyclohexane. A light yellow-solid (455.18 mg, 1.39 mmol, 58%).
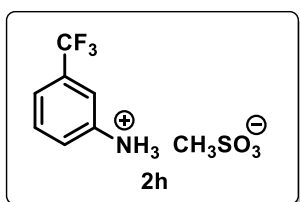
¹H NMR (400 MHz, DMSO-D6): δ [ppm] = 7.46 (td, J = 8.1. 1.1 Hz, 1H), 7.26-7.20 (m, 3H), 6.98 (s, 3H).

13C NMR (101 MHz, CDCl$_3$): δ [ppm] = 150.15, 131.81, 131.49, 131.17, 130.85, 128.13, 125.42, 122.72, 120.01, 113.88, 113.84, 108.21.

19F NMR (376 MHz, CDCl$_3$): δ [ppm] = -61.95 (s, 3H).

HRMS for C$_7$H$_8$F$_3$NO$_4$S (ESI$^+$) [M+H]$^+$: calc.: 230.0399; found: 230.0397.

3-Trifluoromethylanilinium methanesulfonate (2h)

Prepared according to the general protocol described in the section 3.1. (GP1) from 3-nitrobenzotrifluoride **1a** (320 µL µL, 2.4 mmol, 400 mм). Here, methanesulfonic acid was used instead sulfuric acid. The product **2h** was obtained by filtration using a sintered glass funnel after washing with cold water and cyclohexane. A light-yellow solid (287.87 mg, 1.13 mmol, 47%).

1H NMR (300 MHz, DMSO-D6): δ [ppm] = ^{1}H NMR (600 MHz, DMSO) δ 8.27 (s, 4H), 7.78 – 7.70 (m, 3H), 7.66 (dt, *J* = 7.6, 1.9 Hz, 1H), 2.49 (s, 4H).

13C NMR (101 MHz, CDCl$_3$): δ [ppm] = 134.08, 131.65, 130.94, 130.72, 130.51, 130.29, 127.77, 126.66, 124.94, 124.91, 124.89, 124.86, 123.05, 121.24, 120.22, 120.20, 120.17, 120.15, 40.04.

19F NMR (376 MHz, CDCl$_3$): δ [ppm] =-62.64 (s, 3H).

HRMS for C$_7$H$_8$F$_3$NO$_4$S (ESI$^+$) [M+H]$^+$: calc.: 162.0525, found:162.0521.
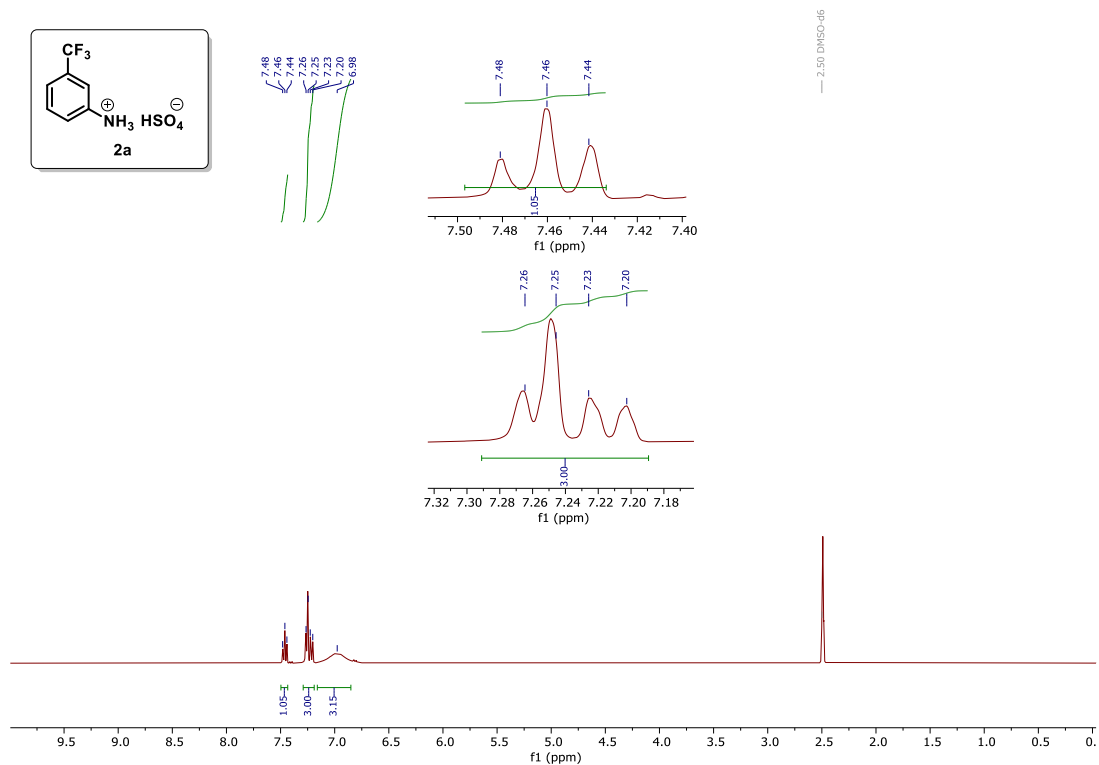
9. NMR Spectra

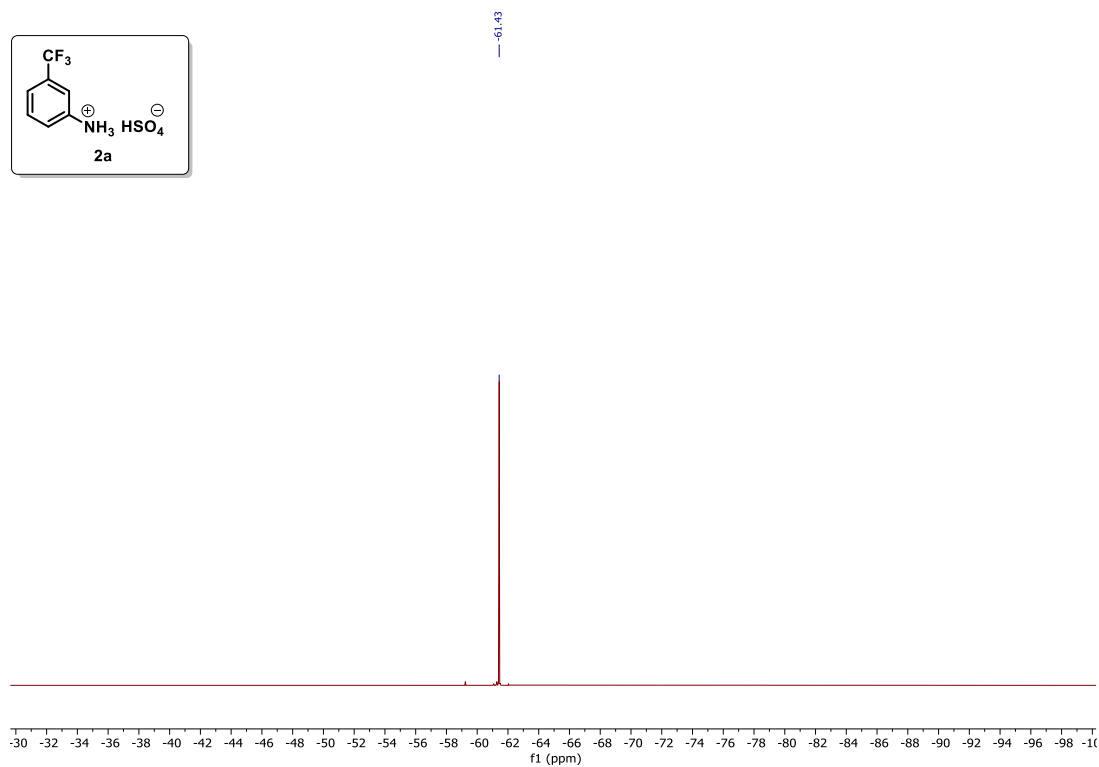**Figure S6**. ^{1}H NMR (400 MHz) **2a** in DMSO at 298 K.
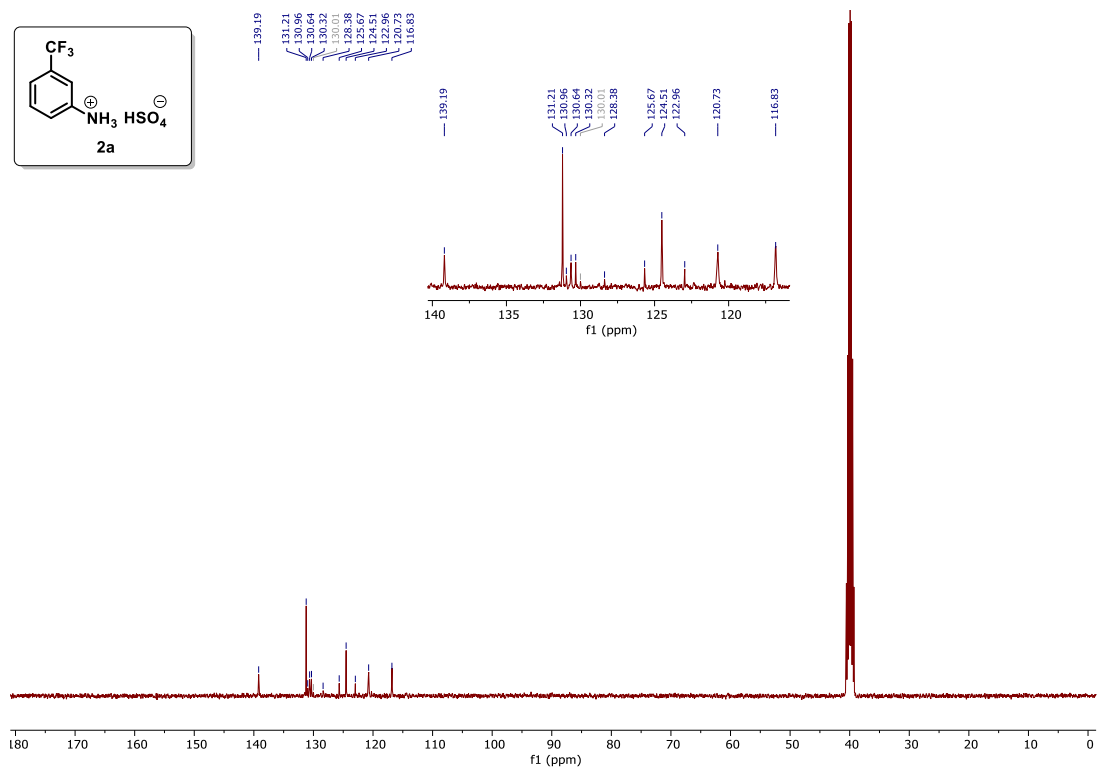

Figure S7. ^{19}F NMR (376 MHz) **2a** in DMSO at 298 K.

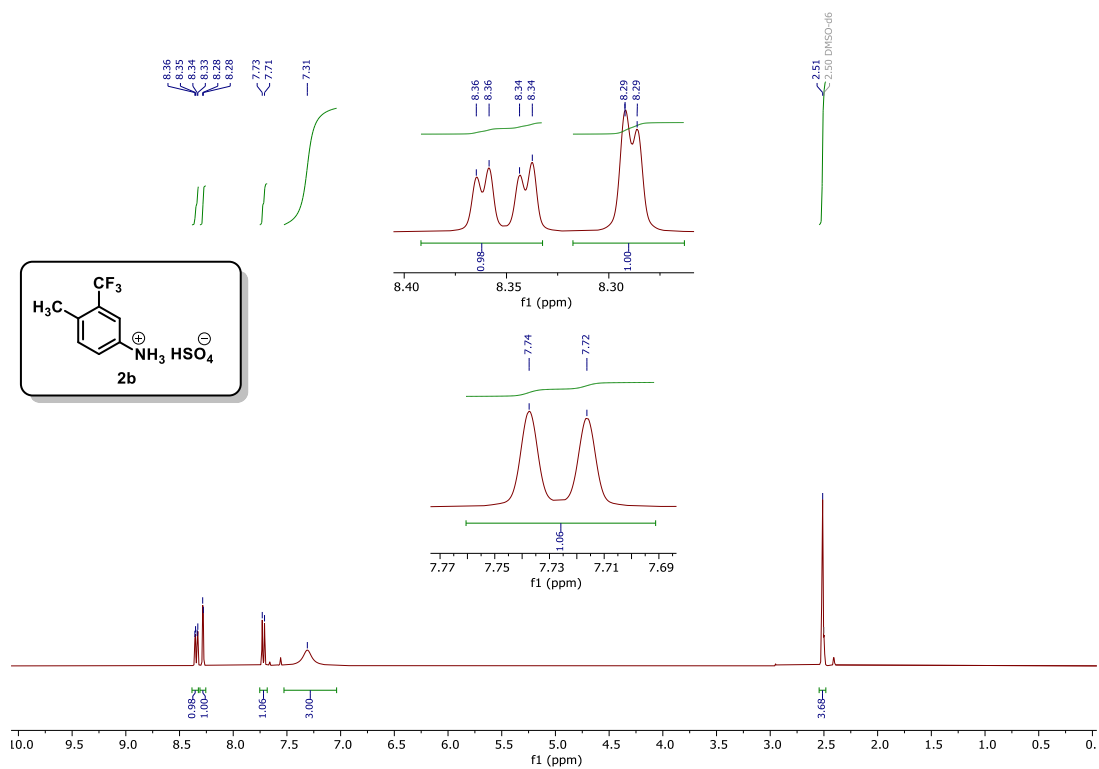**Figure S8**. ^{13}C NMR (101 MHz) **2a** in DMSO at 298 K.

Figure S9. ^{1}H NMR (400 MHz) **2b** in DMSO at 298 K.

Figure S10. ^{19}F NMR (376 MHz) **2b** in DMSO at 298 K.

Figure S11. ^{13}C NMR (101 MHz) **2b** in DMSO at 298 K.
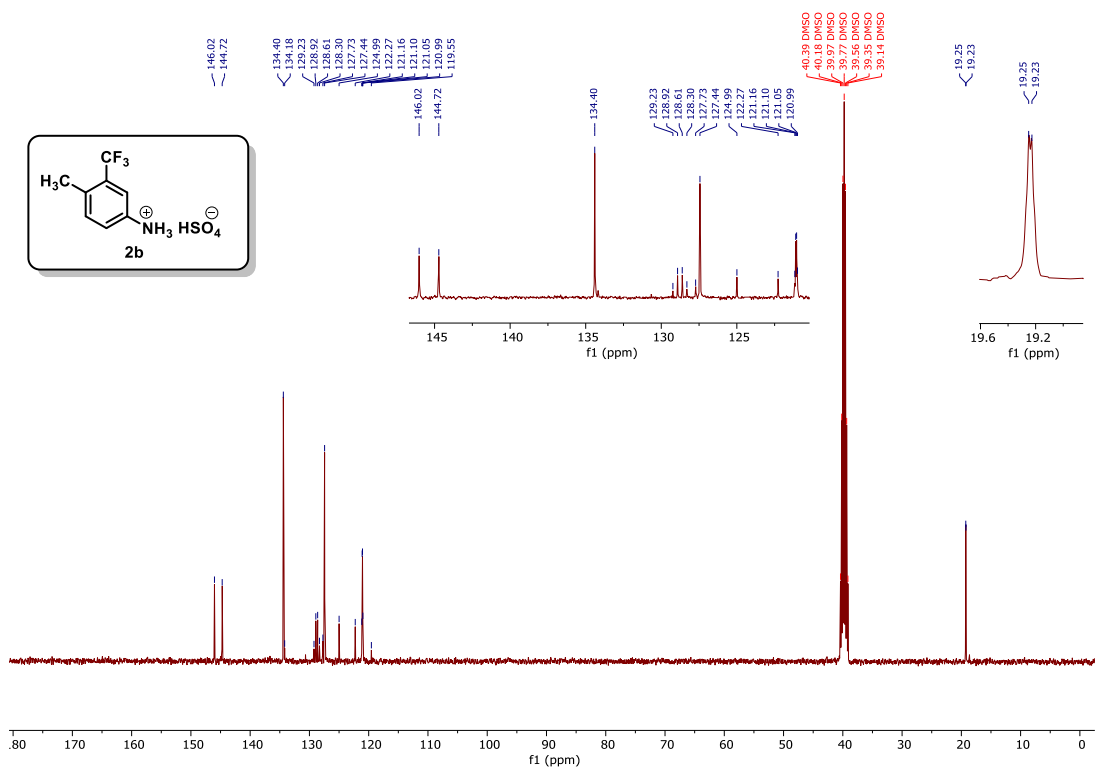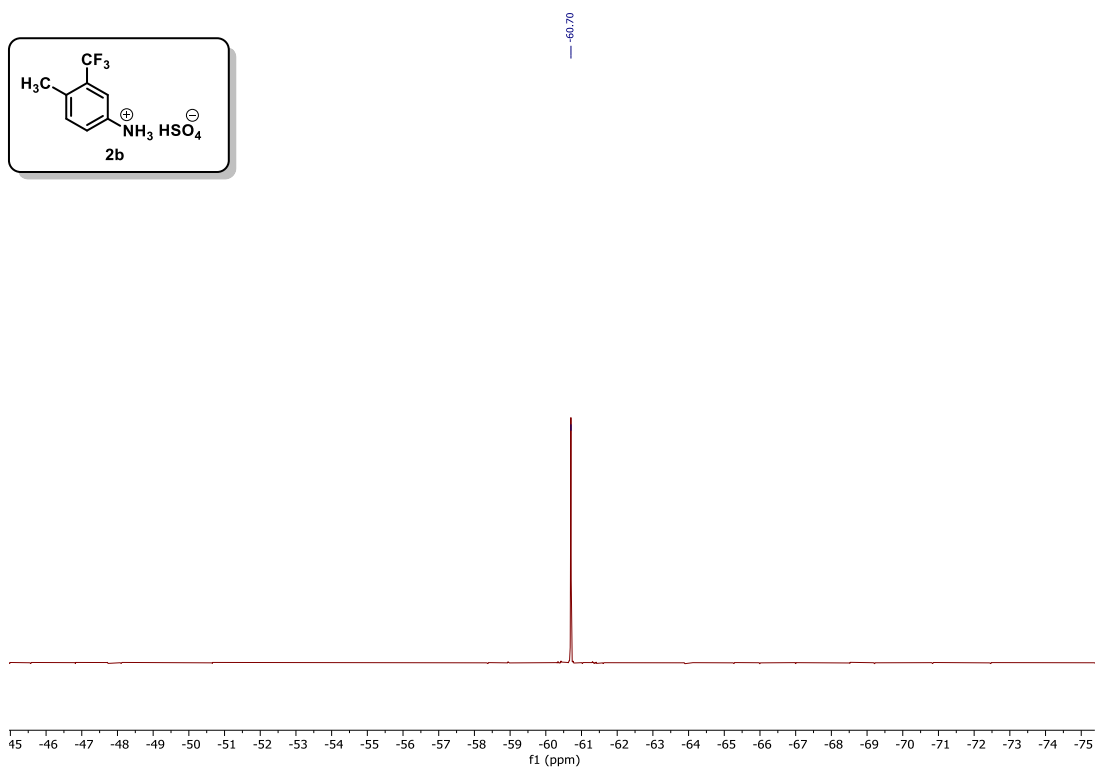
Figure S12. ^{1}H NMR (400 MHz) **2c** in DMSO at 298 K.

Figure S13. ^{19}F NMR (376 MHz) **2c** in DMSO at 298 K.

Figure S14. ^{13}C NMR (101 MHz) **2c** in DMSO at 298 K.

Figure S15. ^{1}H NMR (400 MHz) **2d** in DMSO at 298 K.

S32

186

Figure S16. ^{19}F NMR (376 MHz) **2d** in DMSO at 298 K.

Figure S17. ^{13}C NMR (101 MHz) **2d** in DMSO at 298 K.
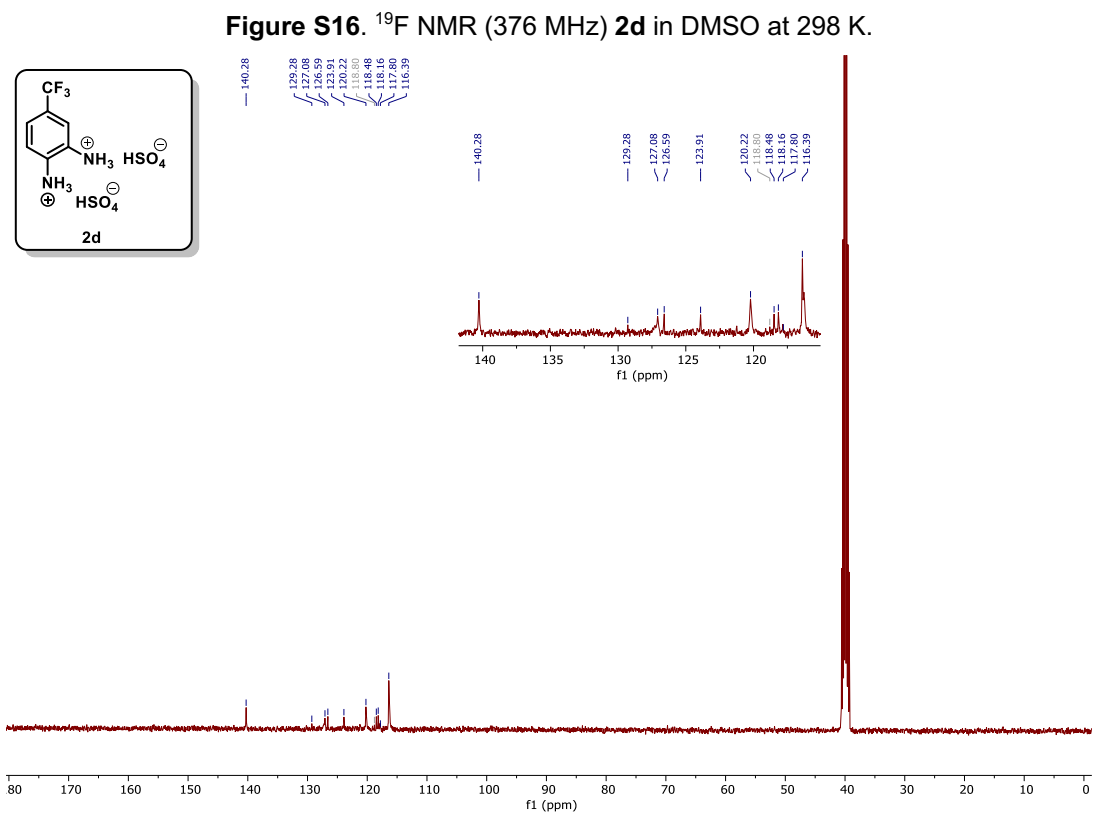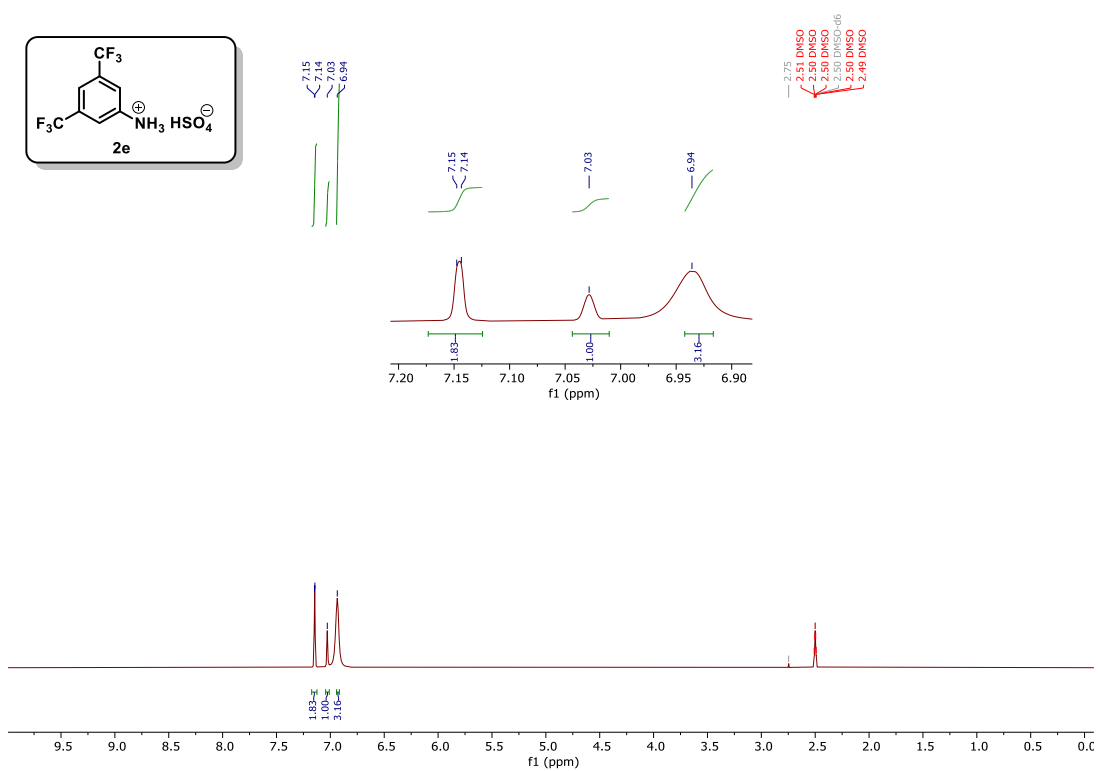
Figure S18. ^{1}H NMR (400 MHz) **2e** in DMSO at 298 K.
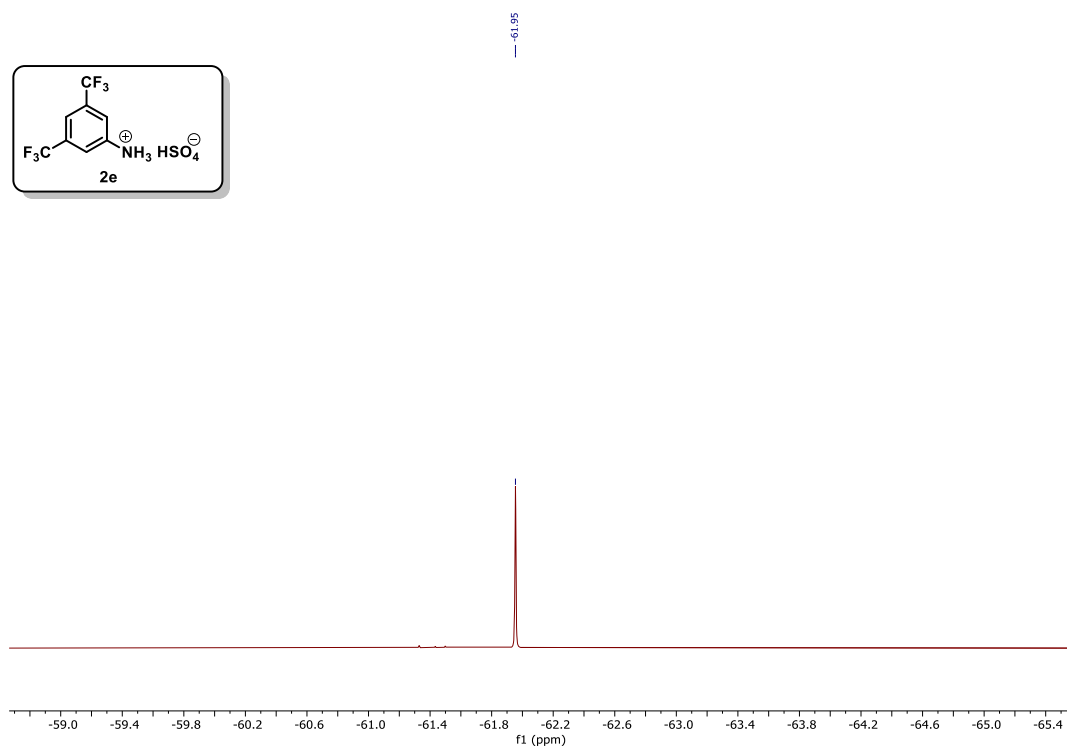
Figure S19. ^{19}F NMR (376 MHz) **2e** in DMSO at 298 K.

S34

188
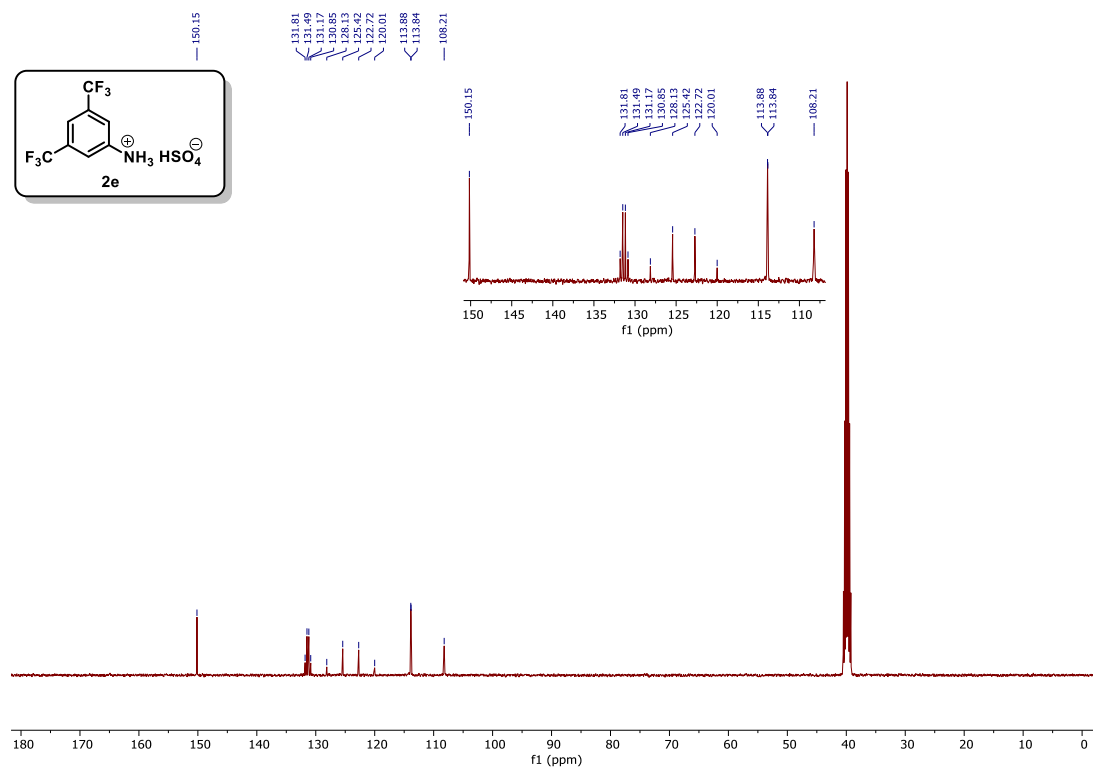
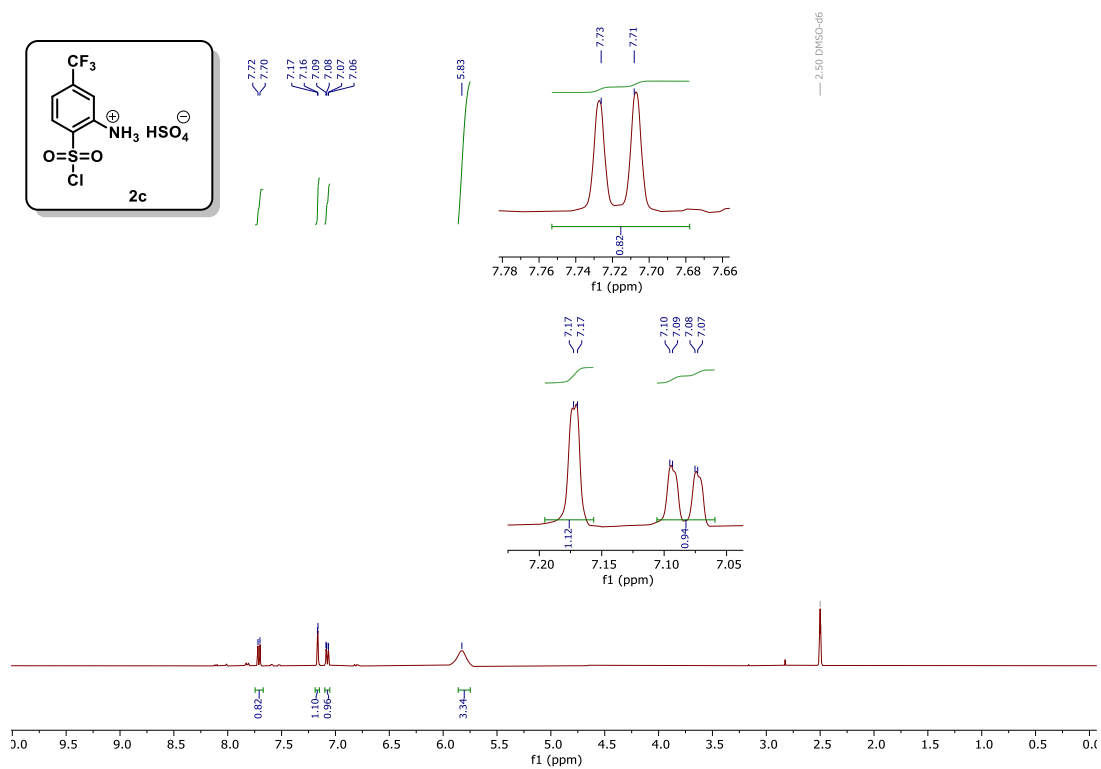**Figure S20**. ^{13}C NMR (101 MHz) **2e** in DMSO at 298 K.
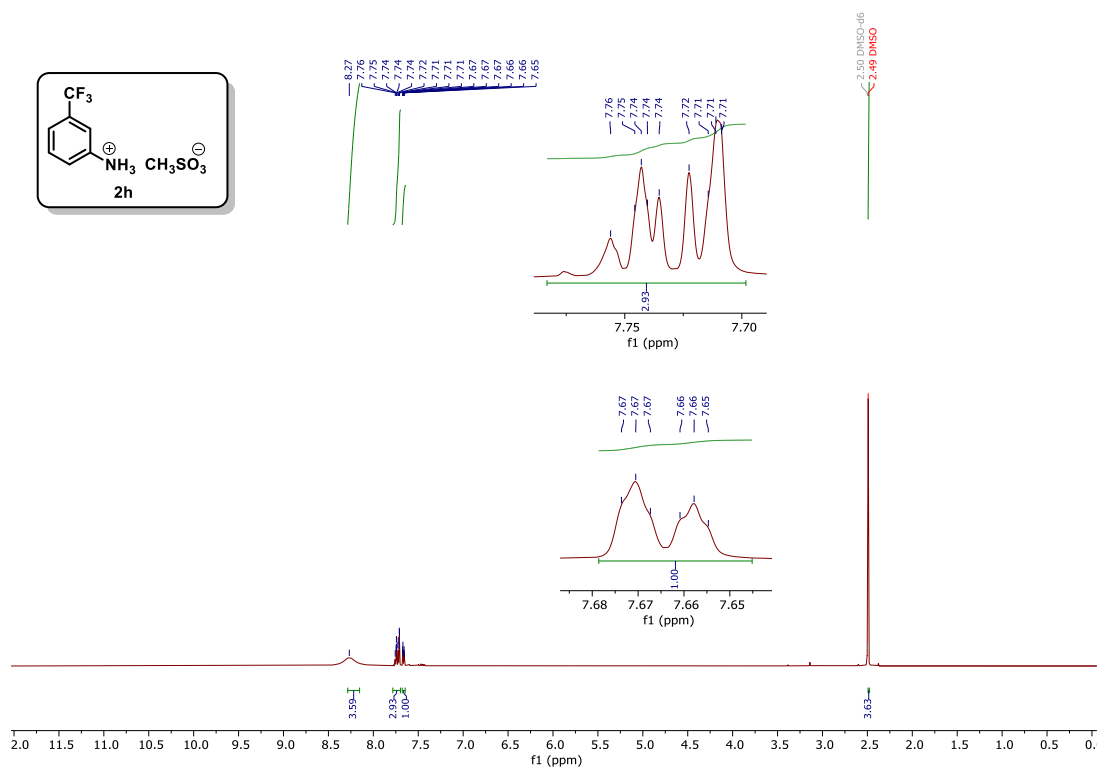
Figure S21. ^{1}H NMR (400 MHz) **2h** in DMSO at 298 K.
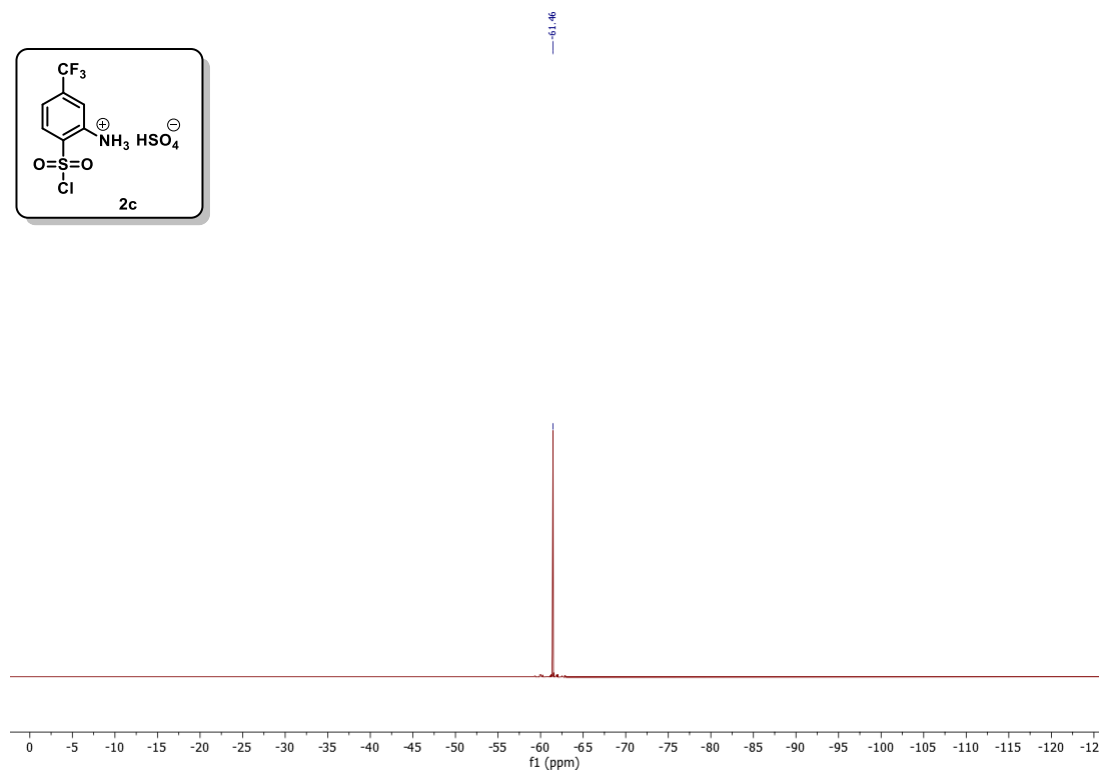
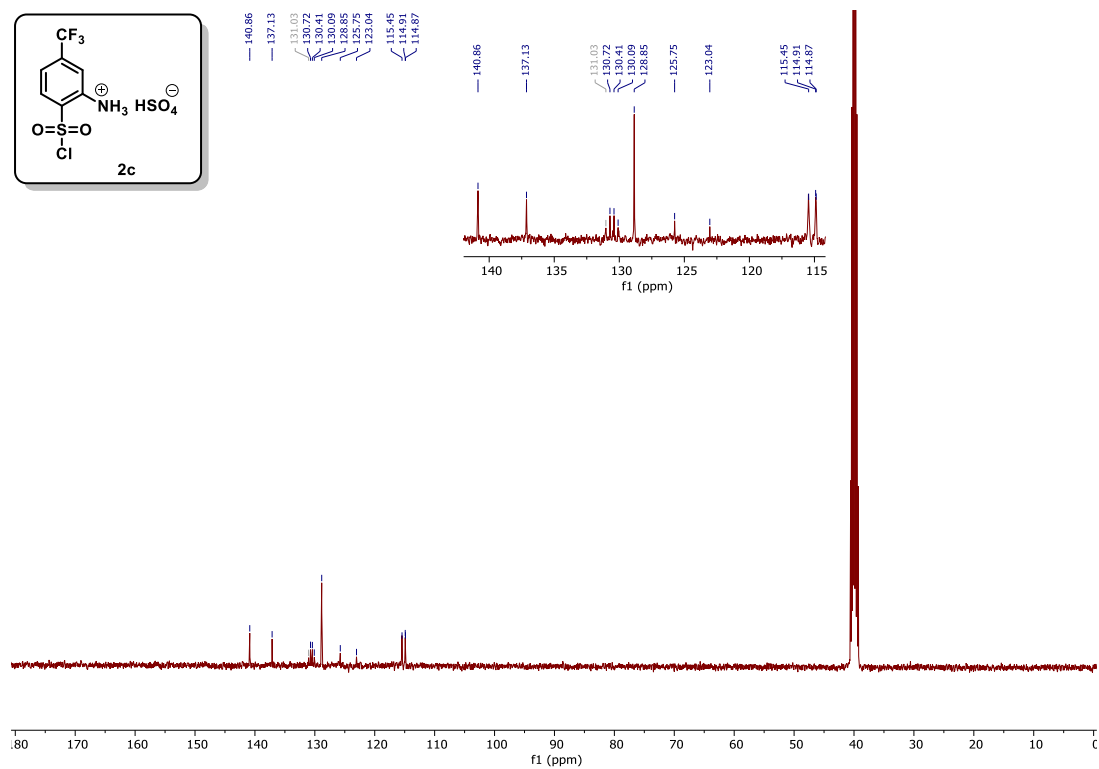**Figure S22**. ^{19}F NMR (376 MHz) **2h** in DMSO at 298 K.

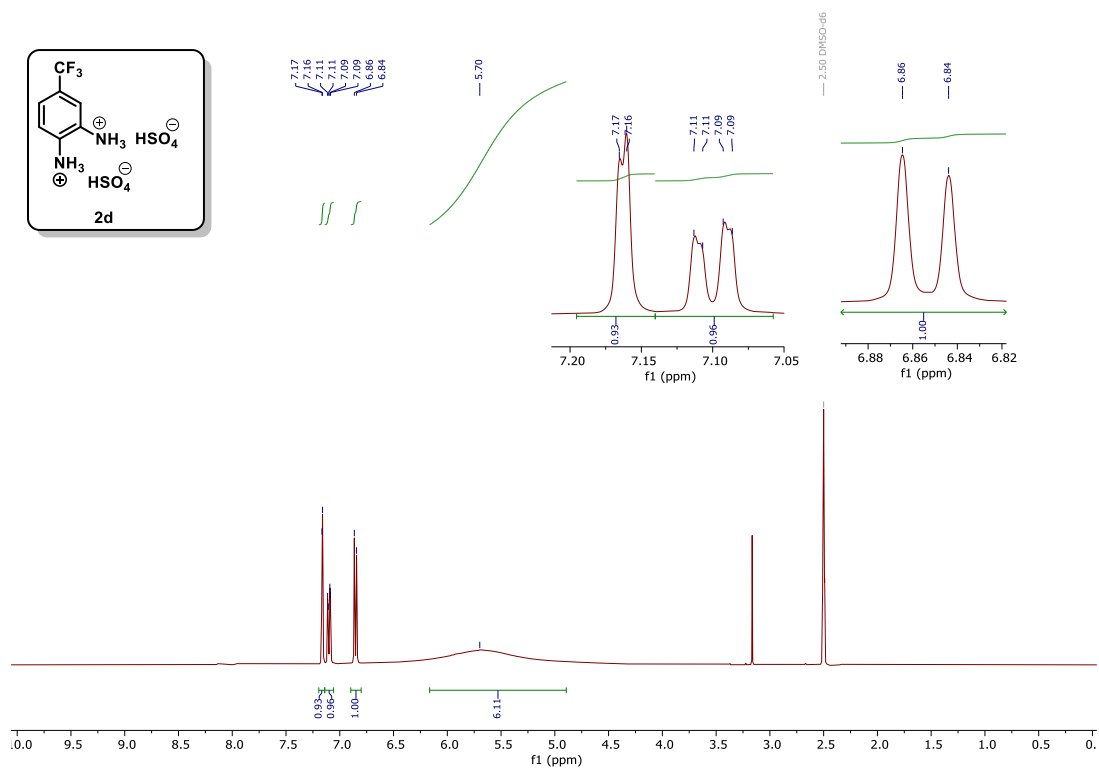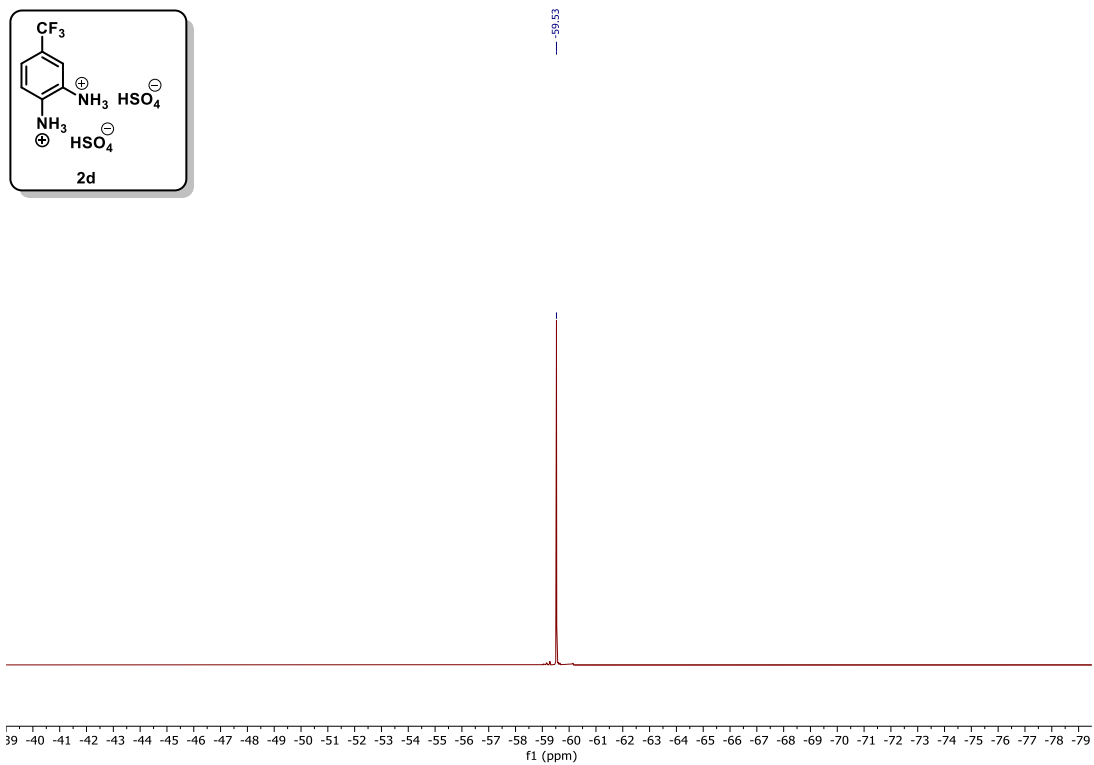**Figure S23**. ^{13}C NMR (101 MHz) **2h** in DMSO at 298 K.
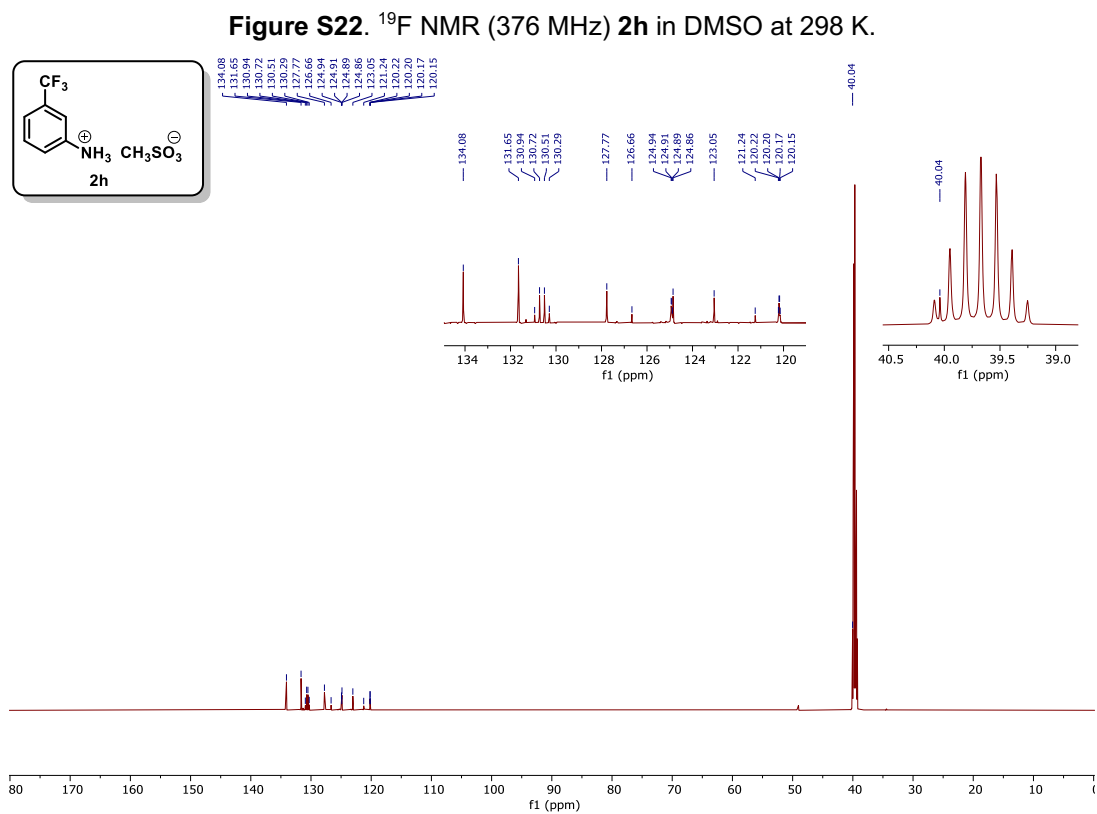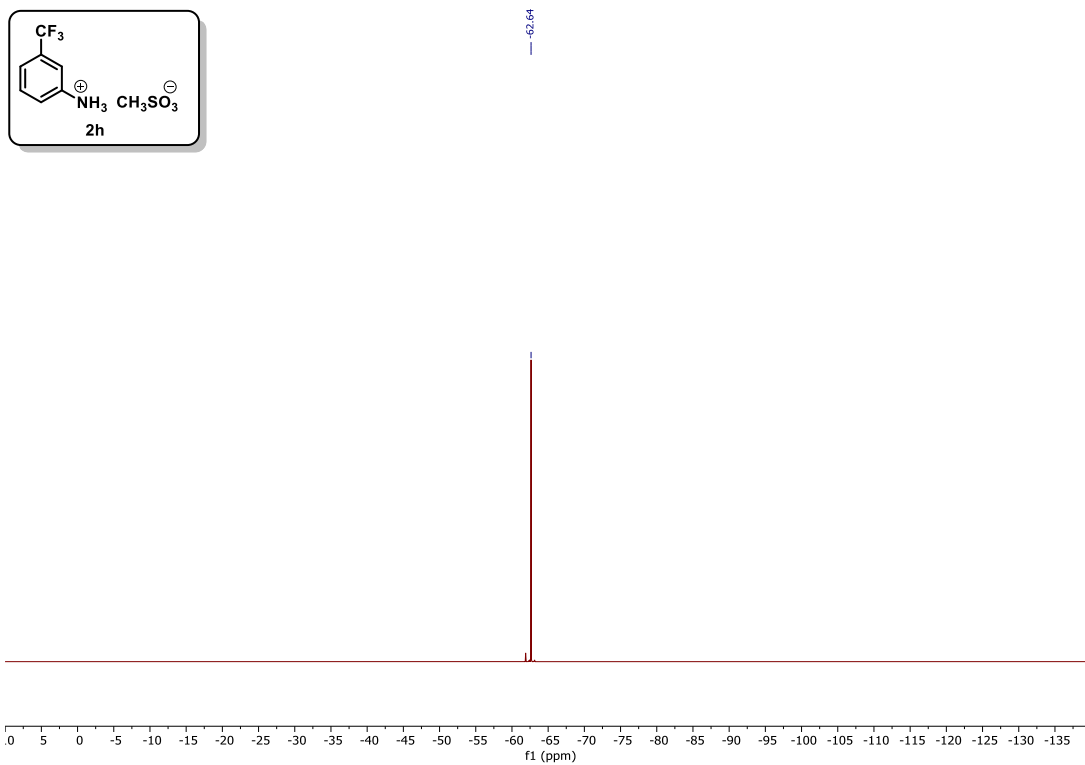
10. IR Spectra of 2c

Sulfonyl chloride exhibits strong characteristic bands in the IR region of 1410-1370, 1204-1166, 408 cm^{-1} and 586 cm^{-1}, S-Cl symmetric stretch. These stretches can be seen in the IR of **2c** spectrum,
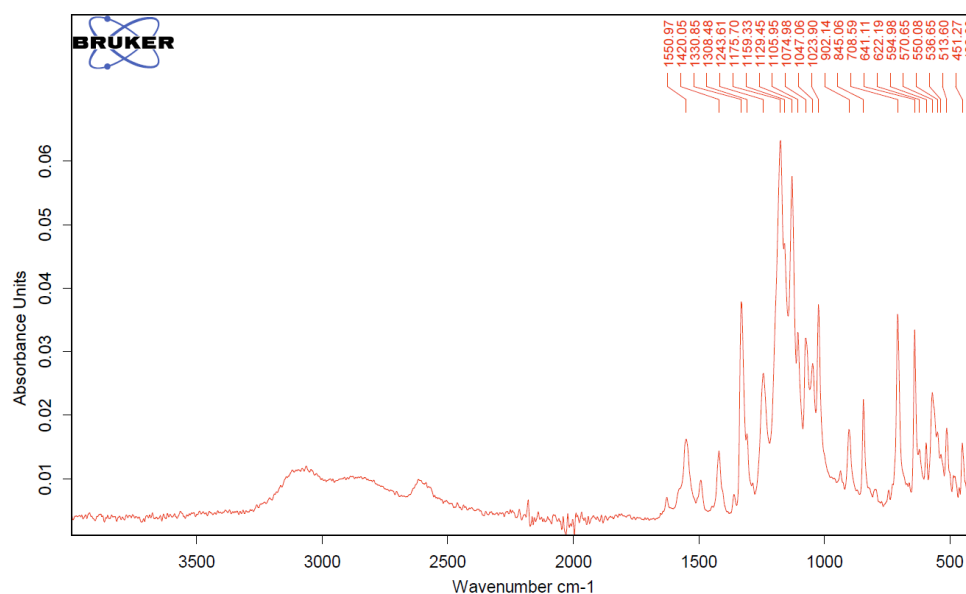
Figure S24. Spectra of IR of **2c**.

11. Photos of Synthesized 3-Trifluoromethylanilinium Bisulfate Derivates (2a-e and h)
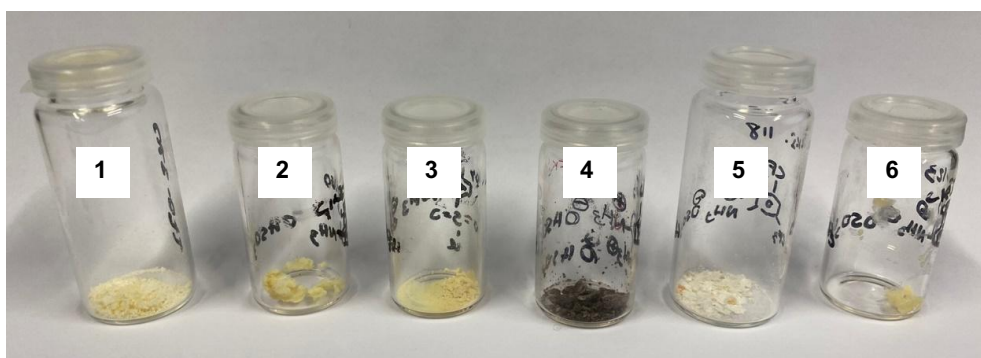
Figure S25. Samples of 3-trifluoromethylanilinium bisulfate derivates: (**1**) 3-trifluoromethylanilinium bisulfate (**2a**); (**2**) 3-(trifluoromethyl)-4-methylanilinium bisulfate (**2b**); (**3**) 5-trifluoromethyl-2-sulfochlorid-anilinium bisulfate (**2c**); (**4**) 4-(trifluoromethyl)-1,2-phenylenediaminium bisulfate (**2d**); (**5**) 3,5-bis(trifluoromethyl)anilinium (**2e**); (**6**) 3-trifluoromethylanilinium methanesulfonate (**2h**).
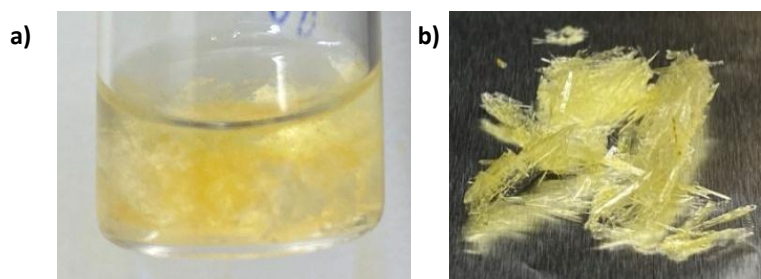
Figure S26. a) and b) 3-trifluoromethyllanilinium bisulfate (**2a**), bright yellow crystals.

12. Photo of Electrodes Used in Batch Reactions (7.0 x 1.0 x 0.3 cm)
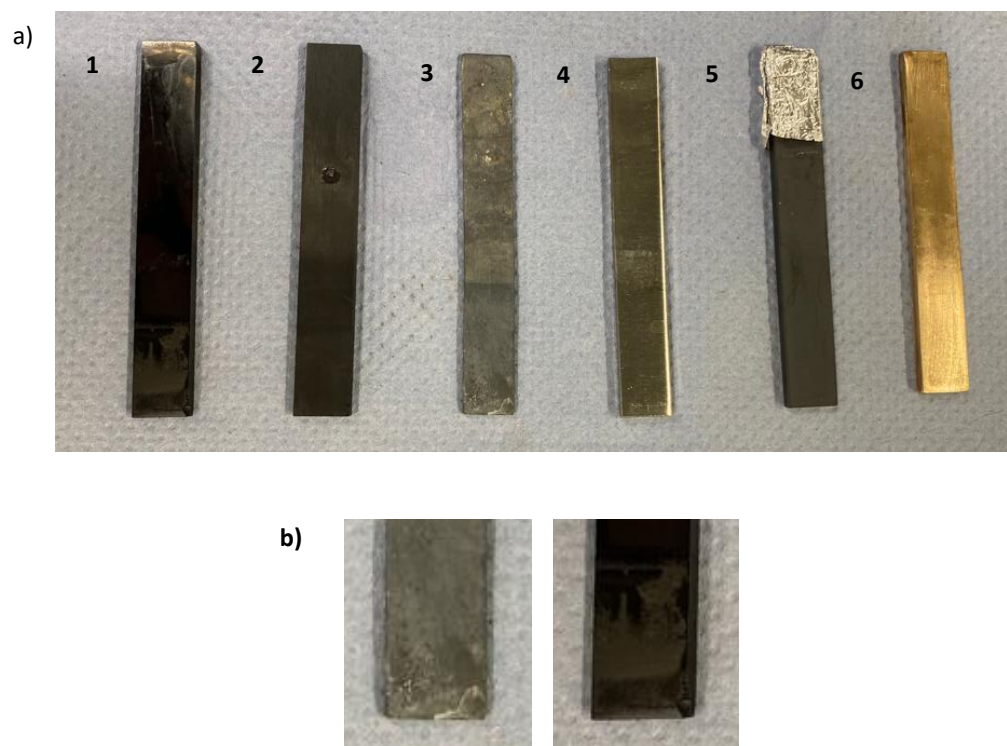
Figure S27. a) 1 x 7 cm^{-2} electrodes: (**1**) glassy carbon electrode; (**2**) graphite electrode; (**3**) Lead electrode; (**4**) Stainless steel electrode; (**5**) BDD electrode; (**6**) CuSn7Pb15 electrode; b) Examples of corroded electrodes: lead and glassy carbon electrode.

S38

13. Photo of the Flow Systems Used
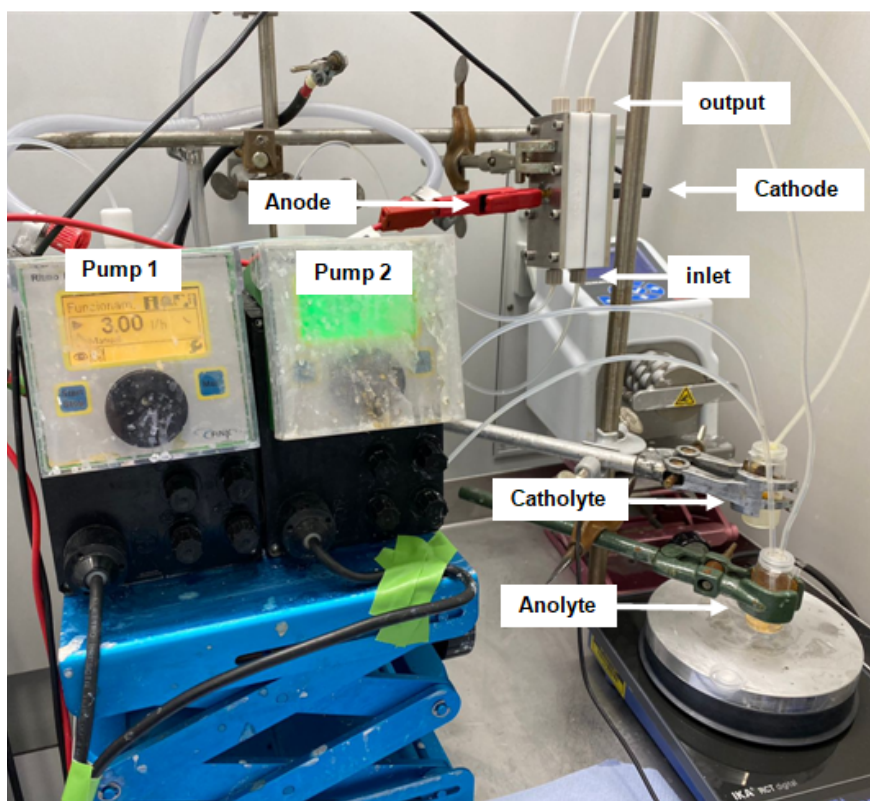
Figure S28. Photo of the flow system (electrodes 2 x 6 cm^2, graphite and CuSn7Pb15).
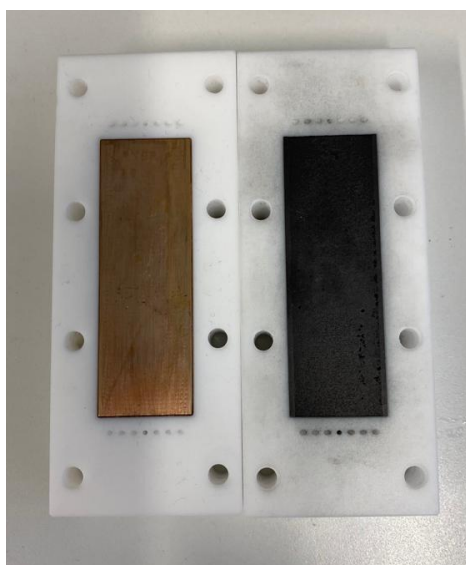
Figure S29. Photo of flow cell (electrodes 2 x 6 cm^2, CuSn7Pb15 and graphite).
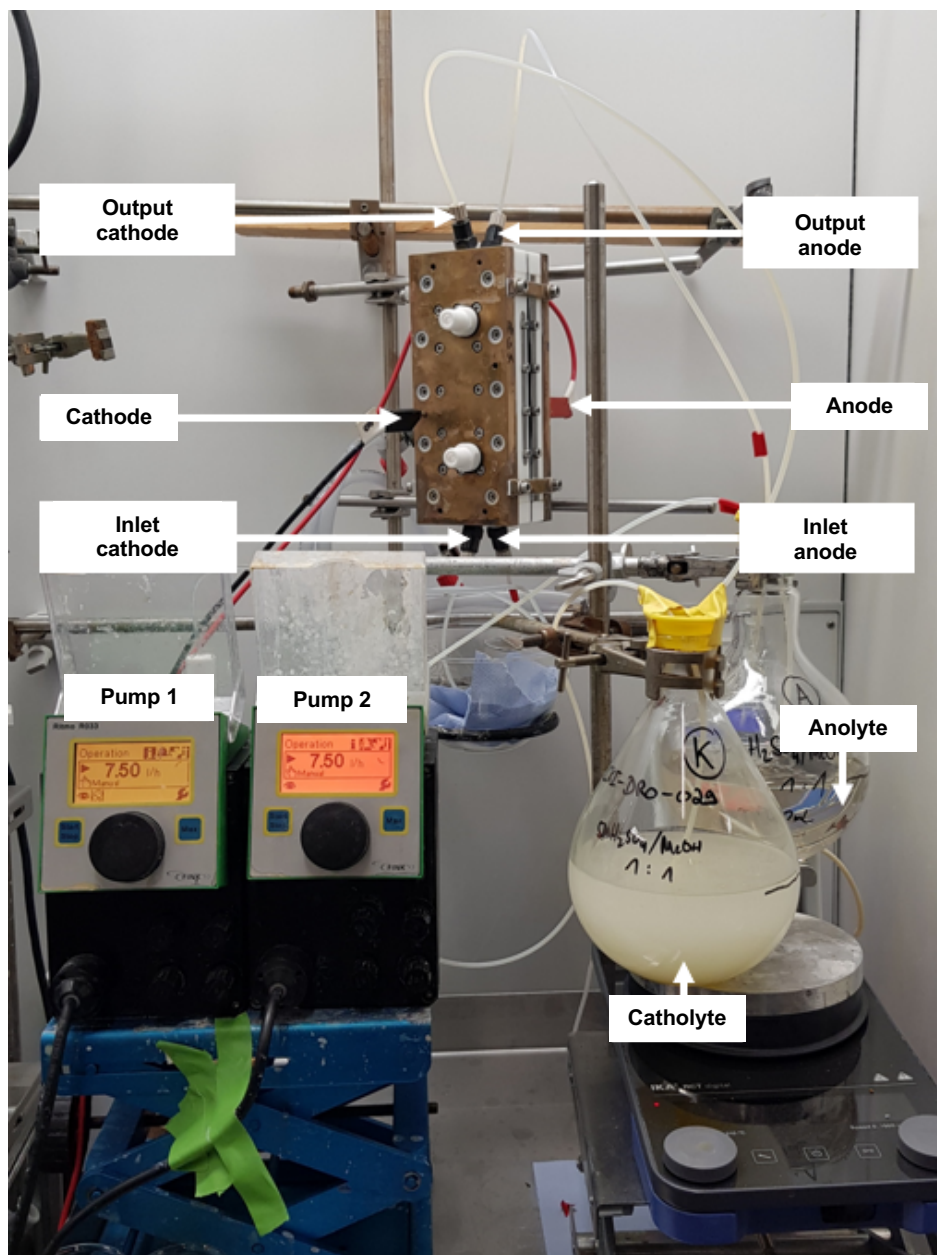
Figure S30. Photo of the flow system (electrodes 4 x 12 cm^2, graphite and CuSn7Pb15).
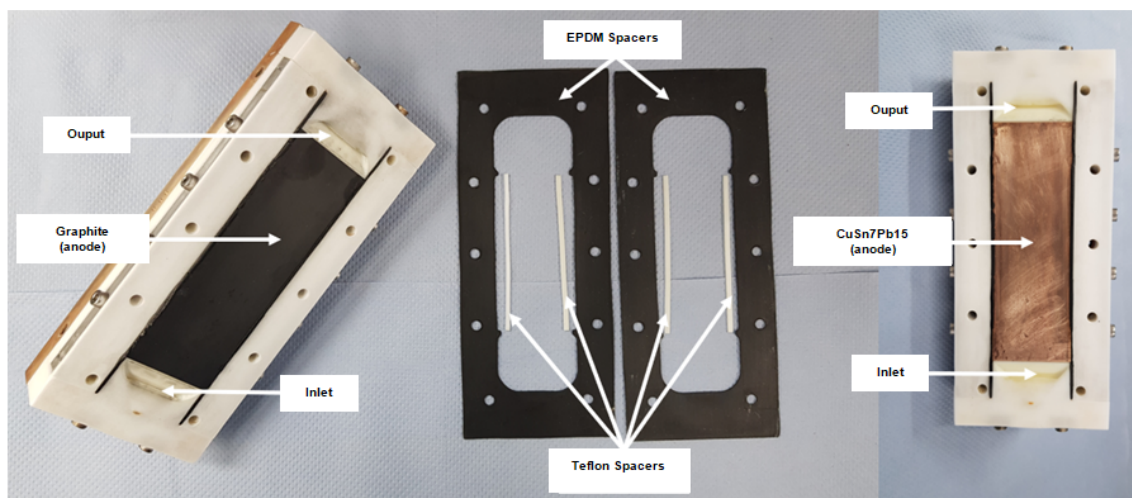
Figure S31. Photo of a flow cell (electrodes 4 x 12 cm^2, graphite and CuSn7Pb15).

Figure S31-A. Used Nafion^{TM} N324 membrane.
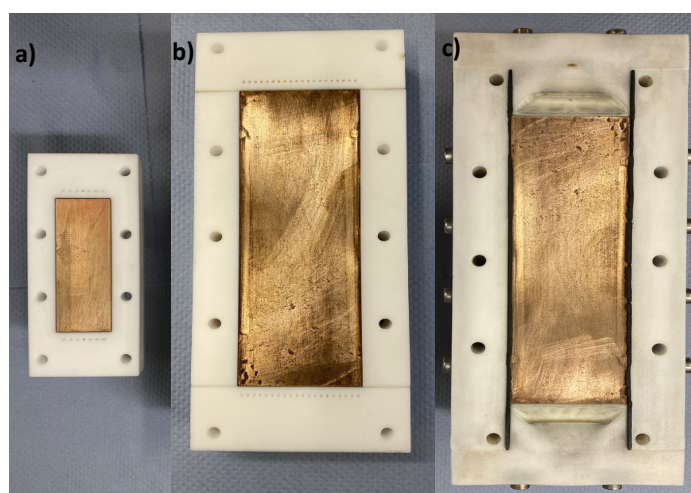
Figure S32. Photo of different half flow cell (electrodes of CuSn7Pb15). a) 2 x 6 cm^2 CuSn7Pb15 electrode with microchannel inlets; b) 4 x 12 cm^2 CuSn7Pb15 electrode with microchannel inlets; c) 4 x 12 cm^2 CuSn7Pb15 electrode with macrochannel inlets;

S41
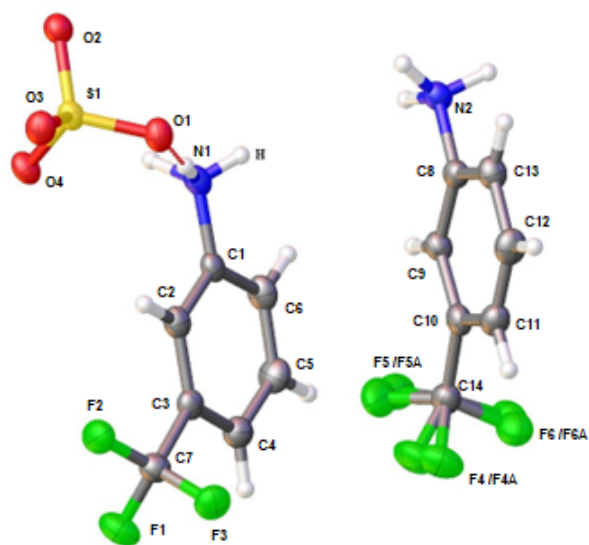
14. X-ray Analysis

Figure S33. Molecular structure of **2a** from X-ray crystallographic analysis.
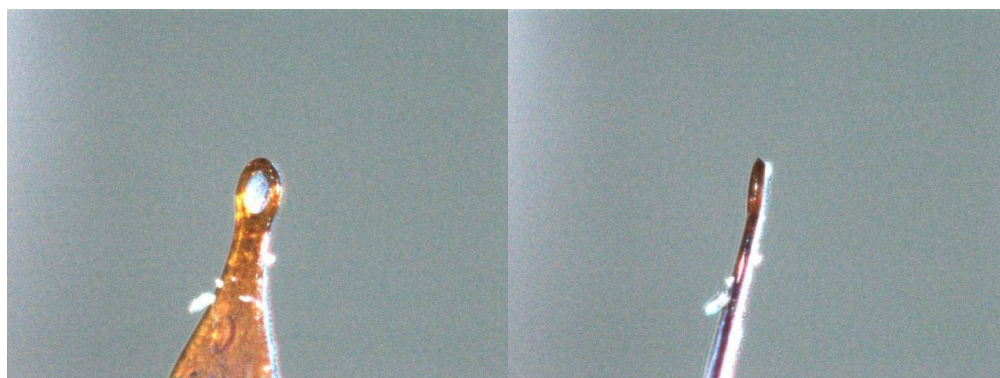
Figure S34. Images of the Crystal on the Diffractometer.

14.1. Additional Tables to X-ray Analysis

Table S16. Crystal data and structure refinement for test_gauss_twin1_hklf4.

Identification code	test_gauss_twin1_hklf4
Empirical formula	$C_{14}H_{14}F_6N_2O_4S$
Formula weight	420.33
Temperature/K	122.9(3)
Crystal system	triclinic
Space group	P-1
a/Å	5.7266(3)
b/Å	9.4077(4)
c/Å	16.0095(12)

α/°	94.555(5)
β/°	97.394(5)
γ/°	95.446(4)
Volume/Å^3	847.79(9)
Z	2
ρ$_{calc}$g/cm^3	1.647
μ/mm^{-1}	2.545
F(000)	428.0
Crystal size/mm^3	0.115 × 0.079 × 0.011
Radiation	CuKα (λ = 1.54184)
2Θ range for data collection/°	9.484 to 147.924
Index ranges	-7 ≤ h ≤ 5, -11 ≤ k ≤ 11, -19 ≤ l ≤ 19
Reflections collected	5802
Independent reflections	5802 [R$_{int}$ = ?, R$_{sigma}$ = 0.0435]
Data/restraints/parameters	5802/36/297
Goodness-of-fit on F^2	1.071
Final R indexes [I>=2σ (I)]	R$_1$ = 0.0565, wR$_2$ = 0.1665
Final R indexes [all data]	R$_1$ = 0.0773, wR$_2$ = 0.1744
Largest diff. peak/hole / e Å^{-3}	0.41/-0.54

Structure Quality Indicators

Reflections:
Refinement:

d min (Cu) CIF	0.80	I/σ CIF	23.0	Rint CIF	n/a	complete	99%
Shift CIF	0.006	Max Peak CIF	0.4	Min Peak CIF	-0.5	GooF CIF	1.071

Table S17. Fractional Atomic Coordinates (×10^4) and Equivalent Isotropic Displacement Parameters (Å^2×10^3) for test_gauss_twin1_hklf4. U$_{eq}$ is defined as 1/3 of of the trace of the rthogonalized U$_{IJ}$ tensor.

Atom	x	y	z	U(eq)
S1	2193.6(15)	7325.5(9)	4792.4(6)	21.6(3)
F2	2179(4)	7751(2)	1507.8(15)	34.1(6)
F3	1980(4)	5961(2)	564.6(15)	35.6(6)
F1	4611(5)	7752(3)	580.4(17)	40.7(6)
O2	-230(5)	7785(3)	4693.0(18)	27.6(6)
O3	3074(5)	7337(3)	5705.7(17)	26.0(6)
O4	3804(4)	8317(3)	4410.2(17)	25.4(6)
O1	2123(5)	5861(3)	4377.1(17)	26.2(6)
F5	3310(50)	650(30)	701(17)	38(3)
F4	400(30)	1850(20)	377(12)	47(3)
F6	3400(40)	2847(17)	1228(11)	48(3)
N1	6530(6)	5503(4)	3912(2)	24.5(7)
N2	2548(6)	951(4)	4077(2)	24.1(7)
C12	1216(7)	798(4)	3227(2)	23.1(8)
C5	6615(7)	5480(4)	3010(2)	23.2(8)

C7	3495(7)	6921(4)	1085(3)	27.8(8)
C6	5025(7)	6189(4)	2514(2)	24.8(8)
C4	8331(7)	4771(4)	2660(3)	28.8(9)
C13	2232(7)	1341(4)	2566(2)	24.4(8)
C10	-2311(7)	-85(4)	2295(3)	31.4(9)
C11	-1051(7)	73(4)	3104(3)	27.4(8)
C14	2078(7)	1634(4)	1023(3)	30.2(9)
C2	6946(7)	5528(4)	1301(3)	28.7(8)
C8	949(7)	1143(4)	1756(3)	26.3(8)
C1	5209(7)	6198(4)	1662(2)	24.5(8)
C3	8489(7)	4800(4)	1808(3)	32.5(9)
C9	-1325(7)	429(4)	1621(3)	29.8(9)
F6A	4120(40)	2570(30)	1259(14)	45(3)
F4A	740(50)	2290(30)	489(16)	46(3)
F5A	2870(60)	570(50)	570(20)	41(4)

Table S18. Anisotropic Displacement Parameters ($Å^2 × 10^3$) for test_gauss_twin1_hklf4. The Anisotropic displacement factor exponent takes the form: $-2\pi^2[h^2a^{*2}U_{11}+2hka^*b^*U_{12}+\ldots]$.

Atom	U_{11}	U_{22}	U_{33}	U_{23}	U_{13}	U_{12}
S1	17.5(5)	20.1(4)	26.7(5)	3.5(3)	0.6(3)	1.8(3)
F2	36.8(14)	32.7(12)	34.0(13)	4.5(10)	1.9(11)	12.8(10)
F3	32.3(13)	38.4(13)	32.2(13)	0.0(10)	-6.3(11)	1.0(10)
F1	41.1(15)	43.4(14)	40.7(14)	21.2(11)	6.4(12)	5.0(11)
O2	21.0(14)	27.6(13)	33.4(15)	1.1(11)	-0.5(11)	5.0(10)
O3	25.7(14)	23.8(13)	28.1(14)	4.0(10)	2.5(11)	0.5(10)
O4	20.3(13)	22.3(12)	33.9(15)	8.1(10)	3.5(11)	-0.6(10)
O1	20.5(13)	23.1(13)	34.0(15)	2.3(11)	0.5(11)	2.1(10)
F5	44(7)	37(5)	38(7)	12(5)	13(5)	16(5)
F4	42(4)	61(8)	40(5)	23(5)	-2(3)	9(5)
F6	62(7)	34(5)	46(4)	4(3)	14(5)	-14(4)
N1	21.9(17)	22.0(16)	29.9(17)	6.6(13)	1.0(14)	3.9(13)
N2	21.2(17)	23.9(16)	26.4(17)	5.0(13)	-0.6(13)	1.5(13)
C12	24.1(19)	20.3(17)	24.6(18)	2.1(14)	0.3(15)	4.8(14)
C5	23.3(19)	16.9(16)	28.3(19)	3.8(14)	0.9(15)	-1.4(13)
C7	27(2)	28.6(19)	27(2)	4.9(15)	2.7(16)	0.4(15)
C6	20.5(18)	21.4(17)	32(2)	2.8(15)	1.4(16)	0.4(14)
C4	21.4(19)	26.2(19)	39(2)	5.0(16)	0.2(17)	5.9(15)
C13	23.9(19)	21.3(17)	28(2)	4.6(14)	2.3(16)	1.0(14)
C10	24(2)	30(2)	37(2)	-1.4(16)	-3.2(17)	-0.3(15)
C11	24(2)	24.6(18)	33(2)	3.4(15)	2.0(16)	1.2(14)
C14	34(2)	27.2(19)	28(2)	2.7(16)	-0.9(17)	5.8(16)
C2	29(2)	27.0(19)	30(2)	1.9(15)	3.4(17)	0.6(15)
C8	29(2)	19.2(17)	31(2)	3.5(15)	3.4(17)	4.9(14)
C1	22.5(19)	21.2(17)	27.6(19)	1.4(14)	-0.9(15)	-1.5(13)
C3	29(2)	33(2)	37(2)	0.1(17)	6.7(18)	8.3(17)
C9	31(2)	28.1(19)	29(2)	0.0(16)	-2.4(17)	4.6(16)
F6A	53(8)	41(7)	38(4)	4(5)	9(6)	-16(5)

| F4A | 56(8) | 47(7) | 40(6) | 21(6) | 4(5) | 19(6) |
| F5A | 48(10) | 39(5) | 39(9) | 7(6) | 13(6) | 6(7) |

Table S19. Bond Lengths for test_gauss_twin1_hklf4.

Atom	Atom	Length/Å	Atom	Atom	Length/Å
S1	O2	1.485(3)	C5	C4	1.390(5)
S1	O3	1.483(3)	C7	C1	1.507(5)
S1	O4	1.472(3)	C6	C1	1.382(5)
S1	O1	1.476(3)	C4	C3	1.379(6)
F2	C7	1.340(4)	C13	C8	1.394(5)
F3	C7	1.345(4)	C10	C11	1.388(6)
F1	C7	1.345(5)	C10	C9	1.380(6)
F5	C14	1.33(3)	C14	C8	1.495(6)
F4	C14	1.360(17)	C14	F6A	1.39(2)
F6	C14	1.302(16)	C14	F4A	1.31(2)
N1	C5	1.450(5)	C14	F5A	1.34(4)
N2	C12	1.461(5)	C2	C1	1.389(5)
C12	C13	1.382(6)	C2	C3	1.388(6)
C12	C11	1.391(5)	C8	C9	1.390(6)
C5	C6	1.385(5)			

Table S20. Bond Angles for test_gauss_twin1_hklf4.

Atom	Atom	Atom	Angle/°	Atom	Atom	Atom	Angle/°
O3	S1	O2	109.23(16)	C10	C11	C12	118.5(4)
O4	S1	O2	110.12(16)	F5	C14	F4	105.2(12)
O4	S1	O3	108.89(15)	F5	C14	C8	112.0(14)
O4	S1	O1	109.74(16)	F4	C14	C8	110.7(8)
O1	S1	O2	109.36(15)	F6	C14	F5	110.6(12)
O1	S1	O3	109.49(15)	F6	C14	F4	106.7(8)
C13	C12	N2	120.0(3)	F6	C14	C8	111.4(8)
C13	C12	C11	121.5(4)	F6A	C14	C8	113.5(9)
C11	C12	N2	118.4(4)	F4A	C14	C8	115.4(12)
C6	C5	N1	119.7(3)	F4A	C14	F6A	104.9(11)
C6	C5	C4	121.0(4)	F4A	C14	F5A	106.7(17)
C4	C5	N1	119.3(3)	F5A	C14	C8	113.1(19)
F2	C7	F3	106.8(3)	F5A	C14	F6A	102.0(17)
F2	C7	F1	107.3(3)	C3	C2	C1	118.9(4)
F2	C7	C1	112.9(3)	C13	C8	C14	119.7(4)
F3	C7	F1	105.9(3)	C9	C8	C13	120.4(4)
F3	C7	C1	111.7(3)	C9	C8	C14	119.8(4)
F1	C7	C1	111.9(3)	C6	C1	C7	120.9(3)
C1	C6	C5	118.4(4)	C6	C1	C2	121.6(4)
C3	C4	C5	119.6(4)	C2	C1	C7	117.5(4)
C12	C13	C8	118.9(4)	C4	C3	C2	120.5(4)
C9	C10	C11	121.1(4)	C10	C9	C8	119.5(4)

Table S21. Hydrogen Atom Coordinates (Å×10^4) and Isotropic Displacement Parameters (Å^2×10^3) for test_gauss_twin1_hklf4.

Atom	x	y	z	U(eq)
H6	3836.16	6657.39	2753.19	30
H4	9389.35	4270.75	3003.99	35
H13	3776.97	1841.79	2660.75	29
H10	-3877.67	-555.4	2204.06	38
H11	-1722.63	-304.44	3562.65	33
H2	7076.91	5566.65	717.97	34
H3	9661.38	4317.82	1567.39	39
H9	-2193.92	296.16	1068.97	36
H1A	5090(100)	5610(50)	4060(30)	40(13)
H2A	2880(80)	30(50)	4200(30)	31(12)
H1B	7710(90)	6300(50)	4250(30)	43(14)
H1C	6890(80)	4700(50)	4060(30)	30(12)
H2B	3880(100)	1560(60)	4150(40)	52(16)
H2C	1680(100)	1420(50)	4470(40)	47(14)

Table S22. Atomic Occupancy for test_gauss_twin1_hklf4.

Atom	Occupancy	Atom	Occupancy	Atom	Occupancy
F5	0.58(5)	F4	0.58(5)	F6	0.58(5)
F6A	0.42(5)	F4A	0.42(5)	F5A	0.42(5)

Crystal structure determination of [test_gauss_twin1_hklf4]

Crystal Data for $C_{14}H_{14}F_6N_2O_4S$ (*M* =420.33 g/mol): triclinic, space group P-1 (no. 2), *a* = 5.7266(3) Å, *b* = 9.4077(4) Å, *c* = 16.0095(12) Å, *α* = 94.555(5)°, *β* = 97.394(5)°, *γ* = 95.446(4)°, *V* = 847.79(9) Å^3, *Z* = 2, *T* = 122.9(3) K, μ(CuKα) = 2.545 mm^{-1}, *Dcalc* = 1.647 g/cm^3, 5802 reflections measured (9.484° ≤ 2Θ ≤ 147.924°), 5802 unique (R_{int} = ?, R_{sigma} = 0.0435) which were used in all calculations. The final R_1 was 0.0565 (I > 2σ(I)) and *wR$_2$* was 0.1744 (all data).

Refinement model description

Number of restraints - 36, number of constraints - unknown.

Details:

1. Twinned data refinement
 Scales: 0.76224
 0.23776
2. Uiso/Uaniso restraints and constraints
F6 ≈ F6A ≈ F5 ≈ F5A ≈ F4 ≈ F4A: within 2A with sigma of
0.01 and sigma for terminal atoms of 0.01 within 2A
3. Others
 Sof(F6A)=Sof(F4A)=Sof(F5A)=1-FVAR(1)
 Sof(F5)=Sof(F4)=Sof(F6)=FVAR(1)
4.a Aromatic/amide H refined with riding coordinates:
 C6(H6), C4(H4), C13(H13), C10(H10), C11(H11), C2(H2), C3(H3), C9(H9)

This report has been created with Olex2, compiled on 2019.07.11 svn.r3635 for OlexSys.

15. Elemental Analysis

Table S23. Statistics printout of the elemental analysis of **1a**.

Nr. Name	C [%]	H [%]	N [%]
Sample 1	29.05	3.85	4.95
Sample 2	29.02	3.62	4.93
Sample 3	29.88	3.55	4.82
Average	**28.88**	**3.67**	**4.90**
standard dev., abs. [%]	0.27	0.16	0.07
standard dev., rel. [%]	0.93	4.32	1.41
Delta [%]	0.48	0.30	0.13

Table S24. Coefficient expression of the elemental analysis of **1a**.

Modus	CHN		
	N	C	H
Coeff. a	6.87745e-003	-4.658453e-003	1.777033e-003
Coeff. b	2.742802e-005	3.947697e-005	1.367331e-005
Coeff. c	0.000000e+000	0.000000e+000	0.000000e+000
Coeff. d	0.000000e+000	0.000000e+000	0.000000e+000
Coeff. e	0.000000e+000	0.000000e+000	0.000000e+000
Min.:	1384	7717	1936
Max.:	37602	181435	5705
Modification Date:	26.01.2023 12:43:06	26.01.2023 12:43:06	26.01.2023 12:43:06
Coeff. a			2.012443e-002
Coeff. b			1.106611e-002
Coeff. c			0.000000e+000
Coeff. d			0.000000e+000
Coeff. e			0.000000e+000
Min.:			5705
Max.:			59398
Modification Date:			26.01.2023 12:43:06

Elemental analysis was performed to further confirm the equivalence of bisulfate anion and 3-trifluoromethylanilinium cation. The C, N and H contents of the crystals were 28.88, 3.67, and 4.90 wt %, respectively, which demonstrated the successful anionic bond of the one bisulfate anion to the one 3-trifluoromethylanilinium cation plus two water molecule $C_7H_7F_3N(HSO_4)\cdot2H_2O$.

16. Theoretical Background

Basic electrochemical reaction:

1) Cathode: $R\text{-}NO_2 + 6\ e^- + 6\ H^+ \rightarrow R\text{-}NH_2 + 2\ H_2O$
2) Anode: $2\ H_2O \rightarrow 4\ H^+ + 4\ e^- + O_2$
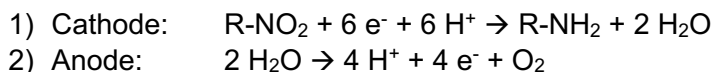
The acid is necessary to keep the pH constant and to supply the H^+ to the reduced nitro-intermediates.

Salt Formation:

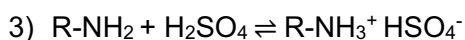3) $R\text{-}NH_2 + H_2SO_4 \rightleftharpoons R\text{-}NH_3^+\ HSO_4^-$

Here one more molecule of acid is necessary to form the product **2a**.

Calculation of charge:

Minimum charge needed: $\qquad Q_{min} = n * 6 * F$

Normalised minimum charge for the conversion of 1 mol: $\qquad \underline{Q_{min} = 6\ F}$

Q_{min}	minimum charge needed for the reduction [C]
n	number of moles [mol]
F	Faraday constant [96,485.322 C mol^{-1}]

Because of the parasitic hydrogen evolution reaction (HER), a charge excess is applied to achieve full conversion of substrate, e.g. twice the minimum charge = 12 *F*.

Example:

For the production of 107 g of **2a**, 800 mL of the catholyte solution was prepared. The solution was composed of **1a** (480 mmol, 600 mM) and H_2O/MeOH; 1:1); electrolyte: 5 M $H_2SO_{4(aq)}$. The amount of H_2SO_4 present in the solution was 4 mol. Taking into account equation "1)", up to 6 equivalents of acid can be consumed to reduce the nitro compound to aniline. Additionally, 1 equivalent is required for salt formation **2a**, as showed in the equation "3)". This totals a theoretical amount of acid of up to 3.4 mol $(7 * 0.48)$. Since HER occurs, an excess is used.
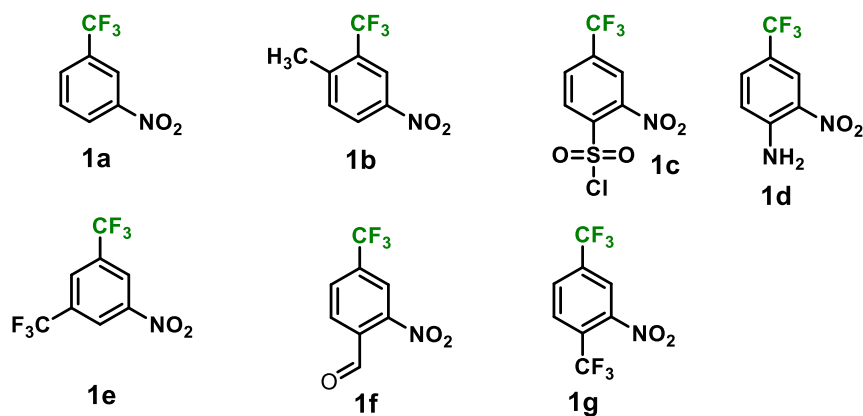
17. Structure of Tested Substrates

Figure S35.Tested compounds.

18. References

(1) Armarego, W. L. F.; Chai, C. L. L. *Purification of Laboratory Chemicals*, Elsevier, Amsterdam, **2013**.

(2) Dolomanov, O. V.; Bourhis, L. J.; Gildea, R. J.; Howard, J. A. K.; Puschmann, H. *OLEX2: A Complete Structure Solution, Refinement and Analysis Program. J. Appl. Cryst*. **2009**, *42*, 339-341.

(3) Gütz, C.; Klöckner, B.; Waldvogel, S. R. *Electrochemical Screening for Electroorganic Synthesis. Org. Process Res. Dev*. **2016**, *20*, 26–32.

(4) Selt, M.; Gleede, B.; Franke, R.; Stenglein, A.; Waldvogel, S. R. *Electrosynthesis of 3,3',5,5'-Tetramethyl-2,2'-biphenol in Flow. J. Flow Chem.* **2021**, *11*, 143–162.

(5) Gütz, C.; Stenglein, A.; Waldvogel, S. R. *Highly Modular Flow Cell for Electroorganic Synthesis. Org. Process Res. Dev*., **2017**, *21*, 771–778.

(6) Gleede, B.; Selt, M.; Gütz, C.; Stenglein, A.; Waldvogel, S. R. *Large Highly Modular Narrow Gap Electrolytic Flow cell and Application in Dehydrogenative Cross-Coupling of Phenols. Org. Process Res. Dev*., **2020**, *24*, 1916–1926.

(7) Arndt, S.; Rücker, R.; Stenglein, A.; Waldvogel, S. R. *Reactor Design for the Direct Electrosynthesis of Periodate. Org. Process Res. Dev.* **2022**, *26*, 2447–2455.

(8) Arndt, S.; Weis, D.; Donsbach, K.; Waldvogel, S. R. *The "Green" Electrochemical Synthesis of Periodate*, Angew. Chem. Int. Ed. **2020**, *59*, *21*, 8036-8041.

(9) Waldvogel, S. R.; Arndt, S.; Weis, D.; Donsbach, K. *Method for preparing periodates*, PCT Int. Appl. WO 2021110928 A1 20210610, 2021.

4 Zusammenfassung

In der vorliegenden Arbeit wurden elektrochemische Reduktionen in vier Themengebieten bearbeitet (Abbildung 4.1).
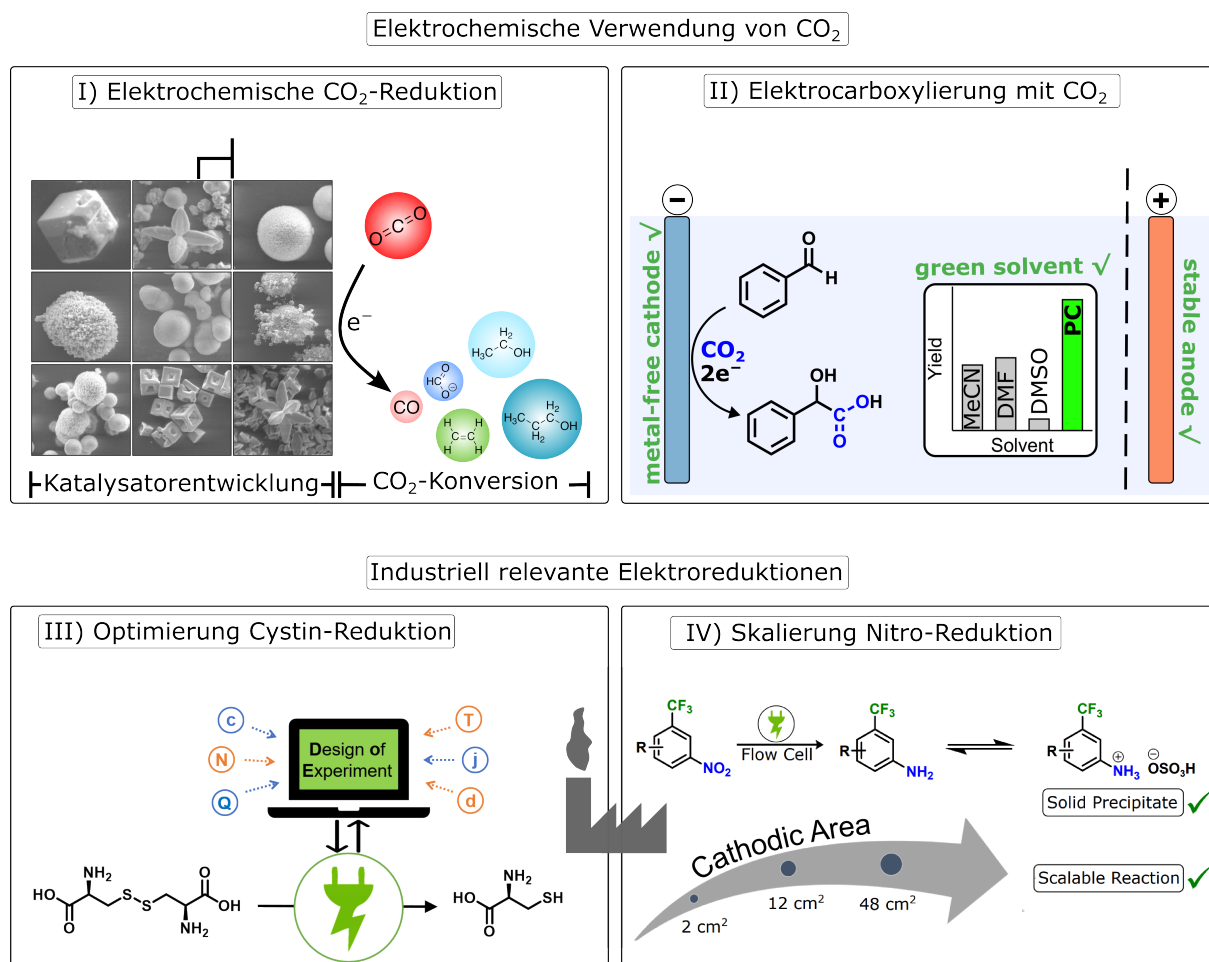
Abbildung 4.1: Graphische Übersicht der bearbeiteten Themengebiete.

Im ersten Komplex wurden Kupfer-basierte Elektrokatalysatoren für die elektrochemische CO_2-Reduktion hergestellt. Mittels hydrothermaler Synthese wurden Kupferoxide hergestellt, wobei unter Verwendung von Additiven die Materialeigenschaften der Katalysatoren beeinflusst wurden. Die Zugabe von Di- und Tricarbonsäuren sowie Aminosäuren hatte signifikanten Einfluss auf die Partikelmorphologie und die Oxidationsstufe des Kupfers. Auf diese Weise konnten zuvor nicht berichtete Cu_2O-Formen erzeugt werden. Außerdem wurden zahlreiche CuO-Katalysatoren mit unterschiedlichen Oberflächenstrukturen hergestellt. Alle Materialien wurden als Elektrokatalysatoren in der elektrochemischen CO_2-Reduktion verwendet und führten mitunter zu deutlich unterschiedlichen Produktverteilungen. Detektierte Produkte waren CO, Formiat, Ethylen, Ethanol und n-Propanol. Dabei wurde tendenziell eine höhere Faraday-Effizienz für C_{2+}-Produkte

erreicht, wenn Kupferoxide bzw. basisches Kupfercarbonat verwendet wurde. Mit einer Stromdichte von $100\,\text{mA}\,\text{cm}^{-2}$ konnte Ethylen mit über $20\,\%$ Faraday-Effizienz hergestellt werden. Katalysatoren aus elementarem Kupfer führten überwiegend zu C_1-Produkten und Wasserstoff. Zusammenhänge von konkreten Materialeigenschaften und den daraus folgenden Unterschieden in der elektrochemischen CO_2-Reduktion wurden nicht offensichtlich. Der wahrscheinliche Grund hierfür ist, dass mit der Veränderung eines Parameters in der Materialsynthese sofort eine Vielzahl von Eigenschaften des Katalysators (Partikelgröße, Morphologie, Korngrößen) beeinflusst wurde. Dennoch konnte aufgezeigt werden, dass die Produktverteilung in der CO_2RR mitunter sensibel auf Variationen in der Katalysatorherstellung reagiert.

Der zweite Themenkomplex behandelte die Inkorporation von CO_2 in organische Moleküle. Dabei wurde Kohlenstoffdioxid verwendet um eine Säuregruppe in Aldehyde und Ketone einzuführen. Auf diese Weise wurden α-Hydroxycarbonsäuren hergestellt. Das erarbeitete Protokoll stellt somit eine Alternative zur konventionellen Synthese mithilfe von hochgiftigen Cyaniden und anschließender Nitrilhydrolyse dar. In der vorliegenden Arbeit wurde außerdem auf die Verwendung von Opferanoden verzichtet, welche im Großteil der Studien von Elektrocaboxylierungen genutzt werden. Dadurch konnte die Kontamination des Elektrolyten mit Metallspezies vermieden werden. Als Lösungsmittel hat sich Propylencarbonat als besonders vorteilhaft erwiesen. Die hohe Polarität sorgt vermutlich für eine Stabilisierung der durch die Reaktion gebildeten geladenen Intermediate sowie des Carboxylats. Die Verwendung von Propylencarbonat ist eine *grüne* und ungiftige Alternative zu den oft genutzten Lösungsmitteln *N,N*-Dimethylformamid und Acetonitril. Mithilfe des entwickelten Protokolls wurde eine Reihe von Ketonen und Aldehyden mit Ausbeuten bis zu $63\,\%$ carboxyliert.

In den weiteren Arbeiten wurden industriell relevante Elektroreduktionen untersucht. Im dritten Themengebiet wurde die elektrochemische Reduktion von L-Cystin zu L-Cystein unter Spaltung des Disulfids betrachtet. Im Anschluss an ein Elektrodenscreening wurde die Reaktion mithilfe statistischer Methoden optimiert. Zunächst wurden in einem Teilfaktorplan mit fünf Parametern die signifikanten Faktoren bestimmt. In der anschließenden Maximierung der Wunschfunktion aus Ausbeute und Faraday-Effizienz konnte die optimale Ladungsmenge bestimmt werden, nach derer die Stromdichte abgesenkt werden muss um die Wasserstofferzeugung zu minimieren. Die erreichte Ausbeute von L-Cystein betrug nach Optimierung über $99\,\%$ bei einer geringen applizierten Ladungsmenge von $2.65\,F$.

Im vierten Themengebiet wurde die Reduktion von 3-Nitrobenzotrifluorid zur entsprechenden Aminoverbindung skaliert. Besonderer Fokus lag auf der Vereinfachung der Produktisolation. Durch das Ausfällen des Produkts als Aminiumsalz während der Reaktion ist es möglich kontinuierlich reines Produkt aus dem Elektrolyten zu entnehmen. Die Reaktion konnte erfolgreich im zweistelligen Grammbereich für mehrere Nitroverbindungen demonstriert werden.

5 Ausblick

Die elektrochemische CO_2-Reduktion ist ein komplexes Forschungsfeld mit zahlreichen Teilgebieten. Diese erstrecken sich von der Katalysatorentwicklung über das Zelldesign, Elektrolyt und Reaktionsbedingungen hin zu techno-ökonomischen Studien. Allein die Katalysatorentwicklung unterteilt sich nochmals viele unterschiedliche Ansätze, wie z.B. die Beeinflussung der Morphologie oder der Einbettung in Polymere zur Veränderung der Katalysatoroberfläche. Die Ansatzpunkte für einen Fortgang der Forschung in der elektrochemischen CO_2-Reduktion sind mannigfaltig. Für eine technische Anwendung der CO_2RR müssen mehrere Hürden genommen werden. Die Faraday-Effizienz (und folglich auch die Energieeffizienz) zur Bildung von C_{2+}-Produkten, wie Ethylen ist für eine wirtschaftliche Produktion zu gering. C_1-Produkte können mithilfe geeigneter Katalysatoren bereits mit sehr guter Selektivität hergestellt werden, jedoch ist auch die Wertschöpfung geringer. Im Fall von Formiat kommt die aufwändige Produktisolation aus dem wässrigen Elektrolyten hinzu. Neben der Verbesserung der Selektivität in Richtung spezifischer C_{2+}-Produkte, ist die Langzeitstabilität des Elektrokatalysators ein entscheidender Gegenstand der Forschung. Durch Anlagerung inerter Intermediate oder durch Abscheidung von Verunreinigungen im Elektrolyten nimmt die Aktivität der eingesetzten Katalysatoren ab.[43] Die Mechanismen des Aktivitätsverlusts sind noch nicht vollständig verstanden und müssen daher weiter erforscht werden. Eine große Herausforderung ist auch die Vielzahl der genutzten Versuchsaufbauten und Techniken, worunter die Vergleichbarkeit und Reproduzierbarkeit der zahllosen Studien leidet. Die Etablierung standardisierter Bedingungen würde erheblichen Mehrwert schaffen.

Die Elektrocarboxylierung unter Verwendung von CO_2 konnte an mehreren Aldehyden und Ketonen demonstriert werden. Eine Ausbeute von 65 % konnte dabei allerdings nicht übertroffen werden. Für die verhältnismäßig geringen Ausbeuten ist die Dimerisierung der Edukte verantwortlich, welche trotz niedrigem Wassergehalts des Lösungsmittels nur zum Teil unterdrückt werden konnte. Ein Ansatzpunkt für weitere Untersuchungen ist die Unterdrückung der Dimerisierung (zusätzlich zum Wasserausschluss), möglicherweise durch weitere Additive oder vorherige Derivatisierung sodass eine Dimerisierung sterisch gehemmt wird. Zukünftige Studien könnten sich außerdem mit der Oxidation der α-Hydroxycarbonsäuren zu α-Ketosäuren beschäftigen. Diese dienen häufig als Acylierungsmittel unter Abspaltung von CO_2. Da zuvor CO_2 inkorporiert wurde, entsteht in der Bilanz kein CO_2-Abfall. Ideal wäre eine anodische Oxidation in einer ungeteilten Zelle, sodass Carboxylierung und Oxidation zur Ketosäure in einer gepaarten Elektrolyse stattfinden (Schema 8). Eine folgende Acylierung kann wahrscheinlich ebenfalls elektrochemisch realisiert werden.

Die in dieser Arbeit durchgeführten Studien zur elektrochemischen Disulfidspaltung haben sich
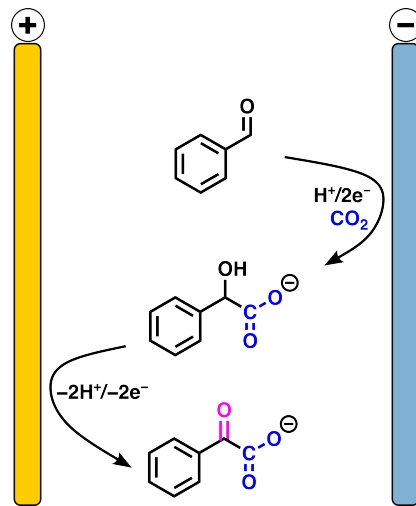
Schema 8: Hypothetische kathodische Carboxylierung eines Aldehyds und anschließende anodische Oxidation zur Ketosäure.

lediglich auf L-Cystin als Substrat beschränkt. Prinzipiell ist die Erweiterung des Substratspektrums auf Proteine bzw. Proteinfragmente denkbar. Hier könnte man das häufig genutzte, giftige 2-Mercaptoethanol ersetzen, welches im Überschuss für Disulfidspaltungen verwendet wird:

$$R{-}S{-}S{-}R + 2\,HS{-}(CH_2)_2{-}OH \rightleftharpoons 2\,R{-}SH + HO{-}(CH_2)_2{-}S{-}S{-}(CH_2)_2{-}OH$$
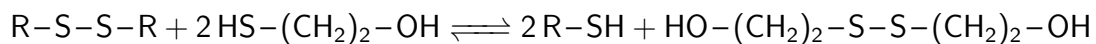
2-Mercaptoethanol wird auch als Stabilisator in Enzymreaktionen eingesetzt um die Oxidation von Proteinen zu verhindern. Das gebildete Mercaptoethanol-Disulfid ließe sich voraussichtlich elektrochemisch wieder zum 2-Mercaptoethanol reduzieren.

In den durchgeführten Arbeiten zur Reduktion von Nitroverbindungen wurde das gebildete Amin als Amminiumsalz ausgefällt und durch einfache Filtration isoliert. Die Feststoffbildung während der Elektrolyse stellt allerdings besondere Anforderungen an das Zelldesign um das Verstopfen von Kanälen zu vermeiden. Ein hoher Feststoffballast im Elektrolyten kann zudem die Zellspannung und damit die Betriebskosten erhöhen. Um Abhilfe zu schaffen, kann eine Filtrationseinheit vor oder nach der Zelle installiert werden, sodass der Feststoff im Batch-recycle-Modus nicht erneut die Zelle durchläuft.

Die Reduktion der Nitrogruppe durchläuft die Bildung des Hydroxylamins als Zwischenstufe. Unter geeigneten Bedingungen ließe sich wahrscheinlich die Bamberger-Umlagerung forcieren, sodass das entsprechende 4-Aminophenol zugänglich gemacht wird.

Literatur

[1] Hammerich, O. und Speiser, B. *Organic electrochemistry: revised and expanded*. CRC Press, 2016.

[2] Hamann, C. H., Hamnett, A. und Vielstich, W. *Electrochemistry*. Weinheim, Germany: Wiley-VCH, 2007, S. 159–164.

[3] Wiebe, A. et al. „Electrifying Organic Synthesis". In: *Angewandte Chemie - International Edition* 57.20 (2018), S. 5594–5619. DOI: 10.1002/anie.201711060.

[4] Horn, E. J., Rosen, B. R. und Baran, P. S. „Synthetic organic electrochemistry: An enabling and innately sustainable method". In: *ACS Central Science* 2.5 (2016), S. 302–308. DOI: 10.1021/acscentsci.6b00091.

[5] Cardoso, D. S. et al. „Organic Electrosynthesis: From Laboratorial Practice to Industrial Applications". In: *Organic Process Research and Development* 21.9 (2017), S. 1213–1226. DOI: 10.1021/acs.oprd.7b00004.

[6] Holzhäuser, F. J., Mensah, J. B. und Palkovits, R. „(Non-)Kolbe electrolysis in biomass valorization-a discussion of potential applications". In: *Green Chemistry* 22.2 (2020), S. 286–301. DOI: 10.1039/c9gc03264a.

[7] Schäfer, H. „Recent synthetic applications of the Kolbe electrolysis". In: *Chemistry and Physics of Lipids* 24.4 (Aug. 1979), S. 321–333. DOI: 10.1016/0009-3084(79)90117-8.

[8] Schulz, L. und Waldvogel, S. „Solvent Control in Electro-Organic Synthesis". In: *Synlett* 30.03 (Feb. 2019), S. 275–286. DOI: 10.1055/s-0037-1610303.

[9] Klein, M. und Waldvogel, S. R. „Counter Electrode Reactions — Important Stumbling Blocks on the Way to a Working Electro-Organic Synthesis". In: *Angewandte Chemie International Edition* (2022). DOI: 10.1002/anie.202204140.

[10] Pollok, D. und Waldvogel, S. R. „Electro-organic synthesis — a 21st century technique". In: *Chemical Science* 11.46 (2020), S. 12386–12400. DOI: 10.1039/d0sc01848a.

[11] Schmidt, V. M. *Elektrochemische Verfahrenstechnik: Grundlagen, Reaktionstechnik, Prozessoptimierung*. John Wiley & Sons, 2012.

[12] Pletcher, D. und Walsh, F. C. *Industrial Electrochemistry*. Dordrecht: Springer Netherlands, 1993. DOI: 10.1007/978-94-011-2154-5.

[13] Heard, D. M. und Lennox, A. J. „Electrode Materials in Modern Organic Electrochemistry". In: *Angewandte Chemie - International Edition* 59.43 (2020), S. 18866–18884. DOI: 10.1002/anie.202005745.

[14] Nitopi, S. et al. „Progress and Perspectives of Electrochemical CO_2 Reduction on Copper in Aqueous Electrolyte". In: *Chemical Reviews* 119.12 (Juni 2019), S. 7610–7672. DOI: 10.1021/acs.chemrev.8b00705.

[15] Couper, A. M., Pletcher, D. und Walsh, F. C. „Electrode materials for electrosynthesis". In: *Chemical Reviews* 90.5 (Juli 1990), S. 837–865. DOI: 10.1021/cr00103a010.

[16] Wei, C. et al. „Approaches for measuring the surface areas of metal oxide electrocatalysts for determining their intrinsic electrocatalytic activity". In: *Chemical Society Reviews* 48.9 (2019), S. 2518–2534. DOI: 10.1039/c8cs00848e.

[17] Raciti, D. und Wang, C. „Recent Advances in CO_2 Reduction Electrocatalysis on Copper". In: *ACS Energy Letters* 3.7 (Juli 2018), S. 1545–1556. DOI: 10.1021/acsenergylett.8b00553.

[18] Biesheuvel, P. M., Porada, S. und Dykstra, J. E. „The difference between Faradaic and non-Faradaic electrode processes". In: *arXiv preprint* (2018), S. 1–16. arXiv: 1809.02930.

[19] Hayyan, M. et al. „Investigating the electrochemical windows of ionic liquids". In: *Journal of Industrial and Engineering Chemistry* 19.1 (Jan. 2013), S. 106–112. DOI: 10.1016/j.jiec.2012.07.011.

[20] Gütz, C. et al. „Leaded Bronze: An Innovative Lead Substitute for Cathodic Electrosynthesis". In: *ChemElectroChem* 5.2 (Jan. 2018), S. 247–252. DOI: 10.1002/celc.201701061.

[21] Seidler, J. et al. „From Screening to Scale-Up: The DoE-Based Optimization of Electrochemical Reduction of L-Cystine at Metal Cathodes". In: *Organic Process Research & Development* 25.12 (Dez. 2021), S. 2622–2630. DOI: 10.1021/acs.oprd.1c00153.

[22] Connor, P. et al. „The Determination of Electrochemical Active Surface Area and Specific Capacity Revisited for the System MnOx as an Oxygen Evolution Catalyst". In: *Zeitschrift fur Physikalische Chemie* 234.5 (2020), S. 979–994. DOI: 10.1515/zpch-2019-1514.

[23] North, M. und Styring, P., Hrsg. *Fundamentals*. De Gruyter, Dez. 2019, S. 285–302. DOI: 10.1515/9783110563191.

[24] Radhakrishnan, S. G. und Roduner, E. „13. Carbon dioxide activation". In: *Fundamentals*. De Gruyter, Dez. 2019, S. 227–248. DOI: 10.1515/9783110563191-013.

[25] Liu, Q. et al. „Using carbon dioxide as a building block in organic synthesis". In: *Nature Communications* 6 (2015). DOI: 10.1038/ncomms6933.

[26] Dabral, S. und Schaub, T. „The Use of Carbon Dioxide (CO_2) as a Building Block in Organic Synthesis from an Industrial Perspective". In: *Advanced Synthesis & Catalysis* 361.2 (Jan. 2019), S. 223–246. DOI: 10.1002/adsc.201801215.

[27] De Luna, P. et al. „What would it take for renewably powered electrosynthesis to displace petrochemical processes?" In: *Science* 364.6438 (Apr. 2019), eaav3506. DOI: 10.1126/science.aav3506.

[28] Fan, Q. et al. „Electrochemical CO_2 reduction to C_{2+} species: Heterogeneous electrocatalysts, reaction pathways, and optimization strategies". In: *Materials Today Energy* 10 (Dez. 2018), S. 280–301. DOI: 10.1016/j.mtener.2018.10.003.

[29] Hori, Y. „Electrochemical CO2 Reduction on Metal Electrodes". In: *Modern Aspects of Electrochemistry*. New York, NY: Springer New York, 2008, S. 89–189. DOI: 10.1007/978-0-387-49489-0_3.

[30] Ren, W. und Zhao, C. „Paths towards enhanced electrochemical CO_2 reduction". In: *National Science Review* 7.1 (2020), S. 7–9. DOI: 10.1093/nsr/nwz121.

[31] Iwanow, M. et al. „Enhanced C_2 and C_3 Product Selectivity in Electrochemical CO_2 Reduction on Carbon-Doped Copper Oxide Catalysts Prepared by Deep Eutectic Solvent Calcination". In: *Catalysts* 11.5 (Apr. 2021), S. 542. DOI: 10.3390/catal11050542.

[32] Kas, R. et al. „Electrochemical CO_2 reduction on Cu_2O-derived copper nanoparticles: Controlling the catalytic selectivity of hydrocarbons". In: *Physical Chemistry Chemical Physics* 16.24 (2014), S. 12194–12201. DOI: 10.1039/c4cp01520g.

[33] Wyndorps, J., Ostovari, H. und Assen, N. von der. „Is electrochemical CO_2 reduction the future technology for power-to-chemicals? An environmental comparison with H_2-based pathways". In: *Sustainable Energy and Fuels* 5.22 (2021), S. 5748–5761. DOI: 10.1039/d1se00975c.

[34] Köster, F., Dinjus, E. und Diñach, E. „Electrochemical selective incorporation of CO_2 into terminal alkynes and diynes". In: *European Journal of Organic Chemistry* 13 (2001), S. 2507–2511. DOI: 10.1002/1099-0690(200107)2001:13⟨2507::aid-ejoc2507⟩3.0.co;2-p.

[35] Mena, S., Bernad, J. und Guirado, G. „Electrochemical incorporation of carbon dioxide into fluorotoluene derivatives under mild conditions". In: *Catalysts* 11.8 (2021), S. 9–11. DOI: 10.3390/catal11080880.

[36] Santiago, S. et al. „Electrocarboxylation of Spiropyran Switches through Carbon-Bromide Bond Cleavage Reaction". In: *ChemElectroChem* 9.8 (2022), e202101559. DOI: 10.1002/celc.202101559.

[37] Gallardo-Fuentes, S. et al. „On the mechanism of CO_2 electro-cycloaddition to propylene oxides". In: *Journal of CO_2 Utilization* 16 (2016), S. 114–120. DOI: 10.1016/j.jcou.2016.06.007.

[38] Moura de Salles Pupo, M. und Kortlever, R. „Electrolyte Effects on the Electrochemical Reduction of CO2". In: *ChemPhysChem* 20.22 (2019), S. 2926–2935. DOI: 10.1002/cphc.201900680.

[39] García de Arquer, F. P. et al. „CO_2 electrolysis to multicarbon products at activities greater than $1\,A\,cm^{-2}$". In: *Science* 367.6478 (Feb. 2020), S. 661–666. DOI: 10.1126/science.aay4217.

[40] Hoang, T. T. H. et al. „Nanoporous Copper–Silver Alloys by Additive-Controlled Electrodeposition for the Selective Electroreduction of CO_2 to Ethylene and Ethanol". In: *Journal of the American Chemical Society* 140.17 (Mai 2018), S. 5791–5797. DOI: 10.1021/jacs.8b01868.

[41] Fan, L. et al. „Strategies in catalysts and electrolyzer design for electrochemical CO_2 reduction toward C_{2+} products". In: *Science Advances* 6.8 (2020), S. 1–18. DOI: 10.1126/sciadv.aay3111.

[42] Xie, M. S. et al. „Amino acid modified copper electrodes for the enhanced selective electroreduction of carbon dioxide towards hydrocarbons". In: *Energy and Environmental Science* 9.5 (2016), S. 1687–1695. DOI: 10.1039/c5ee03694a.

[43] Zhang, W. et al. „Progress and Perspective of Electrocatalytic CO_2 Reduction for Renewable Carbonaceous Fuels and Chemicals". In: *Advanced Science* 5.1 (Jan. 2018), S. 1700275. DOI: 10.1002/advs.201700275.

[44] Kibria, M. G. et al. „Electrochemical CO_2 Reduction into Chemical Feedstocks: From Mechanistic Electrocatalysis Models to System Design". In: *Advanced Materials* 31.31 (2019), S. 1–24. DOI: 10.1002/adma.201807166.

[45] Luo, J. und Larrosa, I. „C-H Carboxylation of Aromatic Compounds through CO_2 Fixation". In: *ChemSusChem* 10.17 (2017), S. 3317–3332. DOI: 10.1002/cssc.201701058.

[46] Wiebe, A. et al. „Electrifying Organic Synthesis". In: *Angewandte Chemie International Edition* 57.20 (Mai 2018), S. 5594–5619. DOI: 10.1002/anie.201711060.

[47] Waldvogel, S. R. und Janza, B. „Renaissance of Electrosynthetic Methods for the Construction of Complex Molecules". In: *Angewandte Chemie International Edition* 53.28 (Juli 2014), S. 7122–7123. DOI: 10.1002/anie.201405082.

[48] Waldvogel, S. R. et al. „Electrochemical Arylation Reaction". In: *Chemical Reviews* 118.14 (Juli 2018), S. 6706–6765. DOI: 10.1021/acs.chemrev.8b00233.

[49] Yan, M., Kawamata, Y. und Baran, P. S. „Synthetic Organic Electrochemical Methods Since 2000: On the Verge of a Renaissance". In: *Chemical Reviews* 117.21 (Nov. 2017), S. 13230–13319. DOI: 10.1021/acs.chemrev.7b00397.

[50] Küngas, R. „Review — Electrochemical CO_2 Reduction for CO Production: Comparison of Low- and High-Temperature Electrolysis Technologies". In: *Journal of The Electrochemical Society* 167.4 (Jan. 2020), S. 044508. DOI: 10.1149/1945-7111/ab7099.

[51] Al-Rowaili, F. N. et al. „A Review on Recent Advances for Electrochemical Reduction of Carbon Dioxide to Methanol Using Metal-Organic Framework (MOF) and Non-MOF Catalysts: Challenges and Future Prospects". In: *ACS Sustainable Chemistry & Engineering* 6.12 (Dez. 2018), S. 15895–15914. DOI: 10.1021/acssuschemeng.8b03843.

[52] Yang, D. et al. „Selective electroreduction of carbon dioxide to methanol on copper selenide nanocatalysts". In: *Nature Communications* 10.1 (Dez. 2019), S. 677. DOI: 10.1038/s41467-019-08653-9.

[53] Lv, K. et al. „Elastic Ag-anchored N-doped graphene/carbon foam for the selective electrochemical reduction of carbon dioxide to ethanol". In: *Journal of Materials Chemistry A* 6.12 (2018), S. 5025–5031. DOI: 10.1039/C7TA10802H.

[54] Hoang, T. T. H. et al. „Nanoporous Copper-Silver Alloys by Additive-Controlled Electrodeposition for the Selective Electroreduction of CO_2 to Ethylene and Ethanol". In: *Journal of the American Chemical Society* 140.17 (Mai 2018), S. 5791–5797. DOI: 10.1021/jacs.8b01868.

[55] Li, F. et al. „Molecular tuning of CO_2-to-ethylene conversion". In: *Nature* 577.7791 (Jan. 2020), S. 509–513. DOI: 10.1038/s41586-019-1782-2.

[56] Möhle, S. et al. „Modern Electrochemical Aspects for the Synthesis of Value-Added Organic Products". In: *Angewandte Chemie International Edition* 57.21 (Mai 2018), S. 6018–6041. DOI: 10.1002/anie.201712732.

[57] Hermeling, D., Hannebaum, H. und Weiper-Idelmann, A. *Process for the preparation of benzaldehyde dialkyl acetals*. 1996.

[58] Röckl, J. L. et al. „Dehydrogenative Anodic C-C Coupling of Phenols Bearing Electron-Withdrawing Groups". In: *Angewandte Chemie International Edition* 59.1 (Jan. 2020), S. 315–319. DOI: 10.1002/anie.201910077.

[59] Kirste, A. et al. „Efficient Anodic and Direct Phenol-Arene C,C Cross-Coupling: The Benign Role of Water or Methanol". In: *Journal of the American Chemical Society* 134.7 (Feb. 2012), S. 3571–3576. DOI: 10.1021/ja211005g.

[60] Kuhl, K. P. et al. „New insights into the electrochemical reduction of carbon dioxide on metallic copper surfaces". In: *Energy and Environmental Science* 5.5 (2012), S. 7050–7059. DOI: 10.1039/c2ee21234j.

[61] Tang, W. et al. „The importance of surface morphology in controlling the selectivity of polycrystalline copper for CO2 electroreduction". In: *Physical Chemistry Chemical Physics* 14.1 (2012), S. 76–81. DOI: 10.1039/c1cp22700a.

[62] Suen, N.-T. et al. „Morphology Manipulation of Copper Nanocrystals and Product Selectivity in the Electrocatalytic Reduction of Carbon Dioxide". In: *ACS Catalysis* 9.6 (Juni 2019), S. 5217–5222. DOI: 10.1021/acscatal.9b00790.

[63] Gawande, M. B. et al. „Cu and Cu-Based Nanoparticles: Synthesis and Applications in Catalysis". In: *Chemical Reviews* 116.6 (März 2016), S. 3722–3811. DOI: 10.1021/acs.chemrev.5b00482.

[64] Singh, J., Kaur, G. und Rawat, M. „A Brief Review on Synthesis and Characterization of Copper Oxide Nanoparticles and its Applications". In: *Journal of Bioelectronics and Nanotechnology* 1.1 (2016). DOI: 10.13188/2475-224X.1000003.

[65] Barreca, D. et al. „Chemical vapor deposition of copper oxide films and entangled quasi-1D nanoarchitectures as innovative gas sensors". In: *Sensors and Actuators B: Chemical* 141.1 (Aug. 2009), S. 270–275. DOI: 10.1016/j.snb.2009.05.038.

[66] Li, S. et al. „One-step hydrothermal synthesis of CuO hollow spheres with high photocatalytic activity". In: *Physica E: Low-dimensional Systems and Nanostructures* 126 (Feb. 2021), S. 114489. DOI: 10.1016/j.physe.2020.114489.

[67] Zhang, F. et al. „One-step hydrothermal synthesis of Cu_2O/CuO hollow microspheres/reduced graphene oxide hybrid with enhanced sensitivity for non-enzymatic glucose sensing". In: *Colloids and Surfaces A: Physicochemical and Engineering Aspects* 602 (Okt. 2020), S. 125076. DOI: 10.1016/j.colsurfa.2020.125076.

[68] Kang, K.-Y. und Chun, B.-S. „Behavior of amino acid production from hydrothermal treatment of fish-derived wastes". In: *Korean Journal of Chemical Engineering* 21.6 (Dez. 2004), S. 1147–1152. DOI: 10.1007/BF02719486.

[69] Pietrucci, F. et al. „Hydrothermal Decomposition of Amino Acids and Origins of Prebiotic Meteoritic Organic Compounds". In: *ACS Earth and Space Chemistry* 2.6 (Juni 2018), S. 588–598. DOI: 10.1021/acsearthspacechem.8b00025.

[70] Newman, J. D. S. und Blanchard, G. J. „Formation of Gold Nanoparticles Using Amine Reducing Agents". In: *Langmuir* 22.13 (Juni 2006), S. 5882–5887. DOI: 10.1021/la060045z.

[71] Lin, Z., Han, D. und Li, S. „Study on thermal decomposition of copper(II) acetate monohydrate in air". In: *Journal of Thermal Analysis and Calorimetry* 107.2 (2012), S. 471–475. DOI: 10.1007/s10973-011-1454-4.

[72] Zhang, Y.-H. et al. „Morphology-controllable Cu_2O supercrystals: Facile synthesis, facet etching mechanism and comparative photocatalytic H2 production". In: *Journal of Alloys and Compounds* 729 (Dez. 2017), S. 563–570. DOI: 10.1016/j.jallcom.2017.09.237.

[73] Vink, B. W. „Stability relations of malachite and azurite". In: *Mineralogical Magazine* 50.355 (1986), S. 41–47. DOI: 10.1017/minmag.1986.050.355.06.

[74] Mansour, S. A. A. „Thermoanalytical investigations of decomposition course of copper oxysalts". In: *Journal of Thermal Analysis* 42.6 (Dez. 1994), S. 1251–1263. DOI: 10.1007/BF02546934.

[75] Zhou, M. et al. „Carbonate-Assisted Hydrothermal Synthesis of Nanoporous CuO Microstructures and Their Application in Catalysis". In: *European Journal of Inorganic Chemistry* 2010.5 (Feb. 2010), S. 729–734. DOI: 10.1002/ejic.200900683.

[76] Anu Prathap, M., Kaur, B. und Srivastava, R. „Hydrothermal synthesis of CuO micro-/nanostructures and their applications in the oxidative degradation of methylene blue and non-enzymatic sensing of glucose/H2O2". In: *Journal of Colloid and Interface Science* 370.1 (März 2012), S. 144–154. DOI: 10.1016/j.jcis.2011.12.074.

[77] Seidler, J. et al. „Novel cuprous oxide morphologies using amino acids and carboxylic acids as structure directing agents in a simple hydrothermal method". In: *Materials Letters* 292 (Juni 2021), S. 129553. DOI: 10.1016/j.matlet.2021.129553.

[78] Paquin, F. et al. „Multi-phase semicrystalline microstructures drive exciton dissociation in neat plastic semiconductors". In: *J. Mater. Chem. C* 3 (2015), S. 10715–10722. DOI: 10.1039/b000000x. arXiv: arXiv:1310.8002v1.

[79] Ortiz, N. und Skrabalak, S. E. „On the dual roles of ligands in the synthesis of colloidal metal nanostructures". In: *Langmuir* 30.23 (2014), S. 6649–6659. DOI: 10.1021/la404539p.

[80] Mourdikoudis, S. und Liz-Marzán, L. M. „Oleylamine in nanoparticle synthesis". In: *Chemistry of Materials* 25.9 (2013), S. 1465–1476. DOI: 10.1021/cm4000476.

[81] Chen, M. et al. „Silver nanoparticles capped by oleylamine: Formation, growth, and self-organization". In: *Langmuir* 23.10 (2007), S. 5296–5304. DOI: 10.1021/la700553d.

[82] Weiss, I. M. et al. „Thermal decomposition of the amino acids glycine, cysteine, aspartic acid, asparagine, glutamic acid, glutamine, arginine and histidine". In: *BMC Biophysics* 11.1 (2018), S. 1–15. DOI: 10.1186/s13628-018-0042-4.

[83] Wiecinska, P. „Thermal degradation of organic additives used in colloidal shaping of ceramics investigated by the coupled DTA/TG/MS analysis". In: *Journal of Thermal Analysis and Calorimetry* 123.2 (Feb. 2016), S. 1419–1430. DOI: 10.1007/s10973-015-5075-1.

[84] Bang, J. H. et al. „Decoration of multi-walled carbon nanotubes with CuO/Cu_2O nanoparticles for selective sensing of H_2S gas". In: *Sensors and Actuators B: Chemical* 344 (Okt. 2021), S. 130176. DOI: 10.1016/j.snb.2021.130176.

[85] Zheng, J. et al. „Nanocomposites of carbon nanotube (CNTs)/CuO with high sensitivity to organic volatiles at room temperature". In: *Procedia Engineering* 36 (2012), S. 235–245. DOI: 10.1016/j.proeng.2012.03.036.

[86] Hammond, O. S. et al. „Deep eutectic-solvothermal synthesis of nanostructured ceria". In: *Nature Communications* 8 (Jan. 2017), S. 14150.

[87] Smith, E. L., Abbott, A. P. und Ryder, K. S. „Deep eutectic solvents (DESs) and their applications". In: *Chemical reviews* 114.21 (2014), S. 11060–11082.

[88] Carriazo, D. et al. „Deep-eutectic solvents playing multiple roles in the synthesis of polymers and related materials". In: *Chem. Soc. Rev.* 41.14 (2012), S. 4996–5014. DOI: 10.1039/C2CS15353J.

[89] Zhang, Q. et al. „Deep eutectic solvents: syntheses, properties and applications". In: *Chem. Soc. Rev.* 41.21 (2012), S. 7108–7146. DOI: 10.1039/C2CS35178A.

[90] Marchel, M., Cieśliński, H. und Boczkaj, G. „Thermal Instability of Choline Chloride-Based Deep Eutectic Solvents and Its Influence on Their Toxicity-Important Limitations of DESs as Sustainable Materials". In: *Industrial and Engineering Chemistry Research* 61.30 (2022), S. 11288–11300. DOI: 10.1021/acs.iecr.2c01898.

[91] Pander, J. E. et al. „Understanding the Heterogeneous Electrocatalytic Reduction of Carbon Dioxide on Oxide-Derived Catalysts". In: *ChemElectroChem* 5.2 (Jan. 2018), S. 219–237. DOI: 10.1002/celc.201701100.

[92] Lum, Y. und Ager, J. W. „Stability of Residual Oxides in Oxide-Derived Copper Catalysts for Electrochemical CO_2 Reduction Investigated with ^{18}O Labeling". In: *Angewandte Chemie International Edition* 57.2 (Jan. 2018), S. 551–554. DOI: 10.1002/anie.201710590.

[93] Reske, R. et al. „Particle size effects in the catalytic electroreduction of CO_2 on Cu nanoparticles". In: *Journal of the American Chemical Society* 136.19 (2014), S. 6978–6986. DOI: 10.1021/ja500328k.

[94] Weatherup, R. S. et al. „Environment-Dependent Radiation Damage in Atmospheric Pressure X-ray Spectroscopy". In: *The Journal of Physical Chemistry B* 122.2 (Jan. 2018), S. 737–744. DOI: 10.1021/acs.jpcb.7b06397.

[95] Zahid, A., Shah, A. und Shah, I. „Oxide Derived Copper for Electrochemical Reduction of CO_2 to C_{2+} Products". In: *Nanomaterials* 12.8 (Apr. 2022), S. 1380. DOI: 10.3390/nano12081380.

[96]   Ren, D., Fong, J. und Yeo, B. S. „The effects of currents and potentials on the selectivities of copper toward carbon dioxide electroreduction". In: *Nature Communications* 9.1 (2018). DOI: 10.1038/s41467-018-03286-w.

[97]   Thevenon, A. et al. „Dramatic HER Suppression on Ag Electrodes via Molecular Films for Highly Selective CO_2 to CO Reduction". In: *ACS Catalysis* 11.8 (2021), S. 4530–4537. DOI: 10.1021/acscatal.1c00338.

[98]   Corbin, N. et al. „Suppressing carboxylate nucleophilicity with inorganic salts enables selective electrocarboxylation without sacrificial anodes". In: *Chemical Science* (2021). DOI: 10.1039/d1sc02413b.

[99]   Miltenberger, K. „Hydroxycarboxylic Acids, Aliphatic". In: *Ullmann's Encyclopedia of Industrial Chemistry*. Weinheim, Germany: Wiley-VCH Verlag GmbH & Co. KGaA, Juni 2000. DOI: 10.1002/14356007.a13_507.

[100]   Ritzer, E. und Sundermann, R. „Hydroxycarboxylic Acids, Aromatic". In: *Ullmann's Encyclopedia of Industrial Chemistry*. Weinheim, Germany: Wiley-VCH Verlag GmbH & Co. KGaA, Juni 2000. DOI: 10.1002/14356007.a13_519.

[101]   Senboku, H. und Katayama, A. „Electrochemical carboxylation with carbon dioxide". In: *Current Opinion in Green and Sustainable Chemistry* 3 (Feb. 2017), S. 50–54. DOI: 10.1016/j.cogsc.2016.10.003.

[102]   Matthessen, R. et al. „Electrocarboxylation: towards sustainable and efficient synthesis of valuable carboxylic acids". In: *Beilstein Journal of Organic Chemistry* 10 (Okt. 2014), S. 2484–2500. DOI: 10.3762/bjoc.10.260.

[103]   Singh, K., Sohal, H. S. und Singh, B. „Synthesis of α-hydroxycarboxylic acids from various aldehydes and ketones by direct electrocarboxylation: A facile, efficient and atom economy protocol". In: *Asian Journal of Chemistry* 33.4 (2021), S. 839–845. DOI: 10.14233/ajchem.2021.23090.

[104]   Senboku, H. et al. „Efficient Synthesis of Mandel Acetates by Electrochemical Carboxylation of Benzal Diacetates". In: *ChemElectroChem* 6.16 (Aug. 2019), S. 4158–4164. DOI: 10.1002/celc.201900200.

[105]   Zhao, S. F. et al. „Electrocarboxylation of acetophenone in ionic liquids: The influence of proton availability on product distribution". In: *Green Chemistry* 16.4 (2014), S. 2242–2251. DOI: 10.1039/c3gc42404a.

[106]   Matthessen, R. et al. „Electrochemical dicarboxylation of conjugated fatty acids as an efficient valorization of carbon dioxide". In: *RSC Advances* 3.14 (2013), S. 4634. DOI: 10.1039/c3ra00129f.

[107]   Saravanan, K. R., Chandrasekaran, M. und Suryanarayanan, V. „Efficient electrocarboxylation of benzophenone on silver nanoparticles deposited boron doped diamond electrode". In: *Journal of Electroanalytical Chemistry* 757 (2015), S. 18–22. DOI: 10.1016/j.jelechem.2015.08.033.

[108] Yang, H. P. et al. „Platinum/nitrogen-doped carbon/carbon cloth: A bifunctional catalyst for the electrochemical reduction and carboxylation of CO_2 with excellent efficiency“. In: *Chemical Communications* 54.33 (2018), S. 4108–4111. DOI: 10.1039/c8cc00969d.

[109] Zhang, K. et al. „Electrochemical reduction of aliphatic conjugated dienes in the presence of carbon dioxide“. In: *Electrochemistry Communications* 12.12 (Dez. 2010), S. 1698–1702. DOI: 10.1016/j.elecom.2010.09.028.

[110] Liu, X.-F. et al. „Recent advances in electrochemical carboxylation reactions using carbon dioxide“. In: *Green Chemical Engineering* 3.2 (2022), S. 125–137. DOI: 10.1016/j.gce.2021.12.001.

[111] Muchez, L., De Vos, D. E. und Kim, M. J. „Sacrificial Anode-Free Electrosynthesis of α-Hydroxy Acids via Electrocatalytic Coupling of Carbon Dioxide to Aromatic Alcohols“. In: *ACS Sustainable Chemistry and Engineering* 7.19 (2019), S. 15860–15864. DOI: 10.1021/acssuschemeng.9b04612.

[112] Anouti, M. M. et al. „Low pressure carbon dioxide solubility in pure electrolyte solvents for lithium-ion batteries as a function of temperature. Measurement and prediction“. In: *Journal of Chemical Thermodynamics* 50.2012 (Juli 2012), S. 71–79. DOI: 10.1016/j.jct.2012.01.027.

[113] König, M. et al. „Solvents and Supporting Electrolytes in the Electrocatalytic Reduction of CO_2“. In: *iScience* 19 (2019), S. 135–160. DOI: 10.1016/j.isci.2019.07.014.

[114] Heard, D. M. und Lennox, A. J. J. „Electrode Materials in Modern Organic Electrochemistry“. In: *Angewandte Chemie* 132.43 (2020), S. 19026–19044. DOI: 10.1002/ange.202005745.

[115] Yuan, G., LI, Z. und JIANG, H. „Electrosyntheses of α-Hydroxycarboxylic Acids from Carbon Dioxide and Aromatic Ketones Using Nickel as the Cathode“. In: *Chinese Journal of Chemistry* 27.8 (Aug. 2009), S. 1464–1470. DOI: 10.1002/cjoc.200990246.

[116] Yuan, G. et al. „Electrosyntheses of α-Hydroxycarboxylic Acids from Carbon Dioxide and Aromatic Ketones Using Nickel as the Cathode“. In: *Chinese Journal of Chemistry* 27.8 (Aug. 2009), S. 1464–1470. DOI: 10.1002/cjoc.200990246.

[117] Lu, Y. et al. „Nanostructured electrocatalysts for electrochemical carboxylation with CO_2“. In: *Nano Select* 1.2 (2020), S. 135–151. DOI: 10.1002/nano.202000001.

[118] Conway, B. E. und Jerkiewicz, G. „Relation of energies and coverages of underpotential and overpotential deposited H at Pt and other metals to the 'volcano curve' for cathodic H2 evolution kinetics“. In: *Electrochimica Acta* 45.25-26 (2000), S. 4075–4083. DOI: 10.1016/S0013-4686(00)00523-5.

[119] McLaughlin, M. H. et al. „Influence of temperature on the electrochemical window of boron doped diamond: a comparison of commercially available electrodes“. In: *Scientific Reports* 10.1 (2020), S. 1–9. DOI: 10.1038/s41598-020-72910-x.

[120] Hashim, Y. et al. „Production of Cysteine: Approaches, Challenges and Potential Solution“. In: *International Journal of Biotechnology for Wellness Industries* 3.3 (Okt. 2014), S. 95–101. DOI: 10.6000/1927-3037.2014.03.03.3.

[121] Takumi, K. et al. „Fermentative Production of Cysteine by Pantoea ananatis". In: *Applied and Environmental Microbiology* 83.5 (März 2017). Hrsg. von Vieille, C. DOI: 10.1128/AEM.02502-16.

[122] Anneliese Reutter-Maier, Brunner, M. und Dassler, T. *Method for production of natural l-cysteine by fermentation*. 2011.

[123] Maier, T. und Winterhalter, C. *Method for production of l-cysteine or l-cysteine derivatives by fermentation*. 1999.

[124] Erlandsson, M. und Hällbrink, M. „Metallic Zinc Reduction of Disulfide Bonds between Cysteine Residues in Peptides and Proteins". In: *International Journal of Peptide Research and Therapeutics* 11.4 (Dez. 2005), S. 261–265. DOI: 10.1007/s10989-005-8113-1.

[125] Yang, W. et al. „Design, synthesis and biological evaluation of bis-aryl ureas and amides based on 2-amino-3-purinylpyridine scaffold as DFG-out B-Raf kinase inhibitors". In: *European Journal of Medicinal Chemistry* 89 (Jan. 2015), S. 581–596. DOI: 10.1016/j.ejmech.2014.10.039.

[126] Wang, Q. et al. „Discovery of 4-cyclopropyl-3-(2-((1-cyclopropyl-1H-pyrazol-4-yl) amino) quinazolin-6-yl)-N-(3-(trifluoromethyl) phenyl) benzamides as potent discoidin domain receptor inhibitors for the treatment of idiopathic pulmonary fibrosis". In: *Acta Pharmaceutica Sinica B* 12.4 (Apr. 2022), S. 1943–1962. DOI: 10.1016/j.apsb.2021.11.012.

[127] Lamberth, C. „Organic Isocyanates and Isothiocyanates: Versatile Intermediates in Agrochemistry". In: *Synthesis* 54.05 (März 2022), S. 1250–1260. DOI: 10.1055/a-1678-8528.

[128] Ung, S. et al. „Ultrasonically activated reduction of substituted nitrobenzenes to corresponding N-arylhydroxylamines". In: *Tetrahedron Letters* 46.35 (Aug. 2005), S. 5913–5917. DOI: 10.1016/j.tetlet.2005.06.126.

[129] Tordeux, M. und Wakselman, C. „The Bamberger reaction in hydrogen fluoride: the use of mild reductive metals for the preparation of fluoroaromatic amines". In: *Journal of Fluorine Chemistry* 74.2 (Okt. 1995), S. 251–254. DOI: 10.1016/0022-1139(95)03257-E.

[130] Belley, M. et al. „Synthesis and reactivity of N-hydroxy-2-aminoindoles". In: *Tetrahedron Letters* 47.2 (Jan. 2006), S. 159–162. DOI: 10.1016/j.tetlet.2005.10.165.

[131] González-Lainez, M. et al. „Effective N -methylation of nitroarenes with methanol catalyzed by a functionalized NHC-based iridium catalyst: a green approach to N -methyl amines". In: *Catalysis Science & Technology* 10.10 (2020), S. 3458–3467. DOI: 10.1039/D0CY00707B.